# Generation of Valuable Products from Carbon Dioxide ($CO_2$) using Bismuth-based Reduced Graphene Oxide (rGO) supported Photocatalytic System

**Thesis submitted by**

**ARINDAM MANDAL**

**Doctor of Philosophy (Engineering)**

**Department of Chemical Engineering**

**Faculty Council of Engineering & Technology**

**Jadavpur University**

**Kolkata, India**

**2024**

# JADAVPUR UNIVERSITY
# KOLKATA – 700032, INDIA

**INDEX NO. D-7/E/312/2018**

## I. Title of the thesis:

Generation of Valuable Products from Carbon Dioxide ($CO_2$) using Bismuth-based Reduced Graphene Oxide (rGO) supported Photocatalytic System.

## II. Name, Designation and Institution of the Supervisor/s:

Dr. Kajari Kargupta, Professor, Department of Chemical Engineering, Jadavpur University, Kolkata-700032, India.

## III. List of Publications:

### International Journal Publications:

[1] Arindam Mandal, Soumyajit Maitra, Subhasis Roy, Baisakhi Hazra, Koustuv Ray and Kajari Kargupta, Selective photo-reduction of $CO_2$ to methanol using Cu-doped 1D-$Bi_2S_3$/rGO nanocomposites under visible light irradiation, New J. Chem. (RSC), 2023,47, 1422-1434. https://doi.org/10.1039/D2NJ03892G

[2] Arindam Mandal, Guruprasad Bhattacharya, and Kajari Kargupta, Enhanced yield of Methanol using rGO-$Bi_2S_3$/CuO heterojunction photocatalyst for $CO_2$ reduction, Journal of Materials Research, 2024. https://doi.org/10.1557/s43578-024-01352-2

## IV. List of Presentation in International Conference

Arindam Mandal, Arundhuti Sarkar, Sayantanu Mondal, Kajari Kargupta, Photocatalytic reduction of $CO_2$ into solar fuels over rGO/$Bi_2S_3$/CuO nanocomposite photocatalysts, International Conference on Chemical Engineering Innovations and Sustainability (ICEIS-2023), Jadavpur University, Kolkata, India, February 26-27, 2023.

## V. List of Presentation in National Conference

Arindam Mandal, Kajari Kargupta, Design of catalyst for photo/electro reduction of $CO_2$ to produce value added chemicals in the two-day WEBINAR organized by R&D Committee, TEQIP-III, Jadavpur University during February 26-27, 2021.

## VI. List of Patents: Nil

## VII. Awards

Best Oral Presentation AwardintheInternational Conference on Chemical Engineering Innovations and Sustainability (ICEIS-2023), organized by Jadavpur University, Kolkata, India, on February 26-27, 2023.

# “Statement of Originality”

I **Arindam Mandal** registered on **05.06.2018** do hereby declare that this thesis entitled” **“Generation of Valuable Products from Carbon Dioxide ($CO_2$) using Bismuth-based Reduced Graphene Oxide (rGO) supported Photocatalytic System”** contains literature survey and original research work done by the undersigned candidate as part of Doctoral studies.

All information in this thesis have been obtained and presented in accordance with existing academic rules and ethical conduct. I declare that, as required by these rules and conduct, I have fully cited and referred all materials and results that are not original to this work.

I also declare that I have checked this thesis as per the “Policy on Anti Plagiarism, Jadavpur University, 2019”, and the level of similarity as checked by iThenticate software is 6%.

Arindam Mandal

**Signature of Candidate**:

**Date:** 07/08/2024

Kajari Kargupta 07/08/2024

**Certified by Supervisor**

(Signature with date, seal)

Professor
CHEMICAL ENGINEERING DEPARTMENT
JADAVPUR UNIVERSITY
Kolkata-700 032

# Certificate from the Supervisor

This is to certify that the thesis entitled "**Generation of Valuable Products from Carbon Dioxide ($CO_2$) using Bismuth-based Reduced Graphene Oxide (rGO) supported Photocatalytic System**" submitted by **Mr. Arindam Mandal** who got his name registered on 05.06.2018 (**INDEX NO. D-7/E/312/2018**) for the award of Ph.D. (Engineering) degree of Jadavpur Unversity, is absolutely based upon his own work under the supervision of **Prof. Dr. Kajari Kargupta** and that neither this thesis nor any part of it has been submitted for any degree/diploma or any other academic award anywhere before.

Kajari Kargupta 07/08/2024

.....

(Signature of the supervisor, date with official seal)

**Prof. Dr. Kajari Kargupta**

Professor
Department of Chemical Engineering
Jadavpur University
Kolkata – 700032, India.

Professor
CHEMICAL ENGINEERING DEPARTMENT
JADAVPUR UNIVERSITY
Kolkata-700 032

*Dedicated to my Parents, my wife and my daughter...*

# Acknowledgement

***I*** *would like to express my gratitude and acknowledgement to everyone who has supported me along this difficult research trip, helping to make it enjoyable and unforgettable. Their assistance, encouragement, and support made my route clearer and simpler to walk.*

*First and foremost, I would like to thank my supervisor, Prof. (Dr.) Kajari Kargupta, who accepted me into her research group at Jadavpur University in Kolkata, India. She is a professor in the Department of Chemical Engineering. I have the utmost regard for her. I had the good fortune to work under a supervisor who allowed me the opportunity to explore on my own while still providing me with helpful advice and support when I needed it. Her technical expertise, unwavering excitement, and priceless advice not only gave me motivation every morning for the duration of my research work, but they also kept me going through the most trying moments. The task has been made possible by her blessings, trust, guidance, patience, and support.*

*My sincere gratitude to Prof. (Dr.) Avijit Bhowal, Professor, Department of Chemical Engineering, Jadavpur University, Kolkata, India for his kind support, technical queries, comments and valuable advices during my research work. My deepest gratitude to all of the professors and other faculty members, as well as to Prof. (Dr.) Papita Das, Head of the Department of Chemical Engineering, for their kind assistance and cooperation. I also like to thank all of the Department's non-teaching staff members. I am appreciative to the Department of Chemical Engineering at Jadavpur University for their assistance and for providing me with the opportunity to use the equipment for research.*

*Also, I would like to express my gratitude to Jadavpur University's Vice Chancellor, Pro-Vice Chancellor, Registrar, and Finance Officer for providing first-rate lab and library space for conducting research there. For their gracious assistance and cooperation, I am thankful to the entire personnel of Jadavpur University's Research Section, Ph.D. Cell, and all other sections.*

*I am thankful to Mr. Ajoy Prodhan, Technical Assistant, NSEL-Lab, Department of Chemical Engineering, Jadavpur University, Kolkata, for his kind help and cooperation during my research. I am also thankful to my dear colleagues Ms. Arundhati Sarkar, Mr. Sayantanu Mandal, Ms. Swagata Das, Mr. Pawan Kumar and my all other friends, seniors, juniors, my all co-authors, NSEL-Lab and entire Department of Chemical Engineering, Jadavpur University, for their help and cooperation in various ways.*

*All of this is possible because of my parents' unwavering support and their great faith in me, which I am submitting my PhD thesis today. My beautiful mother, Mrs. Krishna Mondal, and*

*my loving father, Mr. Utpal Kumar Mondal, are beyond words to convey my immense thanks and respect. My entire existence is due to their selfless giving and gracious favour. My parents have given me everything that I am today. This dissertation would not have been possible without their tremendous love, care, trust, support, and motivation. It brings me great pleasure to thank my brother, my wife, Mrs Rashmi Mandal, and the rest of my family for their constant support, encouragement, and faith in me. Without their backing, I would not have been able to travel this far. My family will always have my gratitude.*

*I apologize to individuals whose names are missing from this list, which will inevitably be incomplete. I appreciate all of your support, advice, and assistance. For the rest of my life, I shall treasure all these memories.*

**Date:** 07/08/2024

**Arindam Mandal**

**Department of Chemical Engineering**

**Jadavpur University**

**Kolkata - 700032**

# Preface

The present thesis, entitled "**Generation of Valuable Products from Carbon Dioxide ($CO_2$) using Bismuth-based Reduced Graphene Oxide (rGO) supported Photocatalytic System**" deals with the synthesis, characterization and photocatalytic performance study of bismuth-based reduced graphene oxide (rGO) supported photocatalysts for selective photo-reduction of $CO_2$ to renewable fuel.In particular, two unresolved research gaps or challenges are addressed in this thesis: (a) achievement of selective photocatalytic $CO_2$ reduction for fuel generation utilizing visible light from the solar spectrum; (b) enhancement in yield of $CO_2$-reduced selective fuel for commercialization. In the context of alternative renewable fuels like methanol ($CH_3OH$), ethanol ($C_2H_5OH$), and formic acid (HCOOH) generation, the photocatalytic $CO_2$ reduction system with the appropriate light source giving 1 sun light intensity is optimized. Photocatalyts, including rGO-supported $Bi_2S_3$, $Bi_2MoO_6$, and $BiVO_4$-based composites, are synthesized by hydrothermal treatment. To achieve the highest yield of selective fuel generation from photocatalytic $CO_2$ reduction process, rGO/$Bi_2S_3$ and rGO/$Bi_2MoO_6$ photocatalyts are modified by the optimal amount of Cu doping, and rGO/$BiVO_4$ photocatalyts are modified by the optimal amount of N-doping. The optimal amount of Cu and N doping in an rGO-supported bismuth-based photocatalyst actually manifests the smallest band gap, the lowest resistance of charge transfer, the lowest recombination rate of electron-hole pair, and the highest absorption edge-red shift for achieving the highest yield of selective photocatalytic $CO_2$-reduced fuel generation. In 1% Cu doped 1D-$Bi_2S_3$/rGO photocatalyst, 100% selective methanol ($CH_3OH$) with the highest yield of 719 μmol $g_{cat.}^{-1}$ $h^{-1}$ as photocatalytic $CO_2$ reduced product is achieved. The 2%Cu-(2D) $Bi_2MoO_6$ nanoribbon/rGO composite exhibits a 100% selective ethanol ($C_2H_5OH$) with the evolution rate of 133.10 μmol $g_{cat.}^{-1}$ $h^{-1}$. It is also found that the 1.5% N-(2.5%)rGO/$BiVO_4$ photocatalyst is the active photocatalyst for increased photocatalytic reduction of $CO_2$ to selective formic acid (HCOOH), with the productivity of 592.80 μmol $g_{cat.}^{-1}$ $h^{-1}$.

# List of Abbreviations

| | |
|---|---|
| **COP** | **Conference of the Parties** |
| **CB** | **Conduction band** |
| **VB** | **Valence band** |
| **IEF** | **Internal electric field** |
| **GO** | **Graphene oxide** |
| **rGO** | **Reduced graphene oxide** |
| **XRD** | **X-ray diffraction** |
| **FTIR** | **Fourier transform infrared** |
| **EDX** | **Energy dispersive X-Ray analysis** |
| **SEM** | **Scanning electron microscopy** |
| **FESEM** | **Field emission scanning electron microscopy** |
| **TEM** | **Transmission electron microscopy** |
| **SAED** | **Selected area electron diffraction** |
| **TGA** | **Thermogravimetric analysis** |
| **XPS** | **X-ray Photoelectron Spectroscopy** |
| **EIS** | **Electrochemical impedance spectra** |
| **MS** | **Mott Schottky** |
| **PL** | **Photoluminescence** |
| **BET** | **Brunauer-Emmett-Teller** |
| **NMR** | **Nuclear magnetic resonance** |
| **GCMS** | **Gas chromatography mass spectrometry** |
| **AQY** | **Apparent quantum yield** |
| **BSNC** | **Bismuth Sulfide rod-shaped nanocapsule** |
| **BMONR** | **Bismuth Molybdenum Oxide nanoribbon** |
| **BV** | **Bismuth Vanadate** |

# LIST OF FIGURES

# LIST OF TABLES

# CONTENTS

# Chapter 1

# Introduction

## Highlights:

- **Significance of photocatalytic $CO_2$ reduction to renewable fuel generation**
- **Significance of rGO-upported bismuth (Bi)-based photocatalytic system**
- **Importance of transition metal (Copper) and non-metal (Nitrogen) doping for selective $CO_2$ reduced product generation**
- **An overview of research presented in this thesis**
- **Graphical representation of research problem and methodology**
- **Content of each chapter of thesis**

## 1.1 Introduction

Energy is needed to provide both basic necessities and maintain better living conditions. The world's fast industrialization and expanding population are driving up the recent unsustainable energy demand. Currently, the consumption of global energy is about $1.5 \times 10^{10}$ KW and it is estimated to achieve $2.3 \times 10^{10}$ KW and $4.5 \times 10^{10}$ KW by 2050 and 2100, respectively. To meet this massive energy demands, the excessive use of fossil fuels raise serious concerns about the rate of $CO_2$ release into the atmosphere. As a result, a global energy gap is created and greenhouse gas $CO_2$ emissions is increased in the world's environment, which are accountable for the severe phase of global warming, which is recently termed as "Global boiling" according to COP 28, Nov. 2023 [1-5]. $CO_2$ emissions are estimated to be ~37 Gigatons annually and are projected to increase to ~43 Gigatons by 2035. The atmosphere has been purged of $CO_2$ to levels higher than 420 parts per million over the last 150 years. In addition, the Intergovernmental Panel on Climate Change (IPCC) projects claim that by the year 2100, the average $CO_2$ emission would increase to 590 parts per million. Such $CO_2$ emission levels have the potential to impact sea level and increase the planet's average temperature. At COP 28, scientists, policymakers and climate economists from 199 countries openly committed to combat climate change, with the ultimate goal of limiting the rise in global temperature after industrialization to less than 2°C. India is ranked 3$^{rd}$ among the top 10 countries in the world (measured in billion tons of $CO_2$ emissions) in Fig. 1.1 [6-10].

It is a crutial topic to capture and transform $CO_2$ into alternative green hydrocarbon fuels, thus tackling the energy and environmental crises simultaneously.To protect our environment and to maintain the carbon cycle, $CO_2$ emissions can be lowered using a variety of strategies, including reduced $CO_2$ emissions at the source, capturing and storing $CO_2$ and repurposing $CO_2$ by convertingit into higher-value compounds [11,12].

There are at least three routes of reducing the amount of $CO_2$ in the atmosphere:

- Direct reduction of $CO_2$ emission
- $CO_2$ capture and storage (CCS)
- $CO_2$ utilization

The most appealing alternative is one that increases our reliance on renewable energy while decreasing our dependence on traditional fossil fuels.

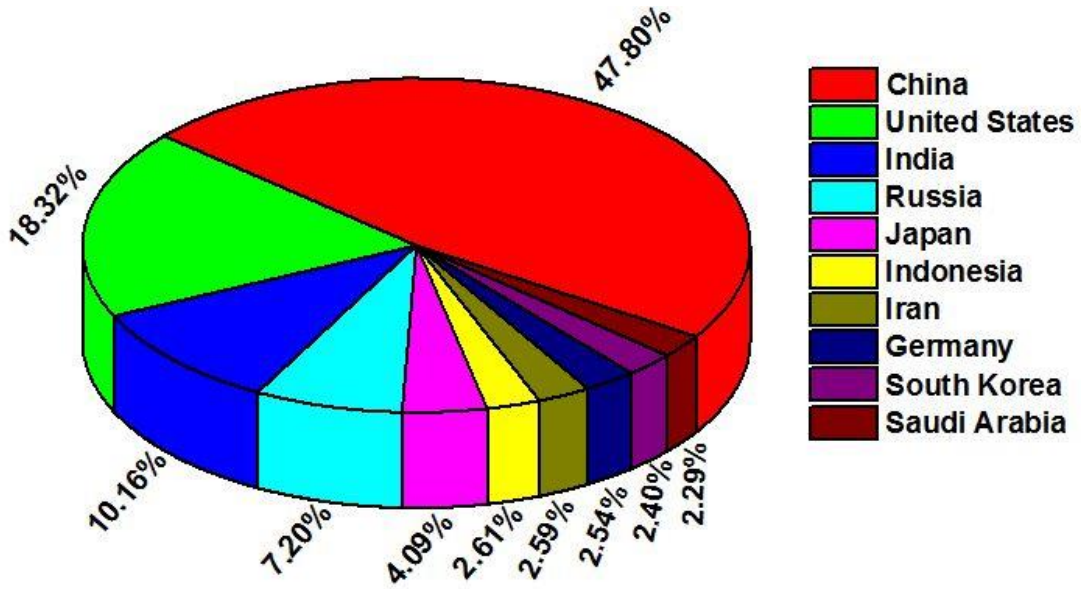


**Fig. 1.1: Top 10 countries with the highest $CO_2$ emissions in the world (Unit: Gigatons $CO_2$) [1-5]**

### 1.1.1 $CO_2$ reduction processes:

Carbon dioxide, an oxidised carbon that is linear and incredibly strong, has excellent thermal stability. Additionally, it is the result of all combustible ignition processes because of the greater band energy of C=O, which has a 750 KJ $mol^{-1}$ value and is present in carbon. Keeping that in mind, scientists have already been taking in different steps to reduce excess $CO_2$ through sequestration and other techniques including capturing. But these techniques are severely constrained as the amount of $CO_2$ that can be captured or sequestered has saturation and permanent limits. Thus, the most effective way to use $CO_2$ without impeding industrial growth and urbanisation is to efficiently transform it into fuels, chemical feedstock and materials that may be consumed in daily life. Numerous $CO_2$ reduction processes shown in Fig. 1.2 can be used to reduce $CO_2$ to other molecules for reducing the accumulation of $CO_2$ in the environment. The conversion of $CO_2$ may be done in numerous ways that includes chemical, biological, thermal, electrochemical and photochemical processes. These technologies, however, have constraints, such as the need for high temperatures and potential energy to split the very stable $CO_2$ molecule, a scarcity of raw materials, the high cost of operation and an unsustainable design. Selecting the appropriate catalysts and process technology is crucial for achieving the selectivity and yield of the products [13-17].

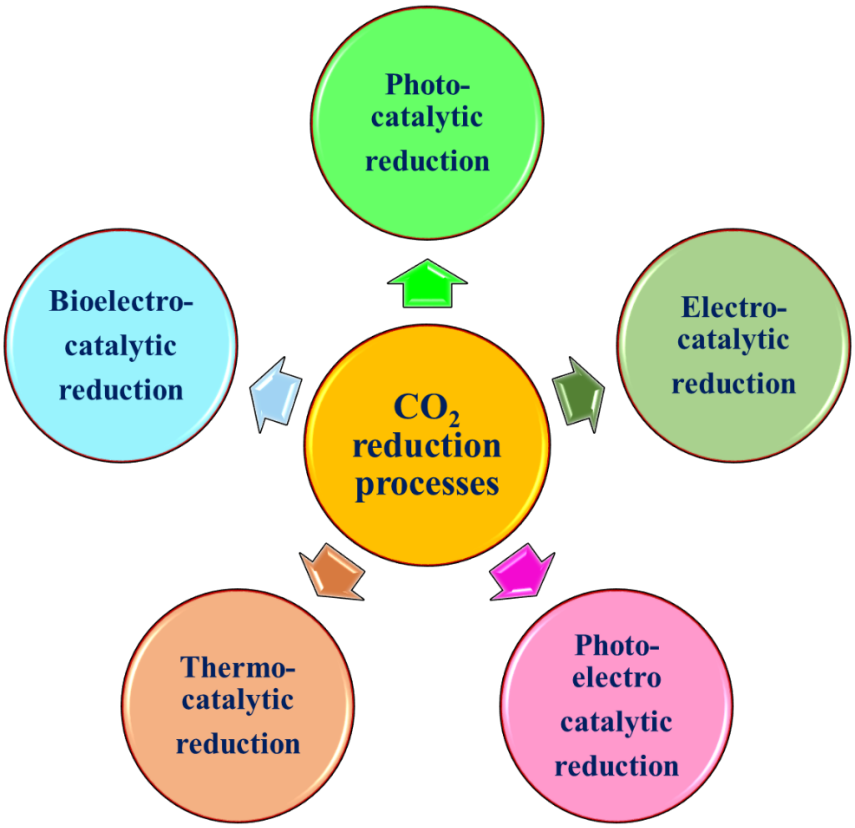


**Fig. 1.2: Schematic representation of the $CO_2$ reduction processes**

#### 1.1.1.1 Photocatalytic reduction of $CO_2$

Among the several $CO_2$ conversion techniques, photocatalytic reduction of $CO_2$ has been acknowledged as a sustainable idea since it uses water and renewable solar energy, both of which are readily available and reasonably priced [18-24]. Photocatalytic $CO_2$ reduction is often recognized as the most effective renewable approach for reducing $CO_2$ concentrations in the environment. This method essentially mimics the basic natural photosynthetic cycle; therefore, no additional energy is required because photocatalysis uses just solar light to convert $CO_2$ into renewablefuels or other key molecules. Photocatalysis is recognized as the most adaptable and sustainable technique due to various advantages, including the utilization of a cost-effective reactant (water), low power requirements, reactions at room temperature, relatively low pressures and no negative environmental consequences. Furthermore, it exceeds competitors in terms of operational expenses, productivity and efficiency [25-28].Utilising photons from the sun and water as reactants, photo-reduction of $CO_2$ is a sustainable and eco-friendly method of producing hydrocarbons. For the purpose of photocatalytically converting $CO_2$ into useful chemicals, a broad range of semiconducting

materials, including CdS [21], $CeO_2$ [22], $TiO_2$ [23], ZnO [24], $Fe_2O_3$ [25], CoO [26-27], $Co_3O_4$ [28], $WO_3$ [29-30], $Bi_2S_3$ [31] and CuO [32], bismuth-based compounds and transition metal complexes, have been thoroughly studied [33–34]. Photocatalytic technology-based $CO_2$ conversion would alleviate environmental issues while providing the world with needed energy but the efficiency of photocatalytic activity and selectivity of photoreduced products are the major issues for photocatalytic $CO_2$ conversion technology. To overcome these problems, the development of new photocatalysts is a preliminary technique to improve the performance of the photocatalytic $CO_2$ reduction process. So, extensive research in the modification of photocatalyst has been done for enhancing charge transfer, separation, improved $CO_2$ adsorption and activation, faster $CO_2$ reduction kinetics and suppression of unfavourable processes for $CO_2$ photoreduction that facilitate yield and selectivity of the product formation [227-230].

This $CO_2$ reduction method actually represents the artificial photosynthesis.

- **Artificial Photosynthesis:**

Conversion of clean solar to chemical energy by photocatalytic reduction of $CO_2$ to valuable chemicals or fuels (such as CO, $CH_4$, $CH_3OH$, $C_2H_4$, HCOOH and so on) using semiconductors [33,40,42,43].

- One of the most promising methodologies:
- Uses renewable sources (solar energy, water) and conversionof $CO_2$ into renewablefuels
- Operates at normal pressure and temperature without requiring considerable energy inputs.
- No such production of hazardous by-products.
- Meets the long-term worldwide energy demands without employing further $CO_2$-producing power sources.

- **Renewable energy (RE) sources:**

  **Solar energy (SE)** or the radiant ionization energy that the sun emits, is the primary sources of energy that is used extensively around the world. Most research attributes multiple technologies to improve the SE system's architecture and boost SE conversion efficiency [13,16,24,43].

**Water** is the most precious and economical renewable energy source for hydropower, $CO_2$-reduced products, etc. Hydropower has the best conversion efficiency—roughly around 90%—among other renewable energy sources when it comes to produce electricity. 20% of the electricity generated globally comes from hydropower [36,37,39,43].

**Wind energy** is the most popular renewable energy source for producing electricity. This is because wind energy has a comparatively easy infrastructure, is affordable and has mature technology. Wind turbine-based power plants transform wind energy into electrical power. Onshore and offshore wind farms are the two varieties [42,43].

- **Renewable fuels:**

The photocatalytic reduction of carbon dioxide to produce valuable fuels like methanol, ethanol and formic acid is one way to mitigate the issue of climate change.

**Formic acid** as a fuel can be incorporated in Direct Liquid Feed Fuel Cell (DLFC). It is also used for producing acetic acid and methanol. Formic Acid can store hydrogen to a huge extent, which is about 4.35% of its weight, acting as a hydrogen carrier. Moreover, at standard temperature and pressure, formic acid can store about 580 times more hydrogen compared to hydrogen gas of the same volume [44].

**Methanol** can be used as a fuel in Direct Methanol Fuel Cells (DMFC), however the efficiency is low. At present, 98 million tonnes of methanol are being produced, per year from fossil fuels like coal and gas, whereas only 0.2 million tonnes per annum of methanol is derived from renewable sources. The production of methanol has increased double fold, compared to previous decade.A significant growth has been observed in China. Renewable methanol can be produced from renewable feedstock: bio-methanol derived from biomass or from carbon dioxide captured by renewable sources. It is predicted that the production of methanol could rise to 500 Mt per annum by 2050. Methanol along with ethanol have been used as additives in fuel blends to be utilised in internal combustion engines [25,32,39,40].

It is exhibited from a Life Cycle Assessment (LCA) of methanol production, that a reduction of about 59% in greenhouse emission can be achieved by renewable method, when compared with the traditional processes from fossil fuels. Renewable methanol can be a potential solution in reduction of carbon dioxide emission and in maintaining

the global temperature within the threshold of 1.5 °C, as agreed upon in the Paris Agreement (2015). By 2050, carbon neutrality emission might be attained by the nations through adopting renewable methanol production strategies [5,7,40].

**Ethanol** as a fuel has been utilised in Direct Ethanol Fuel Cell (DEFC).In 2022, US Government Accountability Office, in coordination with Renewables Fuel Association, released a technology assessment on Carbon Capture, Utlization and Storage (CCU). According to the report, ethanol can be a plausible solution in achieving sustainable CCU. The cost of carbon capture is also the lowest for ethanol: for each metric ton of $CO_2$ captured, the estimated cost is between $0-$35 [19,45].

Methanol, ethanol and formic acid, as sustainable renewable fuels, has been utilised in fuel cells as an alternative aviation and marine fuels. The demand for formic acid, methanol and ethanol will increase gradually if impetus is given to the hydrogen-based economy, in near future [39,44,45].

#### 1.1.1.2 Electrocatalytic reduction of $CO_2$

The electrocatalytic reduction of $CO_2$ is one of the most widely used technologies today; in this technique $CO_2$ is reduced to converting $CO_2$ into other compounds or fuels using electrical energy. This reduction process has several advantages, including operation under mild electrolyzer settings, the ability to employ industrial or municipal wastewaters as electrolytes, promising faradaic efficiency. However, understanding the reaction mechanism is difficult due to the chemistry of electrocatalytic $CO_2$ reduction. This process likewise necessitates a high overpotential, and the electrolyte used is critical for electrocatalytic efficacy as well as avoiding catalyst poisoning and deactivation. In an electrocatalytic reaction, the catalysts should be able to minimise the competitive $H_2$ production reaction anticipated by lowering $CO_2$ at the cathode. This method is also more expensive since more power is required. The product's purity is significantly impacted by the hydrogen evolution process that goes along with the electrocatalytic reduction of $CO_2$ [41,46-49].

#### 1.1.1.3 Photoelectrocatalytic reduction of $CO_2$

Similar to the electrocatalytic approach, photoelectrocatalytic (PEC) $CO_2$ reduction offers a real chance to convert $CO_2$ into useful chemicals and fuels. However, in electrocatalytic

reduction, the applied current supplies the needed electrons, whereas in photoelectrocatalytic reduction, electrons are obtained by excitation of semiconductors under visible light irradiation. PEC also uses a larger range of semiconductors than photocatalytic reduction, with an overall quantum efficiency of 8-12% and an imposed external bias for product selectivity. In terms of research and studies, photoelectrocatalytic reduction of $CO_2$ is still far from being comparable to photocatalysis and electrocatalysis, despite the fact that it seems to combine some of their benefits. Two major obstacles are photoelectrode stability and kinetics [41,46,49].

#### 1.1.1.4 Thermocatalytic conversion of $CO_2$

The chemical reduction of $CO_2$ is accomplished mostly through the thermal-$CO_2$ conversion of $CO_2$ into carbon monooxide or methane, with reactions occurring at temperatures ranging from 500 to $1000^0$ Celsius. Concentrated solar radiation can also be used as an energy source to power these extremely endothermic reactions. However, both high-temperature reactors and sunlight concentration lenses demand significant upfront investment. Furthermore, our understanding of surface chemistry, morphology, chemical, and structural changes remains restricted at high temperatures. Higher temperatures are required for the thermocatalytic reduction of $CO_2$, which raises energy consumption as well as the necessity for the $CO_2$ reduction catalysts to remain active at high temperatures [31,49].

#### 1.1.1.5 Bioelectrocatalytic reduction of $CO_2$

A unique method of reducing $CO_2$ is called "bioelectrocatalytic reduction," in which microorganisms act as catalysts. Because microorganisms need a living environment to function, bioelectrocatalytic reduction can only reduce $CO_2$ under certain experimental settings, and the conversion of $CO_2$ is relatively low, which restricts its practical development.

However, when compared to these methods, photocatalytic $CO_2$ conversion is more environmentally and energy-efficiently friendly and promising since it requires no additional energy and creates very little pollution, especially when using solar energy and in a photocatalytic reaction, the catalysts must have an appropriate semiconductor with a minimum band gap of 1.23 eV [41,46-50].

### 1.2 Fundamentals of Photocatalytic $CO_2$ reduction:

The photocatalytic $CO_2$ reduction approach has garnered a lot of interest recently as a potential solution to the world's energy and environmental challenges because of its exceptional qualities, including low cost and environmental safety. By using solar radiation as a sustainable energy source and a semiconductor photoactive material as a photocatalyst, it may transform and convert anthropogenic $CO_2$ into useful renewablefuels such as gaseous (methane, ethane) and liquid products (methanol, formic acid, formaldehyde, and ethanol). It is also known as "artificial photosynthesis," as it turns water and sun light into valuable chemicals and fuels. This procedure can be employed under low pressure, low temperatureand simple operating conditions with little energy consumption [38-43,51]. It is a workable, environment friendly method that avoids all high-temperature reaction conditions and offers enhanced resistance to catalyst deactivation.Numerous semiconductor photocatalysts, including $TiO_2$ [52], $Ga_2O_3$ [53], MgO [54] and $[Re(bpy)(CO)_3P(OEt)_3]$[55] have been used to encourage the photocatalytic $CO_2$ reduction into liquid/gas products.Due to number of variables, including solubility and by-product creation, the mechanism for photocatalytic $CO_2$ reduction is more complex than that of the other comparable processes, including hydrogen production by water splitting. Three steps make up the photocatalytic $CO_2$ reduction process: (1) solar light absorption and charge generation, (2) separation of charge carriers and (3) $CO_2$ adsorption and redox reactions on the catalystic surface. The schematic representation of the photocatalytic $CO_2$ reduction process is presented in Fig. 1.3. The minima of conduction band (CB) of the photocatalyst, which controls the energy of the photoexcited electrons in photocatalysis, must be less than the reduction potential for the particular reaction to occur. Photocatalysts are mostly preferred for their measurable but surmountable energy difference between the lowest (unoccupied) conduction band and the highest (occupied) valence band. The electrons can travel freely in metals because there isn't a "forbidden" gap between the conduction band (CB) minima and valence band (VB) maxima. It is the difference in free energy that occurs when an indefinitely vast system gains or loses species (electron). The labour needed to incorporate one electron is recognised as the Fermi level ($E_F$), which is a related quantity. An essential feature shared by all semiconductor photocatalysts is the band gap ($E_g$). The band gap is the measure of the energy needed to excite an electron from the valence band (VB) to the conduction band (CB). The wavelength of incident light at which the photocatalytic material responds the best is closely related to the band gap [56-60]. The band gap's value does, however, also have additional implications. For

instance, a band gap of 1.23 eV is ideal for photocatalytic $CO_2$ reduction applications, according to the ultimate efficiency theory, charge carriers like electrons and holes form in the conduction band and valence band of photocatalysts when the subjected to photon energy greater than the bandgap. Next, the electrons are stimulated to move from the conduction band (CB) to the valence band (VB). The highest energy band in which electrons are occupied is VB, while the lowest energy band, CB, is empty at the ground state. The intra-band transitions that occur in electrons and holes are seen in Fig. 1.3. They can proceed by radiative or non-radiative paths to reach the surface, where they can recombine at the trap sites. Alternatively, if recombination proceeds more slowly than the reactions during transitions, these electrons may reach the surface of the semiconductor and interact with surface adsorbed species (in this case, $CO_2$). A driving force, sometimes known as an over potential, for the anticipated chemical processes can be provided by photogenerated electrons at greater reduction potential levels. A chemical species' capacity to acquire electrons is measured by its reduction potential. Higher (more negative) reduction potential species will lose electrons (i.e., get oxidised), whereas lower (more positive) reduction potential species will acquire electrons (i.e., become reduced). Adsorbed $CO_2$ is really reduced by the electrons in the conduction band at the photocatalyst surface and transformed into a number of $CO_2$ photo-reduced products, such as CO, HCOOH, $CH_3OH$, $C_2H_5OH$, $CH_4$, etc. The number of available electrons for the reaction dictates the various product formations. With the holes in the valence band, $CO_2$ and water will initiate an oxidation process [60-65]. The selectivity of the products from photocatalytic $CO_2$ reduction is greatly influenced by the photocatalysts (0D, 1D, 2D). To achieve the enhanced yield of the selective product from photocatalytic $CO_2$ reduction process researches are now concentrating on the modification of the photocatalyst by introducing heterojunction (Z-scheme, S-scheme, type –II) between photocatalysts, doping of transition metals (Cu, Mo, Zn, Ni) or non-metal (N, C, S, P), graphene or reduced graphene oxide as 2D-nanosheets. A lot of study has also been done on the formation of a single product under visible light to lower the cost of product separation. This lowered product's selectivity, however, is very intricate and closely related to the chemical pathways and systems [66-68]. For a chemical reaction to proceed, the products' Gibbs (or Helmholtz under constant volume) free energy must to be lower than the reactant's. In other words, the free energy of the system must decrease. Thus, in addition to the catalyst's physical properties, the parameters of the reaction, such as light intensity, reaction system, pH, temperature and pressure, have a big impact on the different kinds of products. The required reduction potentials for photocatalytic $CO_2$ reduction are listed in Table 1.1

[compared to the normal hydrogen electrod (NHE) at pH=7] [69-73]. The high negative reduction potential (− 1.90 V against NHE) in comparison to the conduction band potential of several semiconductors prevents the one electron reduction from $CO_2$ to $CO_2^{\bullet-}$. Carbon's transition from $sp^2$ to $sp^3$ hybridization is the cause of this extremely negative reduction potential. Certain by-products, such HCOOH (-0.61 V), HCHO (-0.48 V), $CH_3OH$ (-0.38 V), $C_2H_5OH$ (-0.33 V) and $CH_4$ (-0.24 V), have a lesser reduction potential that is closer to the positive of many semiconductors' CB (conduction band) edge potentials.

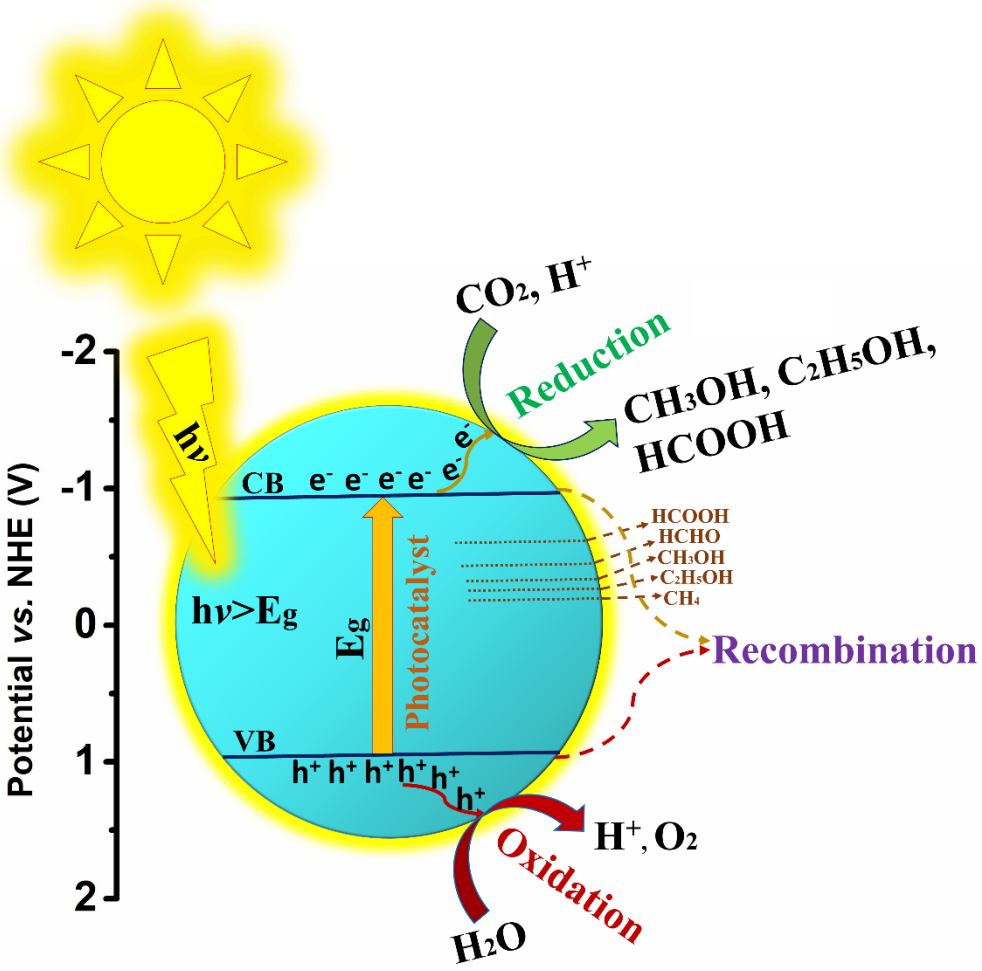


**Fig. 1.3: Schematic representation of the photocatalytic $CO_2$ reduction process**

**Table 1.1: Standard reduction and oxidation potentials of photocatalytic $CO_2$ reduction into various products**

| | Reaction | $E°$ (V) vs. NHE at pH=7 |
|---|---|---|
| Reduction | $CO_2 + e^- \rightarrow CO_2^{\bullet-}$ | -1.90 |
| | $2H^+ + 2e^- \rightarrow H_2$ | -0.42 |
| | $CO_2 + 2H^+ + 2e^- \rightarrow CO + H_2O$ | -0.52 |
| | $CO_2 + 2H^+ + 2e^- \rightarrow HCOOH$ | -0.61 |
| | $CO_2 + 4H^+ + 4e^- \rightarrow HCHO + H_2O$ | -0.48 |
| | $CO_2 + 6H^+ + 6e^- \rightarrow CH_3OH + H_2O$ | -0.38 |
| | $CO_2 + 8H^+ + 8e^- \rightarrow CH_4 + 2H_2O$ | -0.24 |
| | $2CO_2 + 12H^+ + 12e^- \rightarrow C_2H_5OH + 3H_2O$ | -0.33 |
| Oxidation | $H_2O \rightarrow ½\ O_2 + 2H^+ + 2e^-$ | +0.81 |

Thus, the preferable method is proton-coupled electron transfer or electron transfer to combine $CO_2$ along with proton transfer. In terms of increasing order of the formation energy ($\Delta G$) of the by-products, they can be arranged as follows: HCOOH < CO < HCHO < $CH_3OH$ < $CH_4$. Reactions having lesser reduction potential (eg. methanol and ethanol) involve more electrons (6 and 12 electrons, respectively]. Photocatalytic $CO_2$ reduction seems to be a promising pathway for converting $CO_2$ to valuable products considering it to be environment friendly and cost-effective process [73,74]. However, the major challenges of this process towards commercialization are the appropriate selection and yield of a desired product. Thus, the design of tailor-made photocatalyst is crucial to achieve the selectivity and yield of a desirable product.

### 1.2.1 Advantages of photocatalytic $CO_2$ reduction (PCR) technology:

- PCR is a sustainable and environment friendly process.
- It can use solar energy to minimize $CO_2$ and protect the environment from global warming while also producing valuable energy sources like methanol and ethanol etc.
- The PCR process typically operates at ambient temperatures and pressures.
- This process can reduce operating expenses by finding a less expensive, more resilient catalyst to produce selective C1+, C2+ product ($CH_3OH$, $C_2H_5OH$, HCOOH etc).

### 1.2.2 Disadvantages of photocatalytic $CO_2$ reduction (PCR) technology:

- Proper absorption of visible light from solar spectrum and use of visible light active photocatalyst.
- Selectivity and low yield of $CO_2$ reduced product.

**1.3** In context of designing the **tailor-made Photocatalysts** for $CO_2$ reduction to selective valuable product, the following different strategies are adopted and reported in literature:

- Use of nanomaterials (0D, 1D, 2D)
- Use of heterostructure (Type II, Z scheme, S Scheme, Schottky)
- Doping (with noble metal/transition metal/non metal) of the semiconductor photocatalyst

### 1.3.1 0D, 1D and 2D nanomaterials for photocatalytic $CO_2$ reduction:

Utilization of nanomaterials, including quantum dots, nanotubes, nanowires, nanorods and nanosheets, which are shown in Fig. 1.4, can enhance the photocatalytic effectiveness of recent available devices. In order to facilitate the oxidation and reduction process, nanostructured materials have the ability to inject electrons and holes at the $CO_2$-nanomaterial interface as well as transfer charges efficiently. The development of highly efficient photocatalysts for $CO_2$ reduction is made possible due to the special abilities of nanomaterials. Different synthesis techniques combined with various kinds of nanomaterials creates new and efficient photocatalytic components that have the desired properties to absorb full spectrum of sunlight [63-74].

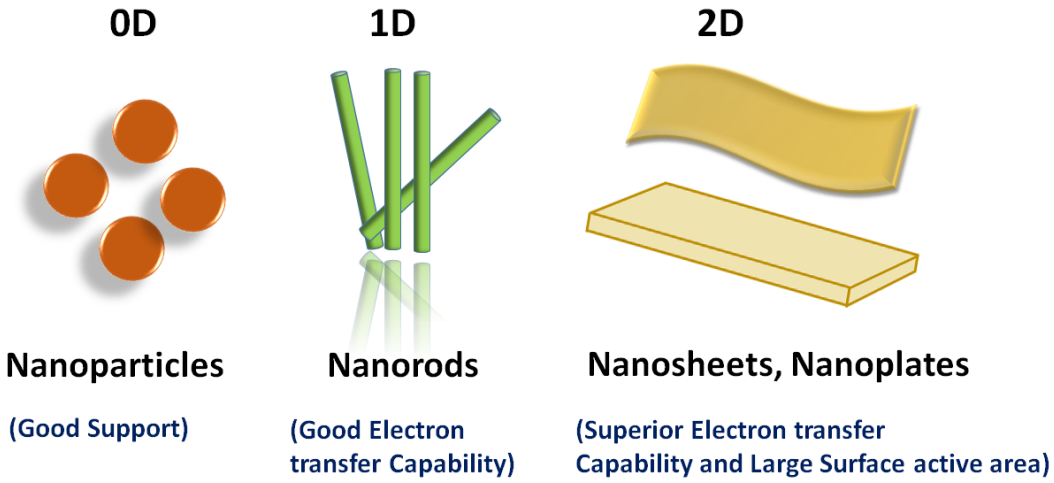


**Fig. 1.4: Schematic diagram of the advantages of 0D, 1D, and 2D layered nanostructures**

#### 1.3.1.1 0D nanomaterials:

0D nanostructures in the form of quantum dots (QD) and nanoparticles are being used as photocatalysts due to their special characteristics in optical, electrical and morphological domains for transforming photocatalytic $CO_2$ reduction to renewable fuels under the influence of sunlight. These properties which are mostly size-dependent, allows QDs and nanoparticles to be employed as co-catalysts as well as pure photocatalysts. The primary reason for QDs' efficacy as photocatalysts is their ability to absorb and scatter sunlight due to their optical characteristics. Notably, as generated electron-hole pairs are in a restricted volume, a decrease in QD size increases the likelihood of charge recombination [74-78].

Furthermore, by creating ideal nanocomposite materials altered by QDs, their usage as efficient photocatalysts in the visible spectrum of sunlight can be made possible by avoiding QDs' effect on charge recombination. In addition to enabling effective charge separation, the usage of QDs as co-catalysts lowers the energy barrier for photocatalytic water splitting. The entire range of noble metal nanoparticles and metal oxide nanoparticles are instances of QDs that can be utilized as co-catalysts in photocatalytic settings. An examination of the literature exhibits that the synthesized process, composition, surface morphology and size of the QDs affects the photocatalytic activity of composite photocatalysts containing QDs. By using QDs as an example, it can easily be pinpointed that the approach to use QDs in the advancement of photocatalytic systems produces hydrogen through solar radiation. The development of composites with nanoscale architectures is the only way that solar hydrogen power engineering can advance further. Moreover, features of 0D nanomaterials that govern the activity of photocatalysts can be changed by functionalized or modified nanomaterials. These characteristics include the band gap, the mobility of photogenerated charges and the absorption and scattering of sunlight [79-83].

#### 1.3.1.2 1D nanomaterials:

Since 1D nanostructures have a high length to diameter ratio along with high absorption and scattering efficiency, they are commonly utilized in photocatalytic $CO_2$ reduction processes that produce renewable fuels in the presence of sunlight. Utilizing these 1D structures as hollow nanoparticles, porous spheres, nanowires, nanorods (NR), and nanofibres is of great interest to researchers. Faster phototransfer with a photoconversion efficiency of 0.098% is achieved by using nanorods. The creation of intricate photocatalytic heterostructures based on 1D nanomaterials modified with metals has garnered a lot of attention lately [84-86].For

instance, adding metal particles of Ag and Au, Cu, and Fe to photocatalysts improved their effectiveness in reducing $CO_2$ to renewable fuels. Compared to the utilization of QD and nanoparticles, such sophisticated photocatalytic systems based on 1D nanostructures provides a number of advantages. 1D nanostructures efficiently absorb and disperse sunlight, forming active centers for photocatalytic processes due to their large specific surface area. Additionally, 1D nanostructures facilitate the effective transfer of charges generated upon the absorption of a quantum of light, hence favorably impacting the rate of $CO_2$ reduction by photocatalysis. According to reports in, the charge transfer for 1D nanostructures such nanowires, nanorods and nanotubes was more than 200 times higher than that of nanoparticles. Likely with 0D nanostructures, the current techniques for creating and employing 1D nanostructures as co- or photocatalysts need to be improved in order to use profitably in ~~the~~ manufacturing large-scale desired renewable fuels [87-97].

**1.3.1.3 2D nanomaterials:**

Two-dimensional (2D) nanomaterials are a family of nanomaterials that have a large specific surface area, exceptional mechanical qualities, high activity and photochemical stability, making it potential candidates for effective photocatalytic systems. Graphene, layered double hydroxides, graphite carbon nitride (g-$C_3N_4$), metal oxides, carbides, nitrides and other materials have been used to make progress.The primary challenges in employing 2D nanostructures as photocatalysts are related to mass transfer enhancement and photocatalytic $CO_2$ reduction efficiency enhancement. The photocatalyst's efficiency is closely correlated with the width of the semiconductor band gap; this gap needs to be larger than 1.23 eV for $H^+$ ions generation, which means light in the infrared spectrum cannot be used. In, multilayered structures of 2D chalcogenides of group III elements, such as $Bi_2S_3$, $Bi_2O_3$, $Bi_2Se_3$ and other Bi-based 2D nanostructures such as $Bi_2MoO_6$, $BiVO_4$are being successfully employed as photocatalysts for photocatalytic $CO_2$ reduction, suggesting a potential solution to this issue [98-104].

On the other hand, renewable fuels are also impacted by the separation of photoinduced charges. Several investigations have demonstrated that the effective separation of photo-induced charges can boost the effectiveness of photocatalytic $CO_2$ reduction under solar radiation by hundredtimes. 2D nanostructures offer some benefits over 0D and 1D nanomaterials in the research and construction of efficient photocatalytic devices for $CO_2$ reduction under solar radiation. Firstly, the depth of light penetration is correlated with the

efficiency of 2D materials to absorb sunlight. 2D nanostructures interact with photons by reflecting and scattering them repeatedly. As mentioned previously, photocatalysts based on 2D nanostructures currently exist and can enhance the range of sunlight absorbed [104-108].

Secondly, the margins of the conduction and valence bands can be shifted through the fabrication of heterostructures from 2D nanomaterials, which changes the potential for oxygen oxidation and $CO_2$ reduction. Thirdly, photocatalysts based on 2D nanomaterials have multiple directions for the transfer of photoinduced charges, which can greatly increase the efficiency of photo-reduction of $CO_2$, as opposed to photocatalysts based on 0D and 1D nanostructures, for which there is only one direction for the transfer of photoinduced charges. It is important to highlight that thickness of 2D nanomaterials play a crucial role in photocatalysts because photo-induced electrons need to be mobile enough to reach the photocatalyst's surface. This is the primary drawback of 2D nanostructure-based photocatalytic devices. Recently, authors have investigated that local heating of photocatalyst improved the mobility of photoinduced charges [96-108].

### 1.3.2 Different types of heterostructures for photocatalytic $CO_2$ reduction:

During light stimulation, electron–hole pairs are created and separated for the photocatalytic process of a pure semiconductor.Subsequently, a redox process takes place to produce fuel products as $CO_2$which is adsorbed on the surface using semiconductor photocatalyst. Ultimately, the catalyst surface releases the $CO_2$ reduced products. As a result, in photocatalytic reactions, photocatalysts can primarily create four different types of heterojunctions: Type-II, Z-scheme, S-scheme and Schottky, respectively. The variations in photocatalytic performances are directly caused by these changes in response processes which have a significant effect on the overall photocatalysis process [109-112].The schematic diagram of the photocatalytic principle for the four different types of heterojunction structures is displayed in Fig. 1.5.

#### 1.3.2.1 Type-II heterojunction:

Most semiconductors have fast electron and hole recombination, which makes photocatalytic processes unlikely to occur. Fig. 1.5(a) displays the schematic diagram of type-II heterostructure's reaction mechanism. In semiconductor-I, a lot of electrons are stimulated from the valence band (VB) to the conduction band (CB) under light irradiation leaving holes in the VB. There is a transfer of electrons from semiconductor-II's CB to semiconductor-I's

CB and of holes from semiconductor-I's VB to semiconductor-II's VB. The effectiveness of photocatalysis is increased by the type-II heterojunction's rapid charge separation which prevents photogenerated excitons from recombining and transports them in space. But substantial reduction and oxidation capacities of the carriers are sacrificed in the process. Furthermore, semiconductor-I can operate as the electron or hole acceptor when semiconductor-II can only be activated by photonic radiation. It is widely acknowledged that charge carriers can accumulate spatially in both scenarios. The type-II heterojunction provides the ideal band locations for the effective separation of photogenerated electron-hole pairs [113-117].

#### 1.3.2.2 Z-scheme heterojunction:

The Z-scheme heterostructure's photocatalytic process exhibits a high photocatalytic efficiency. Fig. 1.5(b) illustrates the unique reaction mechanism of it. Electrons in both semiconductors are stimulated from the VB to the CB when exposed to light, leaving holes in the VB. After that, the weakly reducible electrons are moved from semiconductor-I's CB to semiconductor-II's VB and recombined with the weakly oxidizing holes in the VB. Strong oxidizing and reducing capabilities of the electrons and holes are thus preserved. On semiconductor-II's CB, the reduction reaction will then continue. The oxidation process takes place on semiconductor-I's VB, and the $CO_2$ will be converted to hydrocarbon fuels (CO, $CH_4$, HCOOH, etc.). The product is created when the semiconductor's band gap has the generating potential, and its composition is determined by the catalyst's inherent properties. Hybrid photocatalysts can follow the Z-scheme when the mediator is arranged in a heterojunction. On the other hand, without a mediator, type II and direct Z-scheme heterojunction are both feasible. Subsequently, in order to support the charge transfer mechanism, a thorough strategy is essential. The electronic transportation path of Z-scheme photocatalysts resembles the letter "Z," and it consists of two semiconductors in close proximity to one another. Z-scheme photocatalysts have an optimal redox potential and a high exciton separation efficiency. Furthermore, the creation of an internal electric field (IEF) at the junction of two semiconductors creates a favorable pathway for electron transport, preserving the electron-hole pairs with stronger redox capacities and facilitating the recombination of photogenerated carriers with lower redox potentials. Generally speaking, the difference in the semiconductor work function ($W_f$) causes IEF creation. In particular, when electrons are brought into contact, they have a tendency to go from one semiconductor with a smaller $W_f$ to another with a larger $W_f$ in order to balance their Fermi levels ($E_f$). As a

result, the IEF is formed by the positively and negatively charged sides that give and accept electrons, respectively. For semiconductor-II, semiconductor-II should have a smaller $W_f$ and a higher position of the CB and VB than those of semiconductor-I in order to successfully produce a Z-scheme composite photocatalyst [93,94,116].

#### 1.3.2.3 S-scheme heterojunction:

Prominent scientists have proposed a novel sort of heterostructure called an S-scheme (or Step-scheme) heterojunction. A reduction photocatalyst and an oxidation photocatalyst with staggered band topologies results in S-scheme heterojunction. Although the charge-transfer pathway in the S-scheme is very different, its reaction mechanism is comparable to that of the type-II heterojunction. The electrons in semiconductor-II spontaneously diffuse to semiconductor-I when two semiconductors are in close proximity, as seen in Fig. 1.5(c). This results in the creation of electron accumulation layer and electron depletion layer near the interfaces in semiconductor-II and semiconductor-I, respectively. Consequently, semiconductor-I has a negative charge while semiconductor-II has a positive charge. Simultaneously, an IEF is generated that leads from semiconductor-II to semiconductor-I. The photogenerated electrons in semiconductor-I's CB and the holes in semiconductor-II's VB at the interface area are encouraged to recombine by the band bending. As a result, the absent charge carrier is released by recombination, but the holes in semiconductor-I's VB and the photogenerated electrons in semiconductor-II's CB, have a higher capacity for reduction, that are retained to take part in photocatalytic processes. High redox ability and charge separation are both accomplished in this instance. Mutually beneficial results include strong redox potentials, widespread light adsorption, and effective charge separation. Consequently, S-scheme heterojunctions currently outperform type-II and Z-scheme heterojunctions in photocatalytic $CO_2$ reduction to renewable fuels processes [111,136].

#### 1.3.2.4 Schottky heterojunction:

The schematic diagram of the Schottky heterojunction's photocatalysis mechanism is displayed in Fig. 1.5(d). Photogenerated electron–hole pairs are produced when the catalyst is exposed to light. This process excites a lot of photogenerated electrons from semiconductor-II's VB to its CB while leaving holes on the VB. The electrons then move from semiconductor-II's CB to metal-I, where they undergo a reduction process. The Schottky heterojunction can regulate the production and flow of photogenerated electrons because of its reduced interface voltage and rectification properties. They improve the photocatalytic

performance by more successfully promoting their separations. Additionally, by synchronizing the Fermi energy level, the photon-generated carrier can undergo extremely limited recombination, that enhances the photocatalytic performance [88,98,99].

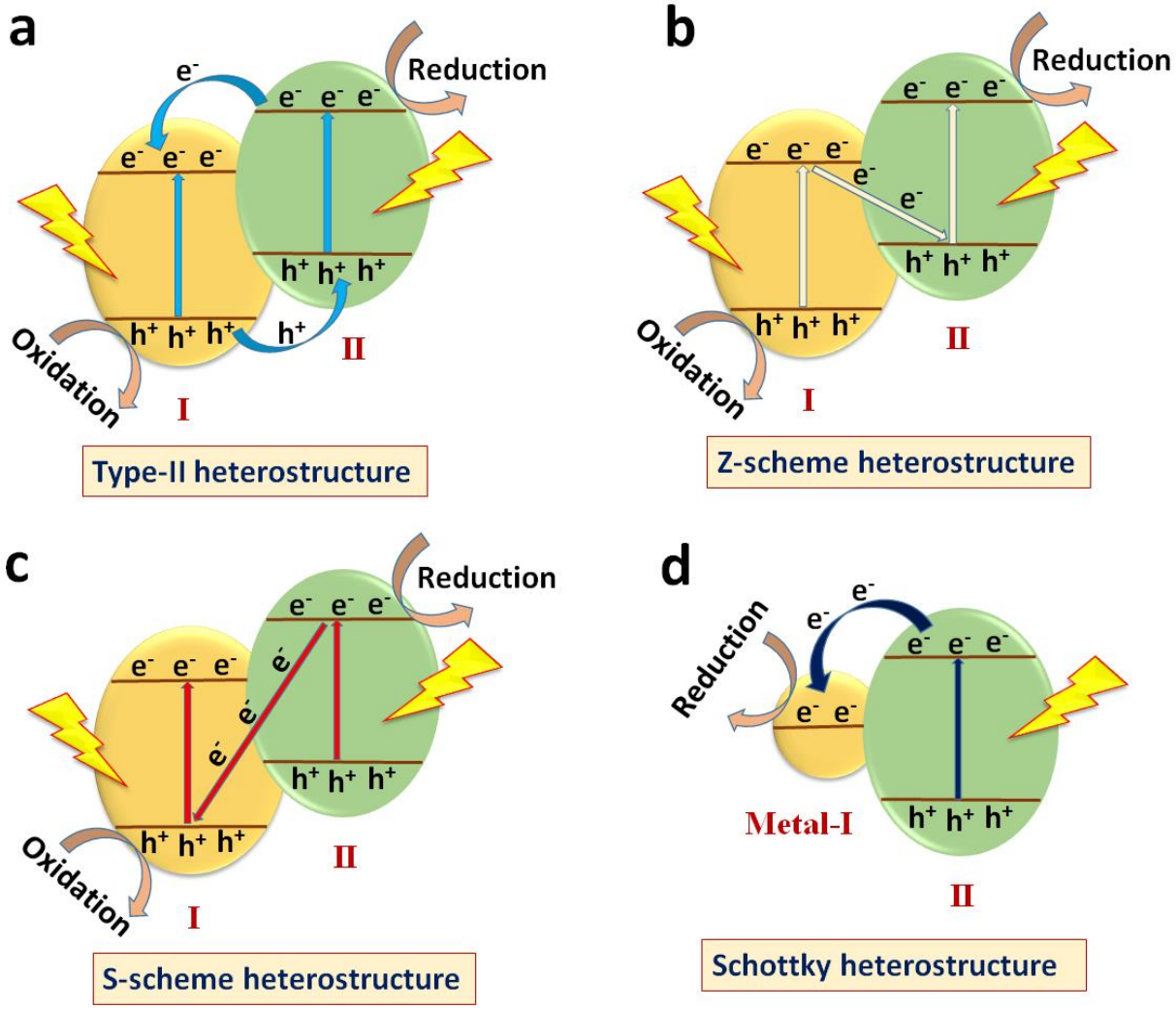


**Fig. 1.5: Schematic picture of the photocatalytic principle of four different types of heterojunction structures**

The most conventional and widely used heterojunction system is the Type-II. This type features the electron transfer on the CB and the hole migration on the VB, respectively also the redox reactions take place on the CB and the VB. Low redox performance is the result of this electron and hole transfer mechanism. The Z-scheme and S-scheme heterojunctions' electron transport mode allows the composite photocatalyst to hold on to the electrons that have greater reducing power and holes with greater oxidizing power. When compared to the

type-II heterojunction system, the Z-scheme photocatalytic system considerably increases the catalytic effect by transferring electrons from the CB of semiconductor-I to the VB of semiconductor-II where they consume the oxidizing holes and weakly reducing electrons. Because of their special charge carrier transfer mechanism, S-scheme photocatalysts possess greater reduction and oxidation ability as well as strong driving force. With the Schottky heterojunction, a reduction reaction occurs rapidly as the electrons go straight from semiconductor-II to the conductor. Consequently, when compared to type-II heterojunctions, Z-scheme, S-scheme, and Schottky heterojunctions have far better redox capacities [118-120].

### 1.3.3 Effect of Doping in Photocatalysts:

Doping is the intentional introduction of foreign elements into an ultra-pure semiconductor to add impurities and manipulate its various characteristics and attributes. The band gap and band structure alignment of a photocatalyst can be adjusted by the strategic doping of transition metals and non-metals. The quantity and distribution of products in a photocatalyst system are controlled by the surface charge and charge transfer mechanism. Unmodified semiconductor photocatalysts with photon energies between 1.7 and 3.1 eV are unable to absorb solar light efficiently due to their higher band gaps. An attempt to lower the band gap energy, surface modification of the photocatalysts has been tried by the incorporation of foreign elements i.e. the introduction of oxygen vacancies in semiconductors or the application of stress along the soft direction of a multilayer semiconductor. Recent developments in semiconductor-incorporated doped metal and non-metal materials have been investigated in a number of studies to improve the efficiency of photocatalytic $CO_2$ conversion to renewable fuels [118-126,136].

#### 1.3.3.1 Noble metal doped semiconductors:

$CO_2$ receives electron from doping metal on semiconductors through an electron trap. To escape the holes on the semiconductor surface, the photogenerated electrons are moved from the conduction band of the semiconductor to the doped metal. Due to their Fermi level/electron-accepting areas at an energy slightly below the CB of semiconductors, noble metals such as Cu, Rh, Pd, Ru, Ni, Ag, Pt, and Au are frequently used as dopants with semiconductors for the photocatalytic reduction of $CO_2$ and to aid in visible light response. Pt is one of such metals that are employed extensively in numerous studies. As an illustration,

the $TiO_2$ semiconductor are wet impregnated with 0.5 weight percent Pt in order to prevent extremely poor photocatalytic activity. The reaction rate is accelerated in both the liquid and gas phases by a more uniform dispersion of 0.5 wt% Pt on the $TiO_2$ surface [127].

#### 1.3.3.2 Transition metal doped semiconductors:

Several studies reveal that transition metals possess the ability to increase photocatalytic activity and efficiency because of the high visible light conversion of $CO_2$ to renewable fuels. Transition metals are fascinating as their valence electrons can exhibit a variety of common oxidation states. In photocatalytic technology, transition metals such as Cu, Mo, Co, Ni, Ti, Mn, V and Fe are frequently employed as doping elements to improve semiconductor performance in visible light. A thorough analysis of multiple studies exhibited that excess percentages of dopant metal below the ideal level reduced the photocatalytic performances due to charge recombination for that an appropriate percentage of metal doping on semiconductors increased photocatalytic activity to reach the selectivity. It is well acknowledged that the increased efficiency is attributed to the transition metals in three ways: By trapping photogenerated conduction band electrons that (i) prevent electron-hole recombination; (ii) increase photoreduction efficiency due to Fermi level equilibration; and (iii) offer catalytic sites (thermal) for adsorbed ingredients and intermediates of $CO_2$ conversion reaction. One frequent technique to increase the high dispersion of transitional metal species is to load them onto the framework nanostructure. To enhance the rate of photocatalytic activities of various photocatalysts, transition metal doping is also useful in creating surface reactive sites for increased $CO_2$ adsorption [33,45,66,107,119].

#### 1.3.3.3 Non-metal doped semiconductors:

Several literatures suggests that co-doping of semiconductor photocatalysts with non-metals like C, N, S, B and F results in a significantly lower band gap energy than metal doping which is important for effective photocatalytic activity under visible light irradiation. Nitrogen-doped semiconductors have the most active results when compared to other non-metals because of their narrow band gap. Nitrogen-doped photocatalysts convert carbon dioxide at a faster rate in the presence of water vapor to methane and other hydrocarbons by solar energy. In particular, the transfer of effective carriers to the adsorbing species is facilitated by reduced wall thickness in nanotube arrays. Non-metals also have an impact on the rate of charge transfer and lower electron-hole recombination. In order to attain a high surface area and the immobilization of the catalysts during the photocatalytic irradiation,

other substrate materials are also employed. It is evident that recent methods are not sufficient to be used for the industrial production of fuels. For industrial renewable fuel harvesting from $CO_2$ choosing photocatalysts driven by the sun is therefore crucial [108,109].

## 1.4 Research Gap and/or Process bottlenecks:

Based on literature review the following research gap and /or process bottlenecks are identified.

- Selectivity and low yield of $CO_2$ reduced product are the main drawbacks of photocatalytic $CO_2$ reduction process for commercialization**.**
- Use of visible light active photocatalyst and proper absorption of visible light from solar spectrum.
- Improper separation and migration of the electrons and holes to the reduction and oxidation sites at the surface of the semiconductor photocatalyst and their recombination.
- Insufficient surface reactivity, the process by which molecules of $CO_2$ and $H_2O$ are adsorbed to an excited semiconductor surface and then reduced and oxidized by exchanging electrons.

## ***Goal of the present resarch:***

***Design and Development of visible light active Bismuth-based rGO supported photocatalysts ($Bi_2S_3$, $BiVO_4$, $Bi_2MoO_6$) to promote the photoreduction of $CO_2$ to selective valuable products.***

### 1.5 Bismuth (Bi)-based photocatalysts:

The chemical element bismuth has the atomic number 83 (Group 15) with the symbol Bi. Bismuth, which is categorized as a post-transition metal is in solid state at ambient temperature. It has been observed that bismuth is a delicate element that occurs in both free metal and minerals. The spiral staircase-like structure of bismuth crystals results from the stronger development of bismuth on the outer edges compared to the inner ones. When bismuth is exposed to air, it interacts with oxygen to form layers of bismuth oxide on the crystal surface that vary in thickness and produce different wavelengths and intensities of

scattered light. This is the main reason for the multicolored bismuth crystal's perimeter and its crystal lattice. In comparison to mercury, its heat conductivity is minimal. It seems that bismuth has a boiling point of 1560$^{o}$C and a melting temperature of 271$^{o}$C. Compared to solid bismuth, which is equal to water, liquid bismuth has a higher density. However, among the other chemical elements, bismuth is believed to be the heaviest and most stable [61]. Bismuth is not as toxic as nearby elements. Bi (V) and Bi (III) are the two main oxidation states of bismuth. Bi (III) is a well-liked and stable chemical that readily hydrolyzes in solutions containing water [127-143]

Bismuth-based photocatalysts have emerged as interesting research for novel photocatalysts in recent years due to their exceptional visible-light photocatalytic characteristics, appropriate energy band structure and distinctive physical and chemical features. Photocatalytic technology will be benefitted from research as most of these semiconductor materials have superior photocatalytic capabilities than $TiO_2$ photocatalysts. Additionally, there has been a clear increase trend in the number of publications on Bi-based photocatalysts in recent years. Numerous bismuth-based photocatalysts have been created thus far by researchers, including BiOCl (0D), BiOBr (1D/2D), BiOI (2D) [76,77], $Bi_2S_3$ (1D) [79], $Bi_2MoO_6$ (1D/2D) [80], $BiVO_4$ (0D/1D) [81], $Bi_2O_3$ (1D/2D) [82], and others. From a synthesis standpoint, the most widely used synthetic techniques at the moment for creating bismuth-based photocatalysts are chemical deposition, photoreduction, hydrothermal, solvothermal, ultrasonic synthesis, etc. The main advantages of using bismuth-based photocatalysts are given below:

- The band gap of bismuth-based photocatalysts is typically between 1.0 and 3.0 eV from the perspective of electronic structure.
- The hybridization of the O 2p orbital and the Bi 6s orbital is responsible for the small band gap.
- It helps to increase the migration rate of charge carriers and the separation efficiency of photogenerated electron-hole pairs by moving the valence band (VB) electrons upward.
- Bi-based photocatalysts can be used for hydrogen production, denitrification, CO2 reduction and the degradation of dyes, alcohols, heavy metals and other pollutants from the standpoint of photocatalytic performance.

However, the use of Bi-based photocatalysts in the field of photocatalysis is somewhat restricted because of their short conduction band and relatively low charge carrier separation

efficiency [118,136]. Currently, numerous techniques, including element doping, heterojunction construction, surface precious metal deposition, surface flaws engineering, etc. are being used to increase the photocatalytic activity of bi-based photocatalysts. Element doping can be classified as either metallic or non-metallic based on the characteristics of the elements. Electrons and holes can be attracted to doped metal components and subsequently moved to the reaction contact. The photocatalyst's band gap can be shortened and visible light usage increased by doping it with non-metallic materials. To improve photocatalytic performance, heterojunction can be created by introducing one or more semiconductor photocatalysts to form a structure that promotes the migration of photogenerated charge carriers and effectively reduces the recombination of photogenerated electron-hole pairs. The migration of electrons from the catalyst's surface to the precious metals occurs when the precious metals are deposited on the photocatalyst's surface, creating the Schottky potential barrier. The recombination of photogenerated electron-hole pairs can be efficiently inhibited by the development of a Schottky potential barrier [130-137].

### 1.5.1 Selection of Bismuth(III) Sulfide ($Bi_2S_3$) as photocatalyst:

$Bi_2S_3$ is a common semiconductor photocatalytic material based on bismuth ($E_g$ = 1.3–1.7 eV) due to its widely used spectrum of applications in photocatalysis, photoelectricity and electrochemical hydrogen storage, its benefits include low cost, minimal toxicity and superior photosensitivity. However, $Bi_2S_3$'s use in photocatalysis is restricted because of its high electron-hole pair recombination ratio and poor stability. To address the drawbacks of $Bi_2S_3$, alternative semiconductor materials that are suited for constructing heterojunction structures and element doping can be employed to address the aforementioned issues. $Bi_2S_3$ has been thoroughly researched in the fields of energy and the environment and the hydrothermal method is typically used to manufacture the compound. By intentionally creating surface defects in $Bi_2S_3$, the electronic structure can be modified to increase the number of surface-active sites on the catalyst surface, which promotes photocatalytic $CO_2$ reduction. With increase in the conductivity of $Bi_2S_3$ and by accelerateing electron transfer, the catalyst photocorrosion can be reduced. This will increase the effectiveness of charge carrier separation from photogenerated sources and enhance the performance of photocatalytic degradation. A series of heterojunction structure can be formed with other appropriate semiconductor photocatalysts. Furthermore, literature has exhibited that $Bi_2S_3$ possesses a strong photothermal impact as well. The combination of photocatalysis and photothermal

catalysis can have a synergistic effect that expands the potential applications of $Bi_2S_3$[31,41,78,111,138].

### 1.5.2 Selection of Bismuth Molybdate ($Bi_2MoO_6$) as photocatalyst:

Despite having a narrow band gap (2.4–2.8 eV), $Bi_2MoO_6$'s strong electron-hole pair recombination rate and slow charge transfer rate prevents it from being used widely in photocatalysis. $MoO_6$'s octahedral structure and $[Bi_2O_2]2þ$ nanosheets make up $Bi_2MoO_6$. $Bi_2MoO_6$'s multilayer structure encourages the extension of its visible light absorption wavelength to 500 nm. It also possesses strong thermal and chemical stability at the same time. The literature demonstrates that photocatalytic $CO_2$ reduction and photocatalytic pollutant degradation are achieved by the application of element doping, self-doping, surface defect creation, and heterojunction structure development. The specific surface area of $Bi_2MoO_6$ may change as a result of element doping altering the lattice structure. In order to increase the band gap energy, self doping can alter the catalyst's crystallinity as well as the locations of CB and VB. The development of surface imperfections may exhibit additional active sites on the catalyst's surface, hence enhancing the efficiency of photocatalytic degradation. Additionally, by creating a heterojunction structure with other semiconductor materials, the efficiency of electron-hole pair separation can be increased. Furthermore, modifying the shape of $Bi_2MoO_6$ during heterojunction formation is another way to enhance its photocatalytic activity. By adding surfactants and adjusting the calcination duration and temperature, the morphology can be manipulated. While current $Bi_2MoO_6$ modification procedures have demonstrated excellent efficacy in pollutant degradation, future research should focus more on water splitting and $CO_2$ photoreduction of $Bi_2MoO_6$[80,113,114].

### 1.5.3 Selection of Bismuth Vanadate ($BiVO_4$) as photocatalyst:

$BiVO_4$ is a representative of the Bi-based photocatalyst family and a non-toxic semiconductor photocatalyst. Tetragonal zircon (z-t), monoclinic scheelite (s-m), and orthoclinic scheelite (s-t) are its three crystal phases. Because of its narrow band gap (2.4–2.5 eV), monoclinic scheelite is superior to the other two crystal phases in photocatalytic applications and light absorption. $BiVO_4$ can be produced by a variety of techniques, including solvothermal, hydrothermal and impregnation calcination. Due to its ease of usage, the hydrothermal technique is frequently employed in the synthesis of $BiVO_4$. A viable method to increase

photocatalytic activity is to build a heterojunction device using $BiVO_4$ and other semiconductors with narrow band gaps. The band bending at the heterojunction structure's interface in the heterojunction system is a result of the potential difference between the two types of photocatalysts, which differs in their CB and VB positions. In order to facilitate the migration and separation of photogenerated carriers, a new electric field is created. However, different photocatalytic pathways can also be provided by defect engineering, facet engineering and element doping, which increase the photocatalytic performance of $BiVO_4$ and expand its light absorption spectrum. Simultaneously, $BiVO_4$ photocatalyst stability is ofgeat concern. While many techniques can enhance the photocatalytic potential of $BiVO_4$-based photocatalysts, photocorrosion is an inescapable occurrence that necessitates the development of novel photocatalysts capable of mitigating its effects [81,115].

However, the use of Bi-based photocatalysts in the field of photocatalysis is somewhat restricted because of their short conduction band and relatively low charge carrier separation efficiency. Currently, numerous techniques, including element doping, heterojunction construction, surface precious metal deposition, surface flaws engineering, etc. are being used to increase the photocatalytic activity of bi-based photocatalysts. Element doping is classified as either metallic or non-metallic based on the characteristics of the elements. Electrons and holes are attracted to doped metal components and subsequently moved to the reaction contact. The photocatalyst's band gap can be shortened and visible light usage are increased by doping it with non-metallic materials. To improve photocatalytic performance, heterojunction can be created by introducing one or more semiconductor photocatalysts to form a structure that promotes the migration of photogenerated charge carriers and effectively reduces the recombination of photogenerated electron-hole pairs [116].

### 1.6 Graphene/reduced Graphene Oxide (rGO) based photocatalysts:

Graphene is a two-dimensional (2D) nanomaterial that has garnered significant attention as a potential candidate for photocatalytic activities due to its unique properties, including its high specific surface area (2630 $m^2\ g^{-1}$), high adsorption capacity, excellent electron mobility (200,000 $cm^2V^{-1}s^{-1}$), exceptional optical transparency (~97.7%), excellent thermal conductivity (3000-5000 $W\ m^{-1}K^{-1}$), ease of chemical modification and electrochemical stability. Graphene and its modifications, such as functionalized graphene (rGO) and graphene composites are now understood to offer a wide range of potential benefits for environmental applications as a result of multiple research efforts. Given their benefits (such

as stability, recyclability, high $CO_2$ adsorption capacity and the presence of functional groups on graphene-based materials), these materials have proven to be superior when it comes to photocatalytic $CO_2$ reduction for its useagerenewable fuel applications. Typically, graphene is a single-atomically thick $sp^2$ hybridized carbon material. However, this functionalized graphene demonstrated stronger electrostatic interaction with adsorbates and larger surface area ($\pi$-$\pi$) interaction, which lead towards preferred adsorption. The advantages of rGO-based photocatalysts for $CO_2$ reduction can be categorized in to six aspects:

- Increasing visible light absorption power.
- Suppressing photoinduced charge carrier recombination
- Increasing specific surface areas
- Enhancing $CO_2$ adsoprtion and activation power
- Increasing nanoparticles-dispersion and decreasing nanoparticles-size
- Enhancing photo-stability

The amount of graphene loading has a significant impact on the photocatalytic activity of reduced graphene oxide (rGO) based photocatalysts. The best catalytic outcome can be achieved with the optimal rGO loading because excessive rGO loading may impede visible light from reaching the catalytic surface that decreases photocatalytic $CO_2$ reduction efficiency [36,68,71,85-87,92,124].

### 1.7 Selection of Copper (Cu) as transition metal doping element:

In the effort to increase the yields of renewable fuels, transition metals and metal oxides that are prevalent on Earth have been thoroughly studied. Several Cu-based photocatalysts produce solar products at tolerable production rates (up to a certain millimoles per hour), indicating significant development in this direction. For longer reaction times, these photocatalysts exhibit a sun to fuel (STF) efficiency of less than 1.0%, which is insufficient for use in commercial settings. Thus, either the STF efficiency should be raised or its selectivity should be shifted toward C1+ products, especially those with higher market value (such as methanol and ethanol), for financial gains, in order to improve these photocatalysts' compatibility with solar photovoltaics. Through C–C coupling, Cu-based photocatalysts direct the selectivity toward C2+ products and Cu regulates this reaction. In order to stabilize the reaction intermediates and link them to create the final C2 + products, Cu must be in an appropriate oxidation state. Because of their intriguing characteristics, Cu-based

photocatalysts with appropriate Cu oxidation states are therefore quite attractive. Cu interacts with $CO_2$ and $H_2O$ because it is a three-dimensional transition metal with various oxidation states. Depending on its oxidation state, it can interact with these reactants by one- or two-electron routes to form adsorbates with various topologies and adsorption strengths. The adsorbates' selectivity to different adsorbents is impacted by these arrangements. This is due to the fact that these adsorbates undergo several reaction processes under illumination, resulting in the transformation of diverse products. Cu-based nanocatalysts are employed in many different catalytic reactions due to their distinctive properties. Controlling the oxidation states of $Cu_2O$/CuO is difficult, though, when light is present. This is because the stability of $Cu_2O$ is decreased by the irreversible redox disproportionation process ($Cu_2O \rightarrow Cu + CuO$). Therefore, to achieve their commercial uses, Cu-based photocatalysts should have their stability increased in addition to their selectivity, even though they show high photoactivity, earth abundanceand non-toxicity [32,118,120,126].

### 1.8 Selection of Nitrogen (N) as non-metal doping element:

Doping of nitrogen is the most efficient and extensive investigation as nitrogen and oxygen shares equivalent structural, electrical and chemical properties like polarizability, electronegativity, coordination numbers and ionic radii. A visible light-driven photocatalyst with band edge potentials appropriate for the photocatalytic $CO_2$ reduction can be created when other elements, like N-2p, with atomic orbitals having potential energy higher than O-2p atomic orbitals are introduced. New VBs are formed in place of O-2p atomic orbitals, resulting in smaller $E_g$ without changing the CB level. The functional material that interests us, N-doped graphene oxide (N-GO), serves as a dual promoter by increasing $CO_2$ adsorption and offering a reactive site for the photocatalytic reaction [121,122].

In view of the present state of the art, the proposed research aims and objectives of the thesis are mentioned below:

### 1.9 Research Objectives:

This thesis addresses the following research goals in linked domains, taking into account the entirety of the research gap:

- Design and synthesis of visible light responsive reduced graphene oxide (rGO) supported Bismuth (Bi)-based ($Bi_2S_3$, $Bi_2MoO_6$, $BiVO_4$) nano-composites.
- Transition metal (Cu)/non-metal (N) doping of rGO supported $Bi_2S_3$ and $Bi_2MoO_6$/$BiVO_4$ nano-composites to achieve specific product (Mthanol/Ethanol/Formic acid)-selective $CO_2$ reduction.
- Characetrization (crystallinity, chemical state, morphological, optical, electrochemical etc.) of synthesized nanocomposites.
- Study of the performance of synthesized doped and undoped nano-composite photocatalysts: determination of optimum doping to maximize the yield of specific product selective $CO_2$ reduction.
- Prediction of mechanism of $CO_2$ photo-reduction.

## 1.10 Methodology

## 1.10.1 Synthesis of photocatalysts

### 1.10.1.1 Synthesis of Graphene Oxide (GO):

The process of synthesizing graphene oxide (GO) involves using the Improved/modifiedHummer's method [85,86]. Concentrated $H_2SO_4$ and $H_3PO_4$ are mixed in a 9:1 (360 ml: 40 ml) ratio and added to graphite flakes (3.0 g, 1 wt. equiv.). Since the reaction is exothermic, $KMnO_4$ (18.0 g, 6 wt. equiv.) is added gradually to the mixture while stirring continuously. The mixture is then cooled at room temperature, diluted with deionized water (400 ml) and treated with 30% $H_2O_2$ to reduce any remaining permanganate and manganese dioxide. The resulting solution is centrifuged multiple times and treated with ethanol and HCl and ethanol. Following centrifugation and washing with deionized water, a chocolate brown residue is obtained. Then it is dried, stored and used as per requirement.

### 1.10.1.2 Synthesis of rGO-$Bi_2S_3$/CuO:

Copper oxide (CuO) loaded rGO-$Bi_2S_3$ nano-hollow flower composites (rGO-$Bi_2S_3$/CuO) are created by mixing rGO solution with $Bi_2S_3$ nano-hollow flower composites at a constant concentration with 2 weight percent of CuO loading [88]. The purpose of this is to look at how CuO loading affects the yield of the $CO_2$ reduction product produced by photocatalysis.

In this work, rGO-$Bi_2S_3$/CuO nanostructures are formed by hydrothermal treatment in order to yield a high yield of products. Independently made $Cu(NO_3)_2.5H_2O$ solutions are added to this standard procedure and stirred continuously for two hours in order to attain two weight percent of CuO loading in the rGO-$Bi_2S_3$ solution. The mixture's pH is also adjusted to 10 using a 2 M NaOH solution. After that, the mixture is placed into a 100 ml Teflon-lined container that is sealed inside a stainless-steel autoclave. It is then placed in the muffle furnace and heated to 180°C for 16 hours to undergo hydrothermal treatment. Following centrifugation, the products are collected, allowed to naturally cool to room temperature, repeatedly cleaned in ethanol and double-distilled water, dried for 12 hours in a heated chamber under vacuum at 70°C, and then calcined for an additional 4 hours at 400°C. CuO loaded $Bi_2S_3$ nano-hollow flower composites are prepared using similar procedures so that their characteristics can be compared. Fig. 1.6 depicts the schematic representation of the synthesis process.

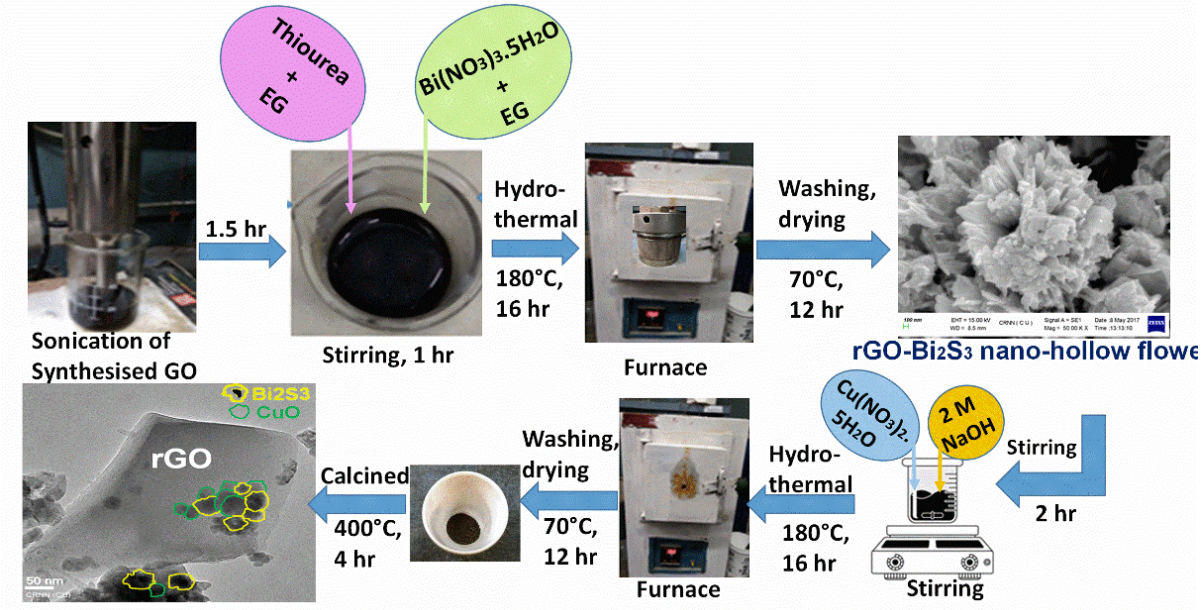


**Fig. 1.6: Schematic representation of the synthesis process of rGO-$Bi_2S_3$/CuO S-scheme heterojunction photocatalyst**

### 1.10.1.3 Synthesis of Cu-doped-$Bi_2S_3$/rGO:

By varying the percentages of Cu loading of 0.5, 1, and 2 weight percent, respectively, with the fixed concentration of $Bi_2S_3$ rod-shaped nanocapsule and rGO solution, the synthesis of copper-doped (1D) $Bi_2S_3$ rod-shaped nanocapsules/rGO has been carried out in order to investigate the impact of Cu doping on the selectivity of the $CO_2$ reduced product. Cu-doped-

$Bi_2S_3$/rGO nanostructures are prepared using hydrothermal treatment in this study in order to produce a highly selective product with a high yield. In this typical procedure, Cu loading into the $Bi_2S_3$/rGO solution is achieved by adding varying volumes of separately dissolved $Cu(NO_3)_2.5H_2O$ to get 0.5, 1, and 2 weight percent of Cu doping. A 3 M NaOH solution was used to bring the mixture's pH down to 8. An additional hour has been spent for stirring the entire concentration. The entire combination was then put inside a 100 ml. stainless steel autoclave with a Teflon lining, sealed, and kept at 160°C for 18 hours. The products are collected after centrifugation and allowed to naturally cool to room temperature. They are then repeatedly cleaned with ethanol and double-distilled water before being vacuum-dried for 12 hours at 70°C in a heated chamber. Cu-doped (1D) $Bi_2S_3$ rod-shaped nanocapsules are manufactured using a similar process for property comparison. Schematic representation of the synthesis process of Cu doped-Bi2S3/rGO photocatalyst is shown in Fig. 1.7.

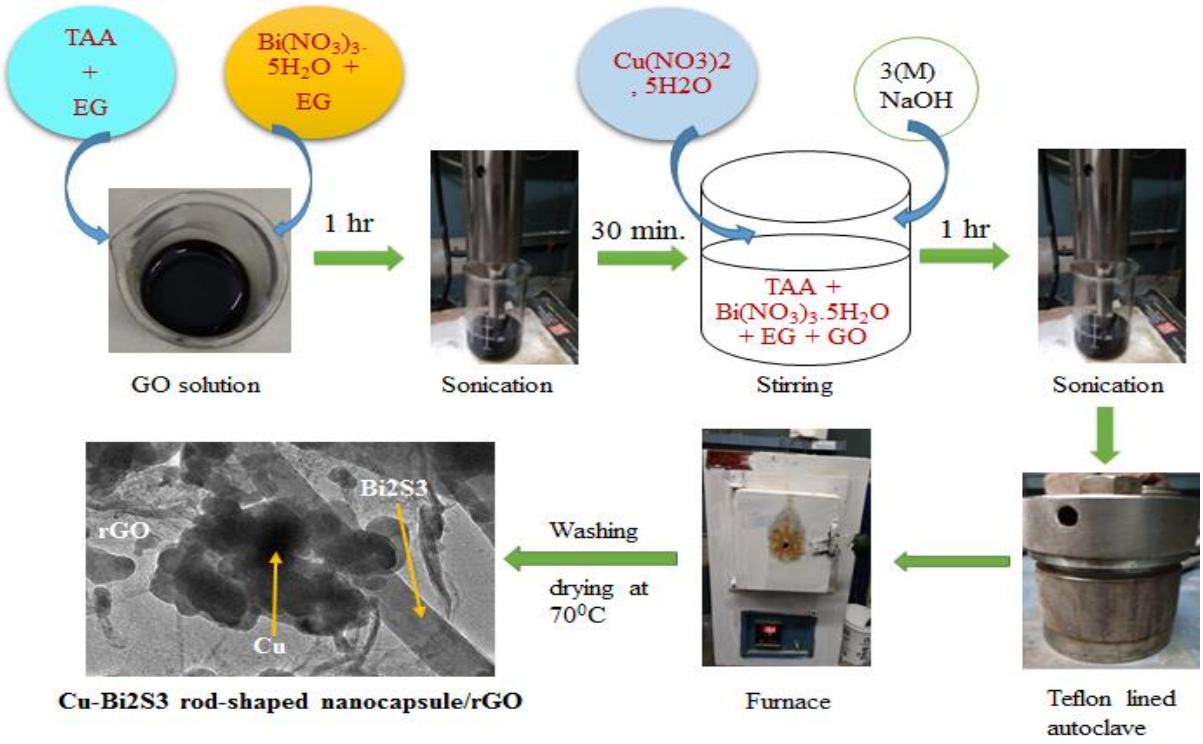


**Fig. 1.7: Schematic representation of the synthesis process of Cu doped-$Bi_2S_3$/rGO photocatalyst**

### 1.10.1.4 Synthesis of Cu doped 2D-$Bi_2MoO_6$nanoribbon/rGO:

In this present work the doping of Cu with different percentages is performed in a fixed weight ratio of 2D-$Bi_2MoO_6$nanoribbon/rGO (1:0.016) composites. To study the performance

of photocatalytic reduction of $CO_2$ to $C_2$-based product based on selectivity and yield of selective product, Cu doped 2D-$Bi_2MoO_6$nanoribbon/rGO composites aresynthesised with different percentages of Cu loading of 1, 2, 3 and 4 wt%, respectively. In this work as the source of Cu different weight of $Cu(NO_3)_2.5H_2O$ are dissolved in 2D-$Bi_2MoO_6$nanoribbon/rGO solution separately to get 1, 2, 3 and 4 wt% Cu doping, respectively.The pH of the mixed solution is maintained to 10 using a 2M NaOH solution. After 1 hour stirring the mixture is poured in an autoclave (Teflon lined stainless steel – 100ml) and the autoclave is transferred into a furnace for hydrothermal heating at 180°C for 20 hours.When the temperature of the Teflon lined stainless steel autoclave reached to the room temperature, the formed product is collected, centrifuged and washed several times with ethanol and deionized water repeatedly and finally dried at 80°C for 14 hours in a hot chamber to acquire Cu doped 2D-$Bi_2MoO_6$nanoribbon/rGO photocatalysts. The above-mentioned synthesis process is showed in Fig. 1.8.

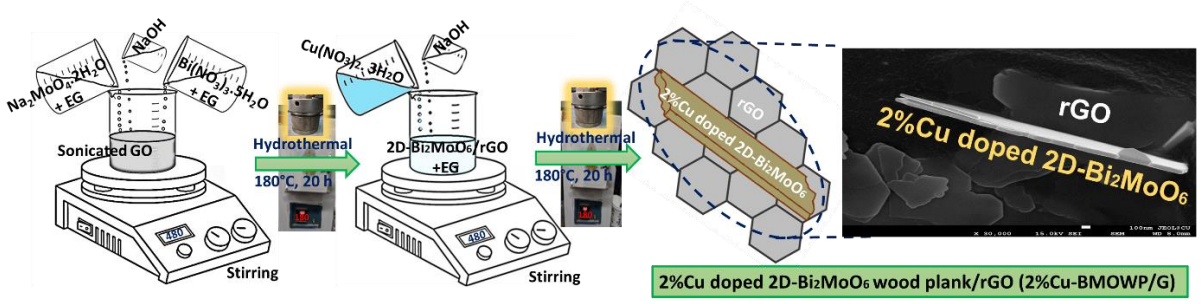


**Fig. 1.8: Schematic representation of synthesis process of 2%Cu doped 2D-$Bi_2MoO_6$nanoribbon/rGO photocatalyst**

### 1.10.1.5 Synthesis of N doped $BiVO_4$/rGO:

In the current work, fixed weight ratio $BiVO_4$/rGO (1:0.025) nanocomposites are doped with varying amounts of nitrogen (N). In order to investigate the effectiveness of photocatalytic reduction of $CO_2$ to C1-based product, N doped rGO/$BiVO_4$ nanocomposites are synthesized with varying percentages of N loading of 1, 1.5, and 2 wt%, respectively, based on selectivity and yield of selected product. In this work, various weights of urea are independently dissolved in (2.5%)rGO/$BiVO_4$ solution as the source of N to obtain 1, 1.5, and 2 weight percent N doping, respectively. Using a 2M NaOH solution, the pH of the combined solution

is kept at 9. Following a 1.5-hour stirring period, the mixture is transferred to a 100ml Teflon-lined stainless-steel autoclave. The autoclave is then placed inside a furnace and heated hydrothermally for a full 24-hour period at 180°C. The formed product is collected, centrifuged, and repeatedly washed with ethanol and deionized water before being dried at 70°C for 12 hours in a hot chamber to obtain N doped rGO/$BiVO_4$ photocatalysts. This process continues until the temperature of the Teflon-lined stainless-steel autoclave reaches room temperature. Fig. 1.9 depicts the synthesis process previously discussed.

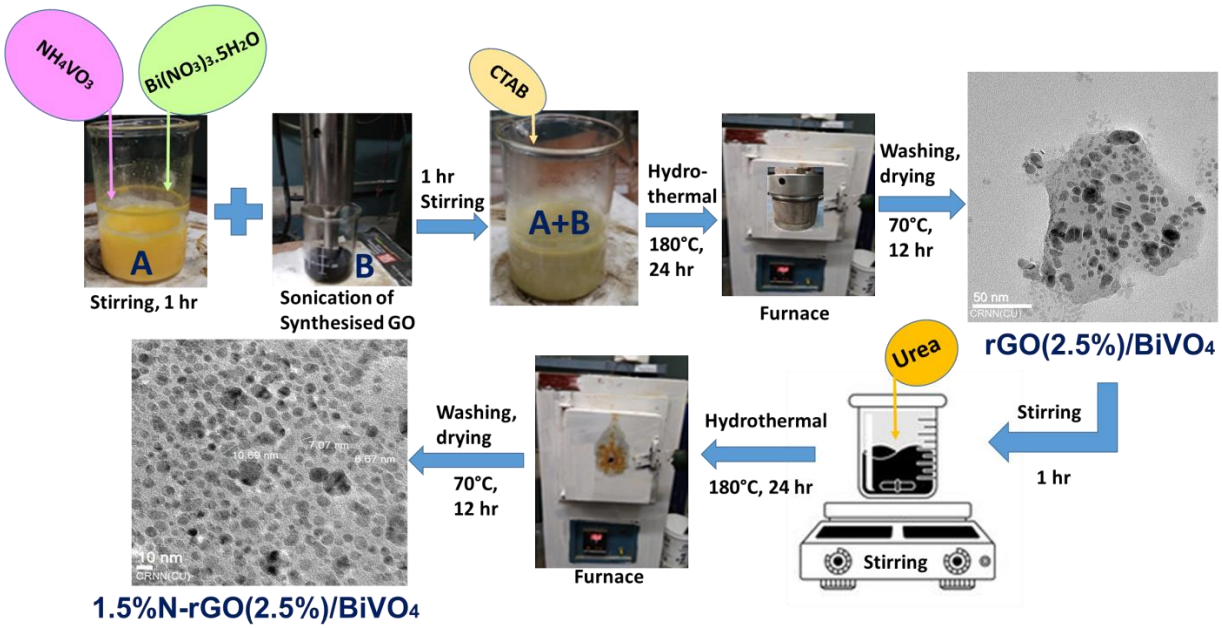


**Fig. 1.9: Schematic representation of synthesis process of 1.5%N-doped (2.5%)rGO/$BiVO_4$ photocatalyst**

## 1.10.2 Characterization Study

In this thesis the below mentioned characterization analysis of synthesised photocatalysts (**rGO-$Bi_2S_3$/CuO, Cu-doped-$Bi_2S_3$/rGO, Cu doped 2D-$Bi_2MoO_6$nanoribbon/rGO and N doped $BiVO_4$/rGO**) have been performed.

### 1.10.2.1 Morphological analysis:

The morphological analysis of the photocatalysts has been done by utilizing Scanning Electron Microcopy and Transmission Electron Microscopy Scanning Electron Microscopy (SEM) involves the scanning of the sample surface with high energy beam of electrons to

produce high resolution images. The samples are studied using scanning electron microscope utilizing 15.0 kV of voltage, for charging electrons. Energy Dispersive X-ray spectroscopy (EDS) set up attached with the SEM instrument is used to detect the elemental composition of the samples. Transmission Electron Microscopy (TEM) involves the transmission of electrons through sample to form an image. The TEM micrographs are obtained by utilizing anelectron beam at a voltage of 200 kV.

**1.10.2.2 Identification of bonds:**

The identification of bonds and the detection of the functional groups present in the synthesized photocatalysts has been determined by Fourier Transform Infrared Spectroscopy (FTIR) in the 400-4000 $cm^{-1}$wavenumber region of FTIR spectrophotometer by forming KBR pellets.

**1.10.2.3 Crystallinity Study:**

The purity and crystalline structure of the synthesized photocatalysts has been studied by using X-ray Diffraction (XRD) in Xpert-PRO diffractometer with Cu K radiation of =0.154060 wavelength applying 40 kV voltages, 30 mA current, 1.2 kW power in the 2θ range for all samples from 10 to 90º. The crystallite size is determined by Scherrer equation [87-90], which is as follows:

$$D = K\lambda / \beta cos\theta \quad (1.1)$$

where θ is the Bragg's diffraction angle, D is the average crystallite size, k= 0.9 is the shape factor, and λ is the X-ray radiation wavelength (1.5406 Å).

**1.10.2.4 Surface Chemical State Analysis:**

The surface chemical states of the different elements present in the photocatalyst composites are studied using X-ray Photoelectron Spectroscopy (XPS) The binding energy of the elements are analysed and the shift of the electron clouds signifies the formation of heterostructures in these nanocomposites. XPS is done employing mono-energetic Al kα x-rays. X-ray photoelectron spectroscopy (XPS: AXIS Supra Model with Al K-1486.6 eV Dual Al K/Mg K Achromatic X-ray Source) is used to examine the chemical state composition, defect type, concentration and variation in band structure in the sample.

**1.10.2.5 Surface area and thermogravimetricanalysis:**

The $N_2$ adsorption and desorption isotherms, specific surface area, and pore diameter of synthesised samples have been evaluated by Brunauer-Emmett-Teller (BET) Instrument (QuantachromeR ASiQwin™, Quantachrome Instruments version 3.01 at 77.35 K.

PerkinElmer TGA 4000 has been used to conduct thermogravimetric analysis (TGA) in nitrogen atmosphere at a temperature of 850°C with a scan rate of 15°C.

### 1.10.2.6 Optical property measurement

#### 1.10.2.6.1 UV-Vis Spectrocopy

The optical nature of the samples is analysed using UV-Vis Spectroscopy using UV-Vis Spectrophotometer. UV-Vis Spectroscopy is a type of spectroscopy technique where the electronic transitions are studied when the sample is exposed to light. The band gap of the synthesized photocatalysts is determined by Tauc plot [100-105] analysis following the equation:

$$[\alpha h\nu] = A\left[h\nu - E_g\right]^{\frac{n}{2}} \quad (1.2)$$

Where '$E_g$' (eV) is the bandgap of the photocatalyst, 'h' is Planck's constant, 'c' is the speed of light, 'ν' is the frequency of light, 'A' is the absorption coefficient, 'n' is 1 for direct bandgap and '4' for indirect bandgap of semiconductors.

#### 1.10.2.6.2 Photoluminescence Spectroscopy (PL)

The photoluminescence spectroscopy (PL) of the samples is carried out to study the degree of rate of recombination between the photogenerated electrons and holes. The PL spectroscopy is done using a Fluorescence Spectrophotometer.

#### 1.10.2.6.3 Electrochemical Impedance Spectroscopy (EIS) analysis:

Electrochemical-measurements have been performed at room temperature by an electrochemical workstation of AUTO204-FRA32M-S with a standard three-electrode cell. Glassy Carbon coated in the synthesised sample, an Ag/AgCl electrode -saturated KCl, and a Pt wire have been utilised as working, reference, and counter electrodes, respectively. Electrochemical impedance spectroscopy (EIS) has been performed in the 0.2 M aqueous KCl medium (pH: 7.0) with an applied potential of -0.5V vs. Ag/AgCl in 3 M KCl by introducing an AC voltage of 10 mV amplitude in the frequency range of 0.1 to 100000 Hz.

#### 1.10.2.6.4 Mott Schottky analysis (MS):

M-S plots analysis provides an estimation of the flat-band potentials ($E_{FB}$) of photocatalysts at potential V vs. Ag/AgCl. The $E_{FB}$ values of photocatalysts are calculated as a certain potential V vs. NHE, respectively using the Nernst equation: $E_{NHE}$ (V) = $E_{Ag/AgCl}$ + 0.197. Actually, for the n-type photocatalyst the $E_{CB}$ is essentially ~0.1 higher than $E_{FB}$ [89]. Therefore, the $E_{CB}$ of photocatalysts can be determined based on the equation:

$$E_{VB} - E_{CB} = E_g \quad (1.3)$$

## 1.10.3 Performance Study and analysis

#### 1.10.3.1 Photocatalytic reactor set-up:

Two different photocatalytic $CO_2$ reduction reactors are used to assess the photocatalytic activity of the synthesized photocatalysts: the first one is based on a 125-watt high-pressure visible lamp (Fig. 1.10(a)) and the second one is based on a 100-watt Xenon lamp of a solar simulator (Newport Oriel LCS 100, Manual Shutter, 94011A), (Fig. 1.10(b)) supported by an AM-1.5G air mass filter, where the light intensity is 100 mW/cm$^2$ and the light area is 16.82 cm$^2$. To evaluate the photocatalytic activity, 0.025 g of every photocatalyst is used in a 100-mL hollow-quartz reactor separately. Prior to visible light irradiation, $CO_2$ gas (99.9% pure) with a low flow rate is supplied into the degassed reactor to reach 1 atm pressure. The 80 ml of ultrapure water consisting of 0.5 M $NaHCO_3$ as hole-scavengers is used in the quartz reactor to make a $CO_2$ absorbed solution (saturated) and to achieve the maximum $CO_2$ adsorption on the photocatalyst's active sites. The entire process is carried out in the dark for 60 minutes under magnetic stirring conditions to eliminate all oxygen dissolved in the saturated solution. 0.025 g of photocatalysts are added to the aforesaid saturated solution, and the photocatalytic reaction is implemented for 8 hours at 20°C, under the visible light irradiation of the prescribed 125-watt high-pressure visible lamp and 100-watt Xenon lamp with constant stirring speed. In the both cases UV-protector arrangement is also used to allow visible light to enter the photocatalytic reactor. After 8 h illumination of light the photocatalytic $CO_2$-reduced products are collected from the reactor solution by a thin pipe connected to the syringe, and the concentration of each product is determined by gas chromatography mass spectrometry (GCMS) equipment: Agilent-7890A system and GC (FID) and GC (TCD), with helium as the carrier gas.

Three different types of blank reactions are carried out to ensure that the products are generated only as a result of photocatalytic $CO_2$ reduction.

- In the absence of a photocatalyst, the whole experiment is carried out under the same operating circumstances.
- The entire experiment is carried out in complete darkness in the presence of a photocatalyst under identical working circumstances.
- The blank experiment is performed under the illumination of a Xenon lamp and the presence of a photocatalyst in the photocatalytic quartz-reactor without purging $CO_2$ gas.

The pure grades of ethanol and methanol are also utilised for analysis to ensure the quality of the $CO_2$-reduced product. In this thesis the photocatalytic activity study has been performed for all synthesised photocatalysts.

- The photocatalytic performance study of all synthesised $Bi_2S_3$-based photocatalysts (rGO-$Bi_2S_3$/CuO S-scheme heterojunction and Cu doped-1D $Bi_2S_3$/rGO) are performed in the photoreactor containing 125-watt high-pressure visible lamp, which is shown in Fig. 1.10(a).
- The photocatalytic performance study of all synthesised 2D-$Bi_2MoO_6$ nanoribbon-based photocatalysts and $BiVO_4$based photocatalysts (Cu doped 2D-$Bi_2MoO_6$ nanoribbon/rGO and N doped $BiVO_4$/rGO) are performed in the photoreactor containing 100-watt Xenon lamp (Solar simulator), which is shown in Fig. 1.10(b).

#### 1.10.3.1.1 Identification of Photocatalytic $CO_2$ reduced products:

In this thesis the photocatalytic $CO_2$ reduced selective product like methanol ($CH_3OH$), ethanol ($C_2H_5OH$) and formic acid (HCOOH) for all synthesised rGO supported Bi-based photocatalyst have been identified and analysed by NMR and GCMS analysis.

- **NMR:** Using nuclear magnetic resonance (NMR) spectroscopy is a sophisticated method of characterization. It is employed to ascertain a sample's molecular structure down to the atomic level. NMR spectroscopy may identify phase shifts, conformational and configurational changes, solubility, and diffusion potential in addition to the molecular structure. The primary application of NMR spectroscopy has been in the study of atom nuclei rather than electrons. NMR spectroscopy are used to map the chemical

surroundings of typical nuclei based on the information it provides. Here $^{13}C$ NMR is used to detect photocatalytic $CO_2$ reduced products in liquid phase [90,91].

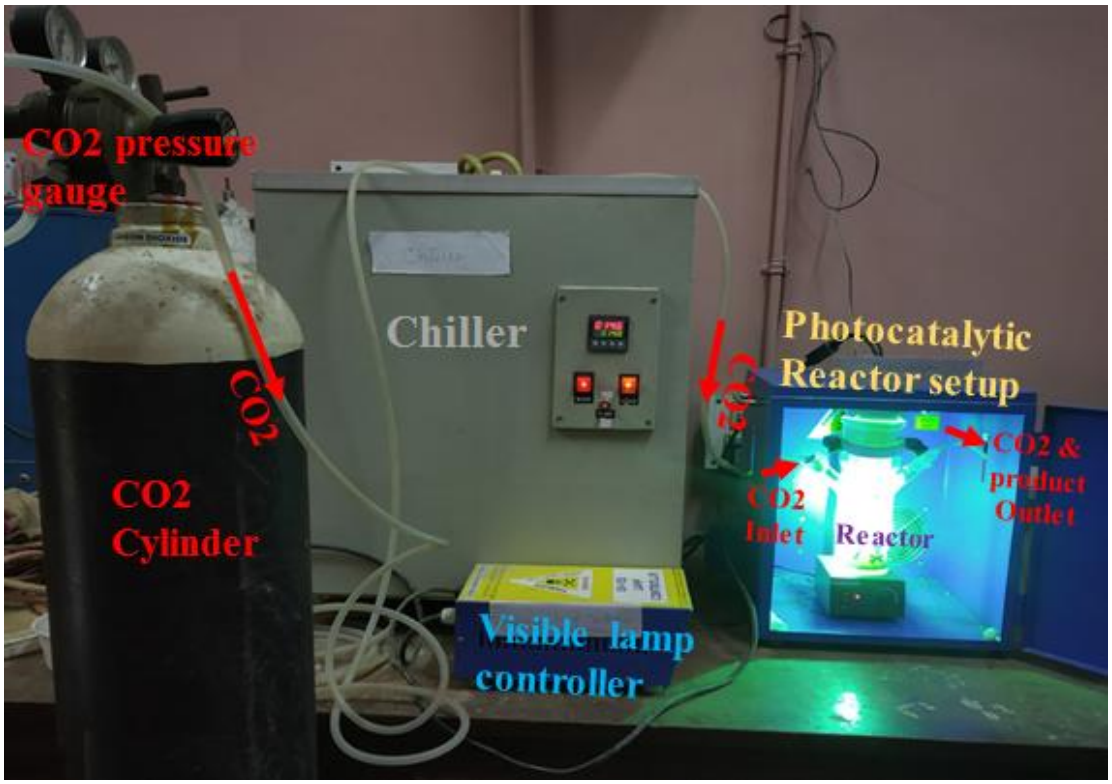


**Fig. 1.10 (a): Photocatalytic $CO_2$ reduction-reactor set-up (125-watt high-pressure visible lamp)**

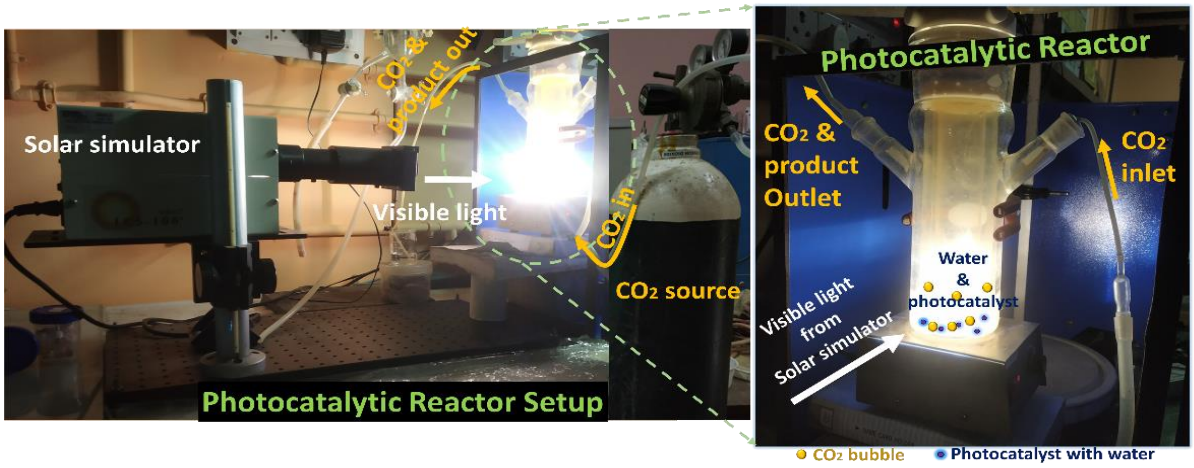


**Fig. 1.10 (b): Photocatalytic $CO_2$ reduction-reactor set-up (100-watt Xenon lamp of solar simulator)**

- **GCMS:** Using gas chromatography mass spectrometry (GCMS) to examine the production of compounds throughout the reduction/oxidation process is an additional method for product detection. Fast time response may be possible as a result, essentially providing real-time information regarding reaction products. GCMS is therefore frequently used for $CO_2$ photoreduction. However, mass spectrometry can often be time-consuming and require high mass resolution to identify and measure the different components when working with mixtures of hydrocarbons. Here each product is determined by gas chromatography equipment: Agilent-7890A system and GC-FID and GC-TCD, with helium as the carrier gas. Blank reactions are also carried out to ensure that the products are generated only as a result of photocatalytic $CO_2$ reduction [92,93].

### 1.10.3.2 Performance Analysis of Photocatalytic $CO_2$ reduction:

The performance of a specific photocatalyst is analysed in terms of (i) photocatalytic activity and (ii) apparent quantum efficiency (AQE) [94-100]. This is applicable for systems when the source of irradiation is solar energy.The AQE of the synthesised photocatalysytys are measured under the irradiation of single band 420 nm by using 420 nm band pass filter.

#### 1.10.3.2.1 Photocatalytic Activity (mol $g_{cat.}^{-1}$ $h^{-1}$):

The efficiency of a photocatalyst in a particular reaction over a predetermined amount of time is essentially represented by photocatalytic activity (mol $g_{cat.}^{-1}$ $h^{-1}$), a unit used to measure the rate of a photocatalytic reaction. Specifically, it indicates how many moles of a reactant are converted per gram of catalyst per hour under light exposure.

$$\text{Photocatalytic Activity (mol } g_{cat.}^{-1} h^{-1}) = \frac{Moles\ of\ photocatalytic\ CO2\ reduced\ product}{g\ of\ photocatalyst \times time\ (h)} \qquad (1.4.1)$$

#### 1.10.3.2.2 Apparent Quantum Efficiency (%):

Quantum yield is a factor to determine the performance of photocatalysts during photocatalytic $CO_2$ reduction. It can be defined as:

$$\text{Q.Y. (\%)} = (Numberofreactedelectrons / Numberofincidentphotons) \times 100 \qquad (1.4.2)$$

If a photon ($E_{photon}$) of wavelength of $\lambda_{inc}$ (nm) is incident during a photocatalytic $CO_2$ reduction reaction, the energy of this one photon calculated using the equation:

$$E_{photon} = hc/\lambda_{inc} \quad (1.5)$$

where h (J·s) is Planck's constant, c ($m \cdot s^{-1}$) is the speed of light , $\lambda_{inc}$ (m) is the wavelength of the monochromatic light that is incident. The energy of the incident monochromatic light ($E_{total}$) is calculated using the following equation:

$$E_{total} = Pst \quad (1.6)$$

here P ($W \cdot m^{-2}$) is the power density of that incident monochromatic light, S ($m^2$) is area that is being irradiated, t (s) is the duration of the exposure of the incident light

The total number of incident photons can be determined from the given equation:

$$\text{Number of incident photons} = E_{total}/E_{ph} = Ps\,\lambda_{inc}t/\,hc \quad (1.7)$$

Apparent Quantum Yield is twice the ratio between numbers of $CO_2$ reduced product molecules evolved by number of incident photons multiplied by 100.

$$\text{A.Q.Y (\%)} = [(2 \times Number\ of\ CO_2 \text{ reduced product molecules})/Number\ of\ incident\ photons] \times 100 \quad (1.8)$$

This can be seen from the equation

$$\text{A.Q.Y(\%)} = [(2\times n_{[CH3OH/C2H5OH/HCOOH],t}\times N_A\times h\times c)/(P\times s\times \lambda_{inc}\times t)] \times 100 \quad (1.9)$$

Where $n_{[CH3OH/C2H5OH/HCOOH],t}$ (mol) is number of molecules of hydrocarbons evolved over the duration t of the incident light, $N_A$ ($mol^{-1}$) is Avogadro's constant.

## 1.11 Overview of Research

The primary focus of this research is the selective photocatalytic reduction of $CO_2$ to a specific desirable product and increase the yield of selective photocatalytic $CO_2$ reduction to renewable fuel, by utilizing doping method. The optimum amount of transition metal (Cu)/non-metal (N) is used in the design of reduced graphene oxide (rGO) supported Bismuth based photocatalytic systems to achieve the highest yields of selective $CO_2$ reduced product.

- ***Design and synthesis of Cu-doped 1D-$Bi_2S_3$/rGO photocatalyst for selective photocatalytic reduction of $CO_2$ to Methanol ($CH_3OH$).***

- ***Design and synthesis of Cu-doped 2D-$Bi_2MoO_6$/rGO photocatalyst for selective photocatalytic reduction of $CO_2$ to Ethanol ($C_2H_5OH$).***

- ***Design and synthesis of N-doped rGO/$BiVO_4$ photocatalyst for selective photocatalytic reduction of $CO_2$ to Formic acid (HCOOH).***

The overall outlook of the thesis is presented in Fig. 1.11 and the schematic of the entire research work is presented in Fig. 1.12.

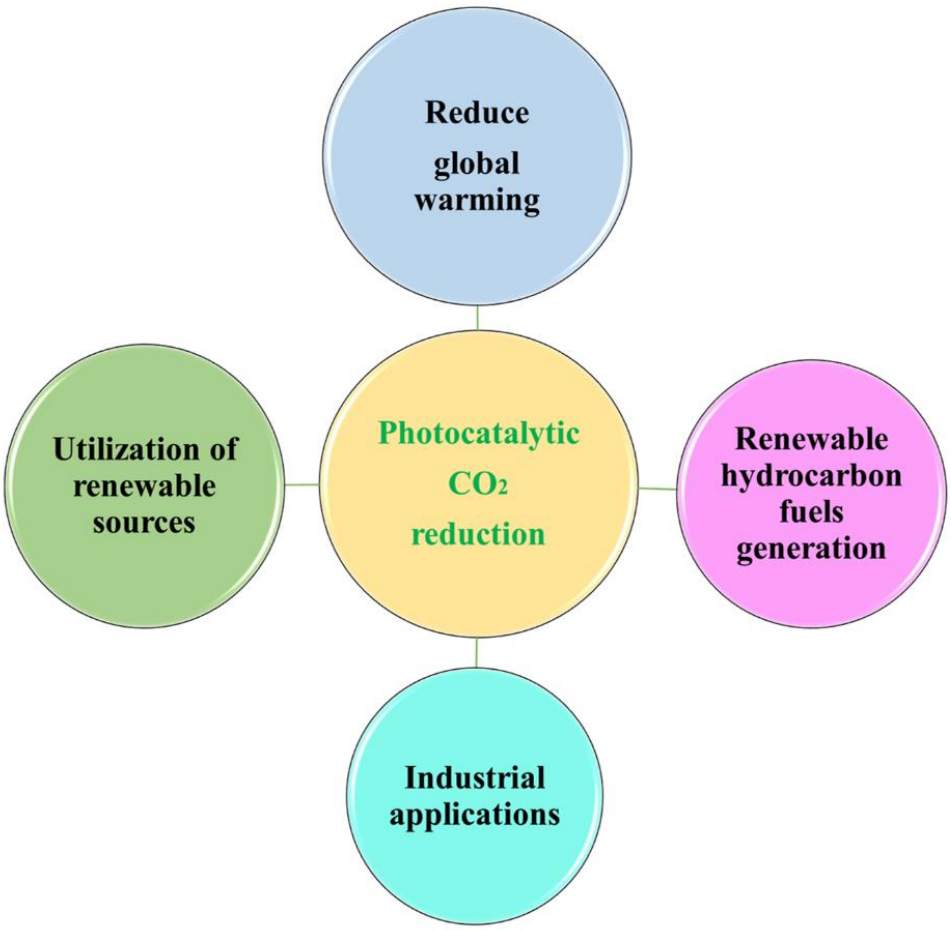


**Fig 1.11 Overall outlook of the thesis.**

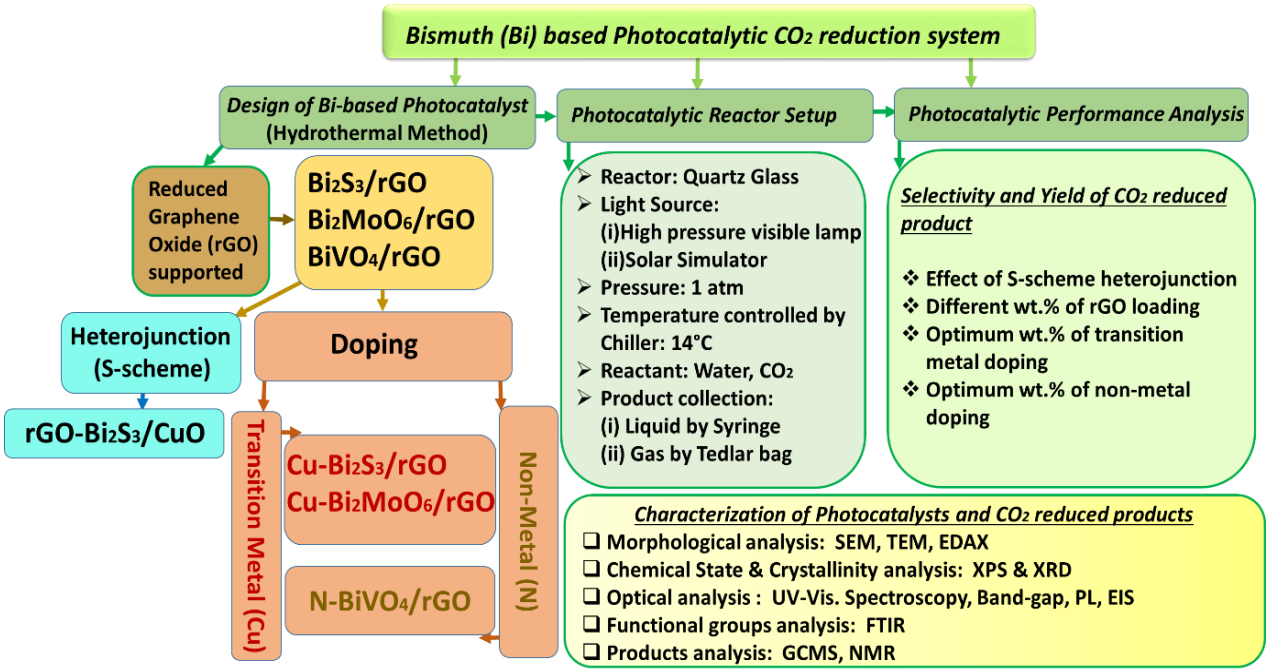


**Fig. 1.12 Schematic of overall research work of the thesis**

### 1.11.1 Brief description of entire research work

Subsequent few paragraphs are dedicated to brief on the chapters presented in this thesis.

***Chapter-2***comprises two problems. **Problem-1** focuses on visible light-induced rGO-$Bi_2S_3$/CuO S-scheme heterojunction photocatalyst which is explored for the production of methanol and formic acid through photocatalytic $CO_2$ reduction. In this work, the effect of CuO loading on rGO-$Bi_2S_3$ nano-hollow flower composite are investigated to improve the yield and selectivity of methanol production. Hydrothermal treatment is used to prepare the rGO-$Bi_2S_3$/CuO S-scheme heterojunction photocatalyst. In UV-vis spectroscopy, the combined actions of rGO and CuO expands the photo-absorbance power of the $Bi_2S_3$ nano-hollow flower to the visible portion of the solar spectrum. Amongst all the synthesised photocatalysts, rGO-$Bi_2S_3$/CuO exhibits a promising band gap (1.75 eV), remarkably reduced charge transfer resistance, and increased conductivity for enhancing the separation efficiency of the photo-generated charge carriers by S-scheme, the least rate of recombination ofelectron–hole pairs, higher thermal stability, and an enhanced specific surface area with a small pore diameter. So rGO-$Bi_2S_3$/CuO S-scheme heterojunction photocatalyst is also

discovered as the best active photocatalyst for enhanced photocatalytic reduction of $CO_2$ to methanol at about 423.52 μmol $g_{cat.}^{-1}$ $h^{-1}$ and also minimise the formic acid production.

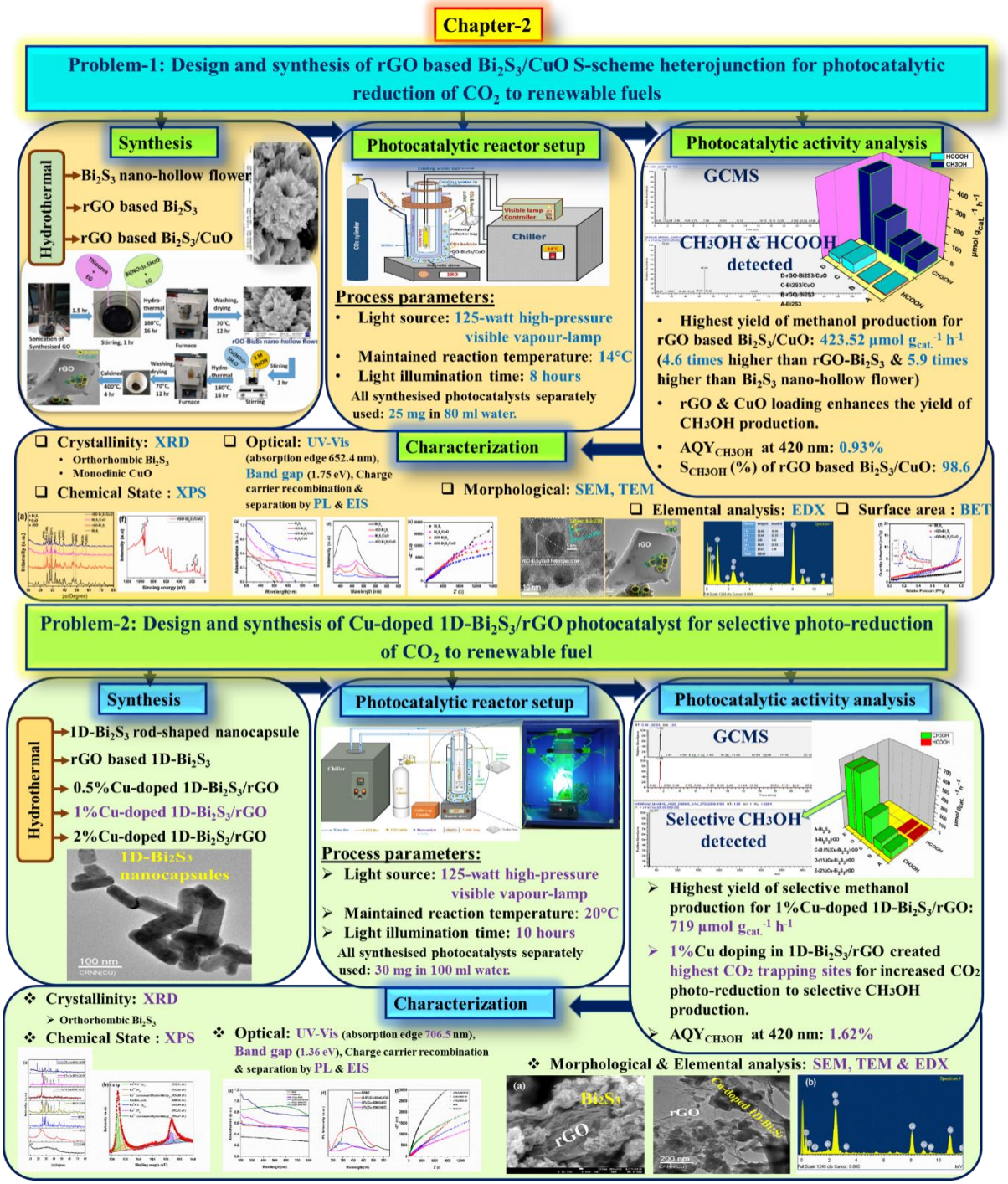


**Fig. 1.13 Overall representation of Chapter-2**

Additionally,rGO and CuO produce new photoinduced reactive zones for charge carriers within the band gap and enhance photocatalytic activity, which may be evidenced by the shifting of the absorption edge (652.4 nm) to the visible spectrum and the effective charge carrier separation. More $CO_2$ capturing sites are generated due to CuO loading in rGO-$Bi_2S_3$ for increased photocatalytic $CO_2$ reduction to methanol, and the selectivity of methanol is further improved to 98.6% by the rGO-$Bi_2S_3$/CuO S-scheme heterojunction photocatalyst. The GCMS analysis of the photocatalytic $CO_2$ reduction to methanol also demonstrats the purity of the product.

**Problem-2** focuses in order to convert $CO_2$ selectively to methanol, a novel Cu-doped one-dimensional (1D) $Bi_2S_3$ rod-shaped nanocapsule/rGO composite is being studied as a photocatalyst. In particular, the effects of Cu doping on product selectivity and band gap tuning are investigated in the context of rGO aided $Bi_2S_3$. $Bi_2S_3$ rod-shaped nanocapsules and 0.5, 1, and 2 weight percent Cu-doped (1D) $Bi_2S_3$ rod-shaped nanocapsules/rGO nanocomposites are synthesized by the hydrothermal technique. The procedure involves converting GO to rGO and adding Cu to (1D) $Bi_2S_3$ rod-shaped nanocapsules at the same time. The photocatalysts are characterized using XRD, FTIR, UV-Vis, photoluminescence, X-ray photoelectron, SEM, TEM, and EDX investigations. The combined impacts of Cu and rGO enhanced the spectral responsiveness of (1D)$Bi_2S_3$ nanocapsules to the visible section of the solar spectrum, as demonstrated by UV-vis spectroscopy. Further evidenced that both Cu doping and the presence of rGO lower the rate of electron hole pair recombination is shown by photoluminescence spectra. The best active photocatalyst for selective photoreduction of $CO_2$ to methanol is determined to be (1%)Cu-doped (1D) $Bi_2S_3$/rGO, which exhibits the lowest band gap (1.36 eV) and least rate of recombination among all the synthesized photocatalysts. It is demonstrated that Cu-doped (1D) $Bi_2S_3$/rGO, for all compositions, allows selective and enhanced synthesis of methanol, in contrast to undoped $Bi_2S_3$/rGO, pure $Bi_2S_3$, and Cu-doped $Bi_2S_3$, which likewise generate formic acid.The improved light absorption and efficient charge carrier separation may be indicators of the enhanced photocatalytic activity because of the loading of rGO and Cu, which is crucial to the doping process in order to create new reactive sites for charge carriers within the band gap. Furthermore, the increased $CO_2$ photoreduction brought about by the band gap tuning achieved by the Cu doping in rGO results in the creation of $CO_2$ trapping sites. The maximum yield of selective photoreduction of $CO_2$ to methanol at around 719 μmol $g_{cat.}^{-1}$ $h^{-1}$ is achieved through increased hybridization

and proper adjustment of the Cu-doped photocatalyst, as demonstrated in this present work. The purity and selectivity of the product are further demonstrated by GCMS measurement of the photoreduction of $CO_2$ to methanol. The overall description of Chapter-2 is depicted in Fig. 1.13.

***So Cu (transition metal) doping in rGO supported $Bi_2S_3$ based photocatalytic system is more effective than the S-scheme heterojunction based photocatalytic system for the highest yield of selective methanol ($CH_3OH$) production.***

## ❖ Achievements:

The photocatalytic reduction of $CO_2$ to 100% selective ***methanol*** with highest yield of 719 µmol $g_{cat.}^{-1}$ $h^{-1}$ is discovered only for 1%Cu-doped (1D)$Bi_2S_3$/rGO photocatalyst. The apparent quantum yield of methanol ($AQY_{CH3OH}$) of 1.62% is determined for (1%) Cu-doped (1D) $Bi_2S_3$/rGO photocatalyst at 420 nm.

Achievement and schematic representation of mechanism of photocatalytic $CO_2$ reduction of **Chapter-2** is shown in Fig. 1.14.

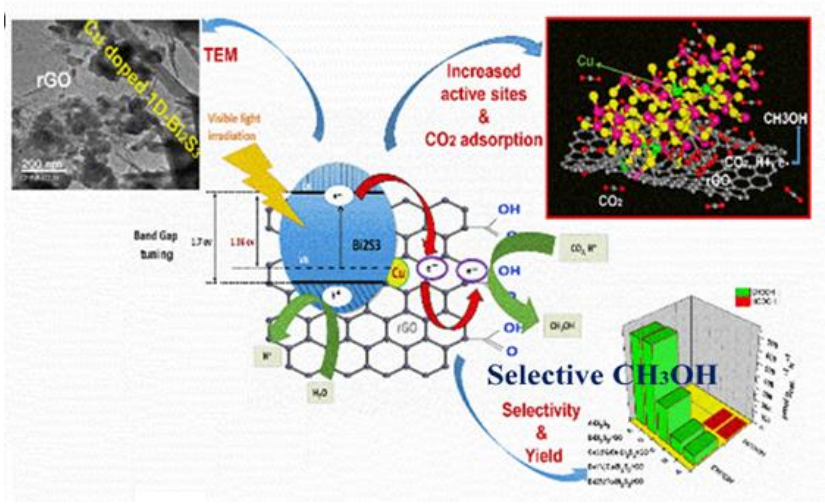


**Fig. 1.14Schematic portrayal of achievement and the mechanism of photocatalytic reduction of $CO_2$ to selective methanol using (1%) Cu-doped (1D)-$Bi_2S_3$/rGO photocatalyst**

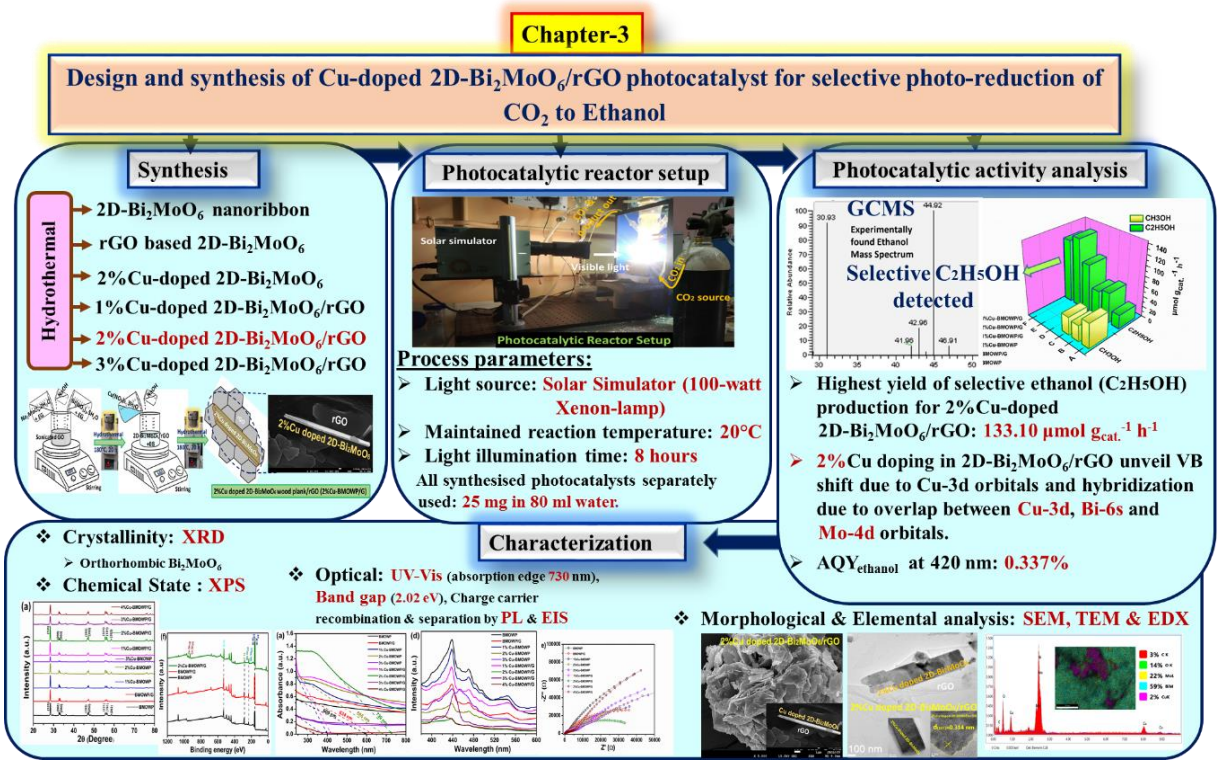


**Fig. 1.15 Overall representation of Chapter-3**

***Chapter-3*** focuses on a novel Cu-doped hydrothermally-produced two-dimensional (2D) $Bi_2MoO_6$nanoribbon/rGO composite is explored as the photocatalyst for selective reduction of $CO_2$ to ethanol. In particular, role of Cu doping of rGO supported $Bi_2MoO_6$ on C2 product selectivity is investigated. Long nanoribbon types pristine 2D-$Bi_2MoO_6$, 2D-$Bi_2MoO_6$nanoribbon/rGO and that doped with varying weight percentages of copper (Cu) are synthesized and characterized by XRD, FTIR, UV-Vis spectroscopy, photoluminescence spectroscopy, X-ray photoelectron spectroscopy, SEM, TEM, EDX, EIS and BET analysis. The photocatalysts with different doping concentrations of Cu (1%, 2%, 3% and 4 wt%) in 2D-$Bi_2MoO_6$nanoribbon/rGO identified as 1%Cu-BMONR/G, 2%Cu-BMONR/G, 3%Cu-BMONR/G, and 4%Cu-BMONR/G, respectively, have been synthesised using hydrothermal treatment. The chemical bonding among Cu, rGO and 2D- $Bi_2MoO_6$nanoribbon (BMONR) forming a two-dimensional (2D) nanoribbon like structure in the case of 2%Cu-BMONR/G as compared to other photocatalysts manifests higher crystallinity, as confirmed by XRD and XPS. Moreover, due to the presence of Cu and rGO the increased absorption edge (730 nm) to the visible spectrum of the solar illumination and the decreased PL intensity for 2%Cu-BMONR/G photocatalyst indicates the enhanced number of photo generated charge carriers

and greater charge separation with lowest rate of recombination, thereby promoting the efficient photocatalytic $CO_2$ reduction. The analysis of selectivity and yield of products of photocatalytic reduction of $CO_2$ using GCMS as well as the quantum efficiency calculations, suggest that Cu doping of $Bi_2MoO_6$-rGO promote the 100% selective ethanol production while both pristine $Bi_2MoO_6$, $Bi_2MoO_6$-rGO photocatalyst produces mixture of methanol and ethanol that means absence of either Cu doping or rGO leads to formation of mixture of methanol and ethanol. The optimum 2%Cu-BMONR/G exhibit an excellent $CO_2$ reduction to selective ethanol production rate of 133.10 µmol $g_{cat.}^{-1}$ $h^{-1}$ with a high selectivity of 100% and apparent quantum yield on the order of 0.337%, as compared to other synthesised photocatalysts in this work. Notably, the introduction of 2%Cu in BMONR/G controls the electronic composition of copper active sites via Mo-C-Cu/Mo-O-Cu bridge accelerating the charge transfer from BMONR to $CO_2$ trapping sites on rGO-Cu interface and at the same time promoting excellent charge transfer. A band gap value of 2.02 eV, which is estimated using experimental UV-vis data. Therefore, the photogenerated electrons from $Bi_2MoO_6$ (a n-type semi-conductor) will be transported through rGO (an electron acceptor) and taken away by the Cu atom to fulfil its electron vacancy in $3d^9$ orbital; rGO being an electron acceptor, separates the photo-excited electrons and holes at the interface of the junction and facilitates the adsorption of chemical molecules on the surface of the photocatalyst. The mechanism indicates that the formation of $C_2H_5OH$ via the formaldehyde pathway, promotes the synthesis of selective ethanol and thereby decreases the energy barrier of C-C interaction. This study serves as a motivation for further refining the photocatalytic system to achieve effective, sustainable, and commercially feasible photocatalytic $CO_2$ reduction. It describes a photocatalytic system that efficiently delivers the surface activation and selective reduction of $CO_2$ to ethanol. The overall representation of chapter-3 is shown schematically in Fig. 1.15

***So the 2% Cu (transition metal) doped rGO supported $Bi_2MoO_6$ based photocatalytic system is one of the best photocatalytic $CO_2$ reduction process for the highest yield of selective ethanol ($C_2H_5OH$) production.***

- **Achievements:**

The photocatalytic reduction of $CO_2$ to 100% selective ***ethanol*** with highest yield of 133.10 µmol $g_{cat.}^{-1}$ $h^{-1}$ is discovered only for 2%Cu doped 2D-$Bi_2MoO_6$nanoribbon/rGO (2%Cu-

BMONR/G) photocatalyst. The apparent quantum yield of ethanol ($AQY_{C2H5OH}$) of 0.337% is also determined for 2%Cu doped 2D-$Bi_2MoO_6$nanoribbon/rGO photocatalyst at 420 nm.

Achievement and schematic representation of mechanism of photocatalytic $CO_2$ reduction to selective ethanol of **Chapter-3** is shown in Fig. 1.16.

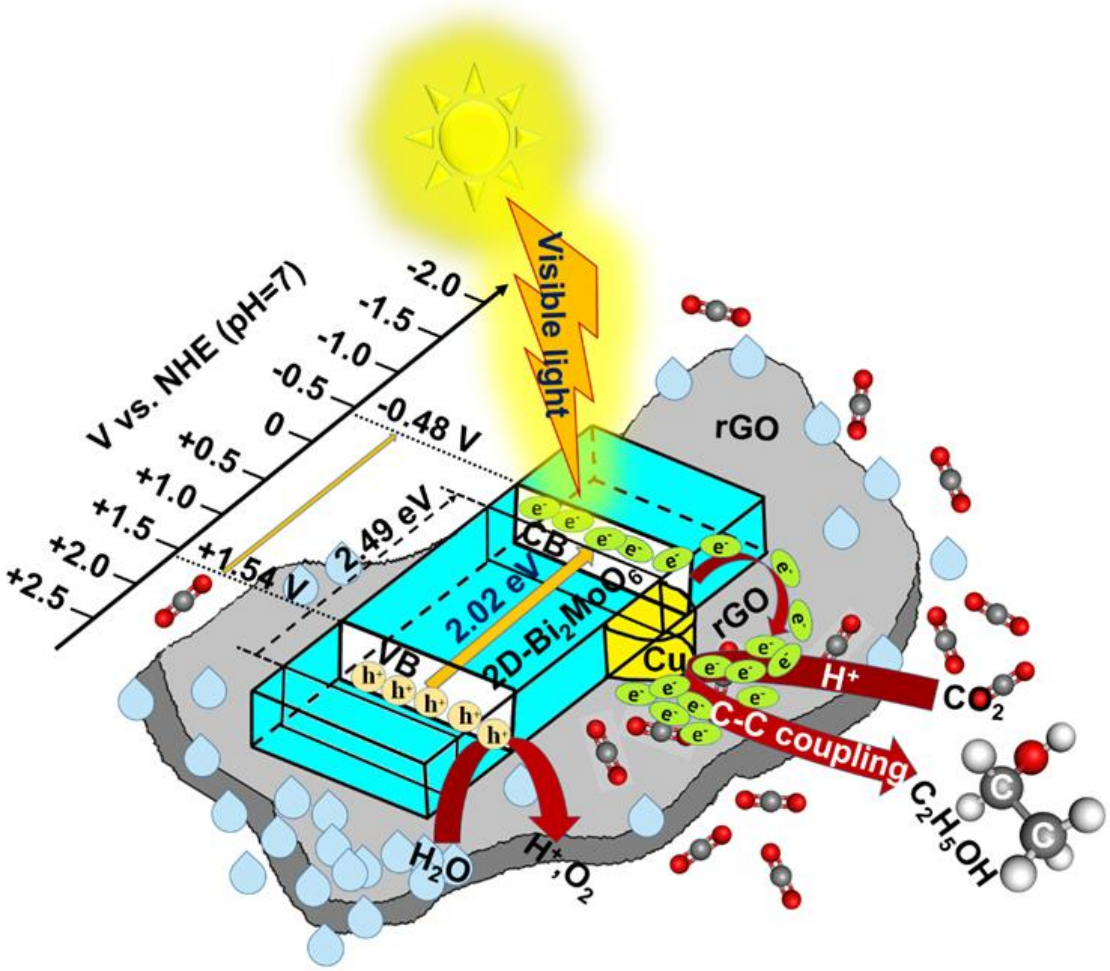


**Fig. 1.16 Schematic portrayal of achievement and the mechanism of photocatalytic reduction of $CO_2$ to selective ethanol using 2%Cu doped 2D-$Bi_2MoO_6$nanoribbon/rGO (2%Cu-BMONR/G) photocatalyst**

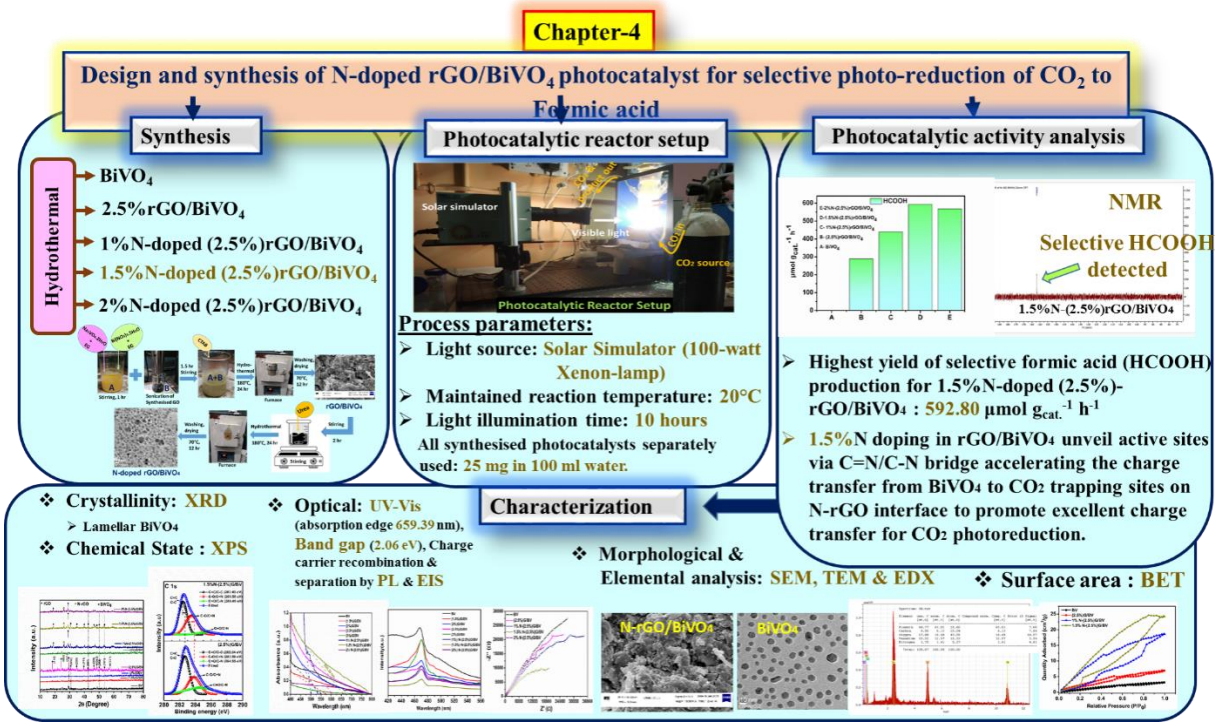


**Fig. 1.17 Overall representation of Chapter-4**

***Chapter-4*** focuses on a N-doped rGO/$BiVO_4$ nanocomposite, is explored as the photocatalyst for selective reduction of $CO_2$ to formic acid. Specifically, the impact of N doping on C1 product selectivity in rGO-supported $BiVO_4$ is examined. XRD, FTIR, UV-Vis, photoluminescence, X-ray photoelectron, SEM, TEM, EDX, EIS, and BET analysis are used to synthesize and describe the lamellar structure of pure $BiVO_4$, the ideal quantity of rGO/$BiVO_4$, and that doped with varied weight percentages of Nitrogen (N). Hydrothermal treatment was used to synthesize the photocatalysts with varying N doping concentrations (1%, 1.5%, and 2 wt%) in rGO/$BiVO_4$, which are identified as 1%N-(2.5%)G/BV, 1.5%N-(2.5%)G/BV, and 2%N-(2.5%)G/BV, respectively. In comparison to other photocatalysts, the chemical interaction between N, rGO, and $BiVO_4$ in the 1.5%N-(2.5%)G/BV instance forms a hexagonal-like structure that exhibits superior crystallinity, as demonstrated by XRD and XPS. Furthermore, because N and rGO are present, the visible spectrum of solar illumination has an increased absorption edge (659.39 nm), and the 1.5%N-(2.5%)G/BV photocatalyst has a decreased PL intensity. These results suggest that there are more photogenerated charge carriers and greater charge separation with a lower rate of recombination, which will facilitate the efficient reduction of $CO_2$ through photocatalysis. N doping rGO/$BiVO_4$ appears to enhance the 100% selectivity of formic acid generation, according to GCMS and NMR

analyses of the selectivity and yield of products of photocatalytic reduction of $CO_2$. In comparison to other synthesized photocatalysts in this work, the optimal 1.5%N-(2.5%)G/BV exhibits a good $CO_2$ reduction to selective formic acid production rate of 592.80 µmol $g_{cat.}^{-1}$ $h^{-1}$ with a high selectivity. The extensive experimental research exhibits the mechanism underlying 1.5%N-(2.5%)G/BV's exceptional performance. The addition of 1.5% nitrogen (N) to (2.5%)G/BV is noteworthy because it promotes excellent charge transfer while also speeding up the charge transfer from $BiVO_4$ to $CO_2$ trapping sites on the N-rGO interface by controlling the electronic composition of nitrogen active sites via the C=N/C-N bridge. Based on experimental UV-vis data, a band gap value of 2.06 eV is estimated, which indicates that N doping narrows the band gap and facilitates substantial visible light absorption. As a result, the photogenerated electrons from $BiVO_4$ will be transferred to N-rGO. As an electron acceptor, N-rGO helps to adsorb $CO_2$ on the surface of the photocatalyst by separating photo-excited electrons and holes at the junction interface. According to the mechanism, N's presence in this photocatalytic system boosts the yield of selective formic acid. In order to obtain efficient, long-lasting, and economically viable photocatalytic $CO_2$ removal, this study provides incentive for additional improvements to the photocatalytic system. In order to facilitate the selective reduction of $CO_2$ to formic acid, it provides a photocatalytic system that effectively lowers the charge transfer barrier. Fig. 1.17 provides a schematic illustration of the total chapter-4 representation.

***So the 1.5% N (non-metal) doped rGO supported $BiVO_4$ based photocatalytic system is one of the best photocatalytic $CO_2$ reduction process for the highest yield of selective formic acid (HCOOH) production.***

- **Achievements:**

The photocatalytic reduction of $CO_2$ to 100% selective ***formic acid*** with highest yield of **592.80** µmol $g_{cat.}^{-1}$ $h^{-1}$ is discovered only for 1.5%N doped (2.5%) rGO/$BiVO_4$ (1.5%N-(2.5%)G/BV) photocatalyst. The apparent quantum yield of formic acid ($AQY_{HCOOH}$) of 0.0148% is determined for 1.5%N-(2.5%)rGO/$BiVO_4$ photocatalyst at 420 nm.

Achievement and schematic representation of mechanism of photocatalytic $CO_2$ reduction to selective formic acid of **Chapter-4** is shown in Fig. 1.18.

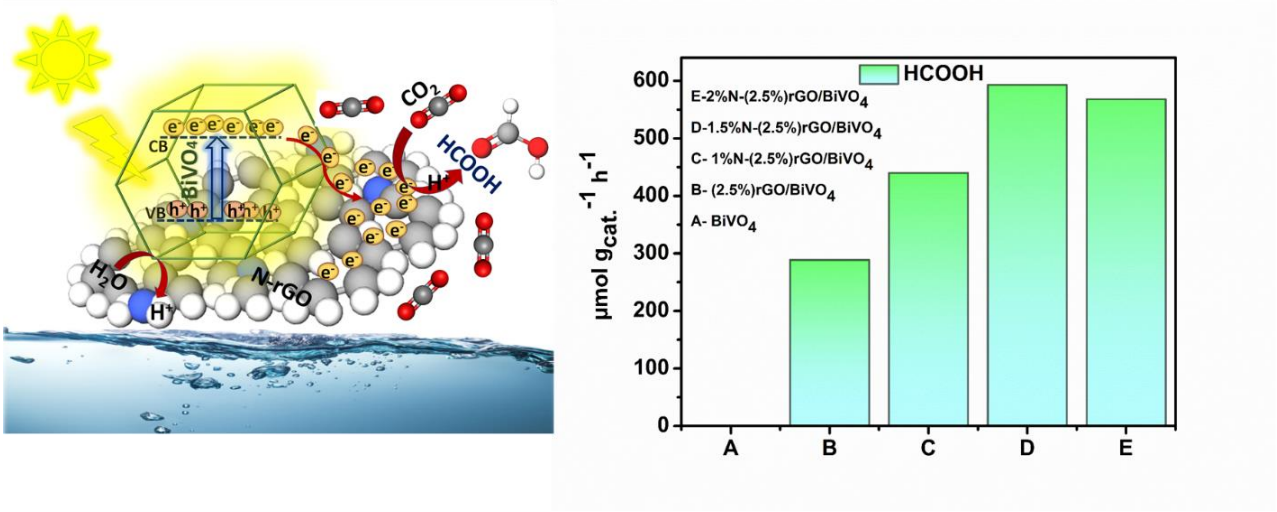


**Fig. 1.18 Schematic portrayal of achievement and the mechanism of photocatalytic reduction of $CO_2$ to selective formic acid using 1.5% N-doped (2.5%)rGO/$BiVO_4$ (1.5%N-(2.5%)G/BV) photocatalyst**

***Chapter 5*** concludes the outcomes of the research work presented in this thesis and mentions the future scope of research in the related field.

# Chapter 2

## *Synthesis, characterization and photocatalytic performance study of rGO-$Bi_2S_3$/CuO S-scheme heterojunction photocatalyst and Cu doped (1D)-$Bi_2S_3$ rod-shaped nanocapsule/rGO photocatalyst for photo-reduction of $CO_2$ to methanol.*

**Highlights:**

- rGO-$Bi_2S_3$ nano-hollo flower/CuO S-scheme heterojunction and Cu-doped one-dimensional (1D) $Bi_2S_3$ rod-shaped nanocapsule/rGO photocatalyst are prepared using hydrothermal treatment.
- The synthesised rGO-$Bi_2S_3$/CuO nanocomposite being an efficient, robust, S-scheme heterojunction photocatalyst exhibits the maximum methanol yields of 423.52 μmol $g_{cat.}^{-1}$ $h^{-1}$ along with formic acid (17.48 μmol $g_{cat.}^{-1}$ $h^{-1}$), as photocatalytic $CO_2$ reduced products with a $CH_3OH$ -selectivity of 98.6% .
- The optimum 1 weight percent Cu-doped (1D) $Bi_2S_3$/rGO photocatalyst exhibiting the least band gap energy and electron hole pair recombination rate, diaplays the maximum photocatalytic activity of 719 μmol $g_{cat.}^{-1}$ $h^{-1}$ of methanol as a photocatalytic $CO_2$ reduced product with a selectivity of 100%.

### 2.1.1 Introduction:

Bismuth sulphide ($Bi_2S_3$) is a valuable metal chalcogenide with a wide range of embryonic photocatalytic applications because of its high dielectric permittivity, lamellar structure, broad visible light absorption capacity, low bandgap ($E_g$) (1.3 eV), and notably variable energy band levels [143–146]. As one of the most beneficial semiconductors in the healthcare sector, $Bi_2S_3$ nanoparticles are known for their unique properties of low toxicity and a high bismuth electron count [147–157]. Researchers have also been interested in $Bi_2S_3$ nanostructures because of their unique shape and tubular crystal structure, which show a larger charge capacity and change their physical characteristics. However, due to its small band gap energy, which accelerates the rate at which photogenerated electron hole pairs recombine and reduces its utility, $Bi_2S_3$ has a low separation efficiency [155–163]. To provide the required photocatalytic activity, $Bi_2S_3$ can be combined with other semiconductors that have appropriate energy band topologies [157–165].It has been also noted that when morphological and structural modifications are made, $Bi_2S_3$ nanomaterials exhibit distinct characteristics. For instance, under UV light irradiation, zero-dimension (0D) $Bi_2S_3$ quantum dots exhibit a potent quantum confinement effect, and 1D and 2D $Bi_2S_3$ nanomaterials are able to capture large amounts of solar energy through the absorption of visible (Vis) light [193–200]. The strongest and shortest bonds in $Bi_2S_3$ nanomaterials are Bi-S bonds, which also show a 1D growth nature along [001]. These 1D nanorod-shaped photocatalysts can improve photocatalytic performance by increasing charge capacity, creating pathways for electron transfer, and increasing the probability of reactions on surface active sites for photoreduction [201-209]. $Bi_2S_3$ nanomaterials often take the form of 1D nanowires, 1D nanoribbons, 1D nanorods, or 3D nanoflowers made up of 1D units [209-215]. 1D photocatalysts, as opposed to other, differently shaped photocatalysts, produce controlled and aligned channels for electron transport. $Bi_2S_3$ nanorod-shaped photocatalysts in particular are more palatable because of their distinctive tubular structure, which can demonstrate an enhanced charge capacity [215-221]. Additionally, the tubular nanorods' various contact areas—such as their borders and inner and outer surfaces—can aid in boosting the likelihood of reactions during photocatalytic $CO_2$ conversion.

Under certain conditions, a variety of two-dimensional materials exhibit photocatalytic behaviour, such as MOFs [133], exfoliated $WS_2$ [169], $MoS_2$& g-$C_3N_4$ [178], and graphene [186]. In order to promote photocatalytic activity, two-dimensional nanosheet graphene or reduced graphene oxide (rGO) can be used as an efficient electron acceptor [143, 154, 164,

168, 170]. It has enormous potential for use in a variety of applications, including as drug delivery, energy storage devices, sensors, transistors, optoelectronics, hydrogen generation, $CO_2$ reduction, lubrication, and catalysis [184,197]. Due to their special qualities—such as high specific surface area, high electrical conductivity, high mechanical flexibility, optical transparency, high adsorption capacity, excellent electron mobility, and electrochemical stability—graphene or rGO-based nanomaterials have recently sparked a lot of interest for photocatalytic performance studies [185,186,197]. By efficiently trapping the excited electrons in one-dimensional (1D) semiconductor materials under light irradiation and boosting the photocatalytic activity, mostly reduced graphene oxide forms a barrier for the recombination process [183,184,197].

Due to its exceptional chemical and physical characteristics, such as its large surface area, excellent solar light absorption capacity, and small band gap (1.2 to 1.9 eV), copper oxide (CuO) is among the best p-type semiconductor metal oxides [165–170]. Different morphologies of CuO, including nanosheets, nanotubes, nanorods, nanospheres, and nano-hollow flowers, are especially appealing because of their exceptional stability, high thermal conductivity, photovoltaic qualities, and antibacterial activity. CuO nanoparticles have garnered significant interest for their potential industrial uses because of their distinctive qualities. Photo-catalysis, catalytic applications, solar cells, fuel cells, hydrogen storage systems, super capacitors, and hydrogen storage systems are some of these disciplines [171–180]. For $CO_2$ photoreduction, a light-transporting CuO nanomaterial has shown to be an extremely efficient photocatalyst. A common method for improving visible light energy collection and conversion, raising photocarrier separation efficiency, and adding active sites is to combine p-type CuO with other semiconductor materials [180–190]. As p-type is added to n-type, a p-n junction really forms at the particle surface. This changes the band-gap structure, raises the concentration of charge carriers, and stops charge recombination. Consequently, compared to a single n or p component, loading of p-type CuO [171, 174, 177, 180] on n-type $Bi_2S_3$ [127, 128] should greatly enhance the photocatalytic $CO_2$ reduction performance. Using CuO nanoparticles with a large surface area and uniform morphologies would further increase the capacity and conductivity of these nanomaterials [179–183].

By creating potent active adsorption sites that speed up the selective photo-reduction of $CO_2$, transition metal Cu is added to metal oxide photocatalysts to boost their ability to capture $CO_2$. Usually, the transition metal Cu can start moderate binding sites to increase $CO_2$ adsorption and activate the photocatalyst for $CO_2$ reduction, unlike other metal oxide sites.

Since metal copper (Cu) is widely distributed throughout the earth's crust, a lot of research is being done on low-cost copper-based semiconductors. These might be thought of as the most promising options for selective photocatalytic conversion of $CO_2$ into methanol, formic acid, etc. This occurs because there is a chance that copper ions will trap electrons since the reduction potential difference of $Cu^{2+}$ is greater than the photocatalysts' conduction band edge. In order to get a better yield of selectivity in the renewable fuel generation, the photocatalyst's trapped $Cu^{2+}$ electrons can then donate their electrons to the reaction of $CO_2$ with the reductant [215–217,221].

This chapter suggests two photocatalysts for the photocatalytic reduction of $CO_2$ into renewable fuels in the presence of visible light. Hydrothermally synthesised $Bi_2S_3$/CuO nanocomposites wrapped with rGO promotes the photoconversion of $CO_2$ to $CH_3OH$ (96% selective) and formic acid (HCOOH); but 100% selective $CH_3OH$ production is not achieved. Selectively converting $CO_2$ to a desired hydrocarbon remains one of the main obstacles facing photocatalysis. In this study, this is achieved using Cu doped 1D-$Bi_2S_3$ rod-shaped nanocapsules/rGO photocatalyst. Selectivity for $CO_2$ reduction in a photocatalyst is frequently influenced by several elements, including photon energy, photogenerated charges, catalyst active sites, reactant and intermediate adsorption and stability, and the photocatalyst's suitable CB and VB edges [200-210]. The photogenerated charge density in 1D-$Bi_2S_3$ rod-shaped nanocapsules/rGO photocatalyst, which is mostly supplied by catalytic active sites with improved reactant adsorption and stabilisation of intermediate products, improves selectivity in the photo-reduction of $CO_2$ [210-225].

The definition of major research problems addressed in this chapter are as follows:

- **Problem definition:**

***Problem 2.1*:- Synthesis, characterization and photocatalytic performance study of rGO-$Bi_2S_3$/CuO S-scheme heterojunction photocatalyst for photocatalytic $CO_2$ reduction to methanol.**

***Problem 2.2*:-Synthesis, characterization and photocatalytic performance study of Cu doped (1D)-$Bi_2S_3$ rod-shaped nanocapsule/rGO photocatalyst for selective photo-reduction of $CO_2$ to methanol.**

The specific **objectives** of **Problem 2.1** are enlisted below:

**i.** Design and synthesis of visible light responsive$Bi_2S_3$ nano-hollow flower photocatalysts by incorporating rGO for enhancing the yield of $CO_2$ reduced products.

**ii.** Modification of rGO-$Bi_2S_3$ photocatalysts by CuO to obtain best photoactive S-scheme heterojunction photocatalyst for achieving the yield of selective $CO_2$ reduced product.

**iii.** Characterization of all synthesized photocatalysts by XRD, SEM, TEM, EDX, FTIR, EIS, BET, TGA, and XPS.

**iv.** Photocatalytic performance study of all synthesized nano-composite photocatalysts.

**v.** Prediction of mechanism of $CO_2$ photo-reduction.

### 2.1.2 Experimental

#### 2.1.2.1 Materials:

The chemicals used are all of analytical quality, and they are not further purified before usage. L-ascorbic acid, sodium bicarbonate ($NaHCO_3$), copper nitrate trihydrate ($Cu(NO_3)_2.3H_2O$), bismuth nitrate pentahydrate ($Bi(NO_3)_3.5H_2O$), thiourea ($CH_4N_2S$), and other compounds have been acquired from Sigma-Aldrich. Other chemicals (reagent grade) acquired from Merck include ethylene glycol ($C_2H_6O_2$), graphite flakes, potassium permanganate ($KMnO_4$), sulphuric acid ($H_2SO_4$), hydrogen peroxide ($H_2O_2$), phosphoric acid ($H_3PO_4$), sodium hydroxide (NaOH), hydrochloric acid, and ethanol.

#### 2.1.2.2 Synthesis of rGO-$Bi_2S_3$/CuO

##### 2.1.2.2.1 Synthesis of pristine $Bi_2S_3$:

This synthesis process involves mixing 1.5 g of $Bi(NO_3)_3.5H_2O$ and 0.45 g of thiourea separately in 50 ml of ethylene glycol and stirring constantly for 60 minutes. 2 (M) NaOH solution is added to the blended liquid to bring its pH to 10 after it has been agitated for a further 60 minutes after the two solutions have been blended. The whole mixture is then transferred to a 100 ml teflon-lined container, sealed in a stainless steel autoclave, and maintained for 16 h at 180°C in a muffle furnace for hydrothermal operation. The synthesised

black solid products are recovered after centrifugation and the teflon-lined stainless steel autoclave has cooled. The black precipitate is then repeatedly washed with ethanol and double-distilled water. Following washing, it is vacuum-dried for 12 h at 70°C in a hot air oven. Pure $Bi_2S_3$ nano-hollow floral composites have been found after drying [153, 155, 160].

#### 2.1.2.2.2 Synthesis of rGO-$Bi_2S_3$:

Graphene oxides (GO) are synthesized using a modified Hummers process [166]. Using this standard procedure, the GO sheets are exfoliated by ultrasonicating 5 weight percent of the synthesised GO solution for 90 minutes. The ultrasonicated GO solution is simultaneously supplemented with separately produced solutions containing 1.5 g of $Bi(NO_3)_3.5H_2O$ and 0.45 g of thiourea, while being continuously stirred for an additional 60 minutes. Next, using a 2 (M) NaOH solution, the pH of the stirring solution is adjusted to 10. Following 16 h of hydrothermal treatment of the previously mentioned stirring solution in a 100-ml Teflon-lined container enclosed in a stainless steel autoclave, rGO-incorporated $Bi_2S_3$ nano-hollow flower composites are produced following cooling, multiple washing, and drying processes [155,176].

#### 2.1.2.2.3 Synthesis of rGO-$Bi_2S_3$/CuO:

Copper oxide (CuO) loaded rGO-$Bi_2S_3$ nano-hollow flower composites (rGO-$Bi_2S_3$/CuO) are created by mixing rGO solution with $Bi_2S_3$ nano-hollow flower composites at a constant concentration with 2 weight percent of CuO loading. The purpose of this is to look at how CuO loading affects the yield of the $CO_2$ reduction product produced by photocatalysis. In this work, rGO-$Bi_2S_3$/CuO nanostructures are formed by hydrothermal treatment in order to yield a high yield of products. Independently made $Cu(NO_3)_2.5H_2O$ solutions are added to this standard procedure and stirred continuously for two h in order to attain two weight percent of CuO loading in the rGO-$Bi_2S_3$ solution. The mixture's pH is also adjusted to 10 using a 2 (M) NaOH solution. After that, the mixture is placed into a 100 ml Teflon-lined container that is sealed inside a stainless steel autoclave. It is then placed in the muffle furnace and heated to 180°C for 16 h to undergo hydrothermal treatment. Following centrifugation, the products are collected, allowed to naturally cool to room temperature, repeatedly cleaned in ethanol and double-distilled water, dried for 12 h in a heated chamber under vacuum at 70°C, and then calcined for an additional 4 h at 400°C. CuO loaded $Bi_2S_3$ nano-hollow flower composites are prepared using similar procedures so that their

characteristics can be compared. Fig. 2.1.1 depicts the schematic representation of the synthesis process.

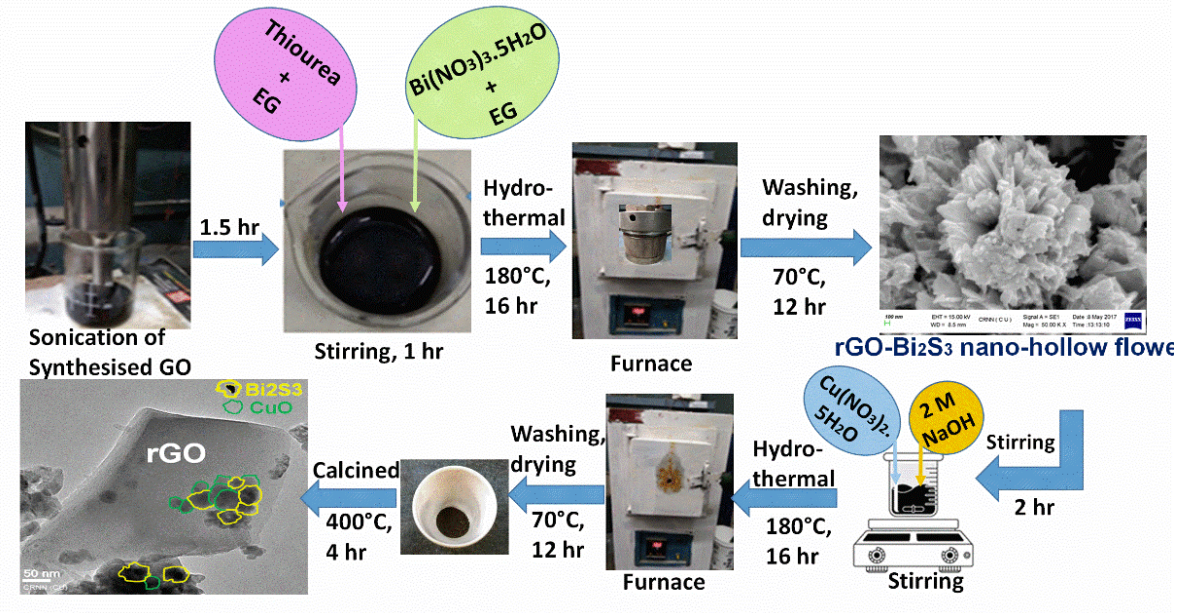


**Fig. 2.1.1: Schematic representation of synthesis process of rGO-$Bi_2S_3$/CuO heterojunction photocatalyst**

### 2.1.2.3 Photocatalytic activity evaluation:

A 125-watt high-pressure visible vapour-lamp is used to evaluate the photocatalytic activity of the generated photocatalysts, rGO-$Bi_2S_3$/CuO, rGO-$Bi_2S_3$, $Bi_2S_3$/CuO, and $Bi_2S_3$, under visible light irradiation. In a 150 mL hollow quartz tube reactor, 0.025 g of each photocatalyst is employed independently to assess the photocatalytic activity. In order to create a saturated $CO_2$ absorbed solution and maximize $CO_2$ adsorption on the photocatalyst's active sites, 80 ml of water containing 0.5 M $NaHCO_3$ as hole scavengers is filled with 99.9% pure $CO_2$ gas at a low flow rate before the quartz reactor is exposed to visible light. To completely remove all of the dissolved oxygen in the saturated solution, the entire procedure is run under magnetic stirring conditions for 60 minutes in the dark. After that, 0.025 g of photocatalysts are added to the previously saturated solution, and the reaction is carried out for 8 h at 20°C, monitored by a chiller, and exposed to visible light from the high-pressure mercury vapour lamp as directed. The stirring speed is kept constant during this time. In order to let visible light into the photocatalytic reactor, UV-protector liquor is also utilized [Fig. 2.1.2] [145]. Next, using helium as the carrier gas and gas chromatography equipment (Agilent-7890A system, GC-FID, and GC-TCD) to measure the concentration of each product, the

photocatalytic $CO_2$-reduced products are collected from the reactor solution via a thin pipe attached to the syringe.

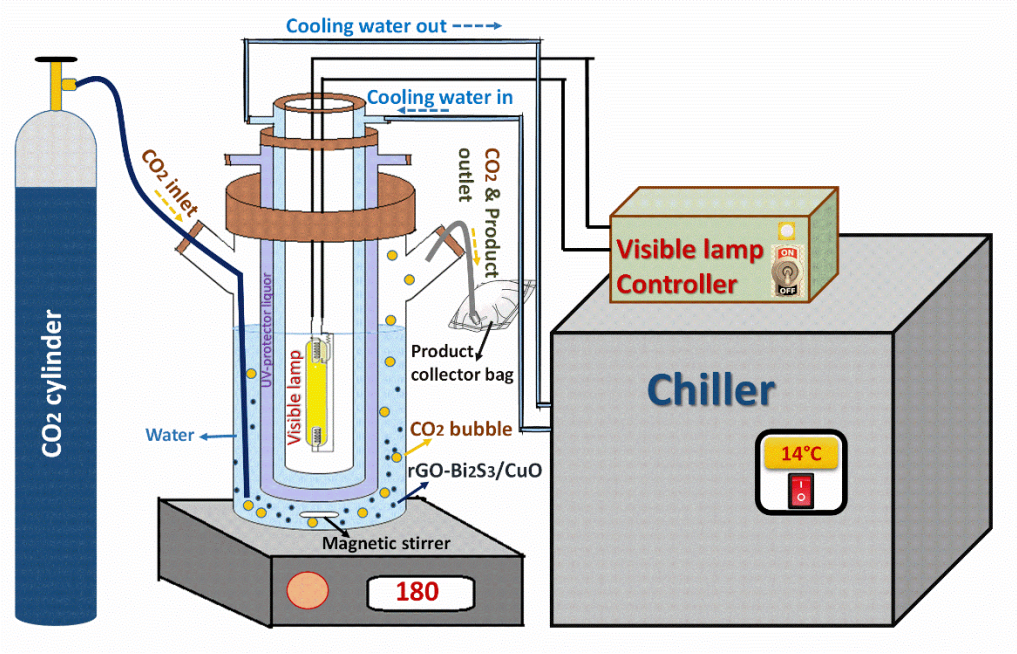


**Fig. 2.1.2: Schematic representation of the experimental reactor setup for photocatalytic activity study of rGO-$Bi_2S_3$/CuO heterojunction photocatalyst**

To make sure that the products are solely produced as a result of photocatalytic $CO_2$ reduction, blank reactions are conducted. The entire experiment is conducted using the identical operating conditions in the absence of a photocatalyst. Second, under the same operating conditions, the entire experiment is conducted in total darkness with a photocatalyst present. Thirdly, a high-pressure mercury vapour lamp is used to illuminate the blank experiment, and the photocatalyst in the photocatalytic quartz reactor is present without any $CO_2$ gas being purged. To guarantee the quality of the $CO_2$-reduced product, analysis is also conducted using the pure grades of formic acid and methanol. The number of reacting electrons divided by the number of incident photons is known as apparent quantum yield, or AQY [146].

$$\text{AQY} = \frac{(\text{Number of reacted electrons})}{\text{Number of incident photons}} \times 100 \qquad (2.1.1)$$

### 2.1.3 Results and discussion:

#### 2.1.3.1 Structural and Morphological characterization:

##### 2.1.3.1.1 XRD analysis:

Fig. 2.1.3(a) displays the XRD patterns of the $Bi_2S_3$, rGO-$Bi_2S_3$, and rGO-$Bi_2S_3$/CuO nanocomposites. The XRD patterns of $Bi_2S_3$ and rGO-$Bi_2S_3$ exhibit similar peaks, mainly in the crystal planes (130), (021), (211), (301), (431), and (060). These peaks are consistent with the usual orthorhombic phase of $Bi_2S_3$ (JCPDS card No. 017-0320) [159]. The XRD pattern of rGO synthesized from GO during the hydrothermal process is also analysed, where the full conversion of GO to rGO is exhibited by the (002) crystalline plane, which corresponds to the distinctive diffraction peak of rGO at approximately 24.3° [158]. The large peaks at 35.75° and 38.88°, respectively, are caused by the (0 0 2) and (1 1 1) planes [139], which show the monoclinic crystallinity of CuO (JCPDS card No. 05-0661) [Fig. 2.1.3(a)] in the rGO-$Bi_2S_3$/CuO heterojunction photocatalyst. The absence of a GO diffraction peak in the other nanocomposites suggests that GO has entirely transformed into rGO throughout the hydrothermal treatment procedure. The XRD characteristics further demonstrate that the low concentration of rGO nanosheets and the CuO and $Bi_2S_3$ diffraction patterns prevent the rGO diffraction peaks at 24.3° from being clearly apparent in the XRD patterns of the rGO-$Bi_2S_3$/CuO heterojunction photocatalyst. Orthorhombic $Bi_2S_3$ crystal planes (021), (301), (431), and (060) are visible in the XRD patterns of the rGO-$Bi_2S_3$/CuO photocatalyst. Thus, the combination of the rGO, $Bi_2S_3$, and CuO phases is visible in the XRD pattern of the rGO-$Bi_2S_3$/CuO heterojunction photocatalyst [Fig. 2.1.3(g)]. In the samples as prepared, no additional phase is detectable, including metallic Cu or cuprous oxide ($Cu_2O$). The average crystallite size (L) of rGO-$Bi_2S_3$/CuO is found to be 16.90 nm using the Debye-Scherrer equation [159].

$$\left[L = {}^{0.9\lambda}/_{\beta\cos\theta}\right] \qquad (2.1.2)$$

where θ is the Bragg angle, β is the full line width at half maximum height of the peak (FWHM), and λ is the X-ray wavelength (0.15406 nm). $Bi_2S_3$, rGO-$Bi_2S_3$, and $Bi_2S_3$/CuO are also found to have typical crystallite sizes of 12.46 nm, 10.17 nm, and 14.40 nm, respectively. Because of the CuO loading in rGO-$Bi_2S_3$, the usual crystallite diameters of rGO-$Bi_2S_3$/CuO are slightly enhanced.

#### 2.1.3.1.2 XPS analysis

X-ray photoelectron spectroscopy (XPS) has been used to explain the purity, electronic state, and chemical state of the components of the rGO-$Bi_2S_3$/CuO heterojunction photocatalyst. The rGO-$Bi_2S_3$/CuO photocatalyst's survey XPS spectrum is shown in Fig. 2.1.3(f), and it shows the peak of each of the expected constituents—Bi, S, Cu, C, and O. Fig. 2.1.3(b-e) displays narrow XPS scans for the constituents Bi, S, Cu, C, and O. As demonstrated in Fig. 2.1.3, the combination of rGO and copper oxide excited the electrons more readily and provided greater efficiency. In the Bi 4f and S 2p XPS studies (Fig. 2.1.3(b)), the entire spectrum may be further deconvoluted into four different peaks, where the peaks present at binding energies of 159.60 eV and 164.90 eV correspond to the $4f_{7/2}$ and $4f_{5/2}$ orbital splittings of the $Bi^{3+}$ state, respectively [146]. Moreover, the orbital splittings of S $2p_{3/2}$ and S $2p_{1/2}$ are matched by the two minor peaks at 162.05 eV and 163.54 eV, respectively. One may deconvolve the high-resolution Cu 2p photoelectrons' spectra in Fig. 2.1.3(c) into seven peaks. The distinctive peaks can be detected at 933.02 eV and 953.12 eV, respectively, and they are associated with $Cu^{2+}$ oxidation state of the photocatalyst. Moreover, the XRD results are consistent with the satellite peaks discovered at 939.32 eV and 941.11 eV, which offer clear evidence of the existence of the $Cu^{2+}$ oxidation state as CuO [147, 150, 174, 175]. The distinctive peaks of Cu 2p shift dramatically in the direction of low binding energy when compared to CuO, suggesting that the Cu element facilitates the rGO-$Bi_2S_3$/CuO interface contact. Electron transfer between semiconductors with differing Fermi levels affected the surface electron density, and the electrons went from a high-energy level to a low-energy level when the binding energy changed. Additionally, it shows that during the contact, one electron is transferred from $Bi_2S_3$ to CuO. The peaks that correspond to the Cu $2p_{3/2}$ and Cu $2p_{1/2}$ that arose at 930.5 eV and 950.4 eV, respectively, are caused by the $Cu^{1+}$ species. The X-ray irradiation of the XPS source throughout the study may have reduced $Cu^{2+}$ to $Cu^{1+,}$ which is why $Cu^{1+}$ species peaks may have developed [176,177]. The high-resolution XPS spectra of C 1s can be deconvoluted into three peaks, as shown in Fig. 2.1.3(d). CuO and rGO-$Bi_2S_3$ interactions are responsible for the two further peaks, which are located at 283.51 eV and 286.07 eV, respectively, and represent the C-O and C=O species in the photocatalyst. C-C bonding is indicated by the altered XPS

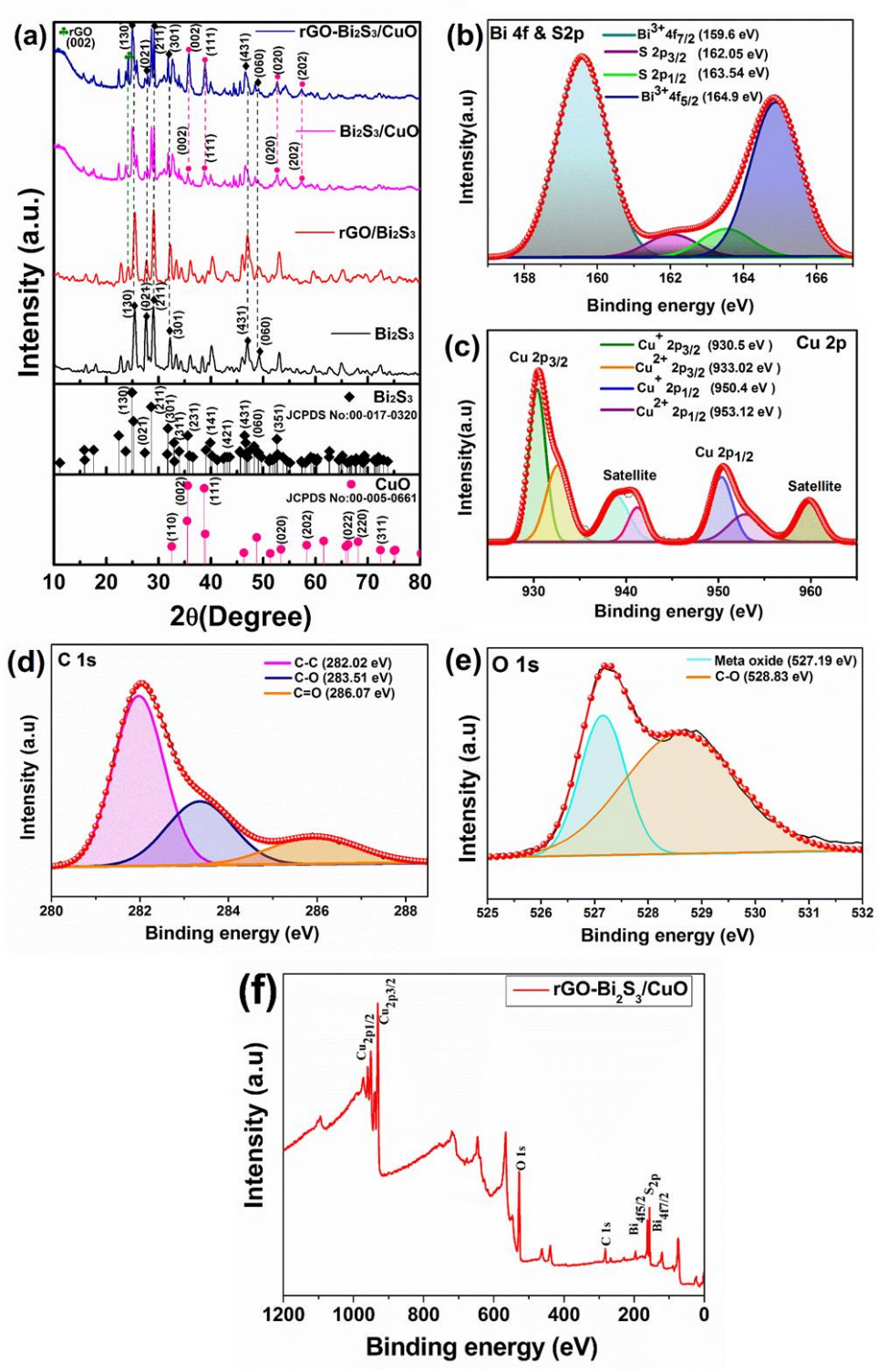


**Fig. 2.1.3: (a) XRD analysis of $Bi_2S_3$, rGO/$Bi_2S_3$, $Bi_2S_3$/CuO and rGO-$Bi_2S_3$/CuO photocatalysts. Core level XPS scan of (b) Bi 4f and S 2p, (c) Cu 2p, (d) C 1s, and (e) O 1s, (f) survey scan of X-ray photoelectron spectra (XPS) of the rGO-$Bi_2S_3$/CuO heterojunction photocatalyst**

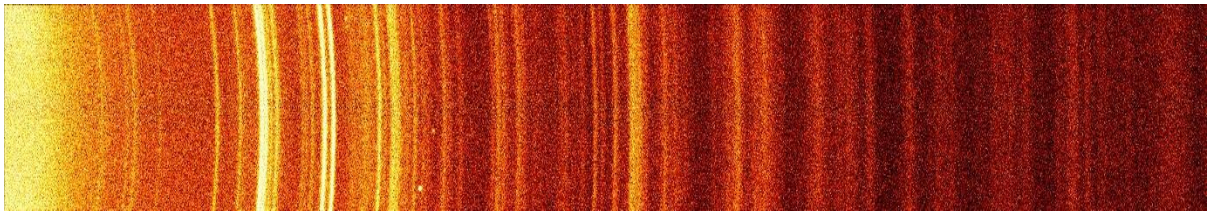

**Fig. 2.1.3 (g): 2D XRD diffraction image of rGO-$Bi_2S_3$/CuO heterojunction photocatalyst**

peak of C1s to a lower binding energy at 282.02 eV. The CuO lattice of O is indicated by the peak at 527.19 eV in the high-resolution O 1s XPS spectra, which are displayed in Fig. 2.1.3(e). C-O bonding is indicated by the peak at 528.83 eV. The XPS spectra of S 2p have been shifted to a lower binding energy, which has increased the catalytic activity of the process. Fig. 2.1.3(f) shows the survey scan of the X-ray photoelectron spectra (XPS) of the rGO-$Bi_2S_3$/CuO heterojunction photocatalyst.

**2.1.3.1.3 SEM & TEM analysis:**

SEM and TEM are used to study the morphological properties of synthesized nanoparticles. The nano-hollow flower-like structure of $Bi_2S_3$ and CuO nanoparticles is seen in Fig. 2.1.4(a) and 2.1.4(b), respectively, based on SEM images. The heterojunction that forms between $Bi_2S_3$ and CuO nanoparticles is shown in Fig. 2.1.4(c) via SEM, and it is also visible in Fig. 2.1.4(e) via TEM. The $Bi_2S_3$/CuO heterojunction nanocomposites are embedded in the rGO sheet, as seen in the TEM picture of Fig. 2.1.4(f-g) and the SEM image of Fig. 2.1.4(d). The XRD analysis and the lattice fringe spacing (dspacing) of 0.356 nm and 0.251 nm, respectively, in the inset HR-TEM image of Fig. 2.1.4(g) confirm heterojunction formation in the rGO-$Bi_2S_3$/CuO photocatalyst. These values represent the (130) crystal plane of orthorhombic Bi2S3 and the (002) crystal plane of CuO. When compared to $Bi_2S_3$ and rGO-$Bi_2S_3$, the heterojunction that is created can offer improved electron transfer and efficient charge separation inside the rGO-$Bi_2S_3$/CuO photocatalyst, which facilitates the photocatalytic reduction of $CO_2$ to methanol.The $Bi_2S_3$ nano-hollow flower and CuO nanoparticles have a strong attachment, as seen in SEM and TEM images, and together they form a strong interconnected network with rGO. This would increase interfacial charge transfer upon visible light irradiation and may be the cause of enhanced photocatalytic reduction of $CO_2$ to methanol and formic acid. A rGO-$Bi_2S_3$/CuO heterojunction photocatalyst with an atomic ratio of Bi:Cu (1:3) is shown in Fig. 2.1.4(h) for elemental

analysis by EDX. The proper integration of CuO and rGO into the $Bi_2S_3$nano-hollow flower is ensured by the presence of C, O, and Cu. In the inset of Fig. 2.1.4(a), a synthetic $Bi_2S_3$ nano-hollow flower is shown [161, 163, 170, 176].

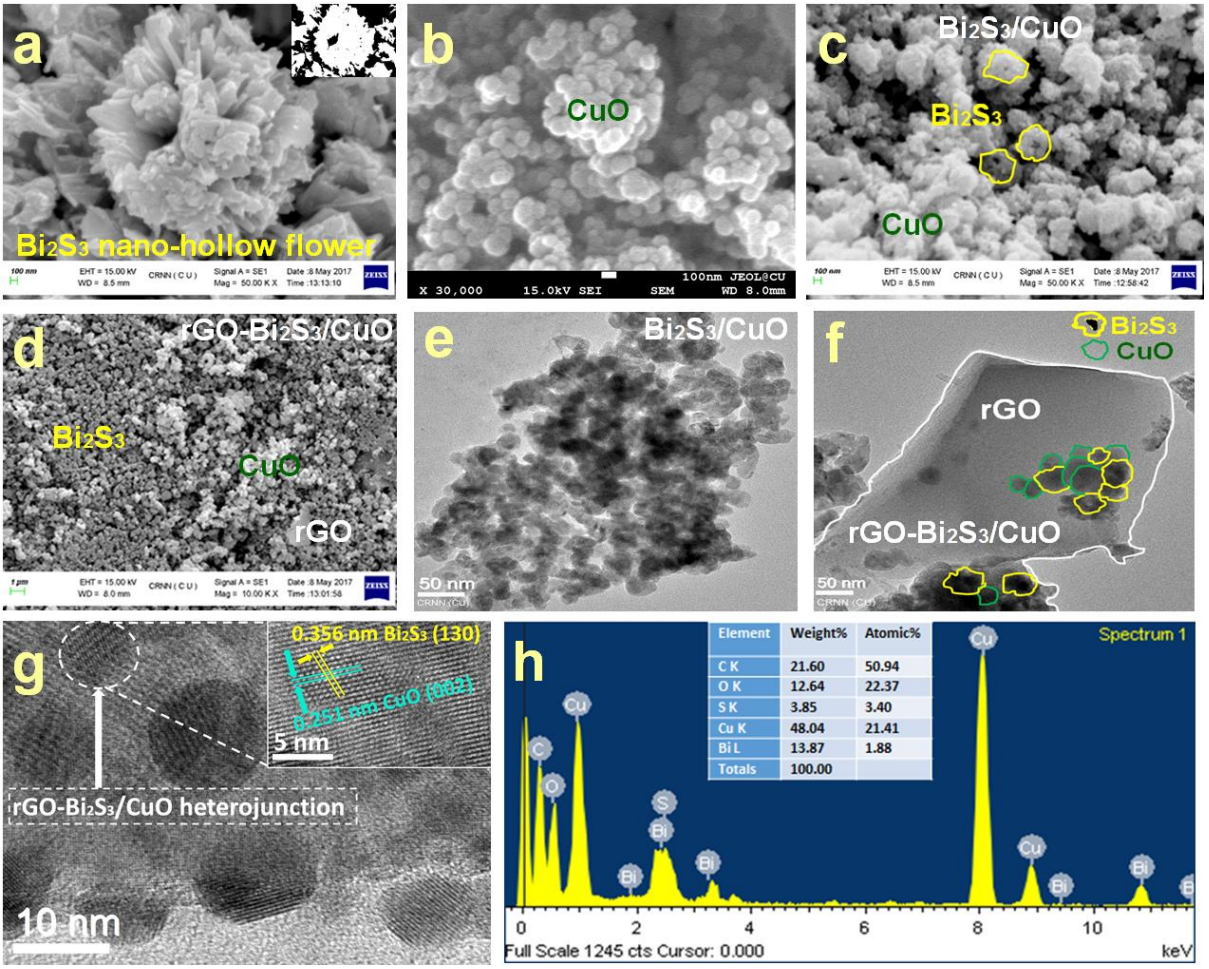


**Fig. 2.1.4: SEM image of (a) $Bi_2S_3$ nano-hollow flower, (b) CuO nanoparticles (c) $Bi_2S_3$/CuO heterojunction, (d) rGO-$Bi_2S_3$/CuO heterojunction photocatalyst. TEM image of (e) $Bi_2S_3$/CuO heterojunction, (f-g) rGO-$Bi_2S_3$/CuO heterojunction photocatalyst, (h) the corresponding EDX chemical analysis of rGO-$Bi_2S_3$/CuO heterojunction photocatalyst**

### 2.1.3.2 Optical characterization

#### 2.1.3.2.1 UV-Vis analysis:

The UV-vis absorption study data for the synthesized $Bi_2S_3$, rGO- $Bi_2S_3$, $Bi_2S_3$/CuO, and rGO- $Bi_2S_3$/CuO photocatalysts are displayed in Fig. 2.1.5(a). In rGO-$Bi_2S_3$ nanocomposites,

CuO loading raises absorbance in the visible spectrum. Fig. 2.1.5(a) also illustrates the increase in absorbance in the visible area, which goes as follows: rGO-$Bi_2S_3$/CuO> $Bi_2S_3$/CuO> rGO-$Bi_2S_3$> $Bi_2S_3$. Furthermore, the absorption edge of rGO-$Bi_2S_3$/CuO heterojunction photocatalyst is observed to be 652.4 nm. Fig. 2.1.5(b) shows that the bandgap energy of rGO-$Bi_2S_3$/CuO heterojunction photocatalyst is 1.75 eV, which is loared as a result of CuO loading in rGO- $Bi_2S_3$ nanocomposites. The synthesised nano-photocatalysts' bandgap energies are estimated using the tauc plot equation (2.1.3), as shown below [176].

$$[\alpha h\nu] = A\left[h\nu - E_g\right]^{\frac{n}{2}} \qquad (2.1.3)$$

where "Eg" (eV) is the bandgap of the photocatalyst, "h" is Planck's constant, "c" is the speed of light, "v" is its frequency, "A" is the absorption coefficient, and "n" is 1 for semiconductors' direct bandgap and "4" for their indirect bandgap. For every synthesized photocatalyst, Table 2.1.1 shows the estimated bandgap energies and absorption edge (nm) values.

**Table 2.1.1 - Estimation of band gap energy and absorption edge values of synthesized nanomaterials**

| Photocatalyst | Absorption edge (nm) | Band gap energy (eV) |
|---|---|---|
| **(i) $Bi_2S_3$** | 500.0 | 1.90 |
| **(ii) rGO-$Bi_2S_3$** | 525.9 | 1.80 |
| **(iii) $Bi_2S_3$/CuO** | 560.5 | 2.24 |
| **(iv) rGO-$Bi_2S_3$/CuO** | 652.4 | 1.75 |

**2.1.3.2.2 FTIR analysis:**

The FTIR spectra of the photocatalysts $Bi_2S_3$, rGO-$Bi_2S_3$, $Bi_2S_3$/CuO, and rGO-$Bi_2S_3$/CuO are displayed in Fig. 2.1.5(c). The presence of rGO is confirmed by the O-H stretching vibration at 3433 $cm^{-1}$ of the FTIR spectra of rGO-$Bi_2S_3$, which indicates that GO [176] is reduced as the hydrothermal reaction proceeds. The distinctive vibrations at 3401, 1639, 1260, and 1103 $cm^{-1}$ in the FTIR spectra of the rGO-$Bi_2S_3$/CuO heterojunction photocatalyst are attributed to the O-H, C=C, C–O–C, and C-O stretching vibrations, respectively, as shown in Fig. 2.1.5(c). It is believed that the hydroxyl form of water, which is adsorbed on the surface of sample, is responsible for the broad peak of rGO- $Bi_2S_3$/CuO at about 3401 $cm^{-1}$. In the FTIR spectra of the $Bi_2S_3$/CuO heterojunction, the weak vibrational bands at 2961,

1403, and 615 $cm^{-1}$ may be attributed to the interaction between CuO and the $Bi_2S_3$ nano-hollow flower. CuO loading in rGO-$Bi_2S_3$ nanocomposites causes a decrease in the peak intensity of the oxygenic groups in the rGO-$Bi_2S_3$/CuO heterojunction photocatalyst [152, 159, 161, 166, 180]. The strong interaction between rGO and the $Bi_2S_3$ nano-hollow flower in rGO-$Bi_2S_3$/CuO may be the cause of the broad absorption peak observed at 1103, 873, and 801 $cm^{-1}$ [152]. CuO may be the cause of the broad vibrational bands at 592 and 522 $cm^{-1}$ in the rGO-$Bi_2S_3$/CuO heterojunction photocatalyst.

**2.1.3.2.3 Photoluminescence (PL) spectra & EIS analysis:**

Photoluminescence (PL) spectroscopy has been utilized to study the recombination, separation, and transfer of photo-generated charge carriers to the reaction site for all synthesised samples exposed to light. The photocatalysts $Bi_2S_3$, rGO-$Bi_2S_3$, $Bi_2S_3$/CuO, and rGO-$Bi_2S_3$/CuO are subjected to PL analysis at an excitation wavelength of 330 nm. The emission spectra are displayed in Fig. 2.1.5(d). The emission spectra of pure materials and composites have been examined between 340 and 650 nm. It is commonly known that photogenerated charge carriers recombine more quickly with increasing PL emission intensity [154, 162]. The PL emission band of $Bi_2S_3$ at 423 nm is caused by the recombination of free carriers. $Bi_2S_3$ charge carrier recombination results in emission bands in the visible spectrum in all samples. A less prominent peak can be seen in Fig. 2.1.5(d) when comparing the rGO- $Bi_2S_3$/CuO photocatalyst to their counterparts, the CuO loaded and unloaded $Bi_2S_3$ nano-hollo flowers. The result suggests that photogenerated electron-hole pairs are significantly reduced by the interface produced between $Bi_2S_3$/CuO and rGO, which facilitates electron transportation and minimizes charge carrier recombination [152, 177]. In this instance, copper oxide also has a major impact on the decrease in charge carriers [165, 183]. Effective charge separation has increased the lifetime of photogenerated charge carriers and enhanced the interfacial charge transfer between rGO and $Bi_2S_3$/CuO. Consequently, reduced electron-hole pair recombination rates enhance the photocatalytic activity of the rGO-$Bi_2S_3$/CuO heterojunction photocatalyst.

The rGO-$Bi_2S_3$ photocatalyst has a smaller arc radius than $Bi_2S_3$ and $Bi_2S_3$/CuO, as shown in Fig. 2.1.5(e). Of all the $Bi_2S_3$, rGO-$Bi_2S_3$, and $Bi_2S_3$/CuO samples, the arc radius of the rGO-$Bi_2S_3$/CuO heterojunction photocatalyst is the smallest semicircle, indicating how much the charge transfer resistance may be reduced by adding CuO. The higher conductivity of the photocatalyst, which raises the separation efficiency of the photo-generated electrons and

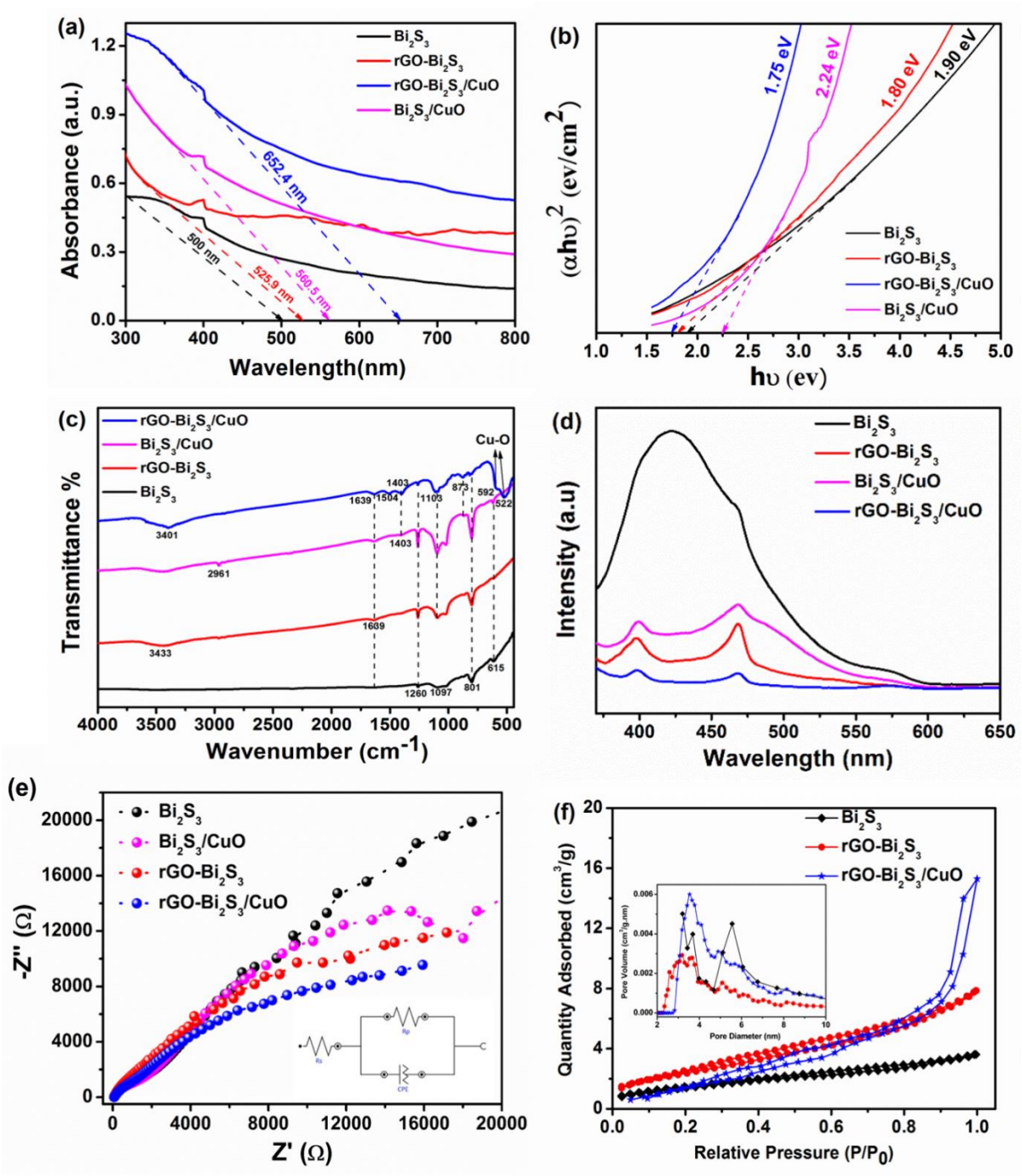


**Fig. 2.1.5: (a) UV-vis absorption spectra, (b) Estimated band gap energy (eV) by the Tauc plot of $Bi_2S_3$, rGO-$Bi_2S_3$, $Bi_2S_3$/CuO, & rGO-$Bi_2S_3$/CuO photocatalysts, (c) FTIR spectra of $Bi_2S_3$, rGO-$Bi_2S_3$, $Bi_2S_3$/CuO & rGO-$Bi_2S_3$/CuO photocatalysts, (d) photoluminescence spectra (PL) of $Bi_2S_3$, rGO-$Bi_2S_3$, $Bi_2S_3$/CuO & rGO-$Bi_2S_3$/CuO photocatalysts an excitation wavelength of 330 nm, (e) EIS curves of $Bi_2S_3$, rGO-$Bi_2S_3$, $Bi_2S_3$/CuO & rGO-$Bi_2S_3$/CuO photocatalysts and artificial circuit (inset of e), (f) Nitrogen adsorption-desorption isotherms and the corresponding pore size distribution curves (inset) of $Bi_2S_3$, rGO-$Bi_2S_3$& rGO-$Bi_2S_3$/CuO photocatalyst**

holes, exhibits the improved photocatalytic performance caused by heterojunction formation in the rGO-$Bi_2S_3$/CuO photocatalyst [159, 160].

#### 2.1.3.2.4 Nitrogen adsorption-desorption isotherms: BET surface area

Fig. 2.1.5(f) displays the matching pore size distribution map of the $Bi_2S_3$, rGO-$Bi_2S_3$, and rGO-$Bi_2S_3$/CuO photocatalysts, as well as the $N_2$ adsorption desorption isotherm for BET surface area.All of the samples had slit pores, as evidenced by the isotherms of pure $Bi_2S_3$, rGO-$Bi_2S_3$, and rGO-$Bi_2S_3$/CuO, which display typical H3 hysteresis loops. The synthesised materials' pore size distributions, which range from 3 to 6 nm and are displayed in the inset of Fig. 2.1.5(f), lend support to the theory that the high surface adsorption is caused by a large number of mesopores. Pure $Bi_2S_3$ has a BET surface area of 2.260 $m^2$/g, while the rGO-$Bi_2S_3$ photocatalyst has a specific surface area of 5.012 $m^2$/g. It is evident that the overall specific surface area of the rGO-$Bi_2S_3$photocatalyst increases as a result of rGO loading in $Bi_2S_3$. Among all the synthesized photocatalysts, the rGO-$Bi_2S_3$/CuO heterojunction photocatalyst in Fig. 2.1.5(f) has the largest specific surface area of 7.398 $m^2$/g. This indicates that the rGO-$Bi_2S_3$/CuO heterojunction photocatalyst's overall specific surface area is increased as a result of CuO loading in rGO-$Bi_2S_3$. Furthermore, there are more surface active sites accessible for the adsorption of reactant molecules ($CO_2$) since rGO-$Bi_2S_3$/CuO has the greatest BET surface area. By decreasing the rate of charge carrier recombination, this raises the yield of photocatalytic $CO_2$ reduction products.

As illustrated in Fig. 2.1.5(g), thermogravimetric analysis (TGA) of pristine $Bi_2S_3$, rGO-$Bi_2S_3$, and rGO-$Bi_2S_3$/CuO has been carried out under $N_2$ from room temperature to 900°C. Here, the TGA study of pure $Bi_2S_3$exhibits a sharp breakdown with a weight drop of 17.66%, about from 450 to 750°C. The loss of sulfur in the form of $SO_2$ is responsible for this weight decrease, and the leftover product finally turns into $Bi_2O_3$ residue. TGA analysis of rGO-$Bi_2S_3$ shows that, in comparison to pristine $Bi_2S_3$, the composite is stable up to 500°C. However, between 500 and 550°C, a very sharp decomposition occurs with an 8.41% weight reduction, primarily representing the combustion of rGO sheets or the breakdown of the graphitic substrate of rGO. The rGO-$Bi_2S_3$/CuO S-scheme heterojunction photocatalyst exhibits the best thermal stability of all the synthesized photocatalysts, according to additional TGA analysis. This is because there is very little decomposition between room temperature and 325°C, with a 3.07% weight reduction. This decomposition is actually the result of the breakdown of oxygen-containing functional groups in rGO sheets and the

removal of adsorbed water. Fig. 2.1.5(g) shows that the rGO-$Bi_2S_3$/CuO heterojunction photocatalyst maintains its thermal stability from 325°C to 900°C. This indicates that there is no more rGO sheet combustion or breakdown, and it is likely that Cu-S and Cu-C interact to limit the further breakdown of $Bi_2S_3$ and rGO, respectively, after 325°C.

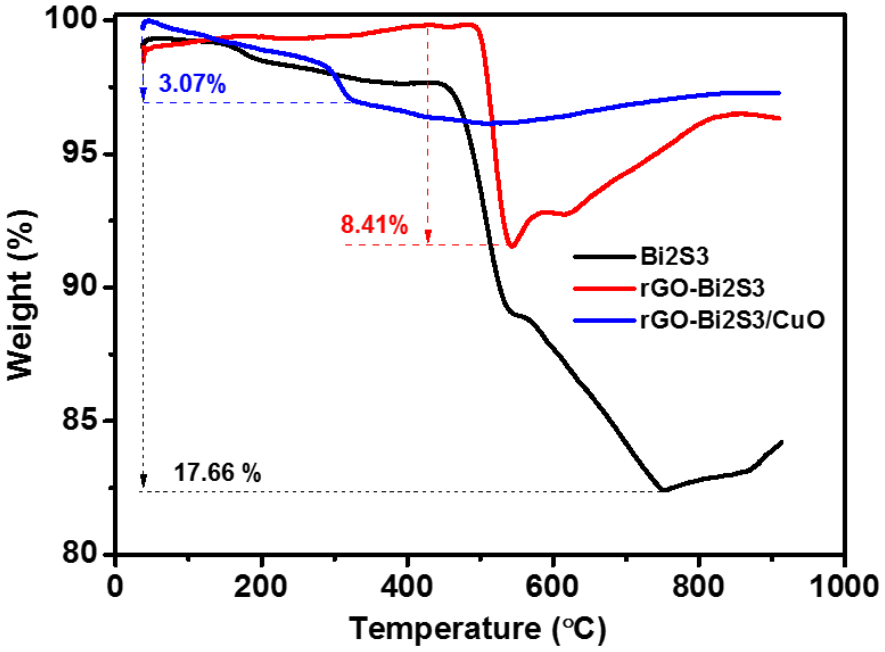


**Fig. 2.1.5 (g): TGA analysis of pristine $Bi_2S_3$, rGO-$Bi_2S_3$& rGO-$Bi_2S_3$/CuO photocatalyst**

### 2.1.3.3 Photocatalytic activity

In this work, the photocatalytic activities of rGO-$Bi_2S_3$, $Bi_2S_3$/CuO, and pure $Bi_2S_3$ nano-hollow floral nanocomposites are examined. Under 10 h of visible light irradiation, photocatalytic $CO_2$-reduced products are identified using the GCMS analytical method. Different synthesized nanocomposites are used to make methanol and formic acid during the photocatalytic $CO_2$ reduction process; these are depicted in Fig. 2.1.6. No further $CO_2$-reduced products, such as formaldehyde, ethanol, or propanol, are present in the liquid phase of the synthesized nanoparticles. No gaseous products are produced during $CO_2$ photoreduction because of the low potential conduction band of $Bi_2S_3$ nano-hollow flower. Using the rGO-$Bi_2S_3$/CuO heterojunction photocatalyst, the GCMS analysis of photocatalytic $CO_2$ reduced products comprising methanol (423.52 μmol $g_{cat.}^{-1}$ $h^{-1}$) and formic acid (17.48

μmol $g_{cat.}^{-1}$ $h^{-1}$) is shown in Fig. 2.1.6(c). The m/z readings of 32.92 and 46.84, respectively, at the retention period of 1.50 min, clearly show the production of methanol and formic acid. The production rates of formic acid and methanol for the $Bi_2S_3$ nano-hollow flower are 25.92 μmol $g_{cat.}^{-1}$ $h^{-1}$ and 71.38 μmol $g_{cat.}^{-1}$ $h^{-1}$, respectively. By adding rGO, the production of methanol in $Bi_2S_3$ increases to 91.93 μmol $g_{cat.}^{-1}$ $h^{-1}$, but the production of formic acid decreases to 14.84 μmol $g_{cat.}^{-1}$ $h^{-1}$.

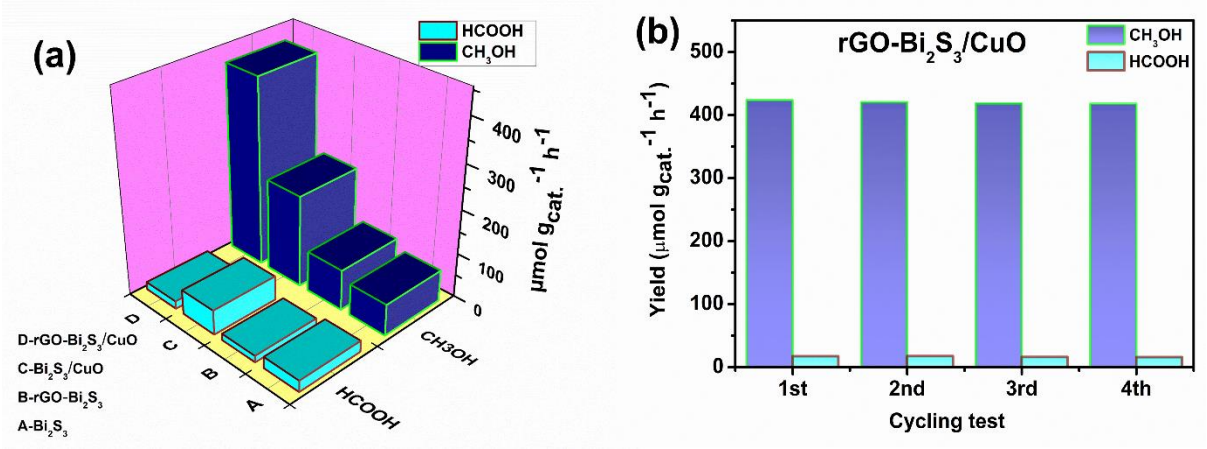


**Fig. 2.1.6: (a) Analysis of the yield of methanol and formic acid production for different photocatalysts, (b) Methanol and Formic acid yields obtained on rGO-$Bi_2S_3$/CuO photocatalysts in four cycling tests**

For comparative purposes, the photocatalytic activity of $Bi_2S_3$/CuO is also examined. GCMS analysis exhibits that pristine $Bi_2S_3$ and rGO-$Bi_2S_3$ exhibit lower liquid phase concentrations of photocatalytic $CO_2$ reduced products, methanol and formic acid, as a result of CuO loading (see Table 2.1.2). The main product found in higher concentrations at the conclusion of the photocatalytic $CO_2$ reduction processes is methanol. Table 2.1.2 shows that the amounts of methanol created increase as follows: rGO-$Bi_2S_3$/CuO <$Bi_2S_3$/CuO < rGO-$Bi_2S_3$/CuO <$Bi_2S_3$. These results also demonstrate that when exposed to visible light, the rGO-$Bi_2S_3$/CuO heterojunction photocatalyst has a remarkable 98.6% selectivity for the photocatalytic conversion of $CO_2$ into $CH_3OH$ (i.e., $S_{CH3OH}$ = 98.6%). The purity of pure methanol (shown by the red curve in Fig. 2.1.6(d) is contrasted with that of the photocatalytic $CO_2$ reduction product of methanol (m/z = 32.83). For the rGO-$Bi_2S_3$/CuO heterojunction photocatalyst at 420 nm, an apparent quantum yield of 0.93% and 0.013%, respectively, for methanol and formic acid ($AQY_{CH3OH}$ and $AQY_{HCOOH}$) is found.

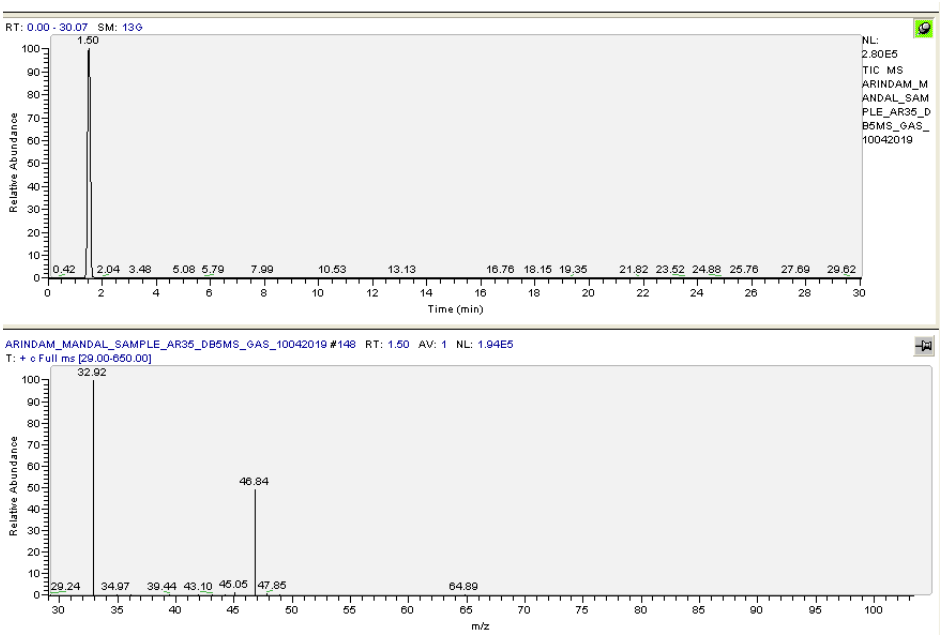


**Fig. 2.1.6(c): GCMS analysis of Photocatalytic $CO_2$ reduced products containing methanol (423.52 µmol $g_{cat.}^{-1}$ $h^{-1}$) and formic acid (17.48 µmol $g_{cat.}^{-1}$ $h^{-1}$) using the rGO-$Bi_2S_3$/CuO heterojunction photocatalyst**

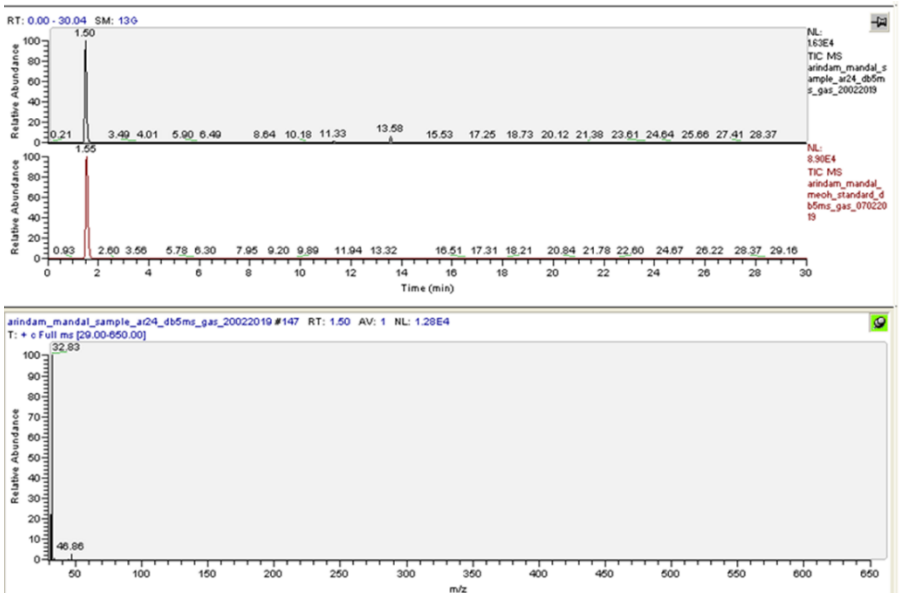


**Fig. 2.1.6(d): Comparison between photocatalytic $CO_2$ reduced methanol (m/z = 32.83) with the pure methanol and the red curve showing the pure methanol**

The yield is defined as the highest amount of $CO_2$-reduced product generated. The high retained methanol production after four cycle testing, as shown in Fig. 2.1.6(b), indicates that the rGO-$Bi_2S_3$/CuO photocatalyst exhibits both good catalytic stability and high

photocatalytic $CO_2$reduction to methanol. The amount of electrons (e-) transmitted in this work for HCOOH and $CH_3OH$ is 2 and 6, respectively, based on the number of electrons required to make 1 mol of each product. The following formula is used to determine the selectivity of methanol ($S_{CH3OH}$):

$$S_{CH_3OH} = 6R_{CH_3OH} / (6R_{CH_3OH} + 2R_{HCOOH}) \quad (2.1.4)$$

Where R manifests the productive rates of $CO_2$ reduced products.

A tiny rate of formic acid and methanol synthesis is attained because of several flaws in the pure $Bi_2S_3$ nano-hollow flower. Here, rGO increases the number of active sites on the catalyst surface, while CuO loading, which lowers the charge recombination process and traps electrons from the pure $Bi_2S_3$ conduction band, increases the photocatalytic activity of the nano-hollow flower. This allows the rGO-$Bi_2S_3$/CuO heterojunction photocatalyst produce less formic acid while simultaneously facilitating a larger methanol yield.

**Table-2.1.2 Photocatalytic $CO_2$ reduced products and yield of synthesised photocatalysts and selectivity of methanol to formic acid production.**

| **Photocatalyst** | **Products & Yield ( µmol $g_{cat.}^{-1}$ $h^{-1}$)** | | **$S_{CH3OH}$ (%)** |
|---|---|---|---|
| | **$CH_3OH$** | **HCOOH** | |
| **$Bi_2S_3$** | 71.38 | 25.92 | 89.2 |
| **rGO-$Bi_2S_3$** | 91.93 | 14.84 | 94.8 |
| **$Bi_2S_3$/CuO** | 207.75 | 55.89 | 91.7 |
| **rGO-$Bi_2S_3$/CuO** | 423.52 | 17.48 | 98.6 |

### 2.1.3.4 Mechanism

The initial stage of the photocatalytic $CO_2$ reduction mechanism is the creation of a surface-bound metastable radical anion ($\cdot CO_2^-$), which is caused by the activation of $CO_2$ on the photocatalyst surface through the absorption of photons from visible light. The complete reduction process then occurs through a number of following phases. Protons and electrons are transferred, hydrogen radicals ($\cdot H$) are produced, C-O bonds are broken, and new C-H bonds are formed, among other processes. In this case, the formaldehyde production pathway is actually followed by the photocatalytic $CO_2$ reduction to methanol and formic acid [144,

147, 192]. According to the formaldehyde route, formic acid (HCOOH) is created when $\cdot CO_2^-$ (ad.) recombines with $H^+$ and electron. After that, the HCOOH recombines with $H^+$ and an electron to create an intermediate formaldehyde (HCHO), which is further reduced to create an H2CHO intermediate. After the generated H2·CHO intermediate recombines with $H^+$ and electrons, photocatalytic $CO_2$ reduction products $CH_3OH$ and HCOOH are produced.

$$\mathrm{rGO/Bi_2S_3/CuO} \xrightarrow{h\nu} h^+ (VB, \mathrm{CuO}) + e^- \left(CB, \frac{\mathrm{Bi_2S_3}}{\mathrm{rGO}}\right) \quad (2.1.5)$$

$$H_2O + h^+ \rightarrow \cdot OH + H^+ \quad (2.1.6)$$

$$H^+ + e^- \rightarrow \cdot H \quad (2.1.7)$$

$$CO_2 + e^- \rightarrow \cdot CO_2^-(\mathrm{ad.}) \quad (2.1.8)$$

$$\cdot CO_2^-(\mathrm{ad.}) + 2H^+ + e^- \rightarrow HCOOH \quad (2.1.9)$$

$$CO_2 + 2H^+ + 2e^- \rightarrow HCOOH$$

$$HCOOH + 2H^+ + 2e^- \rightarrow HCHO + H_2O \quad (2.1.10)$$

$$HCHO + H^+ + e^- \rightarrow H2 \cdot COH \quad (2.1.11)$$

$$H2 \cdot COH + H^+ + e^- \rightarrow CH_3OH \quad (2.1.12)$$

$$CO_2 + 6H^+ + 6e^- \rightarrow CH_3OH + H_2O$$

It has been determined that the absorption edges of rGO-$Bi_2S_3$/CuO and $Bi_2S_3$/CuO are around 560.5 nm and 652.4 nm, respectively. The incorporation of rGO in the $Bi_2S_3$/CuO heterojunction exhibits a broader spectrum of light absorption, suggesting a strong potential for light harvesting. The energy bandgap ($E_g$) of rGO-$Bi_2S_3$/CuO is 1.75 eV, as determined using the tauc plot equation [Fig. 2.1.5(b)]. The flat-band potentials (EFB) of the rGO-$Bi_2S_3$, $Bi_2S_3$/CuO, rGO-$Bi_2S_3$/CuO, and $Bi_2S_3$ photocatalysts are estimated using the Mott-Schottky (M–S) plots presented in Fig. 2.1.6(e) at -0.65 V, -0.85 V, -0.93 V, and -0.62 V vs. Ag/AgCl, respectively. Using the Nernst equation $E_{NHE}$ (V) = $E_{Ag/AgCl}$ + 0.197, the $E_{FB}$ values of rGO-$Bi_2S_3$, $Bi_2S_3$/CuO, rGO-$Bi_2S_3$/CuO, and $Bi_2S_3$ are computed as -0.45 V, -0.65 V, -0.73 V, and -0.42 V vs. NHE, respectively [161–162].

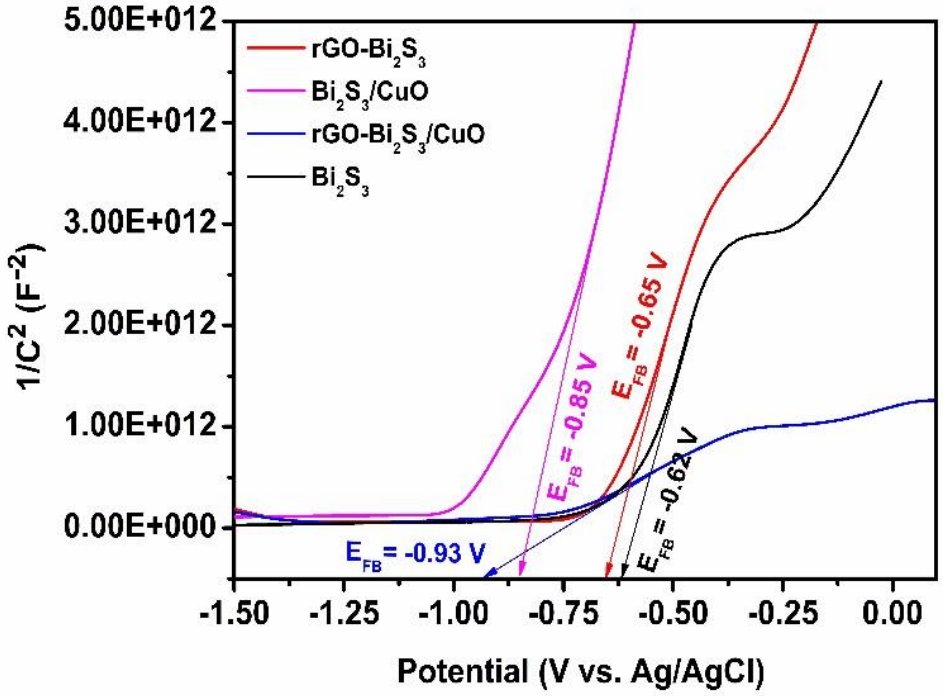


**Fig. 2.1.6(e): Mott-Schottky (M-S) plots of rGO-$Bi_2S_3$, $Bi_2S_3$/CuO, rGO-$Bi_2S_3$/CuO and $Bi_2S_3$ photocatalysts**

The $E_{CB}$ is practically ~0.1 higher than $E_{FB}$ for the n-type photocatalyst [132–133]. Thus, -0.55 V, -0.75 V, -0.83 V, and -0.52 V vs. NHE may be found as the $E_{CB}$ of rGO-$Bi_2S_3$, $Bi_2S_3$/CuO, rGO-$Bi_2S_3$/CuO, and $Bi_2S_3$, respectively. The $E_{VB}$ of rGO-$Bi_2S_3$, $Bi_2S_3$/CuO, rGO-$Bi_2S_3$/CuO, and $Bi_2S_3$ are found to be +1.25 V, +1.49 V, +0.92 V, and +1.38 V vs. NHE, respectively, based on the equation: $E_{VB} - E_{CB} = E_g$ [134-135, 159-160].

EIS measurements in Fig. 2.1.5(e) exhibit the smallest semicircle of rGO-$Bi_2S_3$/CuO with the lowest charge trapping resistance among all samples, and they also illustrate the interfacial charge transfer capacity as a result of rGO incorporation into $Bi_2S_3$/CuO [152, 158, 162]. Furthermore, the smallest photoluminescence (PL) intensity of rGO-$Bi_2S_3$/CuO in Fig. 2.1.5(d) [156, 158] confirms the lowest $e^-$-$h^+$ recombination efficiency. As shown by EIS, M-S, and PL, the combination of CuO and rGO/$Bi_2S_3$ to create a rGO assisted S-scheme heterojunction photocatalyst ensures a notable enhancement in charge separation and migration as well as maximum photo-redox energy to achieve the superior photocatalytic activity. With more photo-induced charge carriers available, the photocatalytic reduction of $CO_2$ to methanol and formic acid can be enhanced [Fig. 2.1.6(a-b)].

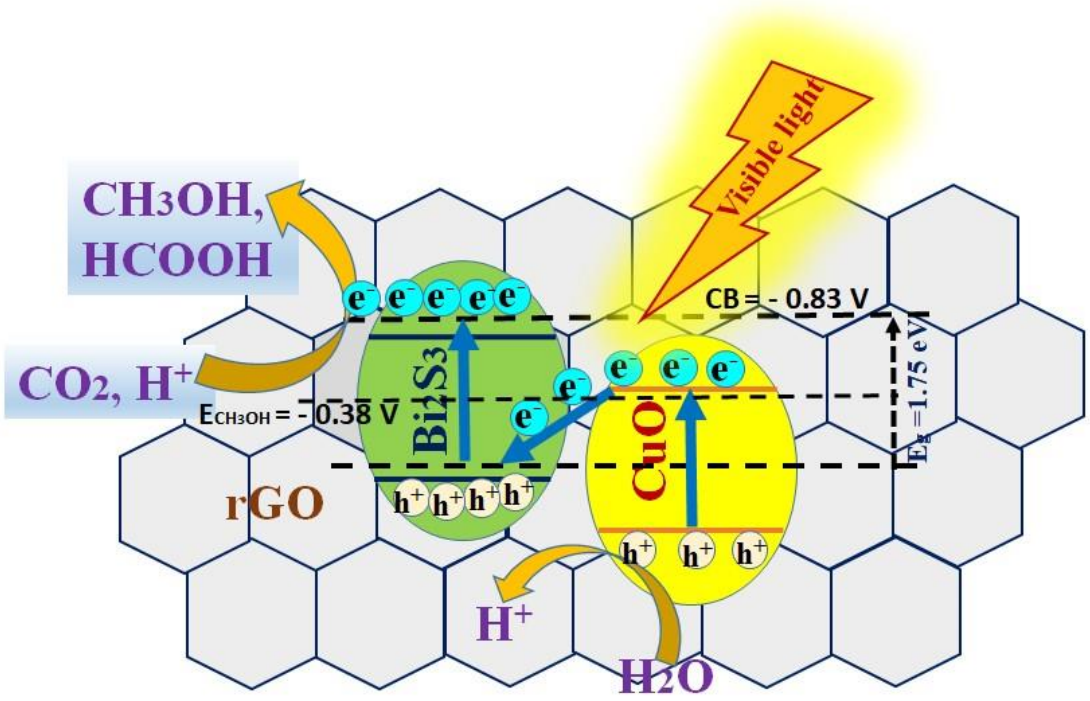


**Fig. 2.1.7: Schematic portrayal of the mechanism of photocatalytic reduction of $CO_2$ to methanol and formic acid using rGO-$Bi_2S_3$/CuO heterojunction photocatalyst under visible light irradiation**

When exposed to visible light, the photo-induced electrons in the CuO-CB move to the $Bi_2S_3$-VB and recombine with its VB holes, confirming the system's unimpaired superior redox power and efficient consumption of low energy electrons/holes [161–165]. Furthermore, strong reductive capabilities of the $Bi_2S_3$-CB allow the electrons to accumulate on the surface and transfer them to the rGO nanosheets, reducing electron-hole pair recombination and facilitating electron transport to the active catalytic zones for photocatalytic carbon dioxide reduction. The rGO's large surface area allows it to absorb $CO_2$. The photo-induced electrons that reduce the adsorbed $CO_2$ into methanol and formic acid are accumulated in the catalytic zones of rGO. Here, rGO serves as an excellent charge migration channel to promote the S-scheme photo-carrier separation [Fig. 2.1.7] and as a favorable photosensitizer to enhance the light response capability of the heterostructure [Fig. 2.1.5(a)] [167,169-171,191,192]. Better sunlight absorption and the separation of photo-carriers with higher redox power are made possible by the rGO supported S-scheme arrangement of $Bi_2S_3$/CuO, which leads to improved photocatalytic performance toward the synthesis of methanol and formic acid. As

illustrated in Fig. 2.1.7, the electrons collected on the CB of rGO-$Bi_2S_3$/CuO are sufficiently negative to reduce $CO_2$, in contrast to the reduction potential of $CH_3OH$ (− 0.38 V vs NHE), and the assembled photo-induced holes typically oxidize water molecules to produce protons ($H^+$). In this case, one mole of $CO_2$ and two moles of $H^+$ are reduced to one mole of formic acid by interacting with two moles of photoinduced electrons; likewise, one mole of $CO_2$ and six moles of $H^+$ are reduced to one mole of methanol and 1.5 moles of oxygen by interacting with six moles of photoinduced electrons. The photocatalytic activity of a number of heterojunction photocatalysts reported in the literature is contrasted with the findings of the current study in Table 2.1.3.

**Table-2.1.3 Comparison of the yield of methanol and formic acid as photocatalytic $CO_2$ reduced products for various photocatalyst with the performance of the photocatalyst of the present investigation**

| **Photocatalyst** | **Reaction medium** | **Products and yield ($\mu mol\ g_{cat.}^{-1}\ h^{-1}$)** | **Ref.** |
|---|---|---|---|
| $Bi_2S_3/TiO_2$ | water | $CH_3OH$: 44.92 | 145 |
| $Bi_2S_3$ QD/$TiO_2$ | isopropanol | $CH_3OH$: 1169.15 | 182 |
| Cu-(1D) $Bi_2S_3$/rGO | water | $CH_3OH$: 719.0 | 183 |
| $Bi_2S_3$/CdS | water | $CH_3OH$: 122.6 | 184 |
| $Bi_2S_3$-SAR | water | $CH_3OH$: 25.94 | 184 |
| rGO–CuO | DMF/water | $CH_3OH$: 51.167 | 186 |
| $In_2O_3$–CuO | $Na_2SO_3$ | $CH_3OH$: 8.87<br>CO: 5.23 | 187 |
| Er-doped $CeO_2$/rGO/CuO | $NaHCO_3$ | $CH_3OH$: 135.6 | 188 |
| ZnO/CuO | water | HCOOH: 238.68<br>$CH_3OH$: 0.30 | 189 |
| N-$TiO_2$/CuO | water | HCOOH: 1980 | 190 |
| rGO-$Bi_2S_3$/CuO | water | $CH_3OH$: 423.52<br>HCOOH: 17.48 | This work |

**2.2.1** The specific **objectives** of **Problem 2.2** are enlisted below:

- **i.** Design and synthesis of visible light responsive(1D) $Bi_2S_3$ photocatalysts by incorporating fixed rGO concentration for enhancing the yield of $CO_2$ reduced products.
- **ii.** Modification of rGO-(1D) $Bi_2S_3$ photocatalysts by different percentage of Cu doping (0.5%, 1%, 2%) to get optimal Cu doping for achieving the highest yield of specific product selective $CO_2$ reduction.
- **iii.** Characterization of all synthesized photocatalysts by XRD, SEM, TEM, EDX, FTIR, EIS, BET, and XPS.
- **iv.** Photocatalytic performance study of synthesized doped and undoped nano-composite photocatalysts.
- **v.** Prediction of mechanism of $CO_2$ photo-reduction.

### 2.2.2 Experimental

#### 2.2.2.1 Materials:

All of the chemicals utilised are analytical grade, and no additional purification is required. Sigma-Aldrich is the source of the employed chemicals, which include copper nitrate trihydrate ($Cu(NO_3)_2.3H_2O$), sodium bicarbonate ($NaHCO_3$), thioacetamide ($C_2H_5NS$), and bismuth nitrate pentahydrate ($Bi(NO_3)_3.5H_2O$). The additional chemicals (reagent grade) utilised in this experiment are acquired from Merck and include ethanol, hydrochloric acid, graphite flakes, potassium permanganate ($KMnO_4$), sulphuric acid ($H_2SO_4$), phosphoric acid ($H_3PO_4$), hydrogen peroxide ($H_2O_2$), and sodium hydroxide (NaOH).

#### 2.2.2.2 Synthesis of Cu-doped 1D-$Bi_2S_3$/rGO

##### 2.2.2.2.1 Synthesis of pristine 1D-$Bi_2S_3$:

In this synthesis procedure, 25 ml of ethylene glycol, 2 g of $Bi(NO_3)_3.5H_2O$, and 0.6 g of thioacetamide (TAA) have been individually combined with constant stirring for 30 minutes. After mixing the two solutions, a 3 M NaOH solution is added to bring the pH of the mixture down to 8. After that, the mixture is stirred for 1 h. Subsequently, the entire mixture is placed into a 100 ml. stainless-steel autoclave that is lined with Teflon, sealed, and allowed to

operate hydrothermally at 160°C for 18 h. Following centrifugation and a natural cooling of the autoclave to room temperature, the black solid products are collected. The black precipitate is then repeatedly cleaned with ethanol and double-distilled water before being vacuum-dried for 12 h at 70°C in a heated chamber. Once dried, pure (1D) rod-shaped $Bi_2S_3$ nanocapsules (BSNC) are discovered [193,194].

#### 2.2.2.2.2 Synthesis of 1D-$Bi_2S_3$/rGO:

The modified Hummers technique has been used to synthesise graphene oxides (GO) [191]. To fully exfoliate the GO sheets in this usual procedure, 10 weight percent of the synthesised GO solution is first subjected to ultrasonication for 120 min. After that, the ultrasonicated GO solution is continuously stirred for an additional 60 min. while a separately prepared solution containing 2 g of $Bi(NO_3)_3.5H_2O$ and 0.6 g of TAA is added. The pH of the mixture is then brought to 8 using a 3M solution of NaOH. rGO-incorporated (1D) $Bi_2S_3$ rod-shaped nanocapsules are discovered after hydrothermally treating the aforementioned combination for 18 h at 160°C in a 100 ml. sealed Teflon-lined stainless steel autoclave. This is done after doing many washes and dryings [193, 204].

#### 2.2.2.2.3 Synthesis of Cu-doped 1D-$Bi_2S_3$/rGO:

By varying the percentages of Cu loading of 0.5, 1, and 2 weight percent, respectively, with the fixed concentration of $Bi_2S_3$ rod-shaped nanocapsule (BSNC) and rGO solution, the synthesis of copper-doped (1D) $Bi_2S_3$ rod-shaped nanocapsules/rGO (Cu-BSNC/rGO) has been carried out in order to investigate the impact of Cu doping on the selectivity of the $CO_2$ reduced product. Cu-BSNC/rGO nanostructures are prepared using hydrothermal treatment in this study in order to produce a highly selective product with a high yield. In this typical procedure, Cu loading into the $Bi_2S_3$/rGO solution is achieved by adding varying volumes of separately dissolved $Cu(NO_3)_2.5H_2O$ to get 0.5, 1, and 2 weight percent of Cu doping. A 3 M NaOH solution is used to bring the pH of mixture down to 8. An additional hour has been spent stirring the entire concoction. The entire combination is then put inside a 100 ml. stainless steel autoclave with a Teflon lining, sealed, and kept at 160°C for 18 h. The products are collected after centrifugation and allowed to naturally cool to room temperature. They are then repeatedly cleaned with ethanol and double-distilled water before being vacuum-dried for 12 h at 70°C in a heated chamber. Cu-doped (1D) $Bi_2S_3$ rod-shaped nanocapsules (Cu-BSNC) are manufactured using a similar process for property comparison.

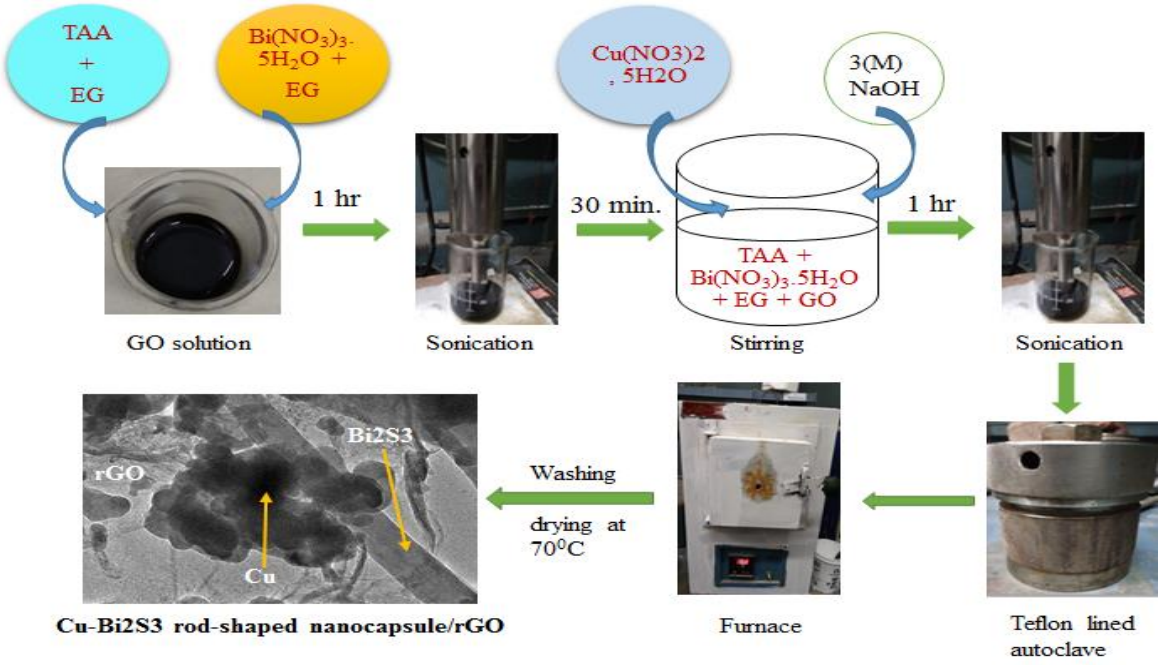


**Fig. 2.2.1: Schematic representation of synthesis process of Cu-doped 1D-$Bi_2S_3$/rGO photocatalyst**

### 2.2.2.3 Photo-reduction of $CO_2$ and Photocatalytic activity evaluation:

Using a 125-watt high pressure mercury vapour lamp-seen in Fig. 2.2.2-the photocatalytic activity of the produced photocatalysts Cu-BSNC/rGO, BSNC/rGO, and BSNC are examined under visible light irradiation. To investigate the photocatalytic activity, 30 mg of each photocatalyst is separately added to a 150 ml quartz tube reactor in this typical experiment.

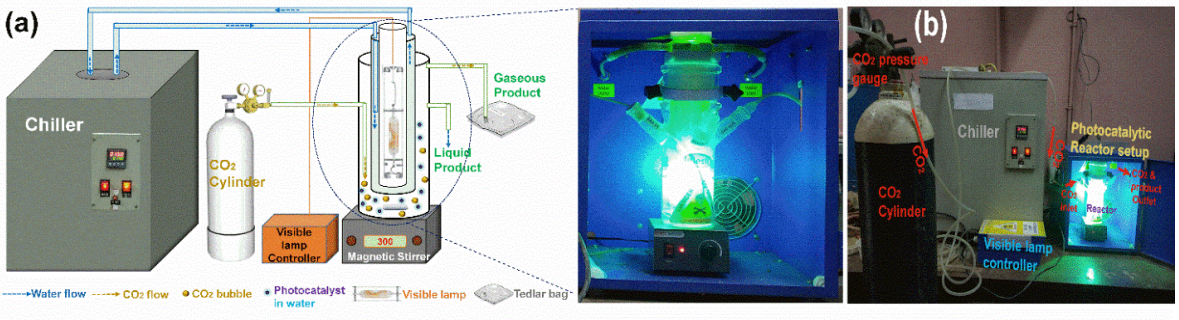


**Fig. 2.2.2: (a) Schematic representation of the experimental set up for performance study of photocatalytic activity of (0.5%, 1% & 2%) Cu-doped BSNC/rGO, BSNC/rGO, BSNC nanocomposites respectively & (b) Real-life Photocatalytic Reactor Setup**

To create a saturated solution and maximize the amount of $CO_2$ molecules that adsorb on the photocatalyst's active sites, pure $CO_2$ gas is fed through 100 milliliters of water that contains 0.5 M $NaHCO_3$ as hole scavengers inside the reactor at the lowest possible flow rate prior to irradiation [194]. To eliminate all dissolved oxygen from the solution, the entire procedure is done in the dark for 40 minutes while magnetic stirring is in place. Subsequently, 30 mg of photocatalyst powder is added to the solution mentioned above. The reaction is then allowed to proceed for 10 h at a temperature controlled by a chiller, while being continuously stirred and illuminated by the designated high pressure mercury vapour lamp. Subsequently, the products of the photocatalytic reduction of $CO_2$ are collected using a needle-type probe that is inserted into the solution of the reactor. Helium is used as the carrier gas in gas chromatographyequipment (Agilent 7890A system) to analyze the products' methanol concentration using GC-FID and GC-TCD. To make sure that the photocatalytic reduction of $CO_2$ is the only source of the product methanol, blank reactions are carried out. Without a photocatalyst, the experiment is carried out using the same setup parameters. Second, under the identical operating conditions, the entire experiment is carried out in complete darkness with a photocatalyst present. Thirdly, the catalyst and high-pressure mercury vapour lamp are present in the reactor system during the blank experiment, and no $CO_2$ gas is purged. Additionally, the pure grade of methanol is employed for analysis in order to attain the purity of the $CO_2$-reduced product.

### 2.2.3 Results and discussion

#### 2.2.3.1 Analysis of crystalline phase:

The XRD patterns of GO, rGO, BSNC, BSNC/rGO, and Cu-BSNC/rGO composites are displayed in Fig. 2.2.3(a). The distinctive GO diffraction peak, located at around 10.1°, is aligned with the (002) crystalline plane, signifying that pure graphite has undergone complete oxidation to form GO sheets [173]. The complete conversion of GO to rGO following an assumed hydrothermal process is demonstrated by the absence of a typical GO peak in the other nanocomposites. Similar peaks can be found in the (130), (211), (221), and (431) crystal planes in the XRD patterns of BSNC and BSNC/rGO. These peaks can be indexed to the standard orthorhombic phase of $Bi_2S_3$ (JCPDS card No. 017-0320) with unit cell constants: a = 11.1490 Å, b = 11.3040 Å and c = 3.9810 Å. The stronger peak of $Bi_2S_3$ at 24.9° obscures the rGO diffraction peaks seen at 24.0° in the Cu-BSNC/rGO pattern [183–

185]. The XRD patterns of synthesized (1%) Cu-BSNC/rGO nanocomposite show diffraction peaks similar to those of

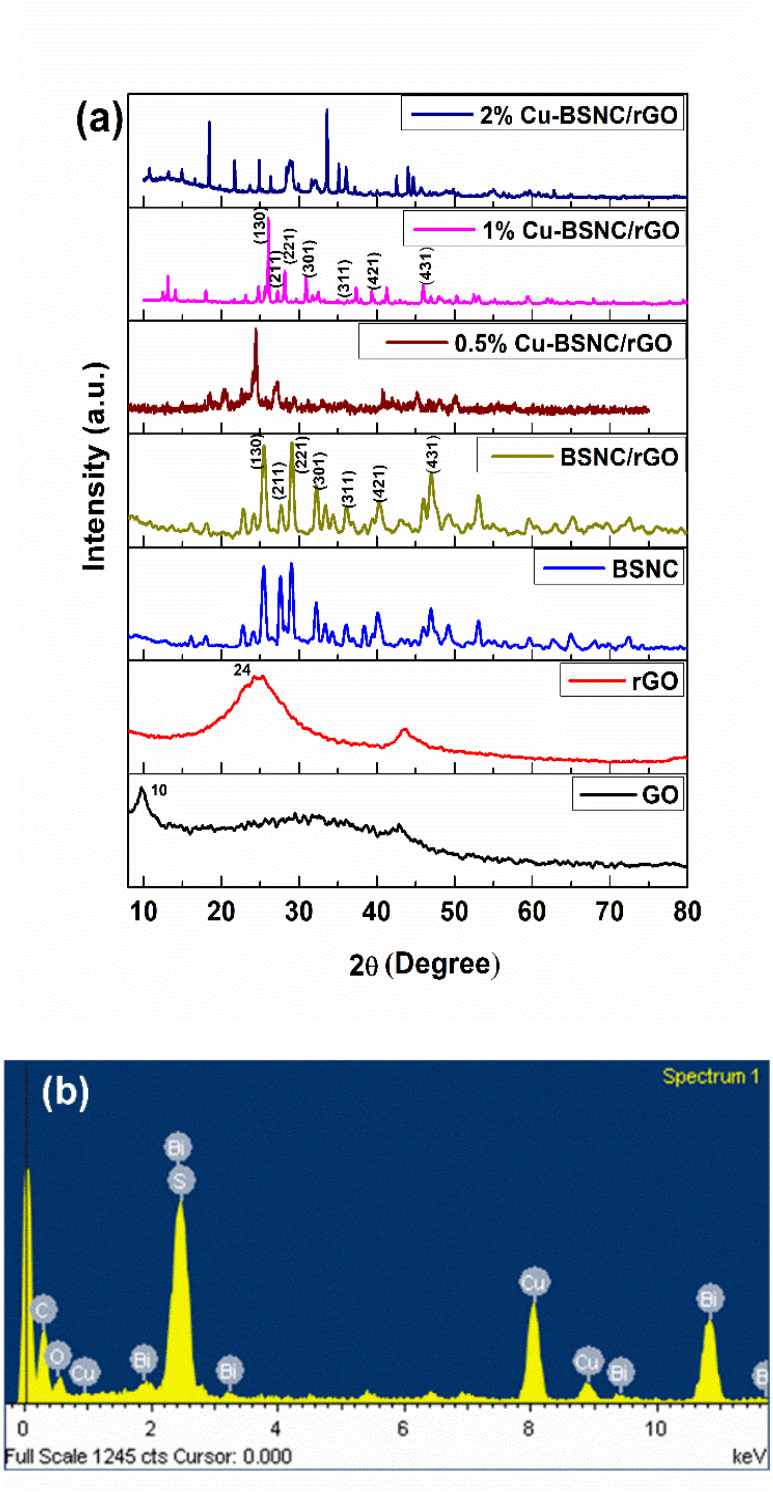


**Fig. 2.2.3: (a) XRD patterns of GO, rGO, BSNC, BSNC/rGO, (0.5%) Cu-BSNC/rGO, (1%) Cu-BSNC/rGO and (2%) Cu-BSNC/rGO nanocomposites. (b) The corresponding EDX chemical analysis of (1%) Cu-BSNC/rGO**

BSNC/rGO; however, the distinctive peaks of Cu and its oxide derivative are absent, possibly because of the low weight percentage of Cu doping. Using the Debye-Scherrer equation, the average crystallite size (L) of (1%) Cu-BSNC/rGO is determined to be 19.86 nm.

$$\left[L = {}^{0.9\lambda}/_{\beta cos\theta}\right] \qquad (2.2.1)$$

where θ is the Bragg angle, β is the full line width at the half maximum height of the peak (FWHM), and λ is the X-ray-wavelength (0.15406 nm). Additionally, it is discovered that the average crystallite sizes of BSNC and BSNC/rGO are roughly 16.61 nm and 15.91 nm, respectively. Cu doping in BSNC/rGO results in significantly larger average crystallite sizes for Cu-BSNC/rGO.

### 2.2.3.2 Morphology, structure and composition analysis

#### 2.2.3.2.1 SEM & TEM analysis:

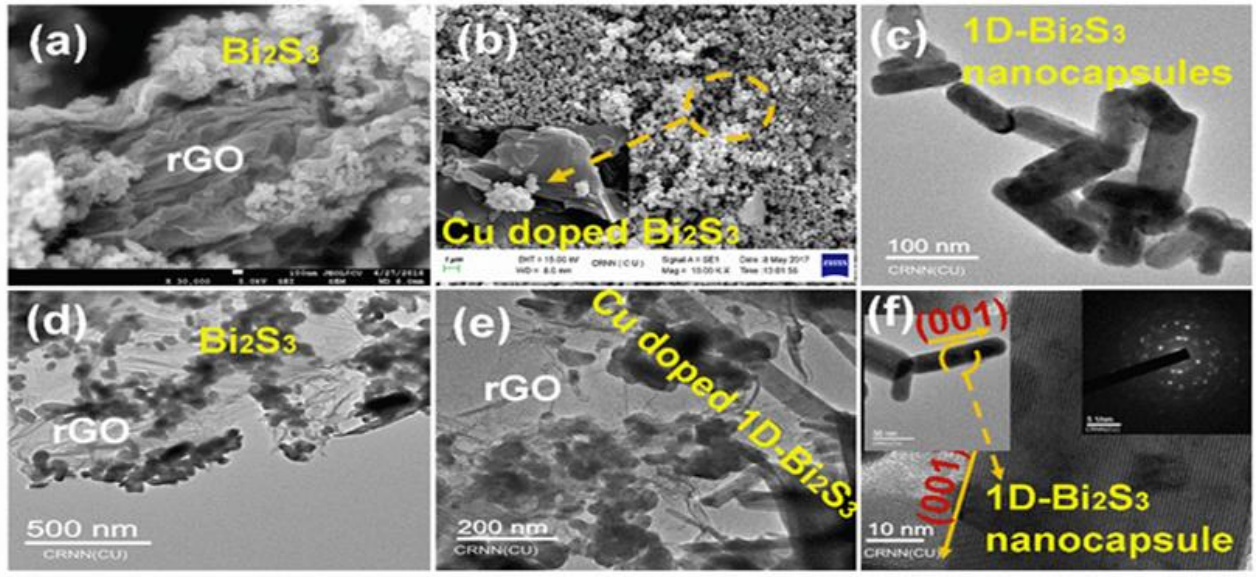


**Fig. 2.2.4: SEM image of (a) 1D-$Bi_2S_3$/rGO [BSNC/rGO], (b) (1%) Cu-doped 1D-$Bi_2S_3$/rGO [(1%) Cu-BSNC/rGO] with a magnified image in the inset. TEM image of (c) 1D-$Bi_2S_3$ rod-shaped nanocapsules [BSNC] (d) 1D-$Bi_2S_3$/rGO [BSNC/rGO], (e) (1%) Cu-doped 1D-$Bi_2S_3$/rGO [(1%) Cu-BSNC/rGO], (f) HR-TEM image of one 1D- $Bi_2S_3$ nanocapsule (inset shows the SAED patterns)**

To examine the morphological properties of nanomaterials as-prepared, SEM and TEM are utilized. The TEM picture of Fig. 2.2.4(c) clearly displays the rod-shaped nanocapsule structure of 1D-$Bi_2S_3$. This structure has an average length of 150–170 nm and width of 30–50 nm. The rod-shaped nanocapsules 1D-$Bi_2S_3$ are embedded in the sheets of rGO, as seen in the SEM image of Fig. 2.2.4(a) and clearly visible in the TEM image of Fig. 2.2.4(d) [183, 184, 188, 207]. Fig. 2.2.4(b) demonstrates that the (1%) of Cu-doped $Bi_2S_3$ attached firmly to the surface of rGO, suggesting close contact between the two. The TEM picture in Fig. 2.2.4(e) further demonstrates this intimate interaction. SEM and TEM images show a strong, interconnected network with rGO formed by the well-attached $Bi_2S_3$ rod-shaped nanocapsule to Cu nanoparticles. This could lead to enhanced selective photocatalytic reduction of $CO_2$ to methanol and play a significant role in interfacial charge transfer upon visible light irradiation. Moreover, EDX displays the elemental analysis of 1% Cu-doped $Bi_2S_3$/rGO with an atomic ratio of 1:1 for Bi:Cu in Fig. 2.2.4(b). The proper incorporation of C and Cu into rod-shaped $Bi_2S_3$ nanocapsules is ensured by their existence. The d-spacing of (200) crystal plane of the orthorhombic $Bi_2S_3$ is displayed in Fig. 2.2.4(f) [208]. This implies that the preferred [001] orientation is followed by the formation of $Bi_2S_3$ nanocapsules [206,207]. The single-crystallinity of the synthesized 1D-$Bi_2S_3$ [188] is indicated by the bright spots in the SAED pattern [inset of picture Fig. 2.2.4(f)]. Additionally, 2% Cu-doped $Bi_2S_3$/rGO is analyzed by EDX [Fig. 2.2.4(g)].

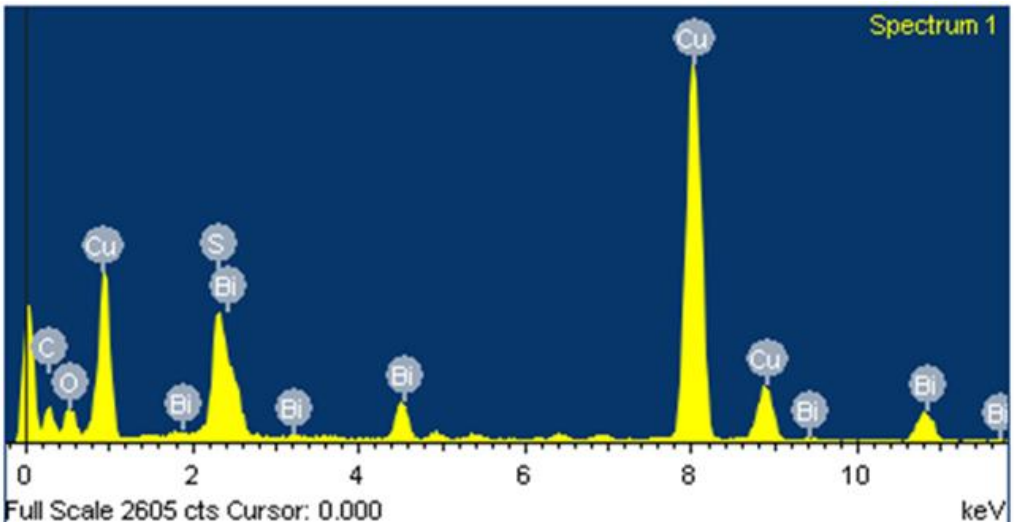


**Fig. 2.2.4 (g): EDX analysis of (2%) Cu-BSNC/rGO [(2 wt%) Cu doped $Bi_2S_3$/rGO]**

#### 2.2.3.2.2 XPS analysis:

The synthesised materials' surface chemical characteristics and surface electronic states are ascertained by the use of X-ray photoelectron spectroscopy (XPS). To look into the change in binding energy, which shows the excitation of the electrons under the experimental conditions, XPS analysis is performed on (1%) Cu-(1D) $Bi_2S_3$/rGO. Fig. 2.2.5 shows that the addition of copper led to increased efficiency and easier electron defusing. The whole spectrum can be further deconvoluted into six individual peaks in the Bi 4f and S 2p XPS studies [Fig. 2.2.5(a)]. The peaks at binding energies of 159.5 eV and 164.82 eV correspond to the $4f_{7/2}$ and $4f_{5/2}$ orbital splittings of the $Bi^{3+}$ state, respectively, and the peaks at 160.2 eV and 165.54 eV also represent the $4f_{7/2}$ and $4f_{5/2}$ orbital splittings of the $Bi^{3+x}$ state. Furthermore, the orbital splittings of S $2p_{3/2}$ and S $2p_{1/2}$ are represented by the two tiny peaks that are visible at 162.10 eV and 163.27 eV, respectively. The whole spectrum in the high-resolution Cu 2p photoelectrons spectra shown in Fig. 2.2.5(b) may be deconvoluted into 7 peaks. The Cu $2p_{3/2}$ and Cu $2p_{1/2}$ orbital splitting of $Cu^0$ or $Cu^+$ species is represented by the strong peaks at 932.11 eV and 951.89 eV, whereas the Cu $2p_{3/2}$ and Cu $2p_{1/2}$ orbital splitting of $Cu^{2+}$ ions in the sample is represented by the lower peaks at 932.85 eV and 952.52 eV. The Cu $2p_{3/2}$ and Cu $2p_{1/2}$ orbital splitting of any copper carbonate or copper dihydroxide present in the sample is responsible for the extremely low peaks at 934.80 eV and 954.47 eV. The satellite peak is located at 948.56 eV. This demonstrates that copper, which is mostly in the $Cu^+$ state, engages in the reaction instead of the $Cu^{2+}$ state. As seen in Fig. 2.2.5(c), the high-resolution XPS spectra of C1s may be deconvoluted into three peaks.

### 2.2.3.3 Optical characterization

#### 2.2.3.3.1 UV-Vis analysis:

The optical response findings of the synthesised pure $Bi_2S_3$ rod-shaped nanocapsule (BSNC), BSNC/rGO, and various copper doping percentages into BSNC/rGO composites are displayed in Fig. 2.2.6(a) with the aid of UV-Vis diffuse reflectance analysis. In comparison to pure 1D-BSNC, BSNC/rGO exhibits an augmentation of its absorbance in the visible region. It is also possible to detect that Cu loading in 1D-BSNC/rGO nanocomposites leads to an increase in absorbance in the visible area. The increase in absorbance in the visible range, seen in Fig. 2.2.6(a), is on the order of (1%) 2 percent Cu-BSNC/rGO> (0.5 percent Cu-

BSNC/rGO> BSNC/rGO> (1 percent Cu-BSNC> pure BSNC). Moreover, the best absorbance peak is seen

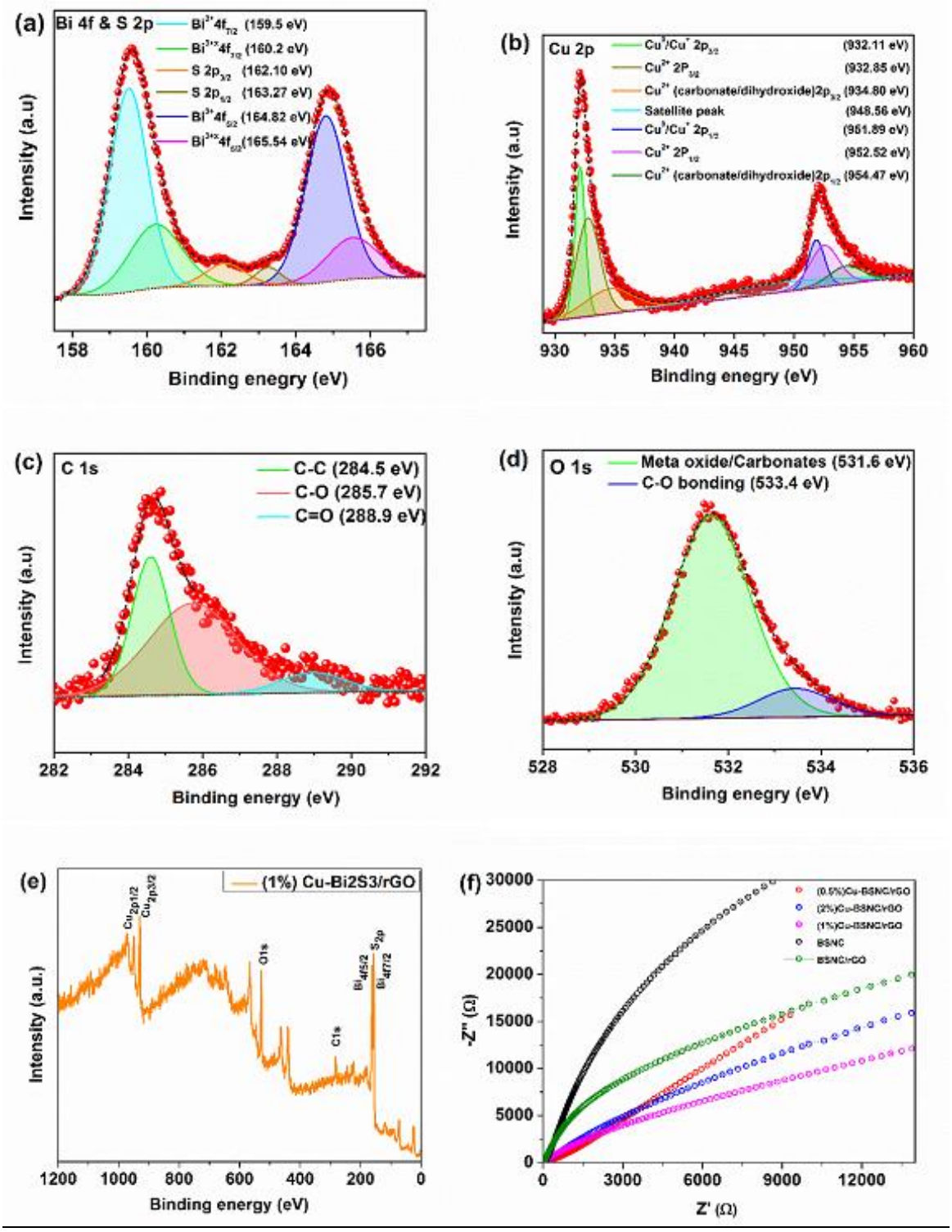


**Fig. 2.2.5: Core level XPS scan of (a) Bi 4f & S 2p, (b) Cu 2p, (c) C 1s, (d) O 1s, (e) Survey scan of X-ray photoelectron spectra (XPS) of (1%) Cu-doped 1D-$Bi_2S_3$/rGO nanocomposite, and (f) EIS curves of pristine BSNC, BSNC/rGO, and Cu-BSNC/rGO series catalysts**

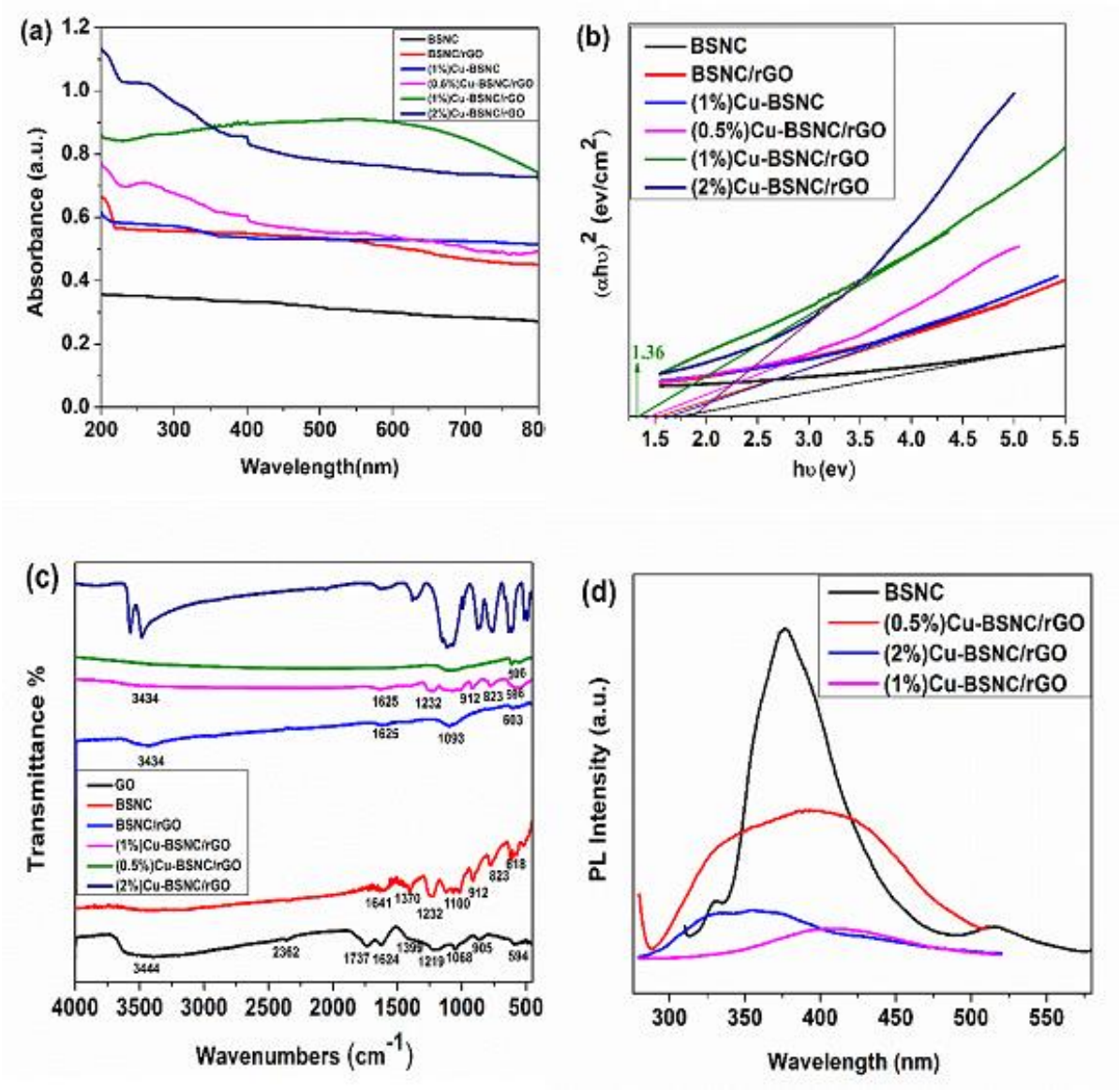


**Fig. 2.2.6: (a) UV-Vis diffuse reflectance spectra, (b) Estimated band gap energy (eV) by the Tauc plot of BSNC, BSNC/rGO, (1%)Cu-BSNC, (0.5%)Cu-BSNC/rGO, (1%)Cu-BSNC/rGO, and (2%)Cu-BSNC/rGO, (c) FTIR spectra of GO, BSNC, BSNC/rGO, (1%)Cu-BSNC/rGO, (0.5%)Cu-BSNC/rGO and (2%)Cu-BSNC/rGO. (d) The photoluminescence spectra (PL) of BSNC, (0.5%)Cu-BSNC/rGO, (2%)Cu-BSNC/rGO and (1%)Cu-BSNC/rGO respectively at excitation wavelength of 270 nm**

in the 300–600 nm range in the (1%) Cu-BSNC/rGO composite. Additionally, it can be shown from Fig. 2.2.6(b) that when the amount of copper in 1D-$Bi_2S_3$ rod-shaped nano-capsules and rGO composites increases, the bandgap energy decreases.The tauc plot equation

(2.2.2) is used to estimate the bandgap energies of all synthesised nano-catalysts, as seen below.

$$[\alpha h\nu] = A\left[h\nu - E_g\right]^{\frac{n}{2}} \quad (2.2.2)$$

where n is 1 for direct bandgap and 4 for indirect bandgap of semiconductors, c is the speed of light, v is its frequency, A is the absorption coefficient, and $E_g$ (eV) is the bandgap of photocatalyst. Table 2.2.1 displays the estimated bandgap energies of all synthesised photo-catalysts.

**Table 2.2.1 - Estimated values of band gap energy of synthesized nanomaterials**

| Name of photocatalyst | Absorption Edge (nm) | Calculated Band gap energy (eV) |
|---|---|---|
| (i) BSNC | 530.2 | 1.70 |
| (ii) BSNC/rGO | 610.6 | 1.51 |
| (iii) (1%)Cu-BSNC | 552.5 | 1.62 |
| (iv) (0.5%)Cu-BSNC/rGO | 649.8 | 1.47 |
| (v) (1%)Cu-BSNC/rGO | 706.5 | 1.36 |
| (vi) (2%)Cu-BSNC/rGO | 478.0 | 1.82 |

**2.2.3.3.2 FTIR analysis:**

The FTIR spectra of the following nanocomposites are displayed in Fig. 2.2.6(c): GO, BSNC, BSNC/rGO, (1%) Cu-BSNC/rGO, (0.5%) Cu-BSNC/rGO, and (2%) Cu-BSNC/rGO. The O-H stretching vibration, which correlates to the samples' interior water molecules, is responsible for the peak at 3444 $cm^{-1}$. The GO exhibits many peaks in Fig. 2.2.6(c), which correspond to the C=O, C=C, C–OH, C–O–C, and C–O stretching vibrations, respectively, at 1737, 1624, 1370, 1219, and 1068 $cm^{-1}$ [178, 183, 191, 193]. The peak intensity of the oxygenic groups in BSNC/rGO composites is lower than that of GO, and it vanishes for Cu doping in BSNC/rGO, indicating that GO is entirely reduced as the hydrothermal process proceeds. The interaction between rGO and a 1D-$Bi_2S_3$ rod-like nanocapsule may be the cause of the broad absorption peak seen between 1100 and 823 $cm^{-1}$[205, 210]. It is possible

that the interaction between rGO and copper-doped 1D-$Bi_2S_3$ rod-like nanocapsules is responsible for the tiny absorption peak seen at 596 $cm^{-1}$.

**2.2.3.3.3 Photoluminescence (PL) spectra & EIS analysis:**

A semiconductor's photocatalytic activity is determined by measuring the photogenerated electron-hole separation in addition to its UV-Vis spectra. At an excitation wavelength of 270 nm, the PL analysis of the following nanocomposites is carried out: BSNC, (0.5%) Cu-BSNC/rGO, (2%) Cu-BSNC/rGO, and (1%) Cu-BSNC/rGO. The emission spectra are shown in Fig. 2.2.6(d). It is commonly recognised that PL spectra may show the processes of migration, transfer, and recombination of photogenerated electron-hole pairs in semiconductors due to the recombination of free carriers. A greater rate of photogenerated charge carrier recombination would be implied by the rise in PL intensity [193].Fig. 2.2.6(d) illustrates that the photocatalyst Cu-BSNC/rGO (1%) exhibits a comparatively weaker peak when compared to the copper-doped and undoped $Bi_2S_3$ rod-shaped nano-capsules. The finding indicates that the interface formed between the 1D-$Bi_2S_3$ rod-shaped nanocapsule (BSNC) and rGO, which transports electrons and minimises charge carrier recombination, greatly reduces the photogenerated electron-hole pair[195, 205, 208]. In this case, copper is also crucial to the decrease in charge carriers [214,222].

In addition, the excited electron travels through the photocatalyst's internal band to the empty electronic states of the rGO sheet through interfacial charge transfer phenomena, which lowers the photoluminescence intensity. This is because doped Cu ions create impurity levels between the VB and CB of BSNC. As the amount of copper doping in the sequence increases, the PL intensity is seen to change. (1%) Cu-BSNC/rGO < 2% rGO/Cu-BSNC < (0.5%)Cu-BSNC/rGO < BSNC, indicating that the (1%)Cu-BSNC/rGO nanocomposites have the lowest rate of electron hole pair recombination, which has increased the photocatalytic activity. EIS analysis is done to validate the PL result. The EIS Nyquist plot of the photocatalysts for BSNC, BSNC/rGO, (0.5%)Cu-BSNC/rGO, (1%)Cu-BSNC/rGO, and (2%)Cu-BSNC/rGO is displayed in Fig. 2.2.5(f). The arc radii of the photocatalysts that are (0.5%)Cu-BSNC/rGO, (1%)Cu-BSNC/rGO, and (2%)Cu-BSNC/rGO are lower than those of BSNC and BSNC/rGO, as can be shown in Fig. 2.2.5(f). The (1%)Cu-BSNC/rGO photocatalyst has the shortest arc radius of any Cu-doped sample, suggesting that Cu-doping can significantly reduce the charge transfer resistance. Better photocatalytic performance is

provided by the photocatalyst's increased conductivity, which also increases the separation efficiency of the photogenerated electrons and holes.

### 2.2.3.4 Photocatalytic activity:

Evaluations are made of the photocatalytic activity of rGO/$Bi_2S_3$, pure $Bi_2S_3$ rod-shaped nanocapsules, and various weight percentages of Cu-doped BSNC/rGO nanocomposites. GCMS is used to evaluate the byproducts of photocatalytic $CO_2$ reduction during 10 h of visible light illumination. It is discovered (Fig. 2.2.7) that employing synthesised varying weight percentages of Cu-doped 1D-BSNC/rGO nanocomposites, the methanol is generated as a 100% selective product. For the various weight percentages of Cu-doped BSNC/rGO nanomaterials, no other products, such as formaldehyde, ethanol, or formic acid, are found in the liquid phase; instead, as illustrated in Fig. 2.2.7 (a), a very small amount of formic acid is found in the liquid phase reaction using the $Bi_2S_3$ rod-shaped nano-capsules and rGO/$Bi_2S_3$ as the photocatalyst. $Bi_2S_3$ rod-shaped nanocapsules have a low conduction band potential, which prevents the detection of gaseous products during $CO_2$ photoreduction. Using a 1D-$Bi_2S_3$ rod-shaped nano-capsule photocatalyst, the GCMS analysis of $CO_2$ reduced products comprising methanol and formic acid is displayed in Fig. 2.2.7 (b). The generation rates of methanol and formic acid for $Bi_2S_3$ nano-capsules are 3.089 μmol $g_{cat.}^{-1}$ $h^{-1}$ and 77.23 μmol $g_{cat.}^{-1}$ $h^{-1}$, respectively. The results of m/z = 32.97 and 46.74, respectively, for a retention period of 1.54 min in Fig. 2.2.7 (b) clearly show the production of methanol and formic acid. When rGO is added to $Bi_2S_3$, the rate of methanol synthesis increases to 102.06 μmol $g_{cat.}^{-1}$ $h^{-1}$; on the other hand, the rate of formic acid production decreases to 2.3169 μmol $g_{cat.}^{-1}$ $h^{-1}$ (which is in line with Fig. 2.2.7 (c)), as the intensity of the peak at m/z=46.74 (formic acid) is reduced. The selective methanol synthesis as a $CO_2$ photo-reduced product is demonstrated in Fig. 2.2.7 (d) and 2.2.7 (e), thanks to the photocatalytic activity of a 1 percent Cu-doped $Bi_2S_3$/rGO nano-catalyst. The absence of a peak at m/z= 46.74 indicates that formic acid generation is not present. The little peak in Fig. 2.2.7 (d) at m/z= 44.88 indicates that a tiny quantity of $CO_2$ is absorbed by the examined material. Referencing Fig. 2.2.7(f) in the accompanying document, GCMS analysis identifies methanol and formic acid as photocatalytic $CO_2$ reduction products in the liquid phase, corroborated by the photocatalytic activity research of (1%) Cu-BSNC. (0.5, 1, and 2 wt%) Cu loading produces methanol with selectivity; (1%) Cu-doped $Bi_2S_3$/rGO photo-catalyst produces the highest methanol production rate, which is seen in Fig. 2.2.7(a) and is around 719 μmol $g_{cat.}^{-1}$ $h^{-1}$. A

comparison is made between the pure methanol grade and the purity of methanol obtained by photoreduction of $CO_2$ to methanol (m/z= 32.83); Fig. 2.2.7(e) illustrates the large peak for methanol at 1.55 min retention time for both cases. The pure methanol grade is indicated by the red curve in this Fig. 2.2.7(e). Fig. 2.2.7 illustrates how Cu doping of $Bi_2S_3$/rGO beyond the optimal loading decreases the photoexciting capacity of $Bi_2S_3$/rGO and results in less methanol being generated. On the other hand, increased Cu loading increases the number of active sites on the catalyst surface, which is favourable to the methanol output.

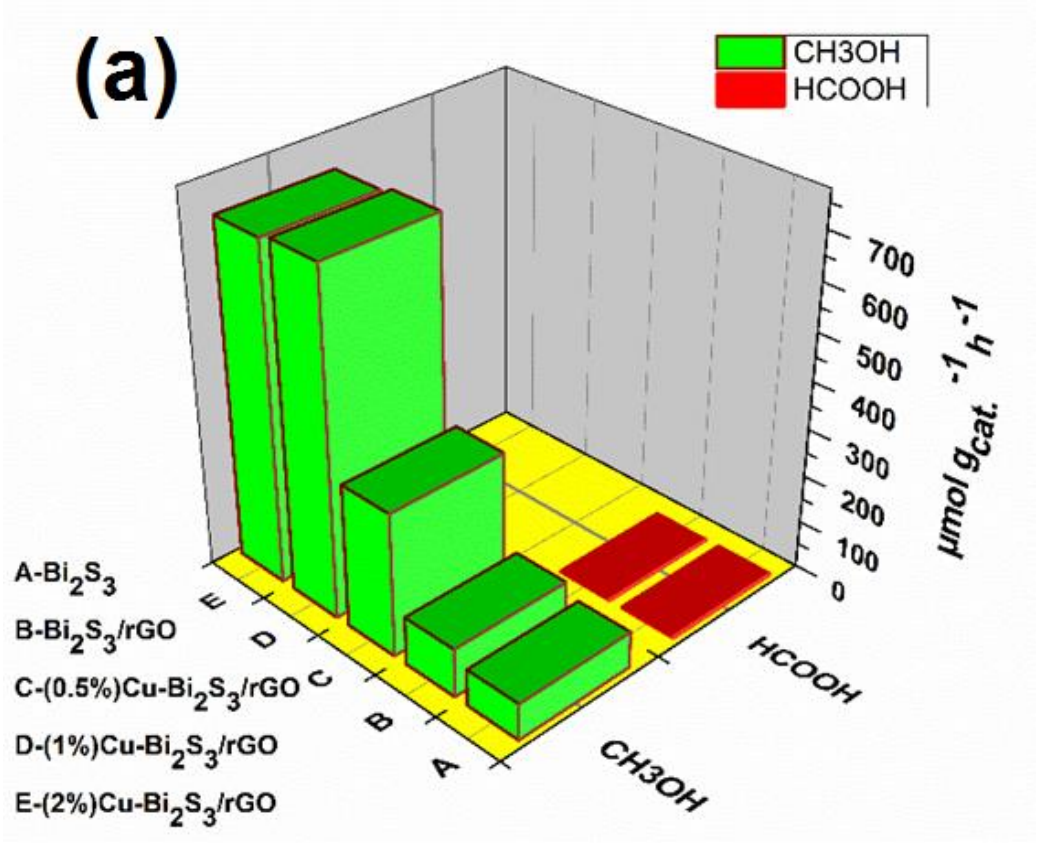


**Fig. 2.2.7: (a) Analysis of selectivity and yield of methanol production for different photocatalysts**

(b)

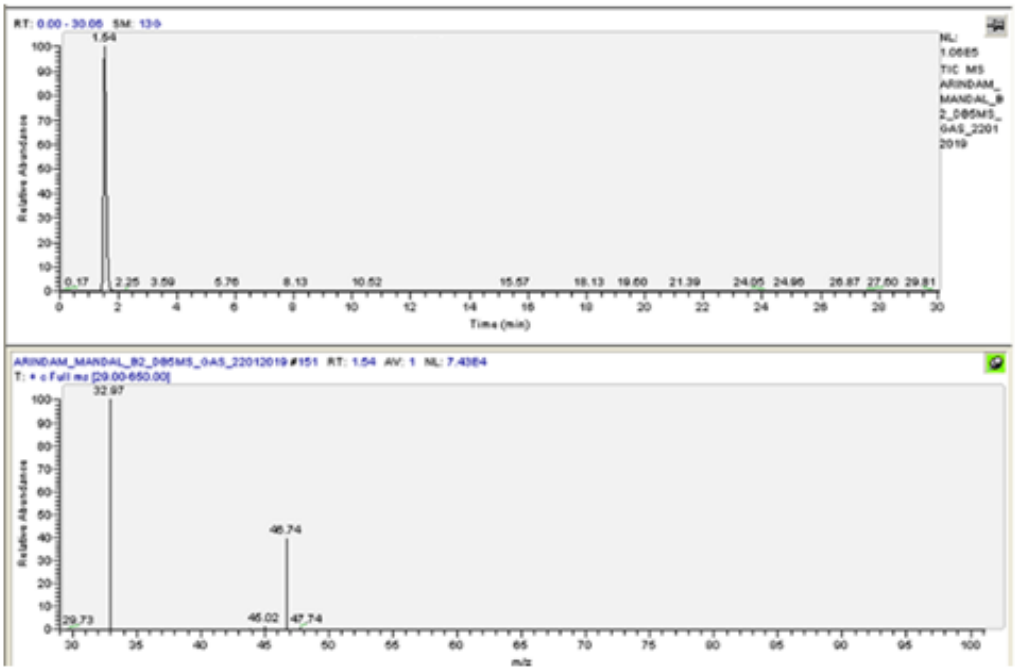


**Fig. 2.2.7: (b) GCMS analysis image of BSNC [$Bi_2S_3$ rod-shaped nanocapsules]**

(c)

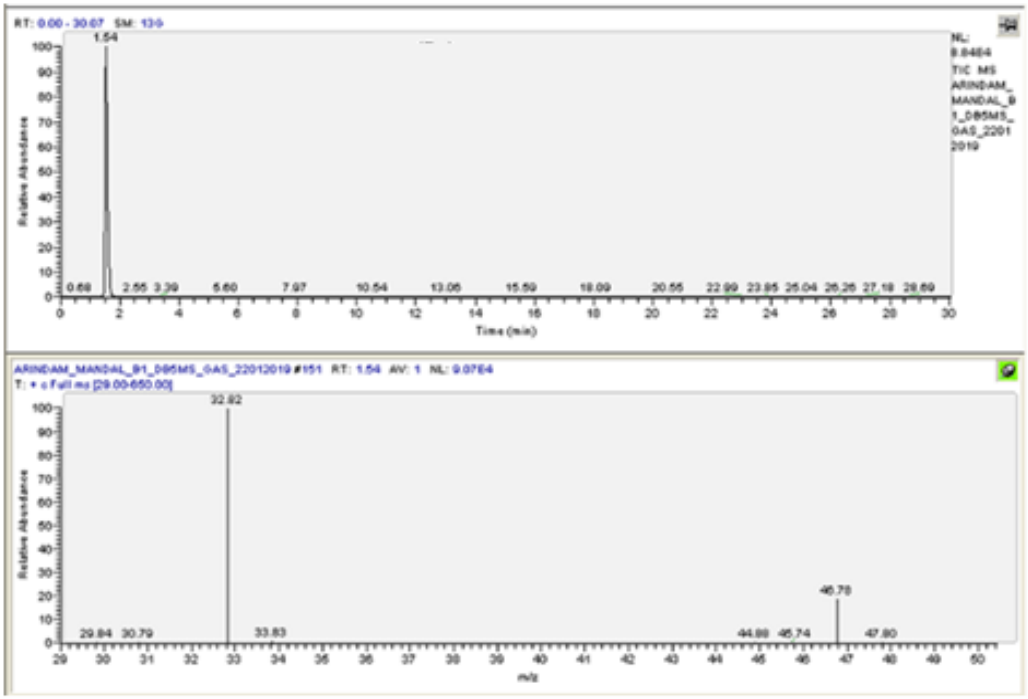


**Fig. 2.2.7: (c) GCMS analysis image of BSNC/rGO [$Bi_2S_3$/rGO]**

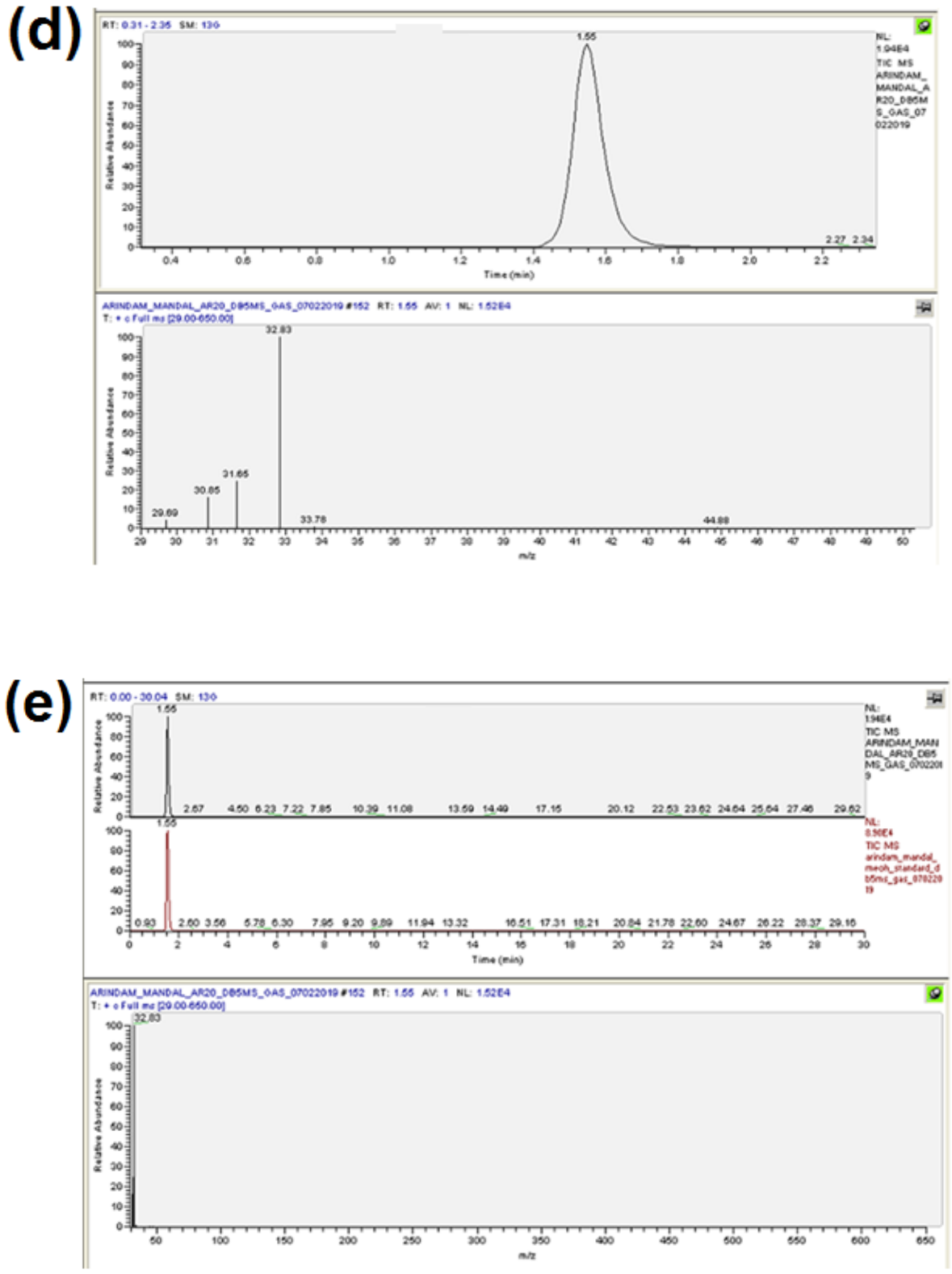


**Fig. 2.2.7: (d-e) GCMS analysis images of (1%) Cu-BSNC/rGO [(1 wt%)Cu doped $Bi_2S_3$/rGO]**

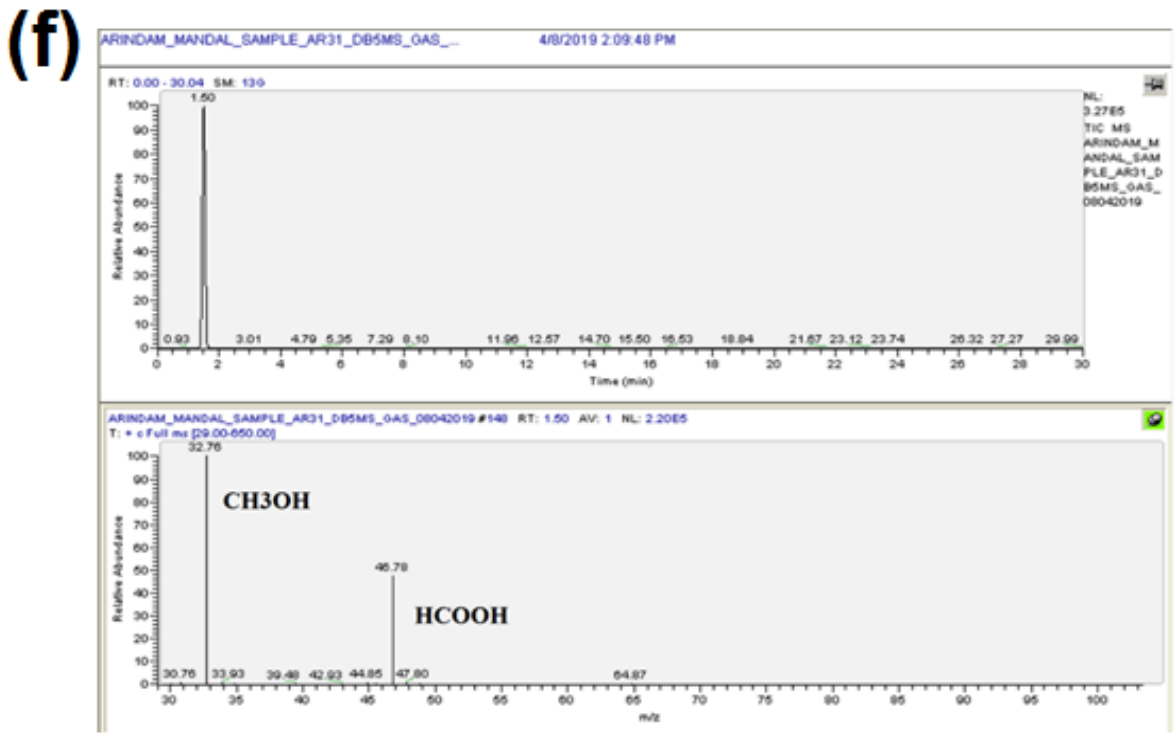


**Fig. 2.2.7: (f) GCMS analysis image of (1%) Cu-BSNC**

When employing a (1%) Cu-doped $Bi_2S_3$/rGO photocatalyst for $CO_2$ photoreduction, the rate of methanol production is significantly greater than the production values reported in the literature for various $Bi_2S_3$-based photocatalysts (see Table 2.2.2). (1%) Cu-doped $Bi_2S_3$/rGO photocatalyst produces the methanol production rateof 215.174 µmol $g_{cat.}^{-1}$ $h^{-1}$ at 420 nm. At 420 nm, the apparent quantum yield (AQY) [227] of 1.62% is found for a $Bi_2S_3$/rGO photocatalyst that is 1 percent Cu-doped. The limited methanol production rate (77.23 µmol $g_{cat.}^{-1}$ $h^{-1}$) is attributed to some flaws in the rod-shaped $Bi_2S_3$ nanocapsules. By capturing electrons from the $Bi_2S_3$ conduction band and reducing the charge recombination process, loading copper into $Bi_2S_3$ rod-shaped nanocapsules improves their photocatalytic performance. This increases the electron availability for $CO_2$ reduction and makes the CB potential of Cu-doped $Bi_2S_3$ rod-shaped nanocapsules/rGO more negative than the redox potential of methanol. Under illumination, the photoinduced electrons can reduce $CO_2$ into $CH_3OH$. As for $Bi_2S_3$ [BSNC], the comparable inaccuracy is 0.04%, whereas the percentage of area beneath the GCMS peak at retention time 1.54 min is 99.96% [Fig. 2.2.7(b)]. The equivalent error for $Bi_2S_3$/rGO [BSNC/rGO] is 0.03%. The percentage of area beneath the GCMS peak at retention time 1.54 min is 99.97% [Fig. 2.2.7(c)]. However, the percentage of

area under the GCMS peak at retention time 1.55 min for (1 wt%) Cu-doped $Bi_2S_3$/rGO [(1%) Cu-BSNC/rGO] is 100% [Fig. 2.2.7 (d) & (e)], which is perfectly matched with the pure sample, demonstrating 100% selectivity accomplishment. Fig. 2.2.7(f) shows the GCMS analysis image of (1%) Cu-BSNC.

### 2.2.3.5 Mechanism:

The activation of $CO_2$ on the catalyst surface to produce a surface-bound metastable radical anion ($\cdot CO_2^-$) is the first stage in photocatalysis. The reduction process then occurs by a sequence of sequential processes that include breaking C-O bonds and forming new C-H bonds, as well as transferring electrons, protons, and/or hydrogen radicals ($\cdot H$). Depending on how $CO_2$ binds to the catalyst surface, the creation of $CH_3OH$ may follow the formaldehyde formation pathway. According to the formaldehyde pathway, water, a medium with a high dielectric constant, favours the formation of HCOOH when the$\cdot CO_2^-$ and$\cdot H$ radicals recombine. Next, the HCOOH interacts with another$\cdot H$ to create a dihydroxymethyl radical ($\cdot CH(OH)_2$), which when another binds to it dehydrates.From H to HCHO. Further reduction of HCHO results in the formation of $CH_3OH$. The better capabilities of 1D $Bi_2S_3$ with doped Cu 2p in the photocatalytic reduction of $CO_2$ are further supported by comparing the experimental results with those from previous experiments [194,202,219–222]. When compared to the undoped $Bi_2S_3$ catalysts, Table 2.2.1 clearly illustrates how much better the transition metal doped $Bi_2S_3$ catalysts' catalytic performance is. In addition, the doped catalysts contribute to a higher yield of hydrocarbon compound selective synthesis. These findings are significantly better than those of the previous investigations. Along with the doping effect of the Cu 2p, the application of the 1D $Bi_2S_3$ rod-shaped nanocapsules enhanced the catalytic areas and catalytic active sites, which in turn raised the photocatalytic efficiency.

In this work, Cu acts as an electron trapping element to prevent the recombination of holes and electrons (as shown by PL spectra), and the quick transfer of excited electrons improves the separation of electrons and holes [219]. As a result, it is simple to transfer the photogenerated electron from the conduction band of the Cu-doped (1D) $Bi_2S_3$ nanocatalyst to the rGO nanosheets, which prevents electron-hole pair recombination and speeds up electron transport to the active catalytic sites for $CO_2$ photoreduction. The rGO is prone to adsorb $CO_2$ because of its vast surface area and numerous faulty spots [221].

$$Cu-doped\,\frac{(1D)Bi2S3}{rGO\ \overset{h\nu}{\rightarrow}}\,h^{+}(VB,Cu-doped(1D)Bi2S3)+e^{-}(rGO) \quad (2.2.3)$$

$$CO2\ +\ e^{-}\ \rightarrow\cdot CO2^{-}(ad) \quad (2.2.4)$$

$$H2O\ +h^{+}\ \rightarrow\cdot OH+H^{+} \quad (2.2.5)$$

$$H^{+}+e^{-}\ \rightarrow\cdot H \quad (2.2.6)$$

$$\cdot CO2^{-}(ad)+2H^{+}+e^{-}\ \rightarrow\ HCOOH \quad (2.2.7)$$

$$HCOOH+2H^{+}+2e^{-}\ \rightarrow\ HCHO\ +\ H2O \quad (2.2.8)$$

$$HCHO+H^{+}+e^{-}\ \rightarrow\ H2\cdot COH \quad (2.2.9)$$

$$H2\cdot COH+H^{+}+e^{-}\ \rightarrow\ CH3OH \quad (2.2.10)$$

---

$$CO2\ +\ 6H^{+}+6e^{-}\ \rightarrow\ CH3OH$$

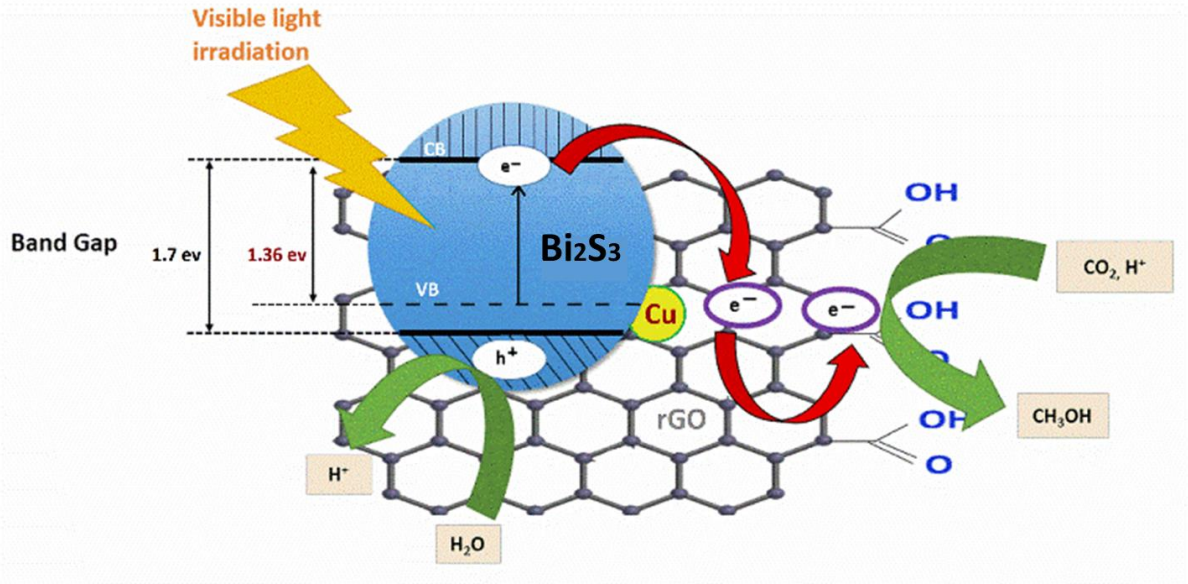


**Fig. 2.2.8: Schematic representation on mechanism of photocatalytic reduction of $CO_2$ into methanol using (1%) Cu-doped $Bi_2S_3$/rGO nanocatalysts under the visible light irradiation**

To achieve the selectivity of product synthesis, the photogenerated electrons on Cu-$Bi_2S_3$ are accumulated at the catalytic sites of rGO and reduce the adsorbed $CO_2$ into the methanol. Protons ($H^+$) are eventually produced by oxidizing the water molecules due to an

accumulation of photogenerated holes, as seen in Fig. 2.2.8. By interacting with 6 mol of photogenerated electrons, 1 mol of $CO_2$ and 6 mol of $H^+$ are reduced to 1 mol of methanol and 1.5 mol of oxygen. The many photo-catalytic methods for $CO_2$ reduction that have been documented in the literature to produce methanol are shown in Table 2.2.2.

**Table 2.2.2– Comparison of the yield & selectivity of methanol production for various photocatalysts with the performance of the present works**

| Photocatalyst | Reaction Medium | Products & Yields ($\mu mol\ g_{cat}^{-1}\ h^{-1}$) | Reference |
|---|---|---|---|
| $Bi_2S_3$-SAR | $CO_2$/Water | $CH_3OH$: 25.94 | 223 |
| $Bi_2S_3$ QD/$TiO_2$ | $CO_2$/isopropanol | $CH_3OH$: 1169.15 | 224 |
| | $CO_2$/Water | | |
| $Bi_2S_3$/CdS | $CO_2$/Water | $CH_3OH$: 122.6 | 225 |
| $Bi_2S_3$/$TiO_2$ | DMF/Water | $CH_3OH$: 44.92 | 226 |
| rGO–CuO | DMF/Water | $CH_3OH$: 51.167 | 227 |
| rGO–$Cu_2O$ | $CO_2$/Water | $CH_3OH$: 35.92 | 227 |
| $WS_2$@$Bi_2S_3$ | $CO_2$/Water | $CH_3OH$: 9.55 | 228 |
| $ZnFe_2O_4$/ | | $C_2H_5OH$: 6.95 | 229 |
| $TiO_2$ (1:1.5) | DMF/Water | $CH_3OH$: 95.89 | |
| rGO@CuZnO@$Fe_3O_4$ | | $CH_3OH$: 110.6 | 230 |
| Cu-(1D) $Bi_2S_3$/rGO | $CO_2$/Water | $CH_3OH$: 719.0 | This work |

## 2.3 Conclusion

The rGO-$Bi_2S_3$/CuO S-scheme heterojunction photocatalyst is prepared by hydrothermal method. The joint effects of rGO and CuO increased the photo-absorbance power of $Bi_2S_3$ nano-hollow flower in the visible range of the solar spectrum. The rGO-$Bi_2S_3$/CuO S-scheme heterojunction photocatalyst exhibits the photocatalytic $CO_2$ reduced products comprising methanol (423.52 μmol $g_{cat.}^{-1}$ $h^{-1}$) and formic acid (17.48 μmol $g_{cat.}^{-1}$ $h^{-1}$) and this photocatalyst also improves the selectivity of methanol to 98.6%. Additionally, the

absorption edge (652.4 nm) shifting to the visible spectrum, a promising band gap (1.75 eV) and the effective charge carrier separation may indicate that rGO and CuO create new photoinduced reactive zones in the interface layer for charge carriers to improve the photocatalytic activity.

Further to achieve 100% selectivity of specific product (methanol) Cu-doped (1D) $Bi_2S_3$ rod-shaped nanocapsules/rGO nanocomposites with variable (wt%) Cu concentration are made by hydrothermal method. The procedure involves converting GO to rGO and adding Cu to (1D) $Bi_2S_3$ rod-shaped nanocapsules at the same time. The combined impacts of Cu and rGO enhanced the spectral responsiveness of (1D) $Bi_2S_3$ nanocapsules to the visible portion of the solar spectrum, as demonstrated by UV-vis spectroscopy. Further evidence that both Cu doping and the presence of rGO lower the rate of electron hole pair recombination is shown by photoluminescence spectra. The best active photocatalyst for selective photoreduction of $CO_2$ to methanol is determined to be (1%) Cu-doped (1D) $Bi_2S_3$/rGO, which exhibits the lowest band gap (1.36 eV) and least rate of recombination among all the synthesized photocatalysts. The improved light absorption and efficient charge carrier separation may be indicators of the enhanced photocatalytic activity because of the loading of rGO and Cu, which is crucial to the doping process in order to create new reactive sites for charge carriers within the band gap. The increased $CO_2$ photoreduction caused by the band gap tuning achieved by Cu doping in rGO leads to the formation of $CO_2$ trapping sites. The maximum yield of selective photoreduction of $CO_2$ to methanol at around 719 μmol $g_{cat.}^{-1}$ $h^{-1}$ is achieved through increased hybridization and proper adjustment of the Cu-doped photocatalyst, as demonstrated in this work. The purity and selectivity of the product are further demonstrated by the GCMS measurement of the photoreduction of $CO_2$ to methanol.

# Chapter 3

## *Synthesis, characterization and photocatalytic performance study of Cu-doped 2D-$Bi_2MoO_6$ nanoribbon/rGO photocatalyst for selective photo-reduction of $CO_2$ to ethanol.*

**Highlights:**

- A novel hydrothermally-produced two-dimensional (2D) $Bi_2MoO_6$nanoribbon/rGO composite doped with varying weight percentages of copper (Cu) (1, 2, 3, and 4%), is synthesized.

- The photocatalyst shows enhanced absorption edge of visible light at 730 nm, the smallest band gap of 2.02 eV, and the lowest rate of electron-hole pair recombination

- The optimum 2 weight % Cu doped two-dimensional (2D) $Bi_2MoO_6$nanoribbon/rGO photocatalyst offers an enhanced yield of selective ethanol production of 133.10 µmol $g_{cat.}^{-1}$ $h^{-1}$with 100% selectivity and 0.337% apparent quantum yield.

### 3.1. Introduction

Recently, Bi-based semiconductor photocatalysts being rich in earth elements have been considered as promising photocatlytic composites, in which the Bi 6s orbital has capacity to reduce the band gap energy and mobilise of photogenerated charge carriers. A variety of Bi-based semiconductors, such as $BiVO_4$, $Bi_2S_3$, $Bi_2O_3$, etc., have been studied exclusively for photocatalytic applications [231-235]. Among them, a typical Aurivillius oxide-Bismuth Molybdate ($Bi_2MoO_6$) as an economical, non-toxic, corrosion-resistant, and efficiently stable n-type semiconductor possesses a unique structure and also contains $(Bi_2O_2)^{2+}$ and $(MoO_4)^{2-}$-layers with O atoms bridging between the layers, which facilitates its wide application as photocatalysts, supercapacitors, energy storage devices, and degradation of organic contaminants [235-238]. 0D/1D/2D $Bi_2MoO_6$ photocatalyst with visible light absorption capacity, good electron conductivity, abundant adsorption sites, and a suitable band gap (2.4-2.8 eV) also has the capability for the reduction of $CO_2$ photocatalytically to the renewable fuels like formic acid, methane, ethane, methanol, ethanol ($C_2H_5OH$), etc. However, the slow migration speed and fast recombination rate of photoinduced electron/hole pairs and the insufficient reduction potential of CB (-0.28 V vs. NHE) for pristine $Bi_2MoO_6$ under the illumination of the visible light spectrum restrict its widespread application. Additionally, in addition to the high rate of recombination of photogenerated charge carriers, unstable interactions between $CO_2$ molecules and the 0D/1D $Bi_2MoO_6$ surface result in less use of reactive adsorbed species and ineffective displacement of reaction products/inactive intermediates, which generally reduces the photocatalytic $CO_2$ conversion rate and the selectivity of the $CO_2$ photo-reduced product of the $Bi_2MoO_6$ photocatalyst[239-241].

To overcome this shortcoming for improving the photocatalytic performance of semiconductor materials, several strategies have been incorporated, such as band structure modification, morphology modification, and defect engineering. The photocatalytic properties of $Bi_2MoO_6$ strongly depend on its structure and morphology [242-245]. According to the review, $Bi_2MoO_6$ can take on several forms, including hollow spheres, nanoparticles, nanoplates, nanosheets, nanotubes, and nanospheres. Among them, two-dimensional (2D) $Bi_2MoO_6$ [2D-$Bi_2MoO_6$] nanosheets provide a more specific surface area, which generates more surface active sites for $CO_2$ adsorption and activation [245-249]. 2D-$Bi_2MoO_6$ nanosheets also contain exposed atoms on the surface to generate suitable vacancies or defects, which can trap electrons and expedite the photoreduction of $CO_2$ to renewable fuels. 2D-$Bi_2MoO_6$ nanosheets also have a thin layer, which actually reduces the migration

distance of photo-generated carriers. Thus, two-dimensional (2D) structures of $Bi_2MoO_6$ increase the performance of photocatalytic $CO_2$ reduction compared with other structures like 0D or 1D $Bi_2MoO_6$. Herein, novel synthesised 2D-$Bi_2MoO_6$nanoribbon-like structures are considered the primary photocatalyst for photoreduction of $CO_2$ in this work[250-253].

Due to its exceptional physicochemical features, reduced graphene oxide (rGO) or graphene, is one of the carbon-based nanomaterials with a unique two-dimensional $sp^2$-hybridized carbon structure. As such, it has drawn a lot of attention in the photocatalytic sector. Graphene or reduced graphene oxide (rGO) nanosheets in particular have great thermal or chemical stabilities, remarkable mechanical and structural flexibility, a huge surface area, and high electrical conductivity [254–256]. According to scientific reports, metal oxide composites based on graphene or reduced graphene oxide could make highly effective photocatalysts. This is because metal oxide and graphene have exceptional synergistic effects that make them suitable for a wide range of applications, including photocatalysis. In addition to providing a platform for the growth of 2D-$Bi_2MoO_6$ nanosheets, rGO-based semiconductor photocatalysts also functioned as an efficient electron acceptor, separating photo-excited electrons and holes at the interface of the junction and facilitating the adsorption of a certain amount of chemical molecules on the surface of the photocatalyst [256-260].

In this study, we have successfully synthesised 2D-$Bi_2MoO_6$nanoribbon-like structures on rGO sheet by adopting the hydrothermally treating techniques. Using the photocatalytic $CO_2$ reduction method, the photocatalytic performance investigation of 2D-$Bi_2MoO_6$nanoribbons/rGO composites have been carried out. The combined action of the 2D-$Bi_2MoO_6$nanoribbons and rGO sheet is likely the reason why the 2D-$Bi_2MoO_6$nanoribbons–rGO composites show stronger photocatalytic activity than the bare 2D-$Bi_2MoO_6$nanoribbons. However, the photoreduced product's improved yield and selectivity have not yet been attained.

In reality, a number of factors, including photon energy, photoinduced charges, the photocatalyst's tunable CB and VB edge, its active zones, the reactants' and intermediates' increased adsorption/ absorption capacity, and the product's desorption from the catalyst surface, influence how $CO_2$ can be selectively reduced by photocatalysis to a particular hydrocarbon product. Here, selectivity in the photocatalytic reduction of $CO_2$ is enhanced by the presence of photogenerated charge density, which is mainly provided by surface reactive sites with improved reactant adsorption and intermediate product stability. The degree of $CO_2$

adsorption in this photocatalytic reduction process is explained by the relative concentrations of the basic and acidic surface sites [261-262]. The photocatalytic activity of reduced graphene oxide (rGO) based composites is significantly increased by further doping with noble metals as Cu [263], Mo [264], Ag [265], or Zn [266]. By creating potent active adsorption sites that speed up the selective photo-reduction of $CO_2$, transition metal Cu is added to metal oxide photocatalysts to boost their capacity to capture $CO_2$. Usually, Cu being the transition metal can generate adequate binding sites to increase the adsorption of $CO_2$ and accelerate the performance of the photocatalyst for photoreduction of $CO_2$, unlike other metal oxide sites. For this reason, a great deal of research is being done on inexpensive copper (Cu)-based semiconductors, such as metal Cu, which is widely distributed throughout the crust of Earth and can be thought of as the most favourable options for selective photocatalytic reduction of $CO_2$ into CO, formic acid, methanol, methane, ethanol, etc. Since the difference in reduction potential of $Cu^{2+}$ is greater than the photocatalysts' conduction band edge, there is a chance that copper ions may trap electrons, which is why this occurs. The trapped $Cu^{2+}$ electrons of photocatalyst can then donate their electrons to the $CO_2$ reaction with the reductant, achieving an enhanced yield through selective production of the renewable fuel [267-271].

The specific **objectives** of this chapter are enlisted below:

- **i.** Design and synthesis of visible light responsive2D-$Bi_2MoO_6$nanoribbon photocatalysts by incorporating fixed rGO concentration for enhancing the yield of $CO_2$ reduced products.
- **ii.** Modification of 2D-$Bi_2MoO_6$nanoribbon/rGO photocatalysts by different percentage of Cu doping (1%, 2%, 3%, and 4%) to get optimal Cu doping for achieving the highest yield ofspecific product selective $CO_2$ reduction.
- **iii.** Characterization of all synthesized photocatalysts by XRD, SEM, TEM, EDX, FTIR, EIS, BET, and XPS.
- **iv.** Photocatalytic performance study of synthesized doped and undoped nano-composite photocatalysts.
- **v.** Prediction of mechanism of $CO_2$ photo-reduction.

The major research problem is addressed in this chapter; the problem definition is as follows:

❖ **Problem definition:**

***Synthesis, characterization and photocatalytic performance study of Cu-doped 2D-$Bi_2MoO_6$nanoribbon/rGO photocatalyst for selective photo-reduction of $CO_2$ to ethanol.***

## 3.2. Experimental section

### 3.2.1. Materials:

The chemicals including bismuth nitrate pentahydrate ($Bi(NO_3)_3.5H_2O$), sodium molybdate dihydrate ($Na_2MoO_4.2H_2O$), sodium bicarbonate ($NaHCO_3$), copper nitrate trihydrate ($Cu(NO_3)_2.3H_2O$), deionised water, and other compounds have been acquired from Sigma-Aldrich. Additional chemicals (reagent grade) acquired from Merck include ethylene glycol ($C_2H_6O_2$), graphite flakes, potassium permanganate ($KMnO_4$), sulphuric acid ($H_2SO_4$), hydrogen peroxide ($H_2O_2$), phosphoric acid ($H_3PO_4$), sodium hydroxide (NaOH), hydrochloric acid, and ethanol.All purchased chemicals have been utilised without any further purification.

### 3.2.2. Synthesis of Cu doped 2D-$Bi_2MoO_6$/rGO

#### 3.2.2.1. Synthesis of pristine 2D-$Bi_2MoO_6$:

In this synthesis procedure, 2.3 g of $Bi(NO_3)_3.5H_2O$ and 0.73 g of $Na_2MoO_4.2H_2O$ are mixed in 25 ml of ethylene glycol separately, under continuously stirring condition for 40 minutes. After that, the complete dissolved of $Na_2MoO_4.2H_2O$ in ethylene glycol, the mixture is poured drop wisely in the mixture of $Bi(NO_3)_3.5H_2O$ and ethylene glycol under stirring for a further 60 minutes and 20 ml deionised water is also added during stirring. The pH of the mixture solution is controlled to 10 by adding 2M NaOH solution drop wisely. Following that, the entire mixture solution is transferred into a stainless steel autoclave (Teflon lined stainless steel – 100ml), and kept in a muffle furnace for hydrothermal heating at 180°C for 20 h. After cooling down the Teflon lined stainless steel autoclave, the entire synthesised yellowish solid composites are collected and performed centrifugation operation, and then the separated yellowish precipitate is washed several times with ethanol and double-distilled water. After washing, the precipitate is dried in a hot air oven under vacuum at 65°C for 24 h. After drying, pristine 2D-$Bi_2MoO_6$nanoribbon (BMONR) like structurecomposites have been discovered [239,244,246,249].

### 3.2.2.2. Synthesis of 2D-$Bi_2MoO_6$/rGO:

Graphene oxides (GO) [262] is synthesised following the modified Hummers method. In this typical method, 0.05 g weight of the previously synthesised GO samples are uniformly mixed in deionised water by ultrasonication of 90 minutes for exfoliating the GO sheets. Separately prepared solutions of 2.3 g of $Bi(NO_3)_3.5H_2O$ and 0.73 g of $Na_2MoO_4.2H_2O$ in 25 ml of ethylene glycol are mixed by aforementioned method and then the entire mixture is added into ultrasonicated GO solution for continuously stirring of another 60 minutes. Then the pH of the whole stirring solution is adjusted to 10 using a 2M NaOH solution. Then the aforementioned stirring solution is transferred in a stainless steel autoclave (Teflon lined stainless steel – 100ml) for hydrothermal heating in the muffle furnace at 180°C for 20 h. After cooling down the Teflon lined stainless steel autoclave, the entire synthesised composites is turned into greenish composites which are collected from autoclave and centrifugation operation is performed for separation of greenish composite and then the separated greenish precipitate is washed with ethanol and double-distilled water. After several times washing, the precipitate is dried in a hot air oven under vacuum at 65°C for 24 h. Finally after drying, 2D-$Bi_2MoO_6$nanoribbon/rGO (BMONR/G) composites have been discovered for photocatalytic $CO_2$ reduction study [256].

### 3.2.2.3. Synthesis of Cu doped 2D-$Bi_2MoO_6$:

In this work copper nitrate trihydrate [$Cu(NO_3)_2 \cdot 3H_2O$] is used as precursor of Cu dopant. In a typical experiment, 2D-$Bi_2MoO_6$ and $Cu(NO_3)_2 \cdot 3H_2O$ are dissolved into deionized water, respectively. The dissolved solutions are mixed according to synthesize 1, 2 and 3 wt% of Cu doped 2D-$Bi_2MoO_6$ nanomaterials. Here 1, 2 and 3 wt% are the weight ratios of Cu/2D-$Bi_2MoO_6$, respectively. The pH value of the acquired solution is adjusted to 10 by adding sodium solution (2M NaOH). The prepared solution is put in an autoclave (Teflon lined stainless steel – 100ml) and transferred into furnace for hydrothermal heating at 180°C for 20 h. When the temperature of the Teflon lined stainless steel autoclave reached to the room temperature, the formed product is collected and washed several times with ethanol and deionized water repeatedly and finally dried at 80°C for 14 h to acquire Cu doped 2D-$Bi_2MoO_6$ (Cu-BMONR) photocatalysts

### 3.2.2.4. Synthesis of Cu doped 2D-$Bi_2MoO_6$nanoribbon/rGO:

In this present work the doping of Cu with different percentages is performed in a fixed weight ratio of 2D-$Bi_2MoO_6$nanoribbon/rGO (1:0.016) composites. To study the performance

of photocatalytic reduction of $CO_2$ to $C_2$-based product based on selectivity and yield of selective product, Cu doped 2D-$Bi_2MoO_6$nanoribbon/rGO composites (Cu-BMONR/G) aresynthesised with different percentages of Cu loading of 1, 2, 3 and 4 wt%, respectively. In this work as the source of Cu different weight of $Cu(NO_3)_2.5H_2O$ are dissolved in BMONR/G solution separately to get 1, 2, 3 and 4 wt% Cu doping, respectively.The pH of the mixed solution is maintained to 10 using a 2M NaOH solution. After 1 h stirring the mixture is poured in an autoclave (Teflon lined stainless steel – 100ml) and the autoclave is transferred into a furnace for hydrothermal heating at 180°C for 20 h.When the temperature of the Teflon lined stainless steel autoclave reached to the room temperature, the formed product is collected, centrifuged and washed several times with ethanol and deionized water repeatedly and finally dried at 80°C for 14 h in a hot chamber to acquire Cu doped 2D-$Bi_2MoO_6$nanoribbon/rGO (Cu-BMONR/G) photocatalysts. The above mentioned synthesis process is showed in Fig. 3.1.

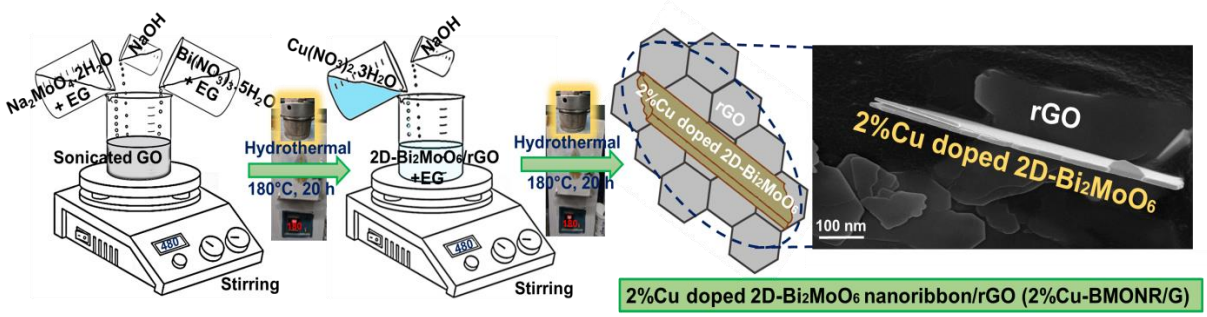


**Fig. 3.1: Schematic representation of synthesis process of 2%Cu doped 2D-$Bi_2MoO_6$nanoribbon/rGO (2%Cu-BMONR/G) photocatalyst**

### 3.2.3. Photocatalytic activity evaluation:

The photocatalytic activity of the produced photocatalysts BMONR, BMONR/G, Cu-BMONR, and Cu-BMONR/G is examined using a 100-watt Xenon lamp of a solar simulator (94011A, Manual shutter, Newport Oriel LCS-100), equipped with an AM1.5G air mass filter, as the source of visible light source, where the light intensity is 100 mW/cm$^2$ and the light area is 16.82 cm$^2$. To evaluate the photocatalytic activity, 0.025 g of every photocatalyst is separately used in a 100-mL hollow-quartz tube reactor. Prior to light (full spectrum) irradiation, $CO_2$ gas (99.9% pure) with a low flow rate is supplied into the degassed reactor to reach 1 atm pressure. The 80 ml of ultrapure water consisting of 0.5 M $NaHCO_3$ acts as hole scavengers inside the quartz reactor to make a saturated $CO_2$ absorbed solution and to achieve

maximum $CO_2$ adsorption on the photocatalyst's active sites [225]. The entire process is carried out in the dark for 60 minutes under magnetic stirring conditions to eliminate all oxygen dissolved in the saturated solution. Following that, 0.025 g of photocatalysts are added to the aforesaid saturated solution, and the photocatalytic reaction is implemented for 8 h at 20°C, under the full band light irradiation of the prescribed 100-watt Xenon lamp with constant stirring speed, which is manifested by Fig. 3.2. UV-protector arrangement is also used to allow mainly visible light to enter the photocatalytic reactor.

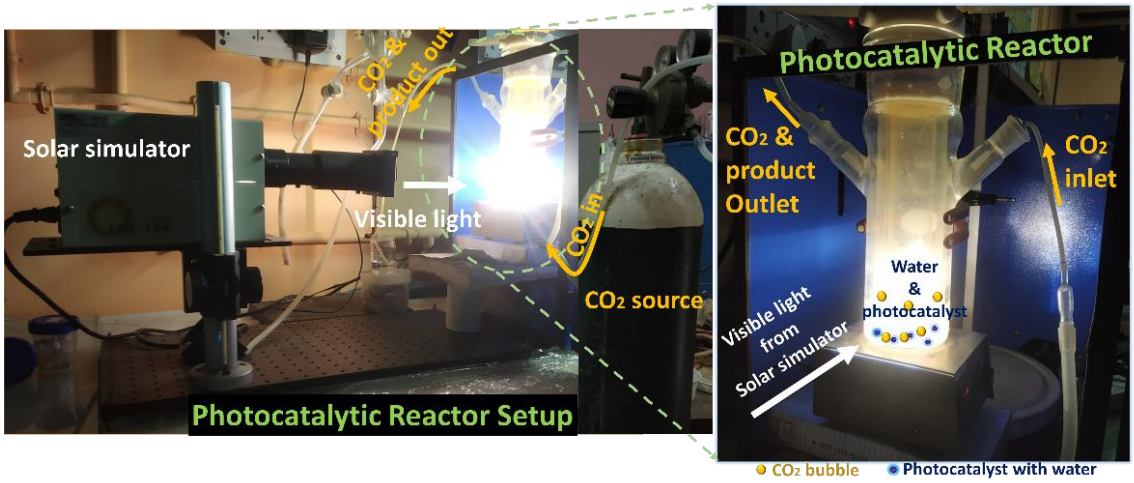


**Fig. 3.2: Schematic representation of the photocatalytic reactor setup for performance activity study of 2%Cu doped 2D-$Bi_2MoO_6$nanoribbon/rGO (2%Cu-BMONR/G) photocatalyst**

After 8 h illumination of light the photocatalytic $CO_2$-reduced products are collected from the reactor solution by a thin pipe connected to the syringe, and the concentration of each product is determined by gas chromatography equipment: Agilent-7890A system and GC-FID and GC-TCD, with helium as the carrier gas. Blank reactions are carried out to ensure that the products are generated only as a result of photocatalytic $CO_2$ reduction. In the absence of a photocatalyst, the whole experiment is carried out under the same operating circumstances. Secondly, the entire experiment is carried out in complete darkness in the presence of a photocatalyst under identical working circumstances. Thirdly, the blank experiment is performed under the illumination of a Xenon lamp and the presence of a photocatalyst in the photocatalytic quartz-reactor without purging $CO_2$ gas. The pure grades of ethanol and methanol are also utilised for analysis to ensure the quality of the $CO_2$-reduced product. The apparent quantum yield (AQY) has been measured under the irradiation of single band 420 nm lights by using 420 nm band pass filter. The photocatalyst solution is irradiated by a 100

Watt Xenon lamp with a 420 nm band-pass filter for 4 h. To calculate the apparent quantum yield (AQY) of the product evolution, the following equation is used [271,272].

$$\text{AQY} = \frac{\text{Number of reacted electrons}}{\text{Number of incident photons}} \times 100 \qquad (3.1)$$

$$= \frac{\text{Number of evolved ethanol (C2H5OH) molecules} \times 12}{\text{Number of incident photons}} \times 100\%$$

### 3.3. Results and discussion

#### 3.3.1 Morphology, Structure, Crystal plane, Composition analysis:

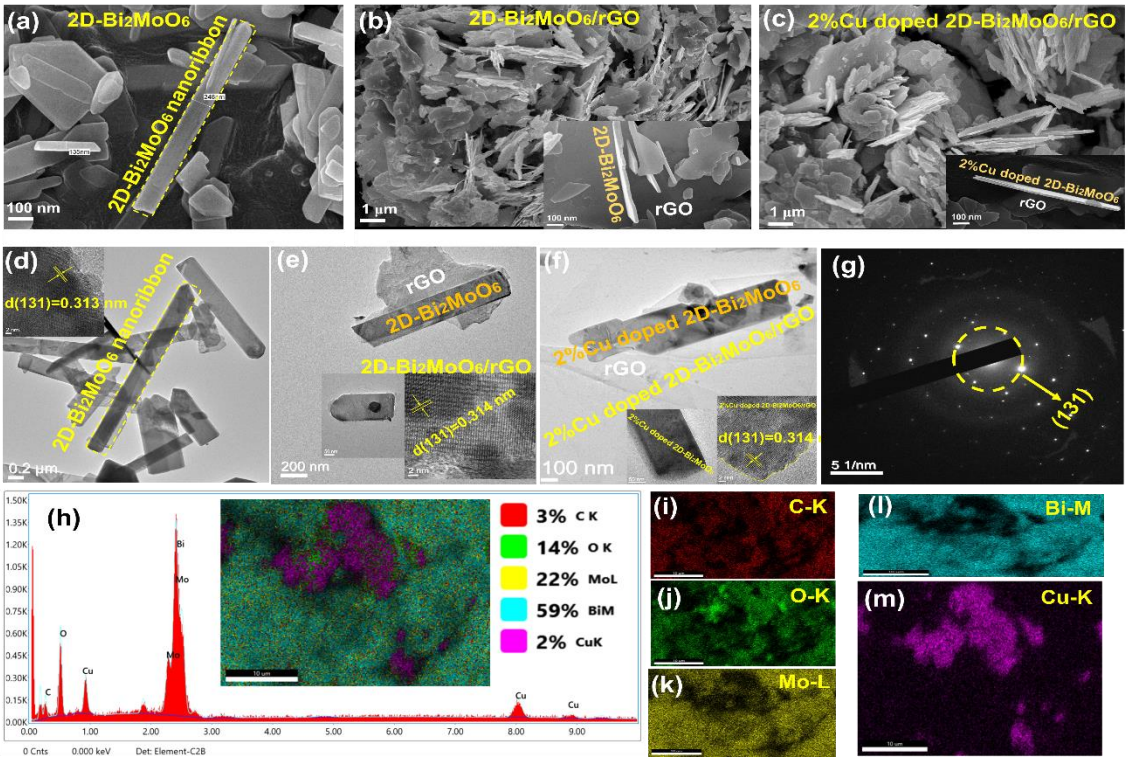


**Fig. 3.3: SEM image of (a) 2D-$Bi_2MoO_6$nanoribbon (BMONR), (b) 2D-$Bi_2MoO_6$nanoribbon/rGO (BMONR/G) with a magnified image in the inset and (c) 2%Cu doped 2D-$Bi_2MoO_6$nanoribbon/rGO composites (2%Cu-BMONR/G) with a magnified image in the inset. TEM image of (d) 2D-$Bi_2MoO_6$nanoribbon (BMONR), (e) 2D-$Bi_2MoO_6$nanoribbon/rGO (BMONR/G), and (f) 2%Cu doped 2D-$Bi_2MoO_6$nanoribbon/rGO composites (2%Cu-BMONR/G) with a magnified image in the inset. (g) SAED patterns of 2%Cu doped 2D-$Bi_2MoO_6$nanoribbon/rGO composites (2%Cu-BMONR/G).(h) EDX spectrum and (i-m)corresponding EDX elemental mapping of 2%Cu doped 2D-$Bi_2MoO_6$nanoribbon/rGO composites (2%Cu-BMONR/G)**

The scanning electron microscopic (SEM) and transmission electron microscopic (TEM) analysis have been conducted to analysis the morphology and nanostructure composition of as-prepared $Bi_2MoO_6$ (BMONR) composites. As shown in Fig. 3.3(a-c), the synthesized $Bi_2MoO_6$ has a two dimensional (2D) long nanoribbon like morphology and Cu doping and rGO incorporation however help 2D-$Bi_2MoO_6$ long nanoribbons to form uniform vertical or slanting arrays on the surface of rGO sheets, which is responsible for increasing the contact area or the exposed surface active zones to enhance the carbon dioxide adsorption.The long nanoribbon shaped structure of 2D-$Bi_2MoO_6$ with an average length of 200 nm –1μm and a width of 100-270 nm with the thickness of approximately 40-60 nm is clearly seen in the Fig. 3.3(a & d) and such thin 2D structure can also act as a medium for rapid mobility of charge carriers [245,246]. In Fig. 3.3(b), the SEM image shows that the 2D-$Bi_2MoO_6$nanoribbons (BMONR) are embedded in the rGO sheets, which is also clearly visible in the TEM image of Fig. 3.3(e). In Fig. 3.3(c), the SEM image also shows the enhanced contact between the 2%Cu doped 2D-$Bi_2MoO_6$nanoribbons (2%Cu-BMONR) and the crumpled rGO sheets, which is also perfectly seen in the TEM of Fig. 3.3(f). The inset TEM image of Fig. 3.3(d) shows the lattice fringe spacing ($d_{spacing}$) of 0.313 nm assigned to the (131) plane of the orthorhombic phase of 2D-$Bi_2MoO_6$ (BMONR), which is also matched with the XRD analysis (Table-3.1). The inset TEM image of Fig. 3.3(e & f) also shows that the lattice fringe spacing ($d_{spacing}$) is increased to 0.314 nm, assigning to the (131) plane of $Bi_2MoO_6$ due to successfully rGO loading and Cu doping, respectively, which can provide better charge separation, efficient electron transfer within the 2%Cu-BMONR/G structure compared with BMONR and BMONR/G; this enhances the selective photocatalytic reduction of $CO_2$ to ethanol [224,228,267]. In Fig. 3.3(g), the SAED image confirms the single crystallinity (131) of the Cu doped 2D-$Bi_2MoO_6$ in 2%Cu-BMONR/G composites. In Fig. 3.3(h), EDX image, showing the elemental analysis of 2%Cu doped 2D-$Bi_2MoO_6$nanoribbon/rGO (2%Cu-BMONR/G) composites, confirms the successful doping of 2%Cu and rGO loading in BMONR composite. In Fig. 3.3(i-m) the corresponding EDX elemental mapping of 2%Cu doped 2D-$Bi_2MoO_6$nanoribbon/rGO composites (2%Cu-BMONR/G) also confirm the presence and uniform distribution of C, O, Mo, Bi, and Cu element, respectively.

### 3.3.1.1 XRD analysis:

Fig. 3.4(a) shows the X-ray diffraction pattern (XRD) of all the as prepared samples. The XRD analysis of rGO, as shown in Fig. 3.4(a), exhibits two distinct peaks in the vicinity of 2θ values of 24.17° and 42.58°. The peak located at approximately 24.17° corresponds to the

(002) crystal plane of rGO. In the case of $Bi_2MoO_6$ (BMONR), the XRD analysis exhibits several distinct peaks at 2θ values of 28.451°, 32.757°, 33.313°, 36.227°, 46.890°, 47.323°, 55.674°, 56.438° and 58.631° which corresponded to the (131), (200), (060), (151), (202), (260), (331), (191) and (262) crystal planes, respectively, of orthorhombic $Bi_2MoO_6$ as per the standard card (JCPDS No.76-2388) [237,256,266].

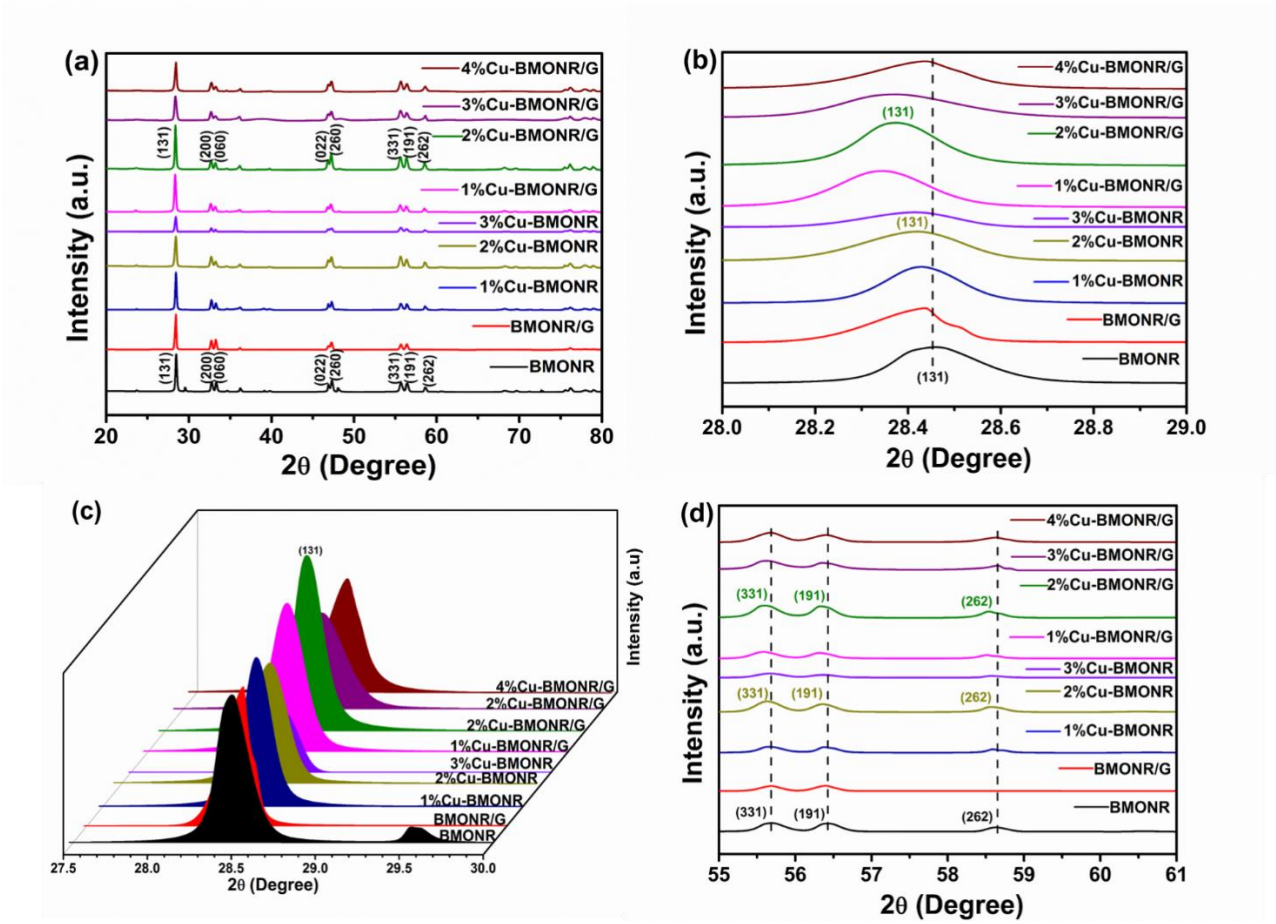


**Fig. 3.4: (a) XRD patterns of 2D-$Bi_2MoO_6$nanoribbon (BMONR), 2D-$Bi_2MoO_6$nanoribbon/rGO (BMONR/G), (1%, 2%, 3%)Cu doped 2D-$Bi_2MoO_6$nanoribbon (1%, 2%, 3%Cu-BMONR) and (1%, 2%, 3%, 4%)Cu doped 2D-$Bi_2MoO_6$nanoribbon/rGO (1%, 2%, 3%, 4%Cu-BMONR/G). (b) XRD peak shifts corresponding to the crystal plane (131) of all synthesised composites. (c) XRD peak intensity enhancement corresponding to the crystal plane (131) of all synthesised composites. (d) XRD peak shifts corresponding to the crystal plane (331), (191), and (262), respectively of all synthesised composites**

The XRD analysis of the 2D-$Bi_2MoO_6$nanoribbon/rGO composite exhibits the characteristic peaks same as of 2D-$Bi_2MoO_6$ and rGO with low intensity because during synthesis very less

amount of GO (1.67% of total weight of $Bi_2MoO_6$) is taken for the hydrothermal treatment. Due to 2 wt% Cu doping in 2D-$Bi_2MoO_6$ composite the XRD analysis of the synthesised 2%Cu-doped 2D-$Bi_2MoO_6$ composite exhibits the characteristic peaks same as the characteristic peaks of $Bi_2MoO_6$ with slightly decreased values of 2θ, which manifest that the Cu is successfully doped in 2D-$Bi_2MoO_6$ composite. In Fig. 3.4, the XRD diffraction pattern of the 2% Cu-doped 2D-$Bi_2MoO_6$nanoribbon/rGO (2%Cu-BMONR/G) composite exhibits several peaks at 2θ values of 28.375°, 32.697°, 33.223°, 36.158°, 46.825°, 47.238°, 55.588°,56.340° and 58.535° corresponding to the (131), (200), (060), (151), (202), (260), (331), (191) and (262) crystal planes, which manifests that due to successfully doping of 2wt% Cu in 2D-$Bi_2MoO_6$/rGO composite the characteristic XRD diffraction peaks of 2D-$Bi_2MoO_6$/rGO (BMONR/G) and 2%Cu-doped 2D-$Bi_2MoO_6$ (2%Cu-BMONR) composite are slightly shifted again towards lower values of 2θ in 2%Cu-doped 2D-$Bi_2MoO_6$/rGO composite. Thus incorporation of Cu and rGO in 2D-$Bi_2MoO_6$ does not change the structure of orthorhombic $Bi_2MoO_6$. In Fig. 3.4(b & d) the angle of 2θ of 2%Cu doped 2D-$Bi_2MoO_6$/rGO corresponding to the (131), (331), (191) and (262) crystal planes decreases by increasing the corresponding interplanar spacing. Fig. 3.4(c) also shows the increased peak intensity of (131) crystal plane which indicates the higher degree of crystallinity of 2% Cu doped 2D-$Bi_2MoO_6$/rGO composite. This happens due to the increment in Cu doping percentage (2 wt%) with the termination of hydroxyl groups (-OH), which promotes greater interlayer spacing. The characteristic diffraction peaks of Cu and its oxide derivative and no other impurities are not observed in 2%Cu-doped 2D-$Bi_2MoO_6$/rGO (2%Cu-BMONR/G) composite due to the low wt% of Cu doping.

Using XRD data of all the notable peaks, the Debye Scherrer equation [269] (3.2) has been used to calculate the crystallite size (D) of the synthesised composites, which are shown in Table 3.1. The average crystallite size of 2%Cu-BMONR/G is 31.68 nm.

$$D = \frac{k\lambda}{\beta \cos\theta} \quad (3.2)$$

where θ is the Bragg's diffraction angle, D is the average crystallite size, k= 0.9 is the shape factor, and λ is the X-ray radiation wavelength (1.5406 Å). On the other hand, crystalline size has a different influence on line widening than strain and defects do. Equation (3.3) is used to determine the strain (ε) caused in the synthesised powders [223,231,243].

$$\varepsilon = \frac{\beta}{4\ tan\theta} \quad (3.3)$$

**Table 3.1: Crystal size (D), Strain and Crystal spacing [$d_{(131)}$] of the synthesised composites**

| Photocatalysts | Crystal size (nm) | Strain | Crystal spacing [$d_{(131)}$] nm |
|---|---|---|---|
| BMONR | 38.05 | 0.065450 | 0.313 |
| 2D-BMONR/G | 40.69 | 0.060976 | 0.314 |
| 1%Cu doped BMONR | 35.54 | 0.070158 | 0.314 |
| 2%Cu doped BMONR | 35.18 | 0.068250 | 0.314 |
| 3%Cu doped BMONR | 39.27 | 0.059102 | 0.314 |
| 1%Cu doped BMONR/G | 33.38 | 0.072641 | 0.314 |
| 2%Cu doped BMONR/G | 31.68 | 0.074296 | 0.314 |
| 3%Cu doped BMONR/G | 29.40 | 0.082981 | 0.314 |
| 4%Cu doped BMONR/G | 32.14 | 0.073069 | 0.314 |

### 3.3.1.2 XPS analysis:

The 2%Cu doped BMONR/G (2%Cu-BMONR/G) composite's surface composition and elemental chemical states have been examined using X-ray photoelectron spectroscopy (XPS). Fig. 3.5(f) shows the survey spectra of the pure BMONR, BMONR/G and 2%Cu-BMONR/G composite, which exhibit characteristic Mo 3d, Bi 4f, O 1s, C 1s, and Cu 2p peaks, without any contaminants. Furthermore, compared to pure BMONR, the 2%Cu-BMONR/G composite's spectrum exhibits a substantially higher C 1s peak, indicating a comparatively high concentration of "C" due to the presence of rGO. Only two peaks, Bi $4f_{3/2}$ and Bi $4f_{5/2}$, with higher binding energies of 159.44 eV and 164.75 eV than BMONR and BMONR/G, respectively, make up the high-resolution Bi 4f XPS spectrum of the 2%Cu-BMONR/G composite [Fig. 3.5(a)], indicating that the Bi in 2D-Bi2MoO6 is in the $Bi^{3+}$ oxidation state.

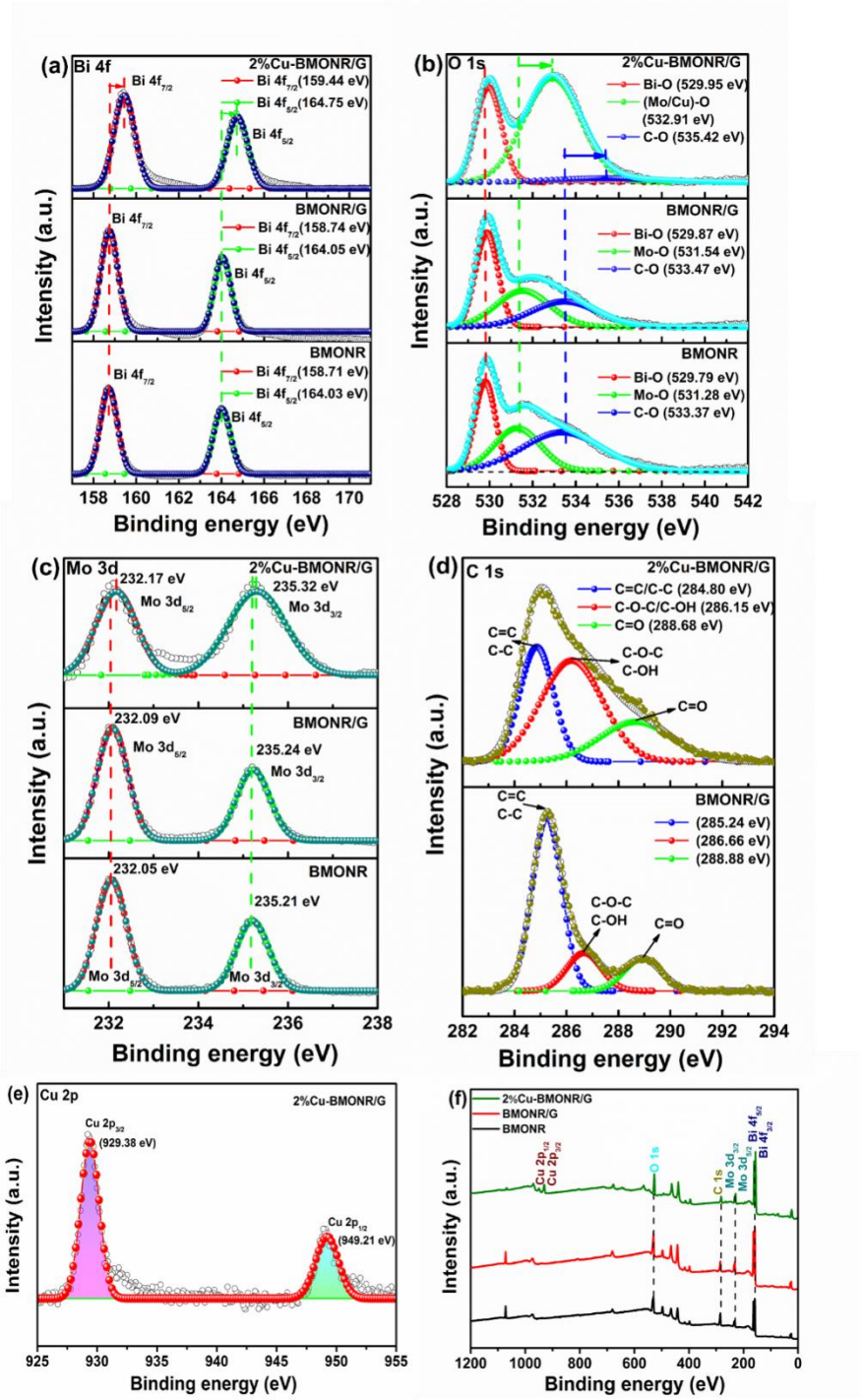


**Fig. 3.5: (a) Comparison of XPS scan of Bi 4f among BMONR, BMONR/G, and 2%Cu-BMONR/G. (b) Comparison of XPS scan of O 1s among BMONR, BMONR/G, and 2%Cu-BMONR/G. (c) Comparison of XPS scan of Mo 3d among BMONR, BMONR/G, and 2%Cu-BMONR/G. (d) Comparison of XPS scan of C 1s between BMONR/G, and 2%Cu-BMONR/G. (e) XPS scan of Cu 2p of 2%Cu-BMONR/G. (f) Comparison of XPS full survey scan among BMONR, BMONR/G, and 2%Cu-BMONR/G photocatalysts**

The O 1s XPS spectra of 2%Cu-BMONR/G composite [Fig. 3.5(b)] show three distinct peaks with higher binding energies of 529.95 eV, 532.91 eV, and 535.42 eV than other composites, which can be indexed to Bi-O, (Mo/Cu)-O, and C-O groups, respectively. However, the O 1s spectrum of 2%Cu-BMONR/G shows the high-intensity peak at 532.91 eV which are attributed to the (Mo/Cu)-O group due to 2%Cu doping in BMONR/G composite. Additionally, two peaks at 232.17 eV and 235.32 eV in the Mo 3d spectra in [Fig. 3.5(c)] are assigned to Mo $3d_{5/2}$ and Mo $3d_{3/2}$, respectively, and exhibit that Mo is present in the $Mo^{6+}$ oxidation state. Fig. 3.5(d) shows the high resolution C 1s spectrum, which exhibits three peaks at 284.80 eV, 286.15 eV, and 288.68 eV. The peak at 284.81 eV is associated with the $sp^2$ carbon (C=C) and $sp^3$ carbon (C-C) in the material, respectively. The peak at 286.15 eV is ascribed to carbonyl carbons (C-O-C) and C-OH, respectively. The peak at 288.68 eV is associated with C=O. Fig. 3.5(e) shows the high resolution Cu 2p spectrum, which manifests two peaks with binding energies of 929.38 eV and 949.21 eV, ascribing to Cu $2p_{3/2}$ and Cu $2p_{1/2}$ , respectively and indicate that Cu is present in the $Cu^{2+}$/ $Cu^{1+}$ oxidation state [237,249,252,257,258].

In the outline of all XPS spectra, when compared to the pure BMONR and BMONR/G, the obvious peak shift can be found over 2%Cu-BMONR/G composite. The occurrence of peak shift to high binding energy value in Bi 4f and Mo 3d spectra and peak shift to low binding energy value in C 1s indicates that Bi and Mo atoms in BMONR play the electron donating role while C atoms in rGO play the electron accepting role. This results confirm that the junction between rGO and 2%Cu-BMONR is firmly constructed, which is further confirmed by the XRD and TEM analysis of 2%Cu-BMONR/G composites. Moreover, the binding energy of O atoms interacting with Cu atoms shifted to the high value while the binding energy of O atoms interacting with Bi or Mo atoms shifted to the low value. This facts manifested that the powerful electron integrated structure has been formed, in which the electrons are transferred from Bi or Mo atoms to Cu atoms. As per C 1s spectra, the shifting of aromatic C=C/C-C peak to the low binding energy value exhibits the strong electron integrated interface between 2%Cu-BMONR and rGO which further accelerate the electrons transportation from Cu atoms to the surface active sites of rGO sheets, where more $CO_2$ can be adsorbed for participating in photocatalytic $CO_2$ reduction process to enhance the yield of selective ethanol production. Finally the XPS analysis confirms that the 2%Cu doped 2D-$Bi_2MoO_6$nanoribbon/rGO composites (2%Cu-BMONR/G) photocatalyst is successfully synthesized.

### 3.3.2 Spectroscopic analysis:

#### 3.3.2.1 UV-VIS Analysis

The optical property of pristine 2D-$Bi_2MoO_6$nanoribbon (BMONR), BMONR/G, (1%, 2%, 3%) Cu-BMONR and (1%, 2%, 3%, 4%) Cu-BMONR/G are scrutinized via UV–vis absorption analysis (Fig. 3.6(a)). The absorption edge of pristine BMONR and BMONR/G locates at approximate 600 nm and 634 nm, respectively and the absorption edge of 2%Cu-BMONR/G locates at approximate 730 nm. Cu doping in BMONR/G composites increases absorbance in the visible region. This characteristic is advantageous for hybrid materials' energy harvesting as it may boost the production of photoinduced electron-hole pairs. The increase in absorbance in the visible region is also shown in Fig. 3.6(a) in the following order: 2%Cu-BMONR/G > 2%Cu-BMONR>BMONR/G >BMONR> 1%Cu-BMONR/G > 1%Cu-BMONR> 3%Cu-BMONR/G > 3%Cu-BMONR> 4%Cu-BMONR/G. In Fig. 3.6(b), it is found that when BMONR is combined with rGO the band gap energy of BMONR is reduced from 2.49 eV to 2.25 eV for BMONR/G as the absorption edge of synthesised BMONR/G composite enhanced to 634 nm. Moreover, during hydrothermal treatment to synthesise BMONR/G composite the oxygen functional groups are reduced and more carbon atoms create strong bond with BMONR to enhance the light absorption capacity. It is also observed in Fig. 3.6(b) that the bandgap energy of the 2%Cu-BMONR/G photocatalyst is further reduced from 2.25 eV (for BMONR/G) to 2.02 eV due to 2%Cu doping in BMONR/G composites. 2%Cu doping in BMONR/G composites also exhibit the highest red shift in the absorption edge (730 nm) among all synthesised composites, which actually manifest the highest visible light energy harvesting capability. This highest enhancement can be achieved due to the proper hybridization of Cu 3d and C 2p states in the valence band, which gives the highest production of photogenerated charge carriers and triggers the selective ethanol production as photocatalytic $CO_2$ reduced product. The Tauc equation[235,266] (3.4), as illustrated below, is used to estimate the bandgap energies of each synthesised photocatalyst.

$$[\alpha h\nu] = A\left[h\nu - E_g\right]^{\frac{n}{2}} \tag{3.4}$$

Where '$E_g$' (eV) is the bandgap of the photocatalyst, 'h' is Planck's constant, 'c' is the speed of light, 'ν' is the frequency of light, 'A' is the absorption coefficient, 'n' is 1 for direct bandgap and '4' for indirect bandgap of semiconductors. Table 3.2 presents

the estimated bandgap energies and absorption edge (nm) values obtained from experimental analysis.

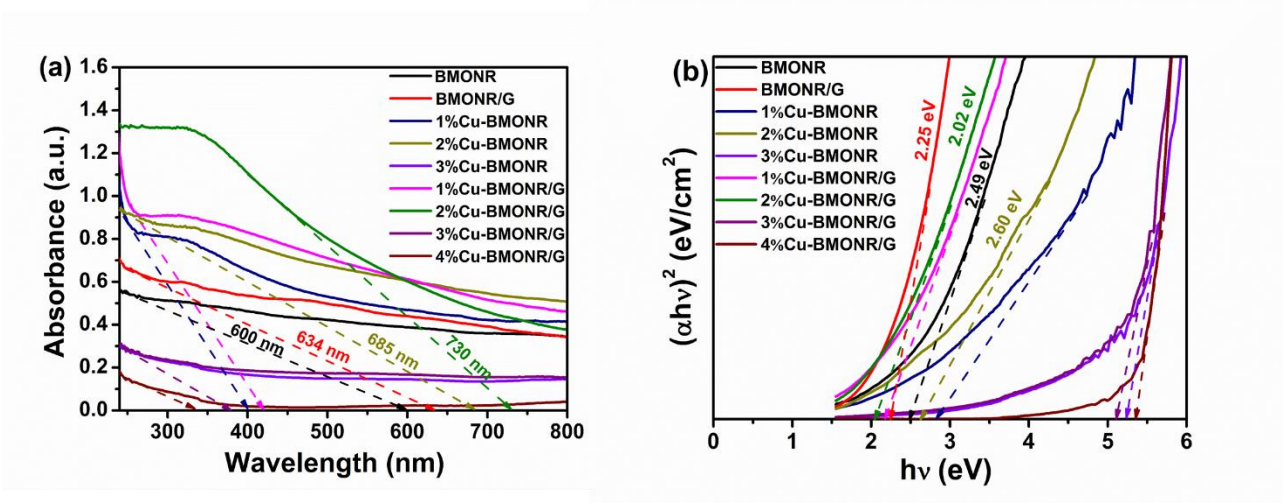


**Fig. 3.6: (a) UV-vis absorption spectra and (b) Estimated band gap energy (eV) by the Tauc plot of BMONR, BMONR/G, (1%, 2%, 3%)Cu-BMONR and (1%, 2%, 3%, 4%)Cu-BMONR/G photocatalysts**

**Table 3.2 A comparison of band gap energy and absorption edge value of synthesised photocatalysts obtained from the experimental analysis.**

| Photocatalyst | Absorption edge (nm) | Band gap energy (eV) |
|---|---|---|
| BMONR | 600.0 | 2.49 |
| BMONR/G | 634.0 | 2.25 |
| 1%Cu-BMONR | 400.8 | 2.81 |
| 2%Cu-BMONR | 685.0 | 2.60 |
| 3%Cu-BMONR | 378.7 | 5.23 |
| 1%Cu-BMONR/G | 420.7 | 2.17 |
| 2%Cu-BMONR/G | 730.0 | 2.02 |
| 3%Cu-BMONR/G | 380.0 | 5.10 |
| 4%Cu-BMONR/G | 335.7 | 5.35 |

### 3.3.2.2 FTIR Analysis

Fig. 3.7(a) shows the FT-IR analysis for exploring the chemical interaction and structure of BMONR, BMONR/G, (1, 2, 3 wt%)Cu-BMONR and (1, 2, 3, 4 wt%)Cu-BMONR/G. The

stretching modes associated with Mo-O, Bi-O, and Mo-O-Mo/Mo-O-Cu bridging are identified as the absorption peaks located between 400 and 1000 $cm^{-1}$. The 2%Cu-BMONR/G composite

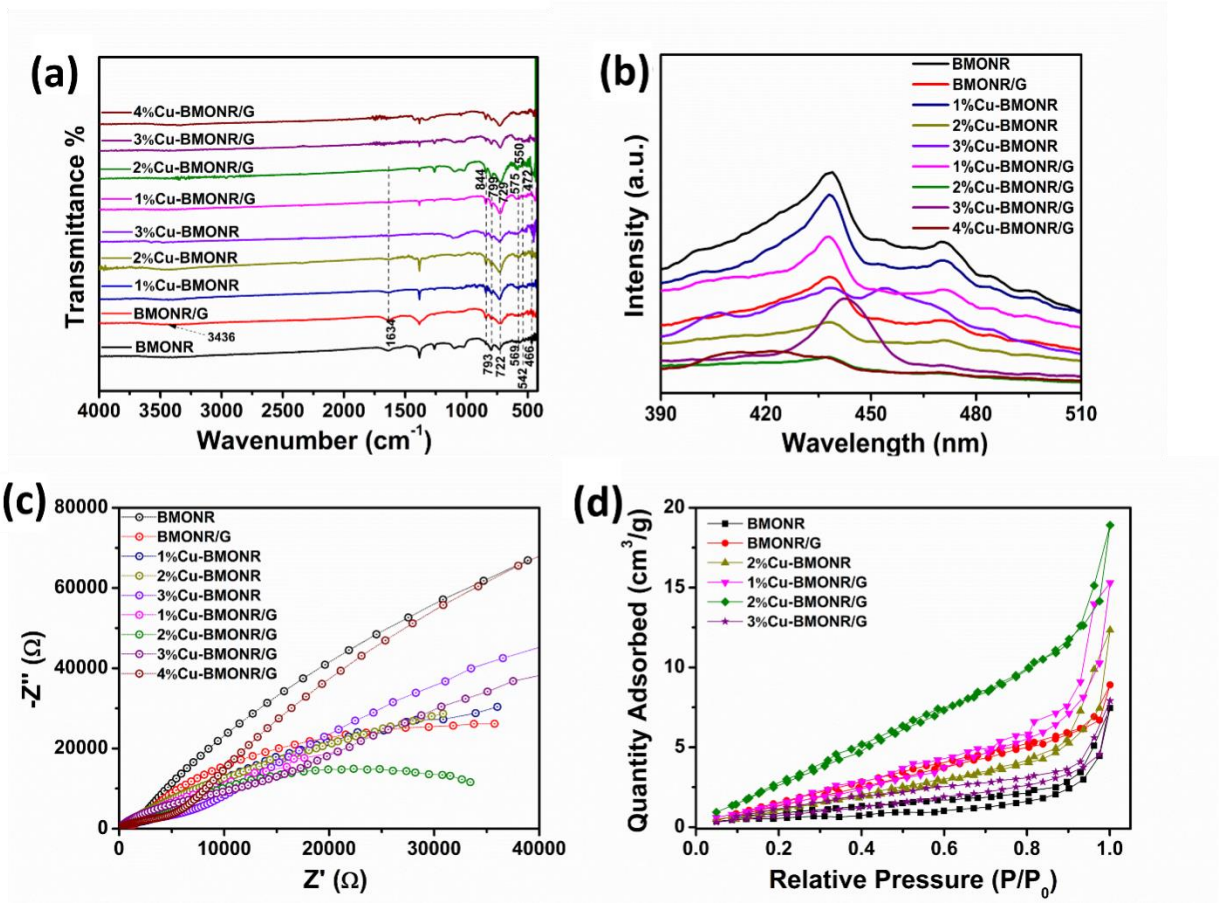


**Fig. 3.7: (a) FTIR spectra of BMONR, BMONR/G, (1%, 2%, 3%)Cu-BMONR and (1%, 2%, 3%, 4%)Cu-BMONR/G photocatalysts, (b) Photoluminescence spectra (PL) of BMONR, BMONR/G, (1%, 2%, 3%)Cu-BMONR and (1%, 2%, 3%, 4%)Cu-BMONR/G photocatalysts an excitation wavelength of 350 nm, (c) EIS curves of BMONR, BMONR/G, (1%, 2%, 3%)Cu-BMONR and (1%, 2%, 3%, 4%)Cu-BMONR/G photocatalysts, (d) Nitrogen adsorption-desorption isotherms of BMONR, BMONR/G, (2%)Cu-BMONR and (1%, 2%, 3%)Cu-BMONR/G photocatalysts**

FT-IR spectra exhibit Bi-O deformation vibration and stretching vibration, respectively, seen at 472 and 575 $cm^{-1}$. The bending and asymmetric stretching of Mo-O, which involves the vibrations of the equatorial oxygen atoms in $MoO_6$ octahedrons, is responsible for the formation of the distinctive bands at 550 and 729 $cm^{-1}$ when detected. Additionally, the

symmetric and asymmetric stretching modes of the $MoO_6$ vibration of the apical oxygen atoms are associated with the absorption bands at 799 and 844 $cm^{-1}$, respectively. The band at 729 $cm^{-1}$ is in good agreement with asymmetric stretching mode of $MoO_6$, which involves equatorial oxygen atom vibrations. The FTIR spectra of 2%Cu-BMONR/G displays two peaks at 3436 $cm^{-1}$ and 1634 $cm^{-1}$, which correspond to reduced O-H functional groups and have lower intensities. This provides proof of the creation of strong bonds between rGO and Cu-BMONR and validates the conversion of GO to rGO following heterojunction formation. The bands in the 1000–1700 $cm^{-1}$ range are caused by $CO_2$ impurities, specifically C=O and C–O stretching. The hydroxyl group of water is implicated in the wide band centred at 3200-3600 $cm^{-1}$ and 1630 $cm^{-1}$, which is adsorbed on the surfaces of the produced samples [238,256,258].

### 3.3.2.3 Photoluminescence (PL) spectroscopy

Photoluminescence (PL) spectroscopy has been used to investigate the migration, transfer, and recombination of photogenerated charge carriers in semiconductor photocatalysts [249,260]. At an excitation wavelength of 350 nm, the PL analysis of the all synthesised photocatalysts is performed, and the emission spectra are shown in Fig. 3.7(b). The PL emission spectra of composites and pure materials have been scanned between 360 and 600 nm. The photocatalytic performance of semiconductor composites is closely related to the photoluminescence intensity. More specifically, an increased PL peak intensity signifies an increased rate of electron-hole pair recombination, which therefore results in a decreased photocatalytic activity. On the other hand, a reduced photoluminescence peak intensity signifies a decreased electron-hole pair recombination rate, leading to an enhanced photocatalytic activity.Fig. 3.7(b) illustrates the major emission peak's centre at 438 nm. The samples included in this investigation have their PL intensities arranged in descending order: BMONR>1%Cu-BMONR>1%Cu-BMONR/G >BMONR/G >3%Cu-BMONR>3%Cu-BMONR/G >2%Cu-BMONR>4%Cu-BMONR/G >2%Cu-BMONR/G.Due to charge carrier recombination in BMONR, every sample has emission bands in the visible region. The interface formed between 2%Cu-BMONRand rGO, in the 2%Cu doping in BMONR/G composite promotes electron transportation and minimises charge carrier recombination. These results confirm that 2%Cu-BMONR/G exhibits the lowest photogenerated electron-hole recombination rate byinterfacial charge transfer between 2%Cu-BMONRand rGO, which facilitate highest photocatalytic $CO_2$ reduction to selective ethanol generation.

### 3.3.2.4 Electrochemical Impedance Spectroscopy (EIS)

The electrochemical impedance spectroscopy (EIS) analysis depicted in Fig. 3.7(c), exhibits that 2%Cu-BMONR/G photocatalyst has a lower arc radius than that of BMONR, BMONR/Gand Cu-BMONR composites. The arc radius of the 2%Cu-BMONR/G photocatalyst is the shortest of all the BMONR, BMONR/G, Cu-BMONR and Cu-BMONR/G composite, demonstrating significant lowering of the photogenerated charge transfer resistance by 2%Cu doping. This phenomenon basically increases the migration rate of high-speed interfacial charge carrier across the contact surface of photocatalyst and due to this the photogenerated electrons and holes are able to separate more effectively, resulting in higher photocatalytic activity [237,246].

### 3.3.3. Nitrogen adsorption-desorption isotherms: BET surface area

The $N_2$ adsorption desorption isotherm for BET surface area and the corresponding pore size distribution plot of BMONR, BMONR/G, 2%Cu-BMONR and (1%, 2%, 3%) Cu-BMONR/G photocatalysts are shown in Fig. 3.7(d). The isotherms of pristine BMONR, BMONR/G, 2%Cu-BMONR and (1%, 2%, 3%)Cu-BMONR/G show typical H3 hysteresis loops, exhibiting the presence of slit pores in all samples. The calculated pore-size distribution manifests the average pore sizes of 2D-$Bi_2MoO_6$nanoribbon (BMONR) and composites in the range of 4 to 36 nm, supporting the hypothesis that there are many mesopores present, which are the source of the high surface adsorption. The BET surface area of pristine BMONR is found to be 7.45 $m^2/g$, whereas BMONR/G photocatalyst shows a 9.07 $m^2/g$ specific surface area [244,246].It is clearly observed that due to rGO loading in BMONR, the total specific surface area of BMONR/G photocatalyst as well as average pore sizes are increased. The BET surface area of 2%Cu-BMONR is found to be 12.42 $m^2/g$. In Fig. 3.7(d), 2%Cu-BMONR/G heterojunction photocatalyst shows the highest specific surface area of 19.06 $m^2/g$ among all synthesised photocatalysts. Since 2%Cu-BMONR/G has the maximum BET surface area, there are more surface-active sites available for the adsorption of reactant molecules ($CO_2$). This increases the yield of photocatalytic reduction $CO_2$ to selective ethanol by lowering the rate of charge carrier recombination.

### 3.3.4 Performance analysis of photocatalytic $CO_2$ reduction:

The 2D-$Bi_2MoO_6$nanoribbon (BMONR), 2D-$Bi_2MoO_6$nanoribbon/rGO (BMONR/G), 2%Cu doped 2D-$Bi_2MoO_6$nanoribbon (2%Cu-BMONR), and (1%, 2%, 3%) Cu doped 2D-$Bi_2MoO_6$

nanoribbon/rGO (1%, 2%, 3%Cu-BMONR/G) composites are assessed for their photocatalytic activity performance during 8 h of visible light-driven photocatalytic $CO_2$ reduction reactions conducted in water at 20°C and atmospheric pressure. Fig. 3.8 demonstrates that Cu doping as well as rGO plays the significant role in producing 100% selective C-2 product, the ethanol. Use of all three Cu doped BMONR/G photocatalysts produce the ethanol while pristine BMONR, BMONR/G as well as Cu doped BMONR produce mixture of the methanol and ethanol (Fig. 3.8(a)). GCMS analysis of products obtained using the optimum 2%Cu-BMONR/G photocatalyst (Fig. 3.8(d)) exhibits that the ethanol with 100% selectivity (refer to Fig. 3.8(b)), is the ultimate product in the liquid phase, and no other carbonaceous compounds, such as HCHO, HCOOH, or CH3OH, are detected. The GC-TCD and GC-FID technologies are used to analyse the gaseous products. The outlet gas produced during the photocatalytic $CO_2$ reduction process contains no $H_2$, $CH_4$, or CO. Furthermore, control studies showed that in the absence of photocatalyst or radiation, no significant amounts of $CH_3OH$ and $C_2H_5OH$ are produced, suggesting that both efficient photocatalysis and illumination are necessary for $CO_2$ reduction. Furthermore, prior to $CO_2$ purging, a photocatalytic $CO_2$ reduction experiment is started within the reactor in a $N_2$ atmosphere, and the absence of any hydrocarbons indicated that $CO_2$ is the only carbon source utilised in the experiment. Using $CO_2$ as the carbon source, mass spectrum peaks of $C_2H_5OH$ are found at 30.93 and 44.92 m/z, respectively, during a retention time of 1.59 min (Fig. 3.9(e)), as seen in Fig. 3.8(d). These peaks closely correspond to those seen in the mass spectrum of pure ethanol, as seen in Fig. 3.8(e). The yields of $CH_3OH$ and $C_2H_5OH$ produced by BMONR, BMONR/G, and 2%Cu-BMONR photocatalysts are shown in Fig. 3.8(a). Additionally, the yields of ethanol ($C_2H_5OH$) are only shown for the synthesised 1%, 2%, and 3%Cu–BMONR/G photocatalysts. Table 3.3 provides a summary of all the alcohol yields in detail. The GCMS analysis of the BMONR composites is displayed in Fig. 3.9(b), the results of which are $CH_3OH$ (49.20 µmol $g_{cat.}^{-1}$ $h^{-1}$) and $C_2H_5OH$ (27.17 µmol $g_{cat.}^{-1}$ $h^{-1}$) (Fig. 3.8(a)). The GCMS analysis of the BMONR/G composites is also displayed in Fig. 3.9(c). As predicted, the BMONR/G composites outperform the BMONR composites in yielding $CH_3OH$ (31.81 µmol $g_{cat.}^{-1}$ $h^{-1}$) and $C_2H_5OH$ (58.80 µmol $g_{cat.}^{-1}$ $h^{-1}$), demonstrating the beneficial influence of the rGO layers by increasing the ethanol production 2.16 times higher than that seen for BMONR. For comparison, a GCMS analysis study of the 2%Cu-BMONR photocatalysts is also carried out, as seen in Fig. 3.9(d). In Fig. 3.8(a), ethanol is produced selectively using 1, 2, and 3 wt% Cu doping; 2%Cu-BMONR/G photocatalysts provide the greatest ethanol yield in 8 h, with 133.10 µmol $g_{cat.}^{-1}$ $h^{-1}$. The ethanol production yield of

2%Cu-BMONR/G is 2.26 times that of BMONR/G composites. As a result of the photocatalytic activity study of the 2%Cu-doped 2D $Bi_2MoO_6$nanoribbon/rGO (2%Cu-BMONR/G) photocatalyst, Fig. 3.9(e)displays the GCMS analysis of the highest selective ethanol formation as a $CO_2$ photo reduced product; no peak is found at m/z = 32.83, which clearly establishes the absence of methanol formation. The GCMS peak in Fig. 3.9(a) at m/z = 43.91 verifies that $CO_2$ is absorbed in the reaction medium prior to the illumination of visible light. The ethanol selectivity of BMONR, BMONR/G, 2%Cu-BMONR, and 2%Cu-BMONR/G composites is displayed in Fig. 3.8(b). 2%Cu-BMONR/G notably has ethanol selectivity of 100%, which is greater than BMONR/G and much higher than 2%Cu-BMONR and BMONR. Achieving 100% selectivity of photocatalytic $CO_2$ reduction to ethanol production is a significant challenge for various $Bi_2MoO_6$-based photocatalysts, according to published research work (Table 3.3). However, in the current research work, the highest yield of 100% selective ethanol production is obtained with 2% Cu doping in $Bi_2MoO_6$/rGO nanoribbon (2%Cu-BMONR/G) photocatalysts among all $Bi_2MoO_6$-based photocatalysts (Table 3.3).

The following formula is used to determine the selectivity of the $12e^-$ reduction product $C_2H_5OH$ ($S_{C2H5OH}$) [273].

$$S_{C_2H_5OH} = 12R_{C_2H_5OH} / (12R_{C_2H_5OH} + 6R_{CH_3OH}) \quad (3.5)$$

In this case, R stands for the products' rate. The number of electrons consumed in the multielectron reaction is represented by the coefficient of R.

The high retained ethanol output after four cycle tests, as shown in Fig. 3.8(c), indicates that 2%Cu-BMONR/G exhibits strong catalytic stability in addition to high photocatalytic $CO_2$ reduction to ethanol.The ethanol production rate of 47.774 μmol $g^{-1}$ $h^{-1}$ and 20.34 μmol $g^{-1}$ $h^{-1}$ is measured for 2%Cu-BMONR/G and BMONR/G, respectively, at 420 nm. Furthermore, AQYs of 2%Cu-BMONR/G and BMONR/G are determined to be around 0.337% and 0.144%, respectively, based on measurements made at 420 nm. The AQY of 2%Cu-BMONR/G composites is approximately 2.34 times higher than that of BMONR/G composites. Cu doping in BMONR/G beyond the optimal loading decreases the photocatalytic activity of 3%Cu-BMONR/G composites and results in less ethanol being created, as seen in Fig. 3.8. Nevertheless, increased Cu loading increases the number of active sites on the catalyst surface, which is favourable to the selective ethanol yield.Further to justify the selective ethanol production as photocatalytic $CO_2$ reduced product of 2%Cu-

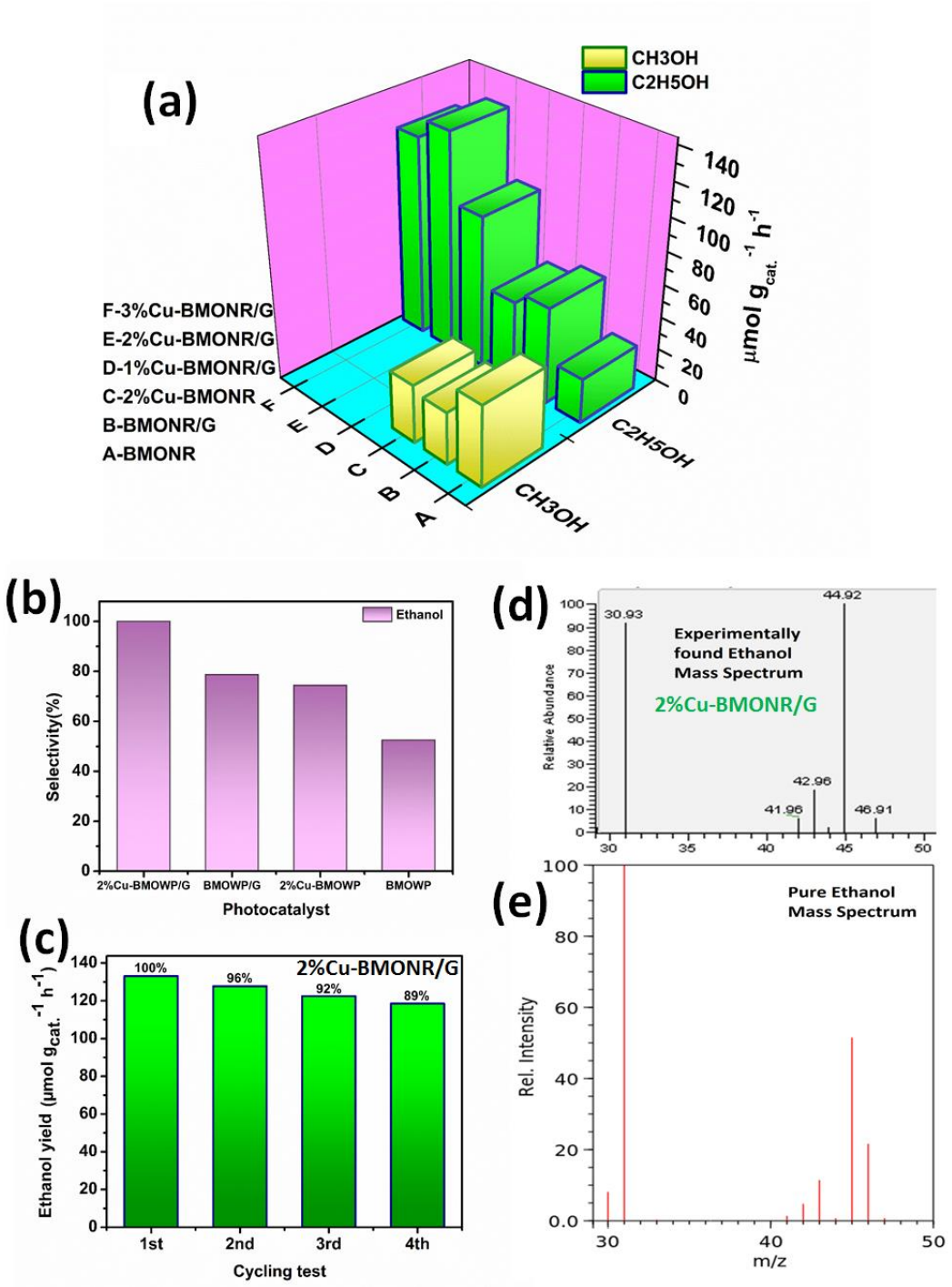


**Fig. 3.8: Photocatalytic $CO_2$ reduction on BMONR, BMONR/G, 2%Cu-BMONR and 1%, 2%, 3%Cu-BMONR/G photocatalysts: (a) Yield of ethanol production rate, (b) product selectivity, and (c) ethanol yields obtained on 2%Cu-BMONR/G composites in four cycling tests. (d) Mass spectrum analysis of the selective ethanol found over 2%Cu-BMONR/G composites. (e) Mass spectrum analysis of the pure ethanol (standard grade)**

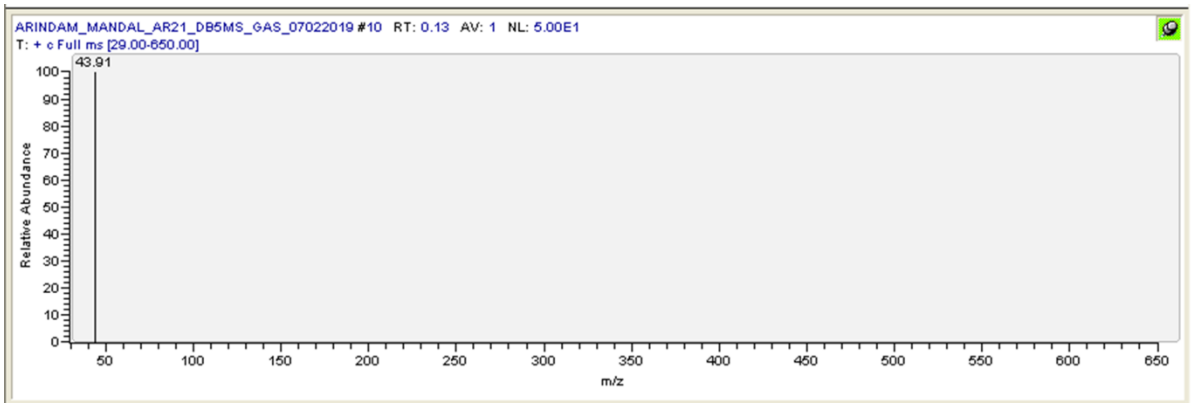


**Fig. 3.9 (a): GCMS analysis image of absorbed $CO_2$ in reaction solution before visible light illumination**

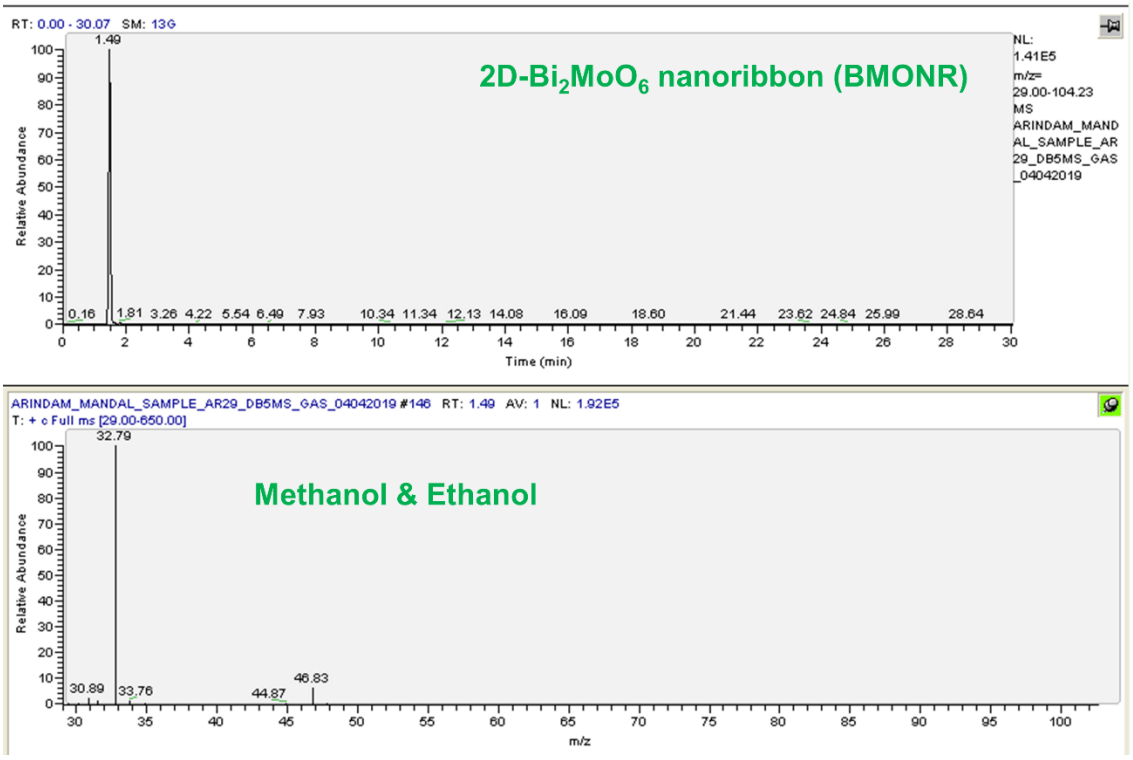


**Fig. 3.9 (b): GCMS analysis image of 2D-$Bi_2MoO_6$nanoribbon (BMONR)**

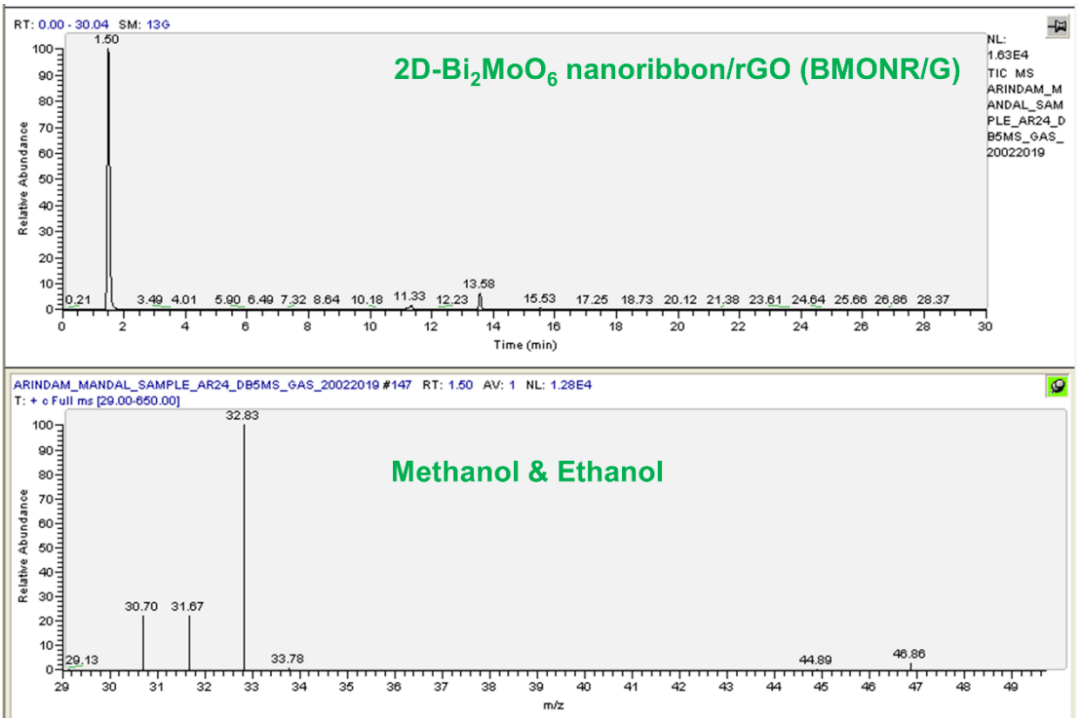


**Fig. 3.9 (c): GCMS analysis image of 2D-$Bi_2MoO_6$nanoribbon/rGO (BMONR/G)**

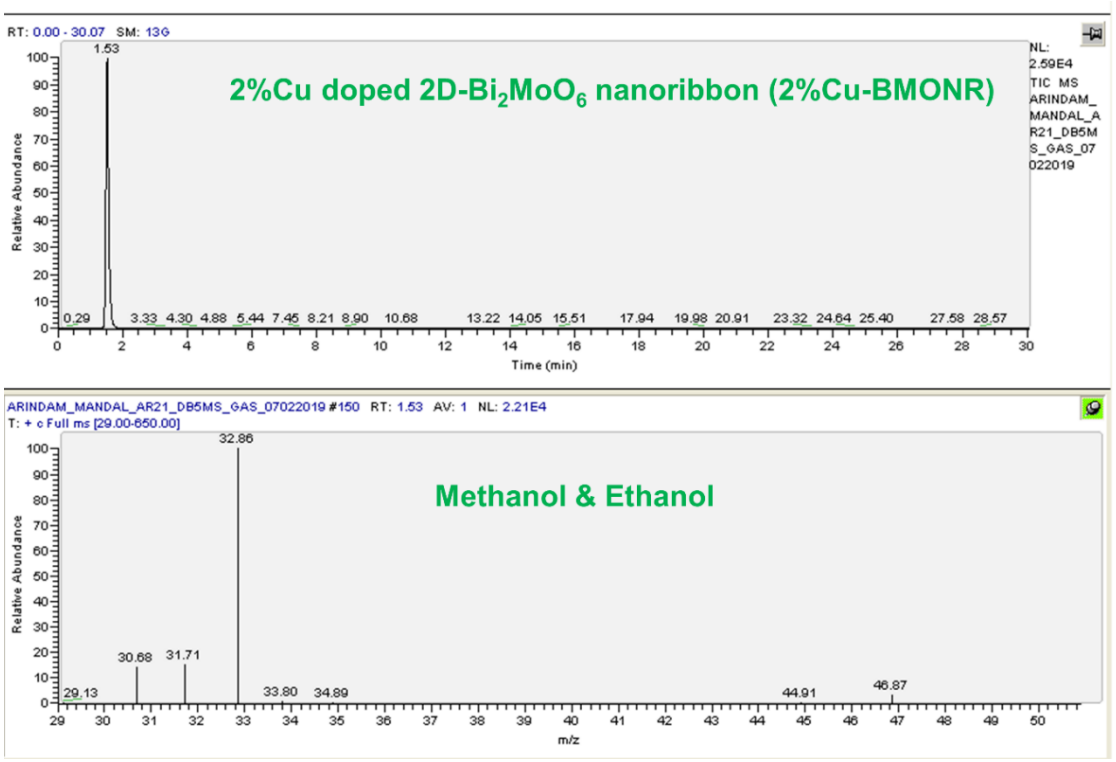


**Fig. 3.9 (d): GCMS analysis image of 2%Cu doped 2D-$Bi_2MoO_6$nanoribbon (2%Cu-BMONR)**

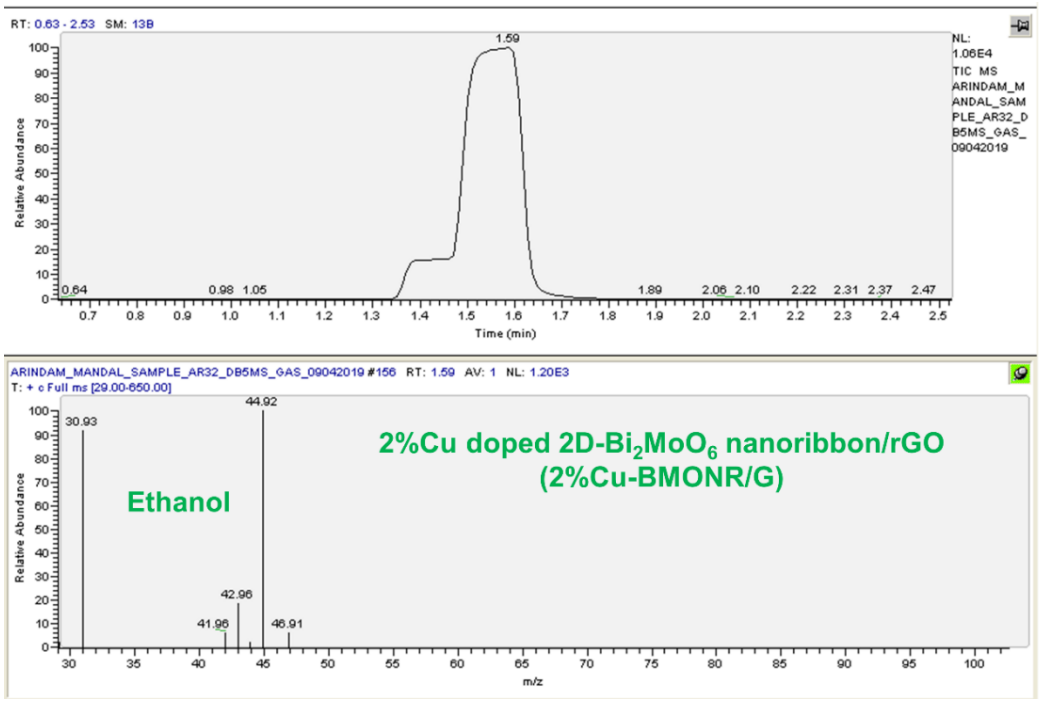


**Fig. 3.9 (e): GCMS analysis image of 2%Cu doped 2D-$Bi_2MoO_6$nanoribbon/rGO (2%Cu-BMONR/G)**

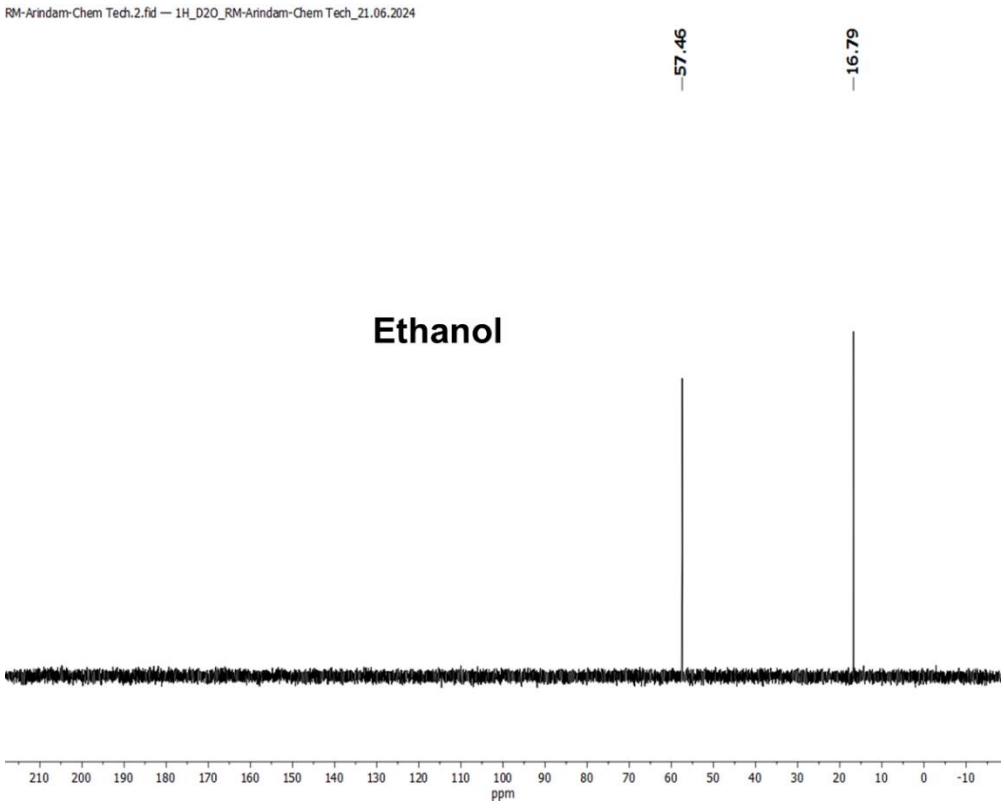


**Fig. 3.10 (a): $^{13}C$ NMR analysis image of 2%Cu doped 2D-Bi2MoO6/rGO nanoribbon (2%Cu-BMONR/G) for detection of only ethanol as product**

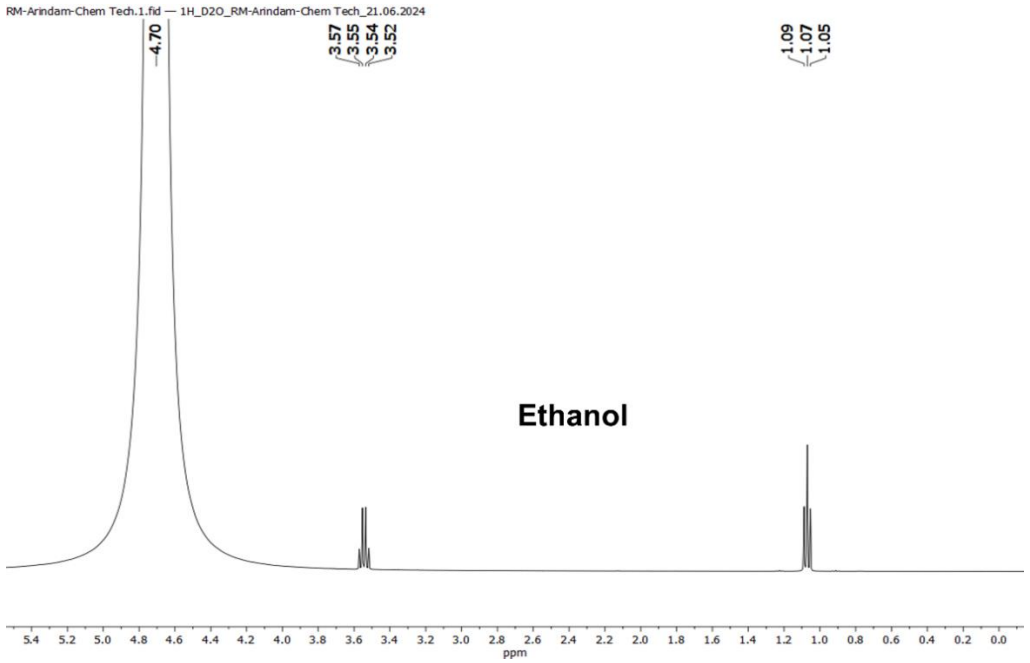


**Fig. 3.10 (b): $^{1}$H NMR analysis image of 2%Cu doped 2D-Bi2MoO6/rGO nanoribbon (2%Cu-BMONR/G) for detection of only ethanol as product**

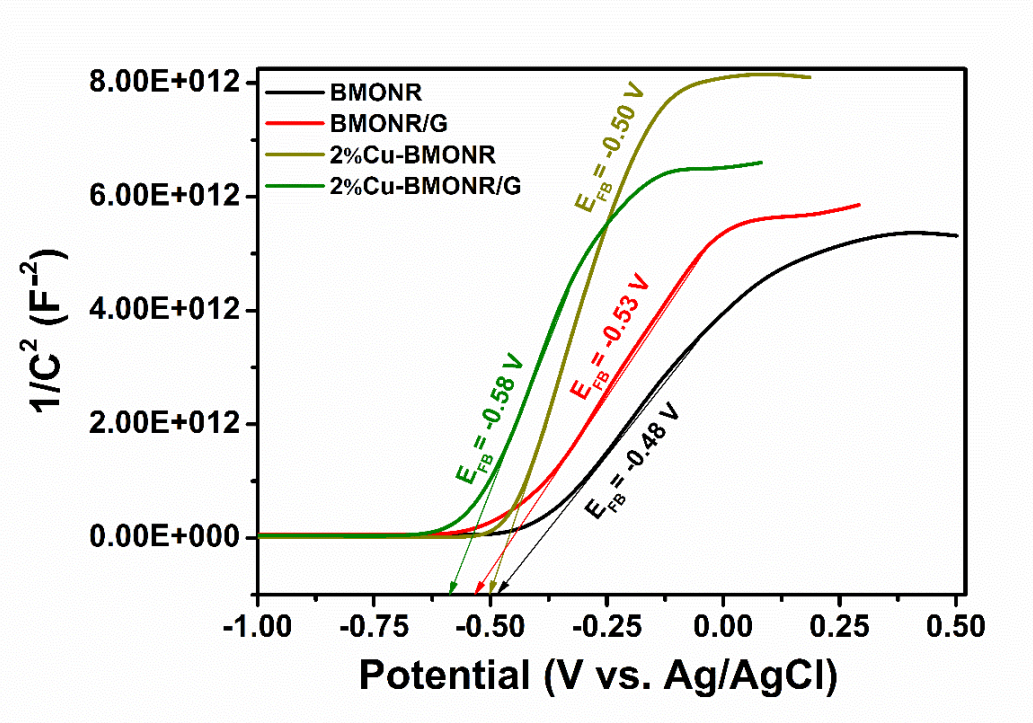


**Fig. 3.11: Mott-Schottky (M-S) plots of BMONR, BMONR/G, 2%Cu-BMONR, and 2%Cu-BMONR/G photocatalysts**

**Table: 3.3 Photocatalytic activity for ethanol production rate and selectivity.**

| Photocatalyst | Method & Reaction medium | Light Source | Photocatalytic activity ($\mu mol\ g^{-1}\ h^{-1}$) | Ref. |
|---|---|---|---|---|
| Ov-$Bi_2MoO_6$ | Hydrothermal, $CO_2$ (g) and water | 300 W Xe arc lamp, 4 h | Methanol: 2.58 Ethanol: 26.63 | [238] |
| Hierarchical flower-like $Bi_2MoO_6$ | Hydrothermal, $CO_2$ (g) and water | 300 W Xe lamp, 4 h | Methanol: 6.20 Ethanol: 4.7 | [245] |
| $Bi_2MoO_6$–$H_2O$ $Bi_2MoO_6$–EG/Et | Hydrothermal, $CO_2$ (g) and water | LED lamp (Stellatech 13 W) | Ethanol: 34.44 Ethanol: 24.43 | [276] |
| Flower-like $Bi_2MoO_6$ | Hydrothermal, $CO_2$ (g) and water | 300 W xenon lamp, 4 h | Methanol: 4.4 Ethanol: 3.7 | [277] |
| $Bi_2MoO_6$ QDs/rGO | Hydrothermal, $CO_2$ (g) and water | 300 W xenon lamp, 4 h | Methanol: 21.20 Ethanol: 14.37 | [277] |
| Hierarchical $CeO_2$/$Bi_2MoO_6$ | Hydrothermal, $CO_2$ (g) and water | 300 W Xe arc lamp, 4 h | Methanol: 8.0 Ethanol: 6.63 | [278] |
| Bi@$Bi_2MoO_6$ | Hydrothermal, $CO_2$ (g) and water | PLS-SXE 300 W, 6 h | Methanol: 0.59 Ethanol:17.93 | [279] |
| 0.1%Cu/ILs/OVs-BMO | Hydrothermal, $CO_2$ (g) and water | 300 W Xe lamp, 4 h | Methanol: 49.53 Ethanol: 28.09 | [280] |
| Cu-$TiO_2$ | Hydrothermal, $CO_2$ (g) and water vapor | UV-LED (Shanghai Maixin, China), 6 h | Methanol: 36.18 Ethanol:79.13 | [281] |
| Cu-$TiO_2$/GO | Hydrothermal, $CO_2$ (g) and water | Philips, 160 W: Mercury lamp (UV), 6 h | Ethanol: 232.51 | [282] |
| Red phosphorus decorated $Bi_2MoO_6$ | Hydrothermal, $CO_2$ (g) and water vapor | Xe lamp (450W), 4 h | Methanol: 31.2 Ethanol: 51.8 | [283] |
| 2D-$Bi_2MoO_6$ nanoribbon | Hydrothermal, $CO_2$ (g) and water | Solar simulator (100 W), 8 h | Methanol: 49.20 Ethanol:27.17 | This work |
| 2D-$Bi_2MoO_6$ nanoribbon/rGO | Hydrothermal, $CO_2$ (g) and water | Solar simulator (100 W), 8 h | Methanol: 31.81 Ethanol:58.80 | This work |
| 1%Cu-(2D)$Bi_2MoO_6$ nanoribbon | Hydrothermal, $CO_2$ (g) and water | 100 W Solar simulator, 8 h | Methanol: 39.87 Ethanol: 44.94 | This work |
| 2%Cu-(2D)$Bi_2MoO_6$ nanoribbon | Hydrothermal, $CO_2$ (g) and water | 100 W Solar simulator, 8 h | Methanol: 35.37 Ethanol: 51.32 | This work |
| 3%Cu-(2D)$Bi_2MoO_6$ nanoribbon | Hydrothermal, $CO_2$ (g) and water | 100 W Solar simulator, 8 h | Methanol: 37.05 Ethanol: 48.70 | This work |
| 1%Cu-(2D)$Bi_2MoO_6$ nanoribbon/rGO | Hydrothermal, $CO_2$ (g) and water | Solar simulator (100 W), 8 h | Ethanol: 92.68 | This work |
| **2%Cu-(2D)$Bi_2MoO_6$ nanoribbon/rGO** | **Hydrothermal, $CO_2$ (g) and water** | **Solar simulator (100 W), 8 h** | **Ethanol: 133.10** | **This work** |
| 3%Cu-(2D)$Bi_2MoO_6$ nanoribbon/rGO | Hydrothermal, $CO_2$ (g) and water | Solar simulator (100 W), 8 h | Ethanol: 121.84 | This work |

.

BMONR/G photocatalyst the $^{13}C$ NMR and $^{1}H$ NMR analysis are also performed and shown in below as Fig. 3.10(a) and 3.10(b), respectively. In $^{13}C$ NMR analysis (Fig. 3.10(a)) two minor shifts at 16.79 ppm and 57.46 ppm are observed, which are assigned to $CH_3$ and $CH_2$ of ethanol, respectively. In $^{1}H$ NMR analysis (Fig. 3.10(b)) two minor shifts at 1.07(t) ppm and 3.55(q) ppm are observed, which are also assigned to $CH_3$ and $CH_2$ of ethanol, respectively. Both the $^{1}H$ NMR and $^{13}C$ NMR are performed taking $D_2O$ as a solvent.

### 3.3.6 Mechanism:

This study demonstrates 2%Cu-$Bi_2MoO_6$/graphene is the highly photo catalytically active nanocomposite compared to all other possibilities. Our theoretical calculations corroborate with the experimental results. Hence a possible reaction mechanism is proposed for the photo catalytic reduction for $CO_2$ into ethanol. The reaction mechanism of $CO_2$ reduction into ethanol can be explained as a 12 electrons mechanism which includes C-C coupling reaction during photocatalytic $CO_2$ reduction. The primary step of the photocatalytic $CO_2$ reduction to ethanol is the absorption of $CO_2$ in the reaction medium. Fig. 3.9(a) confirms the absorption of $CO_2$ (m/z=43.91) in the reaction medium. The second step is the diffusion of absorbed $CO_2$ to the photocatalyst surface. A surface-bound metastable radical anion [$\cdot CO_2^-$ (ad.)] is formed when absorbed photons from visible light illumination activate $CO_2$ on the photocatalyst surface. Subsequent phases in the reduction process involve the transport of protons, electrons, the generation and transportation of hydrogen radicals. The reduction process also includes new C–H bonds breaking and C–O bonds formation. Depending on how $CO_2$ binds to the photocatalyst surface, the creation of $C_2H_5OH$ may follow the formaldehyde formation pathway[253,261,262].In this formaldehyde pathway the $2\cdot CO_2^-$ (ad.) recombines with $2H^+$ with the help of 1 electron to form $2HCOO\cdot$ intermediate (equation 3.11). Then the $2HCOO\cdot$ intermediate breaks down in two $\cdot CO$ intermediate (equation 3.12) and then one $\cdot CO$ intermediate is reduced to form $\cdot CHO$ (equation 3.13). The formed $\cdot CHO$ intermediate is further reduced to $\cdot CH_2OH$ intermediate (equation 3.14) and this $\cdot CH_2OH$ intermediate again recombines with $H^+$ and electron to form $CH_3OH$ (equation 3.15). Then the $CH_3OH$ is further reduced with the help of rest $\cdot CO$ intermediate to form $\cdot CH_3COH$ (equation 3.16) and lastly the formed $\cdot CH_3COH$ intermediate recombines with $2H^+$ (equation 3.17 & 3.18) and produced selective ethanol ($C_2H_5OH$). Finally, by reacting with 12 number of photogenerated electrons, 2 mol of $CO_2$ and 12 mol of $H^+$ are reduced to

produce 1 mol of ethanol and 3 mol of water.In the mechanism (Fig. 3.12) of Cu doped 2D-$Bi_2MoO_6$/rGO (2%Cu-BMONR/G) for photocatalytic $CO_2$ reduction equation 3.6 states that copper (Cu) serves as a transition state for photoelectrons to rest on and separate from photogenerated holes ($h^+$) in the context of the Cu-BMONR/G composite. Equation 3.7 states that the $Cu^{2+}$ radical forms $Cu^+$ when it couples with photoelectrons from BMONR via rGO. $Cu^+$ contributes more electrons to the dissolution of $CO_2$ or $CO_2^{-}$, hence promoting the photocatalytic reaction and yielding selective ethanol. Because $Cu^+$ can recombine with holes to become $Cu^{2+}$, the process is reversible.

The Mott-Schottky (M-S) plots for BMONR, BMONR/G, 2%Cu-BMONR, and 2%Cu-BMONR/G photocatalysts are also analysed to determine the conduction band of samples for undersading the mechanism in Fig. 3.11. Mott-Schottky (M-S) plots analysis provides an estimation of the flat-band potentials ($E_{FB}$) of BMONR, BMONR/G, 2%Cu-BMONR, and 2%Cu-BMONR/G photocatalysts at -0.48 V, -0.53 V, -0.50 V, and -0.58 V vs. Ag/AgCl, respectively. The $E_{FB}$ values of BMONR, BMONR/G, 2%Cu-BMONR, and 2%Cu-BMONR/G are calculated as -0.28 V, -0.33 V, -0.30 V, and -0.38 V vs. NHE, respectively using the Nernst equation: $E_{NHE}$ (V) = $E_{Ag/AgCl}$ + 0.197 [276-279]. Actually, for the n-type photocatalyst the $E_{CB}$ is essentially ~0.1 higher than $E_{FB}$ [280-283]. Therefore, the $E_{CB}$ of BMONR, BMONR/G, 2%Cu-BMONR, and 2%Cu-BMONR/G can be determined as -0.38 V, -0.43 V, -0.40 V, and -0.48 V vs. NHE, respectively. Based on the equation: $E_{VB} - E_{CB} = E_g$ [277-283], the $E_{VB}$ of BMONR, BMONR/G, 2%Cu-BMONR, and 2%Cu-BMONR/G are determined as +2.11 V, +1.82 V, +2.20 V, and +1.54 V vs. NHE, respectively."

In a photocatalytic reaction the reduction potential of methanol, ethanol, and formic acid are −0.38, −0.33 V, and −0.61 V versus NHE, respectively and the electrons gathered on the CB of BMONR($E_{CB}$= -0.38 V), BMONR/G($E_{CB}$= -0.43 V), 2%Cu-BMONR($E_{CB}$= -0.40 V)are sufficiently negative to reduce $CO_2$ to methanol and ethanol and 2%Cu-BMONR/G ($E_{CB}$= -0.48 V) are sufficiently higher negative to reduce $CO_2$ to selective ethanol, but simultaneously it is also found that the electrons gathered on the CB of BMONR, BMONR/G, 2%Cu-BMONR, and 2%Cu-BMONR/G are not sufficiently negative to reduce $CO_2$ to formic acid due to their low $E_{CB}$ than the standard required$E_{CB}$ (−0.61 V versus NHE) for generation of formic acid. So in this work, any formic acid is not found as a photocatalytic $CO_2$ reduction product. The overall mechanism (equation 3.6 to 3.19) of photocatalytic $CO_2$ reduction into ethanol ($C_2H_5OH$) using 2%Cu-BMONR/G photocatalyst is represented by Fig. 3.12.Furthermore, water oxidation happens in a photocatalytic reaction

using a semiconductor's holes from its valence band, and the standard oxidation potential ($E_{VB}$) for water oxidation to generate oxygen ($O_2$) is +0.81 V(vs. NHE), which is much lower than +1.54 V of the 2%Cu-BMONR/G valence band (VB). The resultant holes in the 2%Cu-BMONR/G VB can therefore oxidize $H_2O$ to $O_2$.

The increased binding energies between Cu doped 2D-$Bi_2MoO_6$ and rGO demonstrate the stronger interaction (Fig. 3.12). The generation of Mo−O−Cu/ Mo−C−Cu bonds, where Mo originates from the 2D-$Bi_2MoO_6$ and O and C are from the rGO substrate, is most likely the cause of this. It is possible to comprehend the upshift binding energies of O 1s and Mo 3d by applying the electronegativity theory. Since rGO is largely made up of C atoms with a little amount of O atoms, the 2D-Bi2MoO6 produced in situ on rGO is surrounded by C and O atoms. Electrons from Mo and Bi atoms are drawn to C 2p and Cu 3d orbitals. This lowers the electron density surrounding Bi and Mo and increases the binding energies of the electrons in Bi 4f and Mo 3d orbitals. Cu doping enhances the thickened electron cloud on the surface junction of C-Cu, which facilitates the more $CO_2$ adsorption and reduction.

Cu doping in 2D-$Bi_2MoO_6$/rGO surface shows the lowest PL intensity and lowest arc radius in EIS analysis which demonstrate that Cu doping decreases the recombination rate of the photo generated electron hole pairs and also decreases the charge transfer resistance to accelerate electrons mobility. Therefore, Cu serves as a trap to catch more electrons. The Cu doping promotes more active sites for $CO_2$ adsorption/activation and effectively reduces the photogenerated electron transport distance with lowest recombination rate to stabilize intermediate radicals such as ·CO and, thus, increases the rate of abundant photogenerated electron transfer with low resistance along the Mo-C-Cu/Mo-O-Cu bridge to $CO_2$ trapping sites to decrease the activation barrier for selective ethanol generation. The optimum doping of 2% Cu in the BMONR/G photocatalyst enhances the yield of selective ethanol production by 2.26 times compared with BMONR/G.

$$\text{Cu doped 2D-}Bi_2MoO_6\text{/rGO} + h\nu \longrightarrow e^-\text{ (Cu doped 2D-}Bi_2MoO_6) + h^+\text{ (Cu doped 2D-}Bi_2MoO_6) + e^-\text{ (rGO)} \quad (3.6)$$

$$Cu^{2+} + e^- \longleftrightarrow Cu^+ \quad (3.7)$$

$$Cu^+ + h^+ \longrightarrow Cu^{2+} \quad (3.8)$$

$$H_2O + 2h^+ \longrightarrow \tfrac{1}{2}\,O_2 + 2H^+ + 2e^- \quad (3.9)$$

$$2CO_2 + 2e^- \longrightarrow 2\cdot CO_2^{-}\text{ (ad.)} \quad (3.10)$$

$$2\cdot CO_2^{-}\text{ (ad.)} + 2H^+ + e^- \longrightarrow 2HCOO\cdot \quad (3.11)$$

$$2HCOO^{\cdot} + 2e^{-} + 2H^{+} \longrightarrow 2{\cdot}CO + 2H_2O \quad (3.12)$$

$$2{\cdot}CO + H^{+} + e^{-} \longrightarrow {\cdot}CHO + {\cdot}CO \quad (3.13)$$

$${\cdot}CHO + {\cdot}CO + 2H^{+} + e^{-} \longrightarrow {\cdot}CH_2OH + {\cdot}CO \quad (3.14)$$

$${\cdot}CH_2OH + {\cdot}CO + H^{+} + e^{-} \longrightarrow CH_3OH + {\cdot}CO \quad (3.15)$$

$$CH_3OH + {\cdot}CO + 2H^{+} + 2e^{-} \longrightarrow {\cdot}CH_3COH + H_2O \quad (3.16)$$

$${\cdot}CH_3COH + H^{+} + e^{-} \longrightarrow {\cdot}CH_3CH_2O \quad (3.17)$$

$${\cdot}CH_3CH_2O + H^{+} + e^{-} \longrightarrow \mathbf{CH_3CH_2OH} \quad (3.18)$$

$$\mathbf{2CO_2 + 12H^{+} + 12e^{-} \longrightarrow C_2H_5OH + 3H_2O} \quad \mathbf{(3.19)}$$

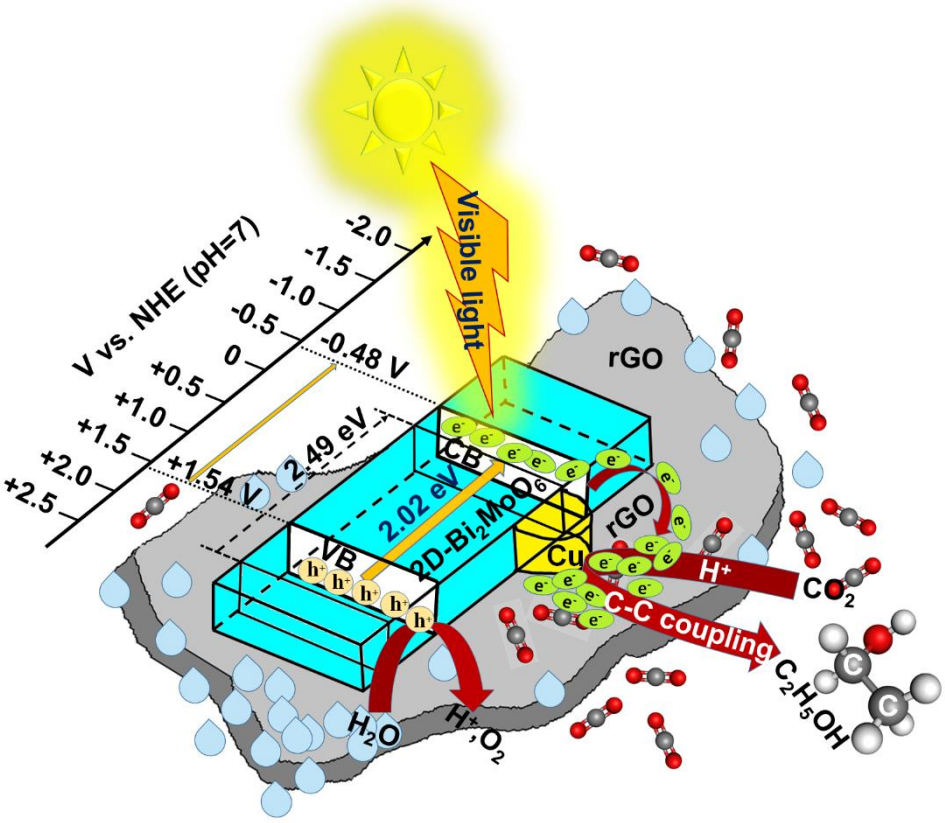


**Fig. 3.12: Mechanism of photocatalytic $CO_2$ reduction into ethanol ($C_2H_5OH$) using 2%Cu doped 2D-$Bi_2MoO_6$ nanoribbon/rGO (2%Cu-BMONR/G) photocatalyst under visible light illumination**

### 3.4. Conclusion:

The photocatalysts with different doping concentrations of Cu (1%, 2%, 3% and 4 wt%) in 2D-$Bi_2MoO_6$nanoribbon/rGO identified as 1%Cu-BMONR/G, 2%Cu-BMONR/G, 3%Cu-

BMONR/G, and 4%Cu-BMONR/G, respectively, have been synthesised using hydrothermal treatment. The chemical bonding among Cu, rGO and 2D- $Bi_2MoO_6$nanoribbon (BMONR) forming a two- dimensional (2D) nanoribbon like structure in the case of 2%Cu-BMONR/G as compared to other photocatalysts manifests higher crystallinity, as confirmed by XRD and XPS. Moreover, due to the presence of Cu and rGO the increased absorption edge (730 nm) to the visible spectrum of the solar illumination and the decreased PL intensity for 2%Cu-BMONR/G photocatalyst indicates the enhanced number of photo generated charge carriers and greater charge separation with lowest rate of recombination, thereby promoting the efficient photocatalytic $CO_2$ reduction. The analysis of selectivity and yield of products of photocatalytic reduction of $CO_2$ using GCMS as well as the quantum efficiency calculations, suggest that Cu doping of $Bi_2MoO_6$-rGO promote the 100% selective ethanol production while both pristine $Bi_2MoO_6$, $Bi_2MoO_6$-rGO photocatalyst produces mixture of methanol and ethanol. The optimum 2%Cu-BMONR/G exhibit an excellent $CO_2$ reduction to selective ethanol production rate of 133.10 μmol $g_{cat.}^{-1}$ $h^{-1}$ with a high selectivity of 100% and apparent quantum yield on the order of 0.337%, as compared to other synthesised photocatalysts in this work. The mechanism behind the remarkable performance of 2%Cu-BMONR/G is exhibited by the comprehensive experimental research. Notably, the introduction of 2%Cu in BMONR/G controls the electronic composition of copper active sites via Mo-C-Cu/Mo-O-Cu bridge accelerating the charge transfer from BMONR to $CO_2$ trapping sites on rGO-Cu interface and at the same time promoting excellent charge transfer for C-C coupling for C2 product generation. A band gap value of 2.02 eV, which is estimated using experimental UV-vis data. Therefore, the photogenerated electrons from $Bi_2MoO_6$ (a n-type semi-conductor) will be transported through rGO (an electron acceptor) and taken away by the Cu atom to fulfil its electron vacancy in $3d^9$ orbital; rGO being an electron acceptor, separates photo-excited electrons and holes at the interface of the junction and facilitates the adsorption of chemical molecules on the surface of the photocatalyst. The mechanism indicates the formation of $C_2H_5OH$ via the formaldehyde pathway, which promotes the synthesis of selective ethanol and decreases the energy barrier of C-C interaction. This study serves as motivation for further refining the photocatalytic system to achieve effective, sustainable, and commercially feasible photocatalytic $CO_2$ reduction. It describes a photocatalytic system that efficiently delivers the surface activation and selective reduction of $CO_2$ to ethanol.

# Chapter 4

## *Synthesis, characterization and photocatalytic performance study of N-doped rGO/$BiVO_4$nanocomposite photocatalyst for selective photo-reduction of $CO_2$ to formic acid.*

**Highlights:**

- (2.5%)rGO/BiVO4 nanocomposite doped with different weight percentages of nitrogen (N) (1, 1.5, and 2%) is manufactured hydrothermally.
- The photocatalyst shows an enhanced absorption edge of visible light at 659.39 nm, the smallest band gap of 2.06 eV, and the lowest rate of electron-hole pair recombination,
- The optimum 1.5 weight % N-doped (2.5%)rGO/BiVO4 nanocomposite photocatalyst offers an enhanced yield of selective formic acid production of 592.80 μmol $g_{cat.}^{-1}$ $h^{-1}$with 100% selectivity and 0.0148% apparent quantum yield.

## 4.1 Introduction

A unique and fascinating family of materials among visible-light-driven semiconductors for photocatalytic $CO_2$ that has been recently evaluated is the bismuth-based photocatalyst. One of the best solar-driven photocatalyst materials discovered to date is bismuth vanadate ($BiVO_4$) [284-286]. Low bandgap, strong chemical and physical stability, high absorption efficiency in the visible range, and low toxicity are just a few of the many intriguing characteristics of $BiVO_4$. Out of the three crystalline phases—the tetragonal zircon type, the monoclinic scheelite type, and orthoclinic scheelite type:the monoclinic phase with the narrow band gap of 2.4 eV ($\lambda$<520 nm) is the most active in the visible spectrum [287-290].$BiVO_4$ can absorb a significant amount of visible light due to its low bandgap. $BiVO_4$ has been studied extensively for $CO_2$ photoreduction up to this point, but the primary barrier is still its low catalytic conversion efficiency. This is mainly caused by a number of interrelated variables, such as weak $CO_2$ adsorption on the $BiVO_4$ surface in the presence of $H_2O$ and quick electron-hole (e-h+) recombination. Many approaches, including increasing $CO_2$ adsorption on $BiVO_4$, band gap engineering, and combining with other semiconductors and co-catalysts, have been tried in the past to increase the catalytic activity of $BiVO_4$. It has been demonstrated that one way to successfully increase the photocatalytic rate of $CO_2$ reduction is to improve the adsorption of $CO_2$ on $BiVO_4$, thereby converting the thermodynamically stable $CO_2$ molecule into more reactive carbon species (e.g., carbamate and bicarbonate) for further reduction. Therefore, techniques such functionalizing the surface with amine-containing groups or expanding the surface area by either forming a porous structure or distributing $BiVO_4$ on high-surface-area supports have been proposed to improve the adsorption and activation of $CO_2$ [290-295].

Due to its large surface area and planar structure connected to the 2D lattice structure made up of $sp^2$-bonded carbon atoms, graphene is thought to be one of the most promising adsorbents currently under development for $CO_2$ absorption and storage. Prior research has demonstrated that selective functionalization with nitrogen dopants can significantly increase $CO_2$ absorption on carbon materials [296-298]. The literature has determined the amounts of $CO_2$ adsorption on virgin graphene and N-graphene (nitrogen doped graphene) materials. The outcomes show how crucial N dopants are in establishing the ideal $CO_2$ adsorption on N-graphene materials since they serve as basic sites for anchoring $CO_2$ molecules. Additionally, the electrical characteristics and local surface reactivity of graphene are both considerably changed by the nitrogen (N) dopants, which raises the possibility of using it in photocatalytic

applications. Thus, the research is still going on the functionalization of N-doping, which will be a successful method to improve graphene materials' $CO_2$ adsorption and $CO_2$ reactivity. However, there haven't been many investigations on N-graphene based photocatalysts for $CO_2$ photoreduction [299-313]. It is also essential to elaborate on the roles that the N dopant plays in $CO_2$ photoreduction.

The specific **objectives** of this chapter are enlisted below:

- **i.** Design and synthesis of visible light responsive $BiVO_4$ photocatalysts by incorporating different weight percentages of rGO concentration to investigate the optimum rGO loading for enhancing the yield of $CO_2$-reduced products.
- **ii.** Modification of (optimum-rGO)/$BiVO_4$ nanocomposite photocatalysts by different weight percentages (1%, 1.5%, and 2%) of nitrogen (N)-doping to get optimal N-doping for achieving the maximum yield of specific product selective $CO_2$ reduction.
- **iii.** Characterization of all synthesized photocatalysts by XRD, SEM, TEM, EDX, Uv-Vis absorbance, Band-gap, EIS, BET, and XPS.
- **iv.** Photocatalytic performance study of synthesized doped and undoped nano-composite photocatalysts.
- **v.** Prediction of mechanism of $CO_2$ photo-reduction.

The major research problem is addressed in this chapter; the problem definition is as follows:

- **Problem definition:**

***Synthesis, characterization and photocatalytic performance study of N-doped rGO/$BiVO_4$nanocomposite photocatalyst for selective photo-reduction of $CO_2$ to formic acid.***

## 4.2 EXPERIMENTAL SECTION

### 4.2.1 Materials:

All of the ingredients and precursors including bismuth nitrate pentahydrate ($Bi(NO_3)_3.5H_2O$), ammonium metavanadate ($NH_4VO_3$), cetyltrimethylammonium bromide (CTAB), sodium bicarbonate ($NaHCO_3$), urea ($CO(NH_2)_2$), deionised water, nitric acid

(HNO3), graphite flakes, potassium permanganate ($KMnO_4$), sulphuric acid ($H_2SO_4$), hydrogen peroxide ($H_2O_2$), phosphoric acid ($H_3PO_4$), sodium hydroxide (NaOH), hydrochloric acid, and ethanol are of analytical quality; they are highly pure materials that are acquired from Sigma Aldrich and used without additional purification.

### 4.2.2 Synthesis of N-rGO/$BiVO_4$:

#### 4.2.2.1 Synthesis of $BiVO_4$:

$BiVO_4$ nanocomposite are synthesized by CTAB modified hydrothermal treatment. Typically, 0.8 mmol $Bi(NO_3)_3 \cdot 5H_2O$ and 0.8 mmol $NH_4VO_3$ are added separately into two solutions of absolute ethanol (10 mL) and stirring for 40 min. at room temperature. Afterwards, two solutions are mixed and further kept it for 30 min. stirring procedure and then the nitric acid solution containing 0.26 g of cetyltrimethylammonium bromide (CTAB) is added drop wise and kept it for another 40 min stirring at room temperature. Then the pH is adjusted to 9 using 2 (M) sodium hydroxide solution and the colour of the final mixture are changed to yellow. The yellow solution is transferred into a 100 mL stainless steel autoclave with a Teflon lining, and it is heated to 180°C for 24 h. To obtain $BiVO_4$ photocatalysts, the reaction mixture is allowed to cool to room temperature. The precipitate is then further filtered, cleaned with distilled water, and dried in a vacuum oven at 70°C for 12 h.[291,292,314].

#### 4.2.2.2 Synthesis of rGO/$BiVO_4$:

The rGO/$BiVO_4$ nanonanocomposites are fabricated through the hydrothermal process. Firstly, different wt% of GO (1.5%, 2%, 2.5%, and 3%) is dispersed in 20 mL of absolute ethanol and de-ionized water mixture separately with sonication for 1 h. In this procedure a fixed amount of synthesized $BiVO_4$ is mixed with 1.5%, 2%, 2.5%, and 3% GO solution separately and after 1 h stirring those mixture are transferred into 100 mL Teflon-lined stainless steel autoclave separately and heated to 180°C for 24 h. After cooling, the prepared nanonanocomposites are washed with DI water and ethanol, and dried in a vacuum oven at 70°C for 12 h. The final products 1.5% rGO/ $BiVO_4$, 2% rGO/ $BiVO_4$, 2.5% rGO/ $BiVO_4$, and 3% rGO/ $BiVO_4$ are labeled as 1.5%G/BV, 2%G/BV, 2.5%G/BV, and 3%G/BV, respectively [315-317].

#### 4.2.2.3 Synthesis of N-rGO/$BiVO_4$:

Graphene oxide (GO) is prepared from graphite flakes by modified Hummer's method. A typical synthesis of nitrogen doped reduced graphene oxide/ $BiVO_4$ composite is as follows: 2.5 wt.% of GO is dispersed in 20 mL of absolute ethanol and de-ionized water mixture with sonication for 1 h. Then, 1:1 molar ratio of Bi $(NO_3)_3 \cdot 5H_2O$ and $NH_4VO_3$ are added separately into two solutions of absolute ethanol (10 mL) and stirring for 1 h at room temperature. The separately prepared Bi $(NO_3)_3 \cdot 5H_2O$ and $NH_4VO_3$ solutions are mixed together and the nitric acid solution containing 0.26 g of cetyltrimethylammonium bromide (CTAB) is added drop wise and kept it for 1 h stirring at room temperature. Then the above mixture is further added to previously prepare 2.5%GO solution and kept it for 1 h stirring. Then the pH is adjusted to 9 using 2 (M) sodium hydroxide solution drop wise and stirred for 30 min. Then, different weight percentage of urea dissolved in distilled water are added to the above solution separately and stirred for 1 h to obtain a stable slurry of 1%, 1.5%, and 2% N-doping in rGO/$BiVO_4$ nanocomposite. The resulting mixtures are transferred into 100 mL Teflon lined stainless steel autoclave and heated to 180°C for 24 h. The reaction mixtures are allowed to cool at room temperature and the precipitates are filtered, washed with distilled water and dried in a vacuum oven at 70°C for 12 h to get final products. The products 1%N-(2.5%)rGO/$BiVO_4$, 1.5%N-(2.5%)rGO/$BiVO_4$, and 2%N-(2.5%) rGO/$BiVO_4$ are labeled as 1%N-(2.5%)G/BV, 1.5%N-(2.5%)G/BV, and 2%N-(2.5%)G/BV, respectively.

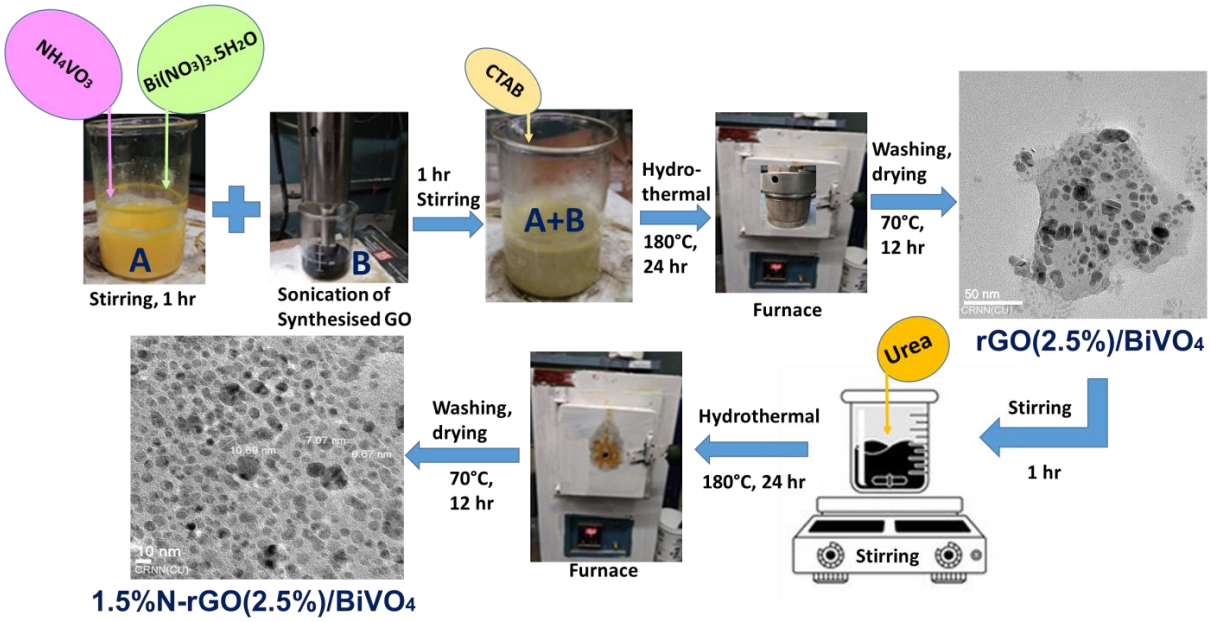


**Fig. 4.1: Schematic representation of synthesis process of 1.5%N-doped (2.5%)rGO/$BiVO_4$ photocatalyst**

### 4.2.3 Photocatalytic activity evaluation:

The photocatalytic activity of the synthesized photocatalysts $BiVO_4$, $rGO/BiVO_4$, and $N\text{-}rGO/BiVO_4$ is studied using a 100-watt Xenon-lamp of a solar simulator (Newport-Oriel-LCS-100, Manual shutter, 94011A), supported by an air mass filter (AM-1.5G), as the source of visible light source. The light intensity of the Xenon-lamp is 100 $mW/cm^2$ and the light area is 16.82 $cm^2$. For the evaluation of the photocatalytic activity, 0.030 g of each photocatalyst is used in a 100-mL hollow-quartz photoreactor separately. Before light (full spectrum) illumination, 99.9% pure $CO_2$ gas with a moderate flow rate is introduced into the degassed reactor to reach 1 atm pressure. To create a saturated solution of $CO_2$ and maximize $CO_2$ adsorption on the active sites of the photocatalyst, 80 ml of ultrapure water containing 0.5 M $NaHCO_3$ as hole-scavengers are added to the quartz reactor. To completely remove all of the dissolved oxygen in the saturated solution, the entire procedure is run under magnetic stirring conditions for 60 min. in the dark. The photocatalytic reaction is then carried out for 8 h at 18°C under the visible light irradiation of the specified 100-watt Xenon lamp with continuous stirring speed, as shown by Fig. 4.2. After that, 0.030 g of photocatalysts are added to the previously stated saturated solution. Additionally, a UV protector setup is employed to let visible light into the photocatalytic reactor. The photocatalytic $CO_2$-reduced products are extracted from the reactor solution after 8 h of light illumination using a thin pipe attached to a syringe. The concentration of each product is measured using gas chromatography mass spectrometry (GCMS) equipment, which includes an Agilent-7890A system, GC (FID), and GC (TCD), using helium as the carrier gas. To make sure that the products come from photocatalytic $CO_2$ reduction alone, blank reactions are conducted.

The entire experiment is conducted using the identical operating conditions in the absence of a photocatalyst. Second, under the same operating conditions, the entire experiment is conducted in total darkness with a photocatalyst present. Thirdly, a Xenon lamp is used to illuminate the blank experiment, and the photocatalyst in the photocatalytic quartz reactor is present without the need to purge $CO_2$ gas. To verify the caliber of the $CO_2$-reduced product, analysis is also conducted using the pure grades of formic acid. A 420 nm band pass filter is used to quantify the apparent quantum yield (AQY). For 4 h, a 100 Watt Xenon lamp with a 420 nm band pass filter is used to illuminate the photocatalyst solution. To calculate the apparent quantum yield (AQY) of the product evolution, the following equation is used [318-320].

$$\text{AQY} = \frac{\text{Number of reacted electrons}}{\text{Number of incident photons}} \times 100 \qquad (4.1)$$

$$= \frac{\text{Number of evolved formic acid (HCOOH) molecules} \times 2}{\text{Number of incident photons}} \times 100\%$$

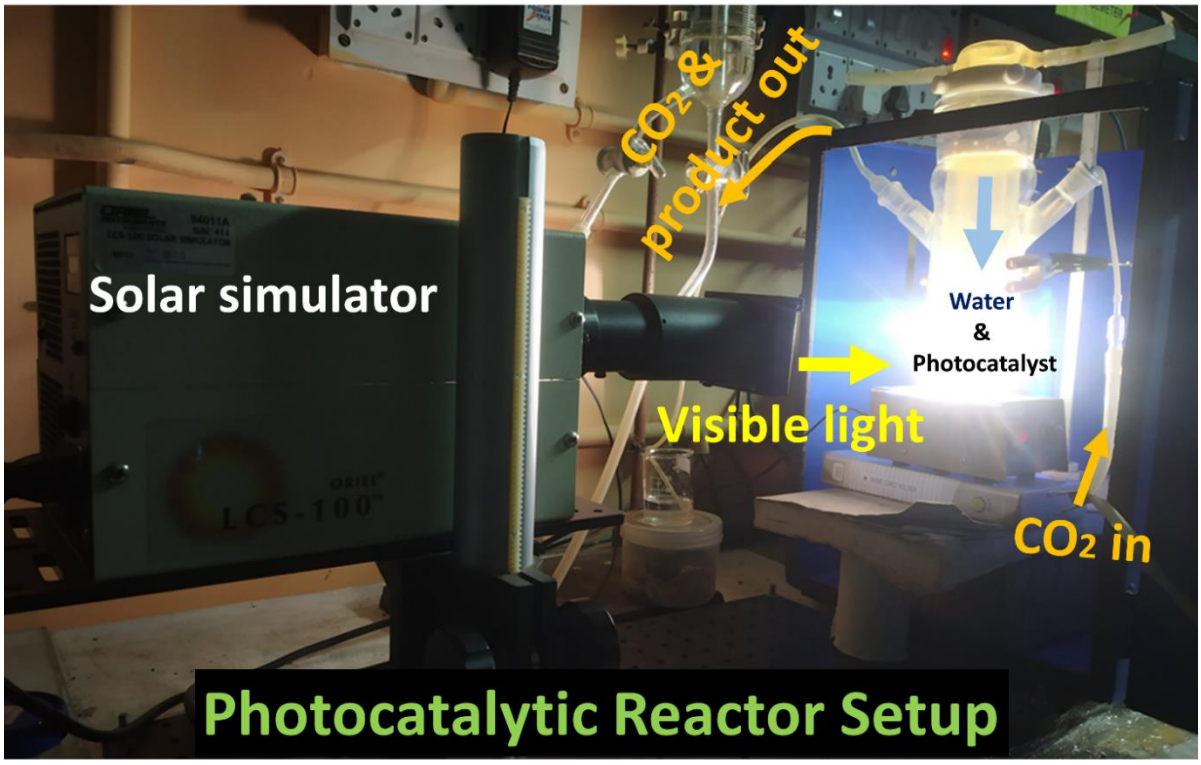


**Fig. 4.2: Schematic representation of the photocatalytic reactor setup for performance activity study of 1.5%N-rGO(2.5%)/$BiVO_4$ (1.5%N-(2.5%)G/BV) photocatalyst**

### 4.3 Results and Discussion

#### 4.3.1 Morphology, Structure, Crystal plane, Composition analysis:

The scanning electron microscopy (SEM) and transmission electron microscopy (TEM) have been conducted to analyse the morphology and nanostructure composition of as-prepared $BiVO_4$ (BV) nanocomposites. As shown in Fig. 4.3(c), the synthesized $BiVO_4$ has a two dimensional nano-hexagonal like morphology. 1.5% N doping and rGO incorporation in

$BiVO_4$ to form uniform nanostructures on the surface of rGO sheets (Fig. 4.3(e)), which is responsible for increasing the exposed surface-active zones to enhance the carbon dioxide

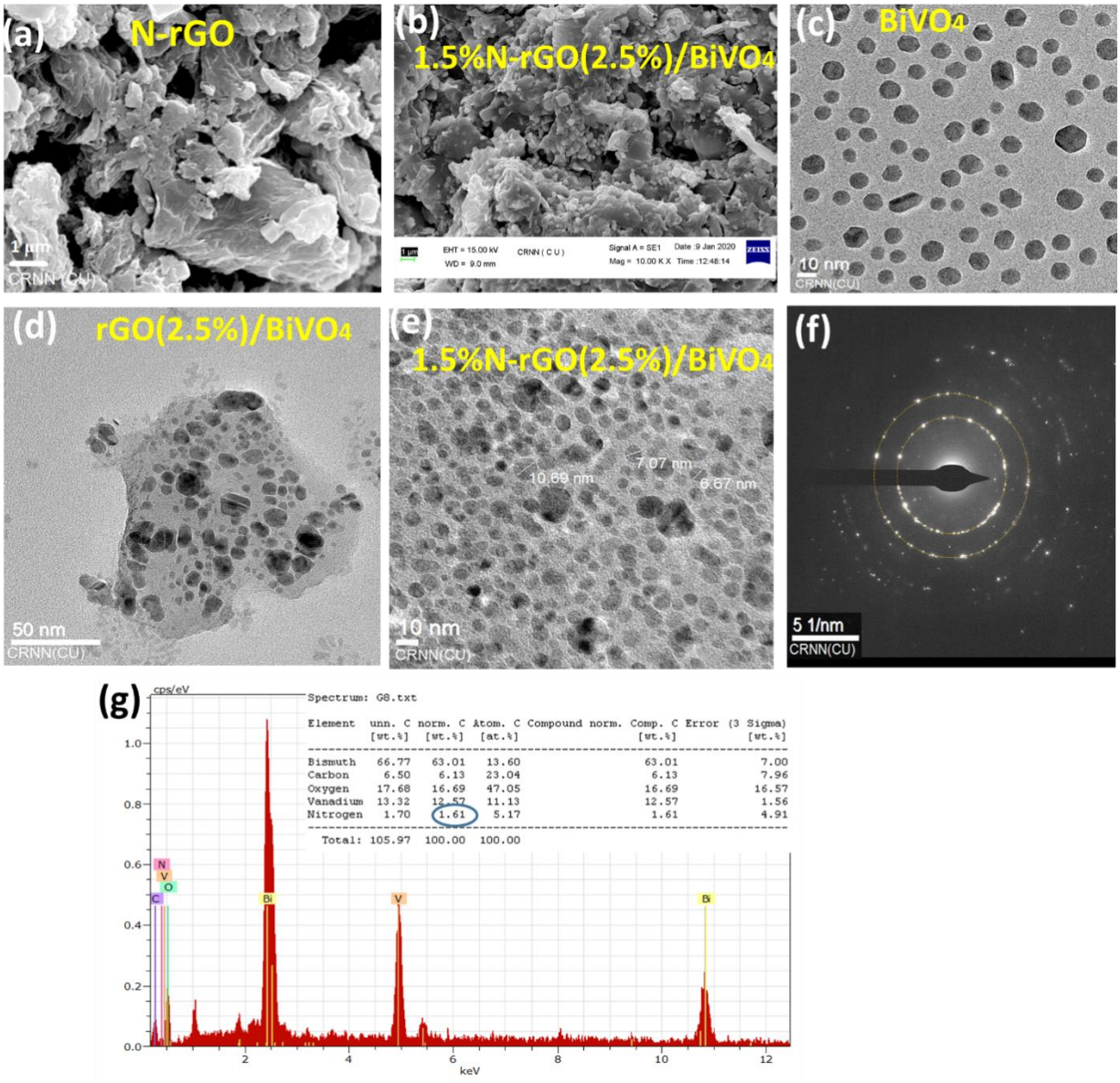


**Fig. 4.3: SEM image of (a) 1.5%N-rGO(2.5%), and (b) 1.5%N-(2.5%)rGO/$BiVO_4$ (1.5%N-(2.5%)G/BV). TEM image of (c) $BiVO_4$ (BV), (d) rGO(2.5%)/$BiVO_4$ ((2.5%)G/BV), and (e) 1.5%N-(2.5%)rGO/$BiVO_4$ (1.5%N-(2.5%)G/BV) nanocomposite. (f) SAED patterns of 1.5%N-(2.5%)rGO/$BiVO_4$ (1.5%N-(2.5%)G/BV) nanocomposite. (g) EDX spectrum of 1.5%N-(2.5%)rGO/$BiVO_4$ (1.5%N-(2.5%)G/BV)**

adsorption. The average size of 1.5%N-(2.5%)rGO/$BiVO_4$ approximately 6-10 nm is clearly seen in the Fig. 4.3(e). In Fig. 4.3(b), the SEM image shows that the $BiVO_4$ (BV) are embedded in the N-rGO sheets, which is also clearly visible in the TEM image of Fig. 4.3(e).

In Fig. 4.3(d), the TEM image also shows the enhanced contact between the $BiVO_4$ (BV) and the crumpled 1.5%N-(2.5%)rGO sheets. The SEM image of Fig. 4.3(a) shows the formation of N-rGO sheet. In Fig. 4.3(f), the SAED image confirms the single crystallinity (121) of the BV in 1.5%N-(2.5%)G/BV nanocomposites. In Fig. 4.3(g), EDX image, showing the elemental analysis of 1.5%N-(2.5%)rGO/$BiVO_4$ (1.5%N-(2.5%)G/BV) nanocomposites, confirms the successful doping of 1.5%N and 2.5%rGO loading in BV composite and the presence of N, C, O, V, and Bi element, respectively.

#### 4.3.1.1 XRD analysis:

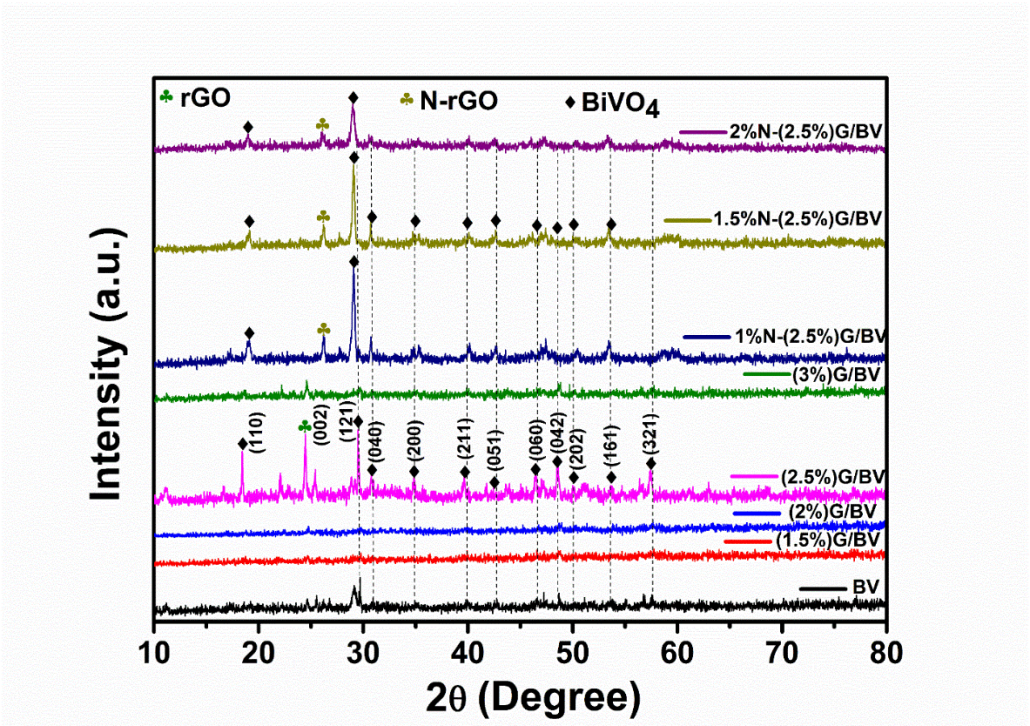


**Fig. 4.4: XRD patterns of $BiVO_4$ (BV), (1.5%, 2%, 2.5%, 3%)G/BV, and (b) (1%, 1.5%, 2%)N-(2.5%)G/BV nanocomposites**

The powder X-ray diffraction determined the crystallinity and crystal phase of the synthesized materials. The XRD pattern (Fig. 4.4) exhibits the formation of monoclinic scheelite $BiVO_4$ with lattice parameters a=0.5205 nm, b=1.1721 nm, and c=0.5019 nm, which are in good agreement with the reported values a=0.5195 nm, b=1.1700 nm, and c=0.5092 nm (JCPDS card No. 014–0688) [314-317]. The $BiVO_4$ is pure monoclinic with hexagonal structure as confirmed by the splitting of the diffraction peaks at 2θ=18.52°, 29.52°, 30.86°, 35.03°, 39.67°, 42.72°, 46.51°, 48.58°, 50.17°, 53.59°, and 57.50°, which can

be indexed to (110), (121), (040), (200), (211), (051), (060), (042), (202), (161), and (321), respectively. The hexagonal truncated structure of $BiVO_4$ is known to provide efficient active sites for photocatalysis under solar visible light irradiation. Actually the use of CTAB in the synthesis procedure leads to the formation of the monoclinic scheelite $BiVO_4$. The XRD analysis of the rGO/$BiVO_4$ composite exhibits the characteristic peaks same as of $BiVO_4$ and the peak located at approximately 24.51° corresponds to the (002) crystal plane of rGO. Due to 1.5 wt% N doping in (2.5%)rGO/$BiVO_4$ composite the XRD analysis of the synthesised 1.5%N-(2.5%)rGO/$BiVO_4$ composite exhibits the characteristic peaks same as the characteristic peaks of $BiVO_4$ with slightly decreased values of 2θ and the rGO peak at 24.51° shifted to 26.22°, indicating the formation of N-rGO, which also manifest that the 1.5%N is successfully doped in (2.5%)rGO/$BiVO_4$ composite during hydrothermal treatment. No additional peaks of N are observed in the XRD pattern, indicating the low wt% of N doping in rGO/$BiVO_4$ nanocomposites. In addition, the mean crystallite size of 1.5%N-(2.5%)rGO/$BiVO_4$ (1.5%N-(2.5%)G/BV) calculated using the Debye–Scherrer formula is approximately 21.52 nm.

#### 4.3.1.2 XPS analysis:

The surface composition and elemental chemical states of 1.5%N-doped rGO(2.5%)/$BiVO_4$ (1.5%N-(2.5%)G/BV) nanocomposites have been analyzed using X-ray photoelectron spectroscopy (XPS). Fig. 4.5(f) shows the survey spectra of the pure $BiVO_4$, rGO(2.5%)/$BiVO_4$ and 1.5%N-(2.5%)G/BV nanocomposite, which exhibit characteristic V 2p, Bi 4f, O 1s, C 1s, and N 1s peaks, without any contaminants. Furthermore, Bi 4f7/2 and Bi 4f5/2, with lower binding energies of 156.39 eV and 161.70 eV than BV and (2.5%)G/BV, respectively, make up the high-resolution Bi 4f XPS spectrum of the 1.5%N-(2.5%)G/BV nanocomposite [Fig. 4. 5(a)], indicating that the Bi in $BiVO_4$ is in the $Bi^{3+}$ oxidation state. The O 1s XPS spectra of 1.5%N-(2.5%)G/BV nanocomposite [Fig. 4.5(b)] show three distinct peaks with lower binding energies of 527.15 eV, 529.52 eV, and 531.15 eV than other nanocomposites, which can be indexed to Bi-O, -OH, and C-O/C=O groups, respectively. However, the O 1s spectrum of 1.5%N-(2.5%)G/BV nanocomposite shows the high-intensity peak at 527.15 eV which are attributed to the Bi-O group due to 1.5%N doping in (2.5%)G/BV nanocomposite. Additionally, two peaks at 513.89 eV and 521.17 eV in the V 2p spectra in [Fig. 4.5(c)] are assigned to V 2p3/2 and V 2p1/2, respectively, and exhibit that V is present in the $V^{5+}$ oxidation state. Fig. 4.5(e) is N 1s spectrum which shows three

different peaks such as 396.81 eV, 400.06 eV and 403.93 eV corresponds to pyridinic-N or C-N bond, pyrrolic-N and quaternary-N,

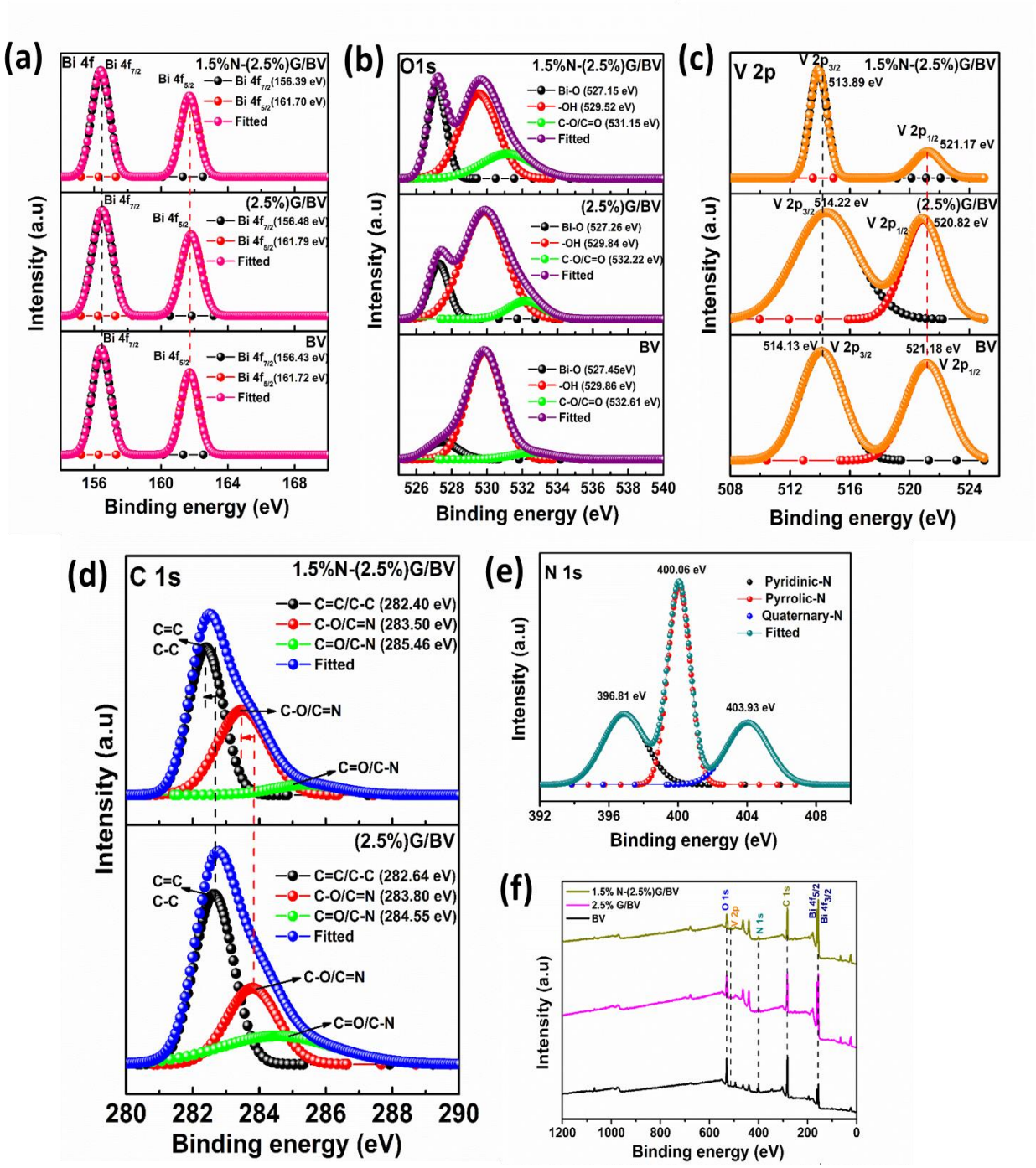


**Fig. 4.5: (a) Comparison of XPS scan of Bi 4f among BV, (2.5%)G/BV, and 1.5%N-(2.5%)G/BV. (b) Comparison of XPS scan of O 1s among BV, (2.5%)G/BV, and 1.5%N-(2.5%)G/BV. (c) Comparison of XPS scan of Mo 3d among BV, (2.5%)G/BV, and 1.5%N-(2.5%)G/BV. (d) Comparison of XPS scan of C 1s between (2.5%)G/BV and 1.5%N-(2.5%)G/BV. (e) XPS scan of N 1s of 1.5%N-(2.5%)G/BV. (f) Comparison of XPS full survey scan among BV, (2.5%)G/BV, and 1.5%N-(2.5%)G/BV photocatalysts**

respectively [292,299,320]. Fig. 4.5(d) shows the high-resolution C 1s spectrum, which exhibits three peaks at 282.40 eV, 283.50 eV, and 285.46 eV. The peak at 282.40 eV is associated with the $sp^2$ carbon (C=C) and $sp^3$ carbon (C-C) in the material, respectively. The peak at 283.50 eV is ascribed to C-O/C=N. The peak at 285.46 eV is associated with C=O.The negative shift of peak to low binding energy value in C 1s indicates that N & C atoms in N-rGO play the electron accepting role.which is further confirmed by the XRD and TEM analysis of 1.5%N-(2.5%)G/BV nanocomposites.As per C 1s spectra, the shifting of C=N or C-N peak exhibits the strong electron integrated interface between $BiVO_4$ and 1.5%N-rGO(2.5%) which further accelerates the electrons transportation from the surface of $BiVO_4$ to active sites of N-rGO sheets; on these active sites more $CO_2$ can be adsorbed for participating in photocatalytic $CO_2$ reduction process to enhance the yield of selective formic acid production. Finally, the XPS analysis confirms that the 1.5%N-doped rGO(2.5%)/$BiVO_4$ nanocomposites (1.5%N-(2.5%)G/BV) photocatalyst is successfully synthesized [305-309].

### 4.3.2 Spectroscopic analysis:

#### 4.3.2.1 UV-Vis Analysis

The optical property of pristine $BiVO_4$, $BiVO_4$/rGO (1.5%, 2%, 2.5%, 3%), and (1%, 1.5%, 2%) N-doped rGO (1.5%, 2%, 2.5%, 3%)/$BiVO_4$ are analyzed by UV–vis absorption spectrum (Fig. 4.6(a)). The absorption edge of pristine $BiVO_4$ and $BiVO_4$/rGO(2.5%) locates at approximate 550 nm and 602 nm, respectively and the absorption edge of 1.5%N-(2.5%)G/BV locates at approximate 659.39 nm. 1.5%N doping in (2.5%)G/BV nanocomposites increases the visible light absorbance. This characteristic is beneficial for enhancing the photoinduced electron-hole pair's production. The increase in absorbance in the visible region is also shown in Fig. 4.6(a) in the following order: 1.5%N-(2.5%)G/BV > 1%N-(2.5%)G/BV > (2.5%)G/BV > (2%)G/BV > BV > (1.5%)G/BV > 2%N-(2.5%)G/BV > (3%)G/BV. In Fig. 4.6(b), it is found that when BV is combined with 2.5%rGO the band gap energy of BV is reduced from 2.50 eV to 2.27 eV for (2.5%)G/BV as the absorption edge of synthesised (2.5%)G/BV composite enhanced to 602 nm. It is also observed in Fig. 4.6(b) that the bandgap energy of the 1.5%N-(2.5%)G/BV photocatalyst is further reduced from 2.27 eV (for (2.5%)G/BV) to 2.06 eV due to 1.5%N doping in (2.5%)G/BV nanocomposites. 1.5%N doping in (2.5%)G/BV nanocomposites also exhibit the highest red shift in the absorption edge (659.39 nm) among all synthesised nanocomposites, which actually manifest the highest visible light energy harvesting capability. This highest enhancement can be

achieved due to the proper hybridization of N 1s, C 2p and V 2p states, which gives the highest production of photo-generated charge carriers and triggers the selective formic acid production as photocatalytic $CO_2$ reduced product. The tauc equation (4.2), [296-298] as illustrated below, is used to estimate the bandgap energies of each synthesised photocatalyst.

$$[\alpha h\nu] = A\left[h\nu - E_g\right]^{\frac{n}{2}} \qquad (4.2)$$

Where '$E_g$' (eV) is the bandgap of the photocatalyst, 'h' is Planck's constant, 'c' is the speed of light, 'ν' is the frequency of light, 'A' is the absorption coefficient, 'n' is 1 for direct bandgap and '4' for indirect bandgap of semiconductors. Table 4.1 presents the estimated bandgap energies and absorption edge (nm) values obtained from experimental analysis.

**Table 4.1 a comparison of band gap energy and absorption edge value of synthesised photocatalysts obtained from the experimental analysis.**

| Photocatalyst | Absorption edge (nm) | Band gap energy (eV) |
|---|---|---|
| $BiVO_4$ (BV) | 550.0 | 2.50 |
| (2%)rGO/$BiVO_4$ | 536.0 | 2.35 |
| (2.5%)rGO/$BiVO_4$ | 602.0 | 2.27 |
| (3%)rGO/$BiVO_4$ | 402.2 | 2.88 |
| 1% N-(2.5%)rGO/$BiVO_4$ | 500.05 | 2.20 |
| 1.5% N-(2.5%)rGO/$BiVO_4$ | 659.39 | 2.06 |
| 2% N-(2.5%)rGO/$BiVO_4$ | 409.25 | 2.78 |

#### 4.3.2.2 Photoluminescence (PL) spectroscopy

The migration, transfer, and recombination of photogenerated charge carriers in semiconductor photocatalysts have been studied using photoluminescence (PL) spectroscopy [308-310]. The PL analysis of all synthesized photocatalysts is carried out at an excitation wavelength of 380 nm, and the emission spectra are displayed in Fig. 4.6(c). Between 420 and 560 nm, the PL emission spectra of pure materials and nanocomposites have been examined. The photoluminescence intensity is directly correlated with the photocatalytic performance of semiconductor nanocomposites. More precisely, a higher PL peak intensity is indicative of a higher rate of electron-hole pair recombination, which lowers photocatalytic activity. Conversely, a lower peak intensity of photoluminescence indicates a lower rate of electron-hole pair recombination, which results in higher photocatalytic activity. The center of the primary emission peak at 470 nm is shown in Fig.4.6(c). The PL intensities of the samples used in this study are listed in descending order: BV > 1.5%G/BV > 3%G/BV >

2%G/BV > (2.5%).G/BV >1%N-(2.5%)G/BV >2%N-(2.5%)G/BV >1.5%N-(2.5%)G/BV. Every sample contains emission bands in the visible spectrum because to charge carrier recombination in BV. In the 1.5%N doping in (2.5%)rGO/$BiVO_4$ composite, an interface is established between 1.5%N-(2.5%)rGO and $BiVO_4$, which facilitates electron transportation and reduces charge carrier recombination. Based on the interfacial charge transfer between 1.5%N-(2.5%)rGO and $BiVO_4$, these results verify that 1.5%N-(2.5%)G/BV exhibits the lowest photogenerated electron-hole recombination rate. This allows for the maximum photocatalytic $CO_2$ reduction, leading to the selective synthesis of formic acid.

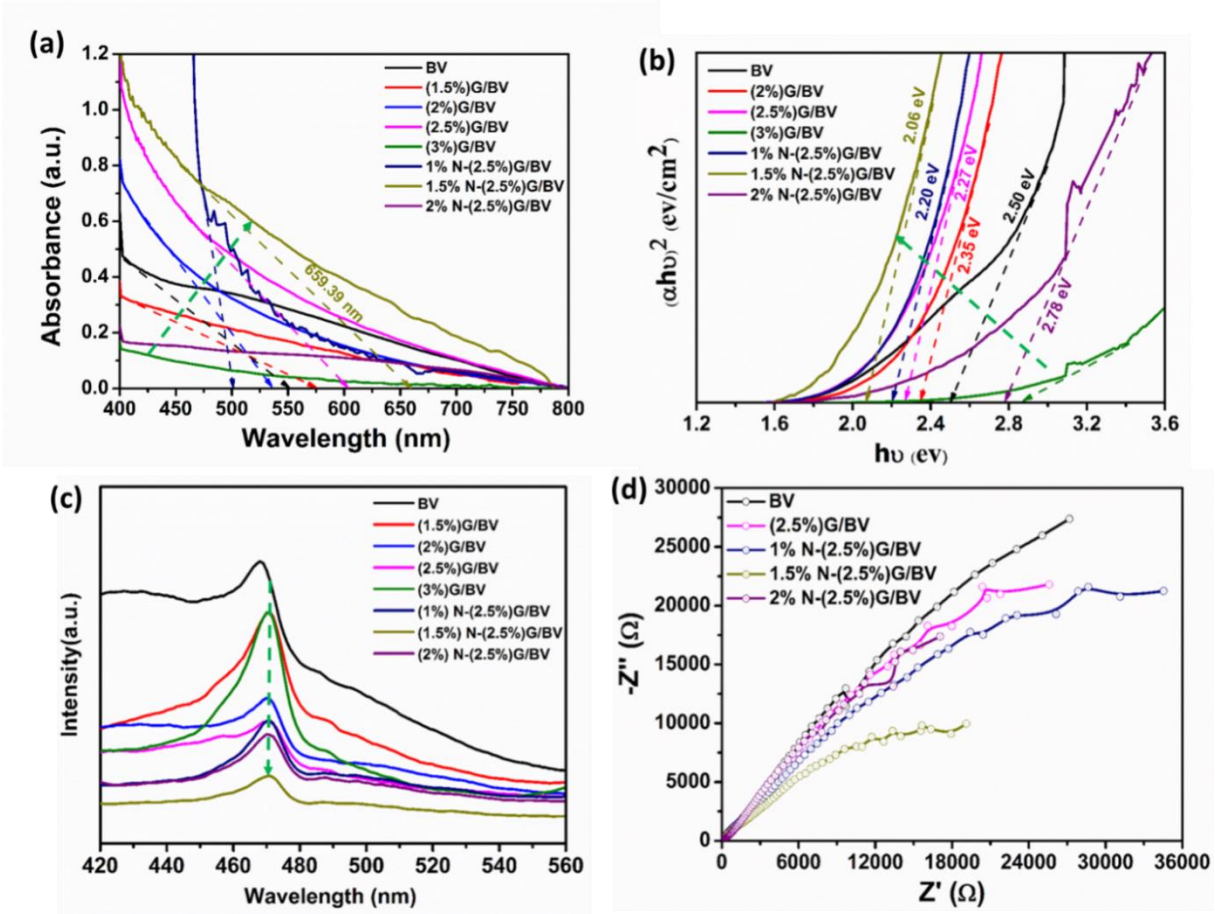


**Fig. 4.6: (a) UV-vis absorption spectra, (b) Estimated band gap energy (eV) by the Tauc plot of BV, (1.5%, 2%, 2.5%, 3%)G/BV, and (1%, 1.5%, 2%)N-(2.5%)G/BV photocatalysts, (c) Photoluminescence spectra (PL) of BV, (1.5%, 2%, 2.5%, 3%)G/BV, and (1%, 1.5%, 2%)N-(2.5%)G/BV photocatalysts an excitation wavelength of 380 nm, (d) EIS curves of BV, (2.5%)G/BV, and (1%, 1.5%, 2%)N-(2.5%)G/BV photocatalysts**

### 4.3.2.3 Electrochemical Impedance Spectroscopy (EIS)

The 1.5%N-(2.5%)G/BV photocatalyst has the shortest arc radius of any BV, G/BV, and N-G/BV composite, according to the electrochemical impedance spectroscopy (EIS) analysis shown in Fig. 4.6(d). This indicates a significant reduction in the photogenerated charge transfer resistance caused by 1.5%N doping. Higher photocatalytic activity is produced as a result of this phenomenon, which essentially speeds up the migration rate of high-speed interfacial charge carriers across the photocatalyst's contact surface. This allows the photogenerated electrons and holes to separate more successfully.

### 4.3.2.4 Nitrogen adsorption-desorption isotherms: BET surface area

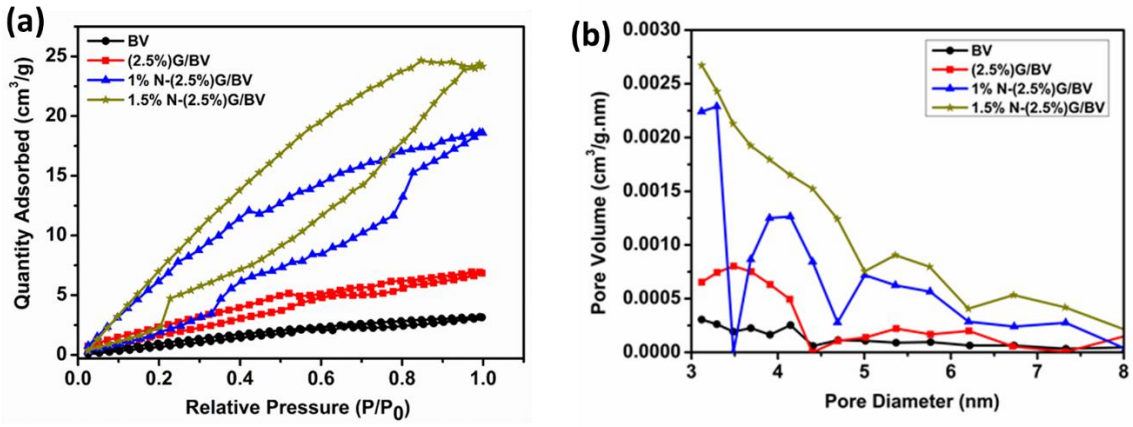


**Fig. 4.7: (a) Nitrogen adsorption-desorption isotherms and (b) pore-size distribution plot of BV, (2.5%)G/BV, and (1%, 1.5%)N-(2.5%)G/BV photocatalysts**

The $N_2$ adsorption desorption isotherm for BET surface area and the corresponding pore size distribution plot of BV, (2.5%)G/BV, 1%N-(2.5%)G/BV and 1.5%N-(2.5%)G/BV photocatalysts are shown in Fig. 4.7. The isotherms of all nanocomposites show typical H3 hysteresis loops, exhibiting the presence of slit pores in all samples. The calculated pore-size distribution in Fig. 4.7(b) manifests the average pore sizes of BV and all nanocomposites in the range of 3 to 6 nm, supporting the hypothesis that there are many mesopores present, which are the source of the high surface adsorption. The BET surface area of pristine BV is found to be 2.82 $m^2/g$, whereas (2.5%)G/BV photocatalyst shows a 6.74 $m^2/g$ specific surface area. It is clearly observed that due to 2.5%rGO loading in BV, the total specific surface area of (2.5%)G/BV photocatalyst as well as average pore sizes are increased. In Fig. 4.7(a), due

to 1.5%N doping in (2.5%)G/BV photocatalyst the highest specific surface area of 25.61 $m^2/g$ is observed for 1.5%N-(2.5%)G/BV photocatalyst among all synthesised photocatalysts. Since 1.5%N-(2.5%)G/BV has the maximum BET surface area, there are more surface-active sites available for the adsorption of reactant molecules ($CO_2$).

### 4.3.3 Performance analysis of photocatalytic $CO_2$ reduction:

The $BiVO_4$ (BV), (2.5%)rGO/$BiVO_4$ ((2.5%)G/BV), 1.5%N-(2.5%)rGO/$BiVO_4$ (1.5%N-(2.5%)G/BV ) nanocomposites are assessed for their photocatalytic activity performance during 8 h of visible light-driven photocatalytic $CO_2$ reduction reactions conducted in water at 18°C and atmospheric pressure. Fig. 4.8 demonstrates the significant role of N-rGO for producing selective C-1 product, the formic acid. Among all three N doped rGO/$BiVO_4$ nanocomposites 1.5%N-doped (2.5%)G/BV photocatalysts produce the highest yield of formic acid (Fig. 4.8(a)). GCMS analysis of $CO_2$ reduced products obtained using the optimum 1.5%N-(2.5%)G/BV photocatalyst (Fig. 4.8(d)) exhibits that the formic acid with 100% selectivity, is the ultimate product in the liquid phase, and no other carbonaceous compounds, such as HCHO, $C_2H_5OH$ or $CH_3OH$, are detected. The GC-TCD and GC-FID technologies are used to analyse the gaseous products. The outlet gas produced during the photocatalytic $CO_2$ reduction process contains no $H_2$, $CH_4$, or CO. Furthermore, control studies showed that in the absence of photocatalyst or light illumination, no significant amounts of HCOOH are produced, suggesting that both efficient photocatalysis and illumination are necessary for $CO_2$ reduction.

Furthermore, prior to $CO_2$ purging, a photocatalytic $CO_2$ reduction experiment is started within the reactor in a $N_2$ atmosphere, and the absence of any hydrocarbons indicated that $CO_2$ is the only carbon source utilised in the experiment. Using $CO_2$ as the carbon source, mass spectrum peaks of HCOOH are found at 29.61 and 32.53 m/z, respectively, during a retention time of 1.94 min, as seen in Fig. 4.8(d). The yields of HCOOH produced by BV, (2.5%)G/BV, 1.5%N-(2.5%)G/BV photocatalysts are shown in Fig. 4.8(a). The GCMS analysis of the BV nanocomposites is displayed in Fig. 4.8(b), the results of which are showing no HCOOH acid generation, which is also supported by NMR analysis in Fig. 4.9(a). The GCMS and NMR analysis of the (2.5%)G/BV nanocomposites is also displayed in Fig. 4.8(c) and Fig. 4.9(b), respectively. As predicted, the (2.5%)G/BV nanocomposites outperform the BV nanocomposites in yielding HCOOH (288.80 μmol $g_{cat.}^{-1}$ $h^{-1}$),

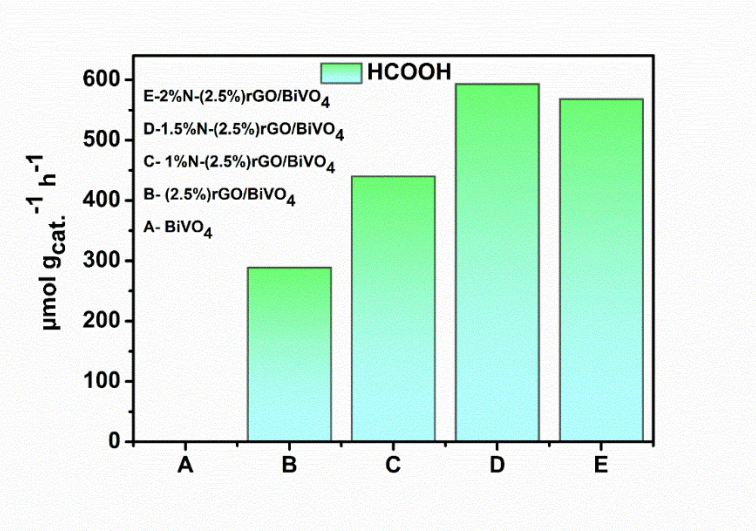


**Fig. 4.8(a): Yield of selective formic acid production rate for $BiVO_4$ (BV), (2.5%)rGO/$BiVO_4$ (2.5%)G/BV, and (1%, 1.5%)N-(2.5%)G/BV based photocatalytic $CO_2$ reduction system**

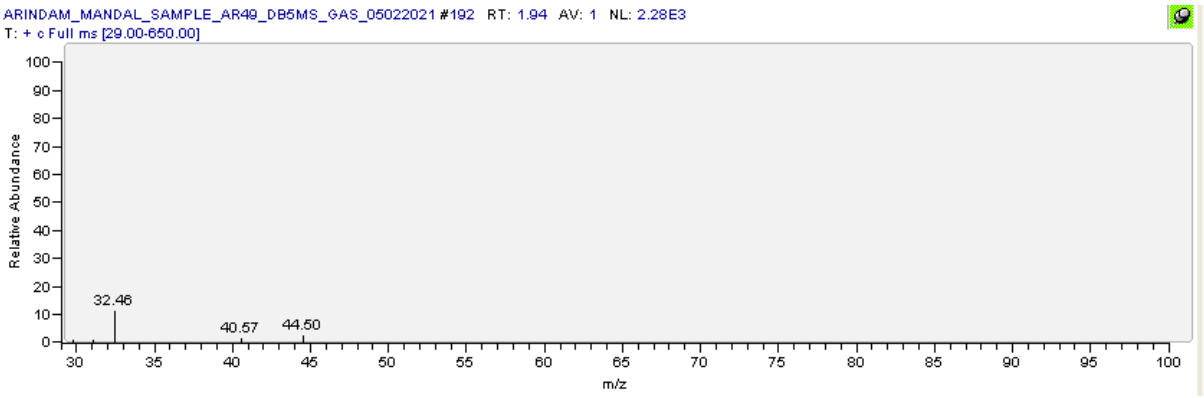


**Fig. 4.8(b): Mass spectrum analysis (GCMS) of the formic acid found over $BiVO_4$ (BV) nanocomposites**

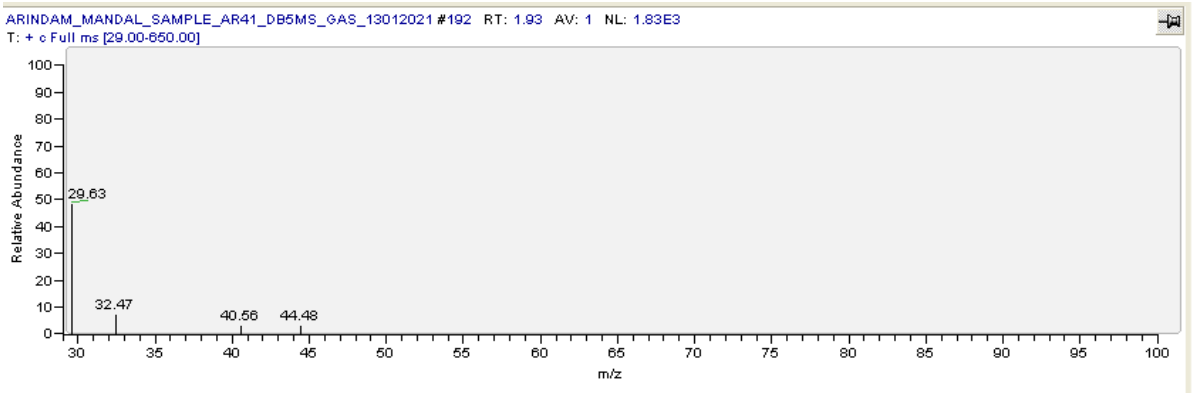


**Fig. 4.8(c): Mass spectrum analysis (GCMS) of the formic acid found over (2.5%)rGO/$BiVO_4$ (2.5%G/BV) nanocomposites**

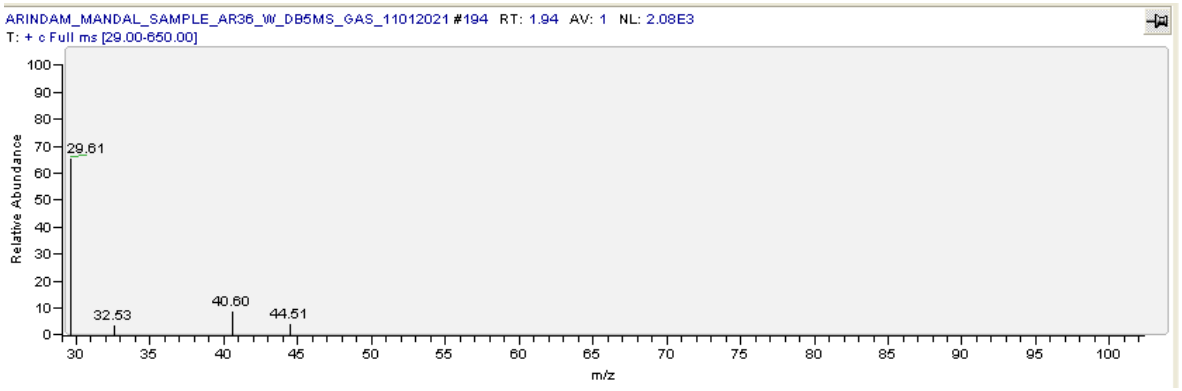


**Fig. 4.8(d): Mass spectrum analysis (GCMS) of the formic acid found over 1.5%N-(2.5%)rGO/$BiVO_4$ (1.5%N-2.5%G/BV) nanocomposites**

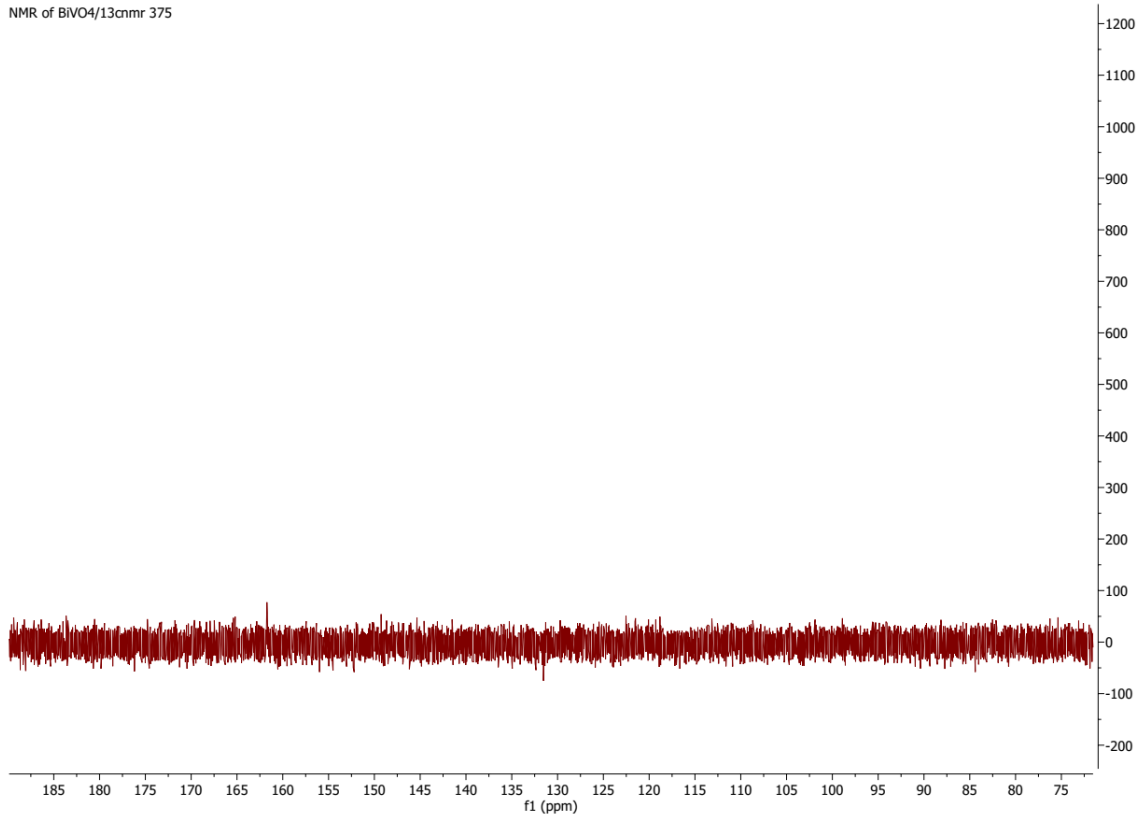


**Fig. 4.9(a): NMR analysis of the formic acid production over $BiVO_4$ (BV) nanocomposites**

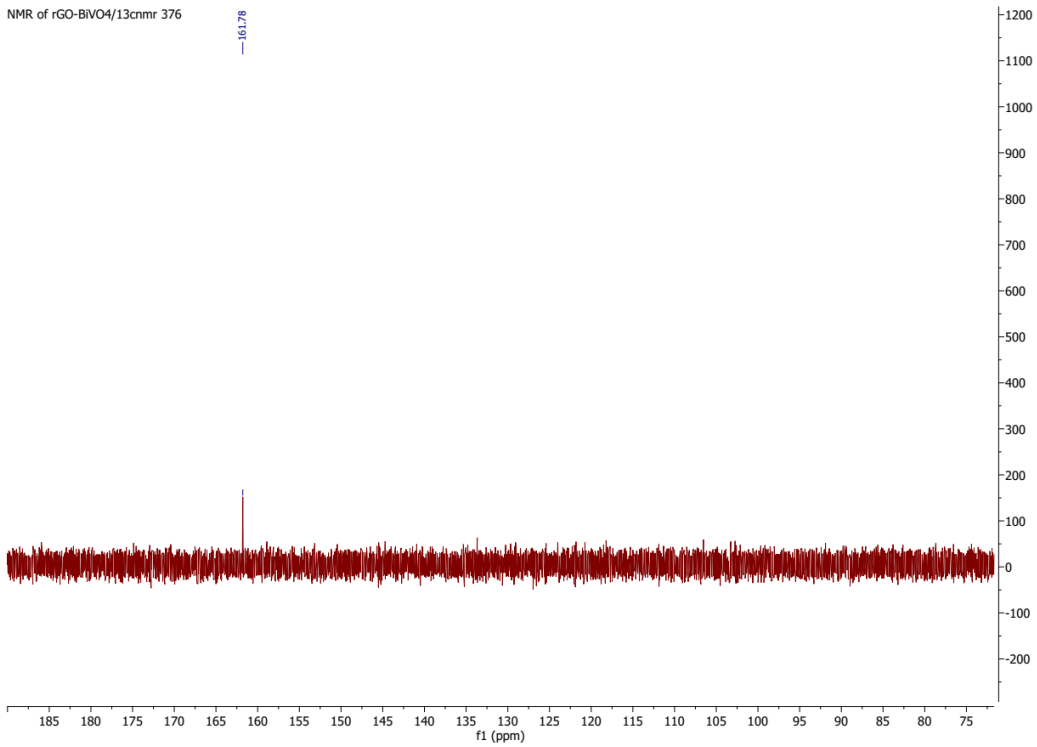


**Fig. 4.9(b): NMR analysis of the formic acid production over (2.5%)rGO/$BiVO_4$(2.5%G/BV) nanocomposites**

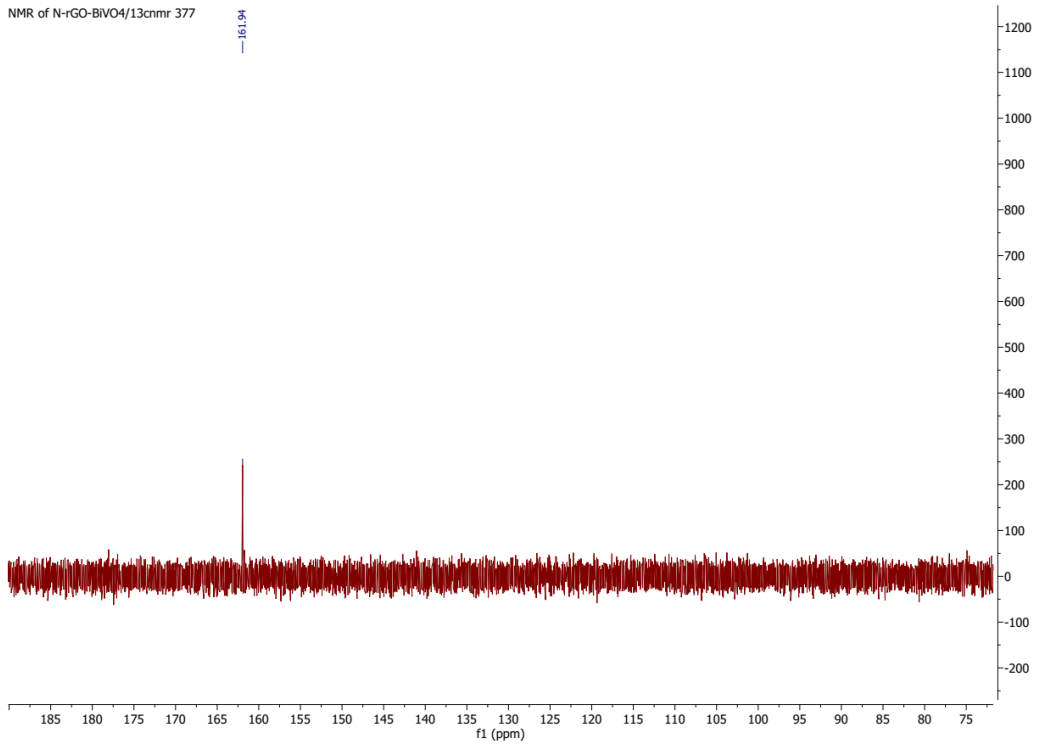


**Fig. 4.9(c): NMR analysis of the formic acid production over 1.5%N-(2.5%)rGO/$BiVO_4$ (1.5%N-2.5%G/BV) nanocomposites**

demonstrating the beneficial influence of the rGO layers. In Fig. 4.8(a), formic acid is produced selectively using 1, 1.5, and 2 wt% N doping; 1.5%N-(2.5%)G/BV photocatalysts provide the greatest formic acid yield in 8 h, with 592.80 μmol $g_{cat.}^{-1}$ $h^{-1}$. The formic acid production yield of 1.5%N-(2.5%)G/BV is 2.05 times that of (2.5%)G/BV nanocomposites. As a result of the photocatalytic activity study of the 1.5%N-(2.5%)G/BV photocatalyst, Fig. 4.8(d) displays the GCMS analysis of the highest selective formic acid formation as a $CO_2$ photo reduced product. The NMR analysis of 1.5%N-(2.5%)G/BV photocatalyst in Fig. 4.9(c) also suggests that 1.5%N doping shows the highest concentration (ppm) of formic acid in the product. Furthermore, AQY of 1.5%N-(2.5%)G/BV and (2.5%)G/BV are determined to be around 0.0148% and 0.0073%, respectively, based on measurements made at 420 nm. The AQY of 1.5%N-(2.5%)G/BV nanocomposites is approximately 2.03 times higher than that of (2.5%)G/BV nanocomposites. N doping in (2.5%)G/BV beyond the optimal loading decreases the photocatalytic activity of 2%N-(2.5%)G/BV nanocomposites and results in less formic acid production, as seen in Fig. 4.8(a). Nevertheless, increased N doping increases the number of active sites on the catalyst surface, which is favourable to the selective formic acid yield.

#### 4.3.4 Mechanism

The initial stage of the photocatalytic $CO_2$ reduction mechanism is the creation of a surface-bound metastable radical anion ($\cdot CO_2^-$), which is caused by the activation of $CO_2$ on the photocatalyst surface through the absorption of photons from visible light. The complete reduction process then occurs through a number of following phases. Protons and electrons are transferred, hydrogen radicals ($\cdot H$) are produced, C-O bonds are broken, and new C-H bonds are formed, among other processes. In this case, the formaldehyde production pathway is actually followed by the photocatalytic $CO_2$ reduction to formic acid [295,321,322], which is shown in Fig. 4.10. According to the formaldehyde route, formic acid (HCOOH) is produced as a result of the photocatalytic reduction of $CO_2$ by $\cdot CO_2^-$ (ad.) recombining with $H^+$ and electron. It is discovered that the absorption edges of 1.5%N-(2.5%)G/BV and (2.5%)G/BV are around 602 nm and 659.39 nm, respectively. The incorporation of N-rGO in $BiVO_4$ exhibits a broader spectrum of light absorption, suggesting a strong potential for light harvesting. The energy bandgap ($E_g$) of 1.5%N-(2.5%)G/BV is 2.06 eV, as determined by the tauc plot equation [Fig. 4.6(b)]. EIS measurements in Fig. 4.6(d) exhibit the shortest semicircle of 1.5%N-(2.5%)G/BV with the lowest charge trapping resistance among all

samples and also illustrate the interfacial charge transfer capacity as a result of N-rGO incorporation into $BiVO_4$.

$$\mathrm{N-rGO/BiVO_4} \xrightarrow{h\nu} h^+ (VB, \mathrm{BiVO_4}) + e^- (CB, \mathrm{N-rGO}) \quad (4.3)$$

$$H_2O + h^+ \rightarrow \cdot OH + H^+ \quad (4.4)$$

$$H^+ + e^- \rightarrow \cdot H \quad (4.5)$$

$$CO_2 + e^- \rightarrow \cdot CO_2^-(\mathrm{ad.}) \quad (4.6)$$

$$\cdot CO_2^-(\mathrm{ad.}) + 2H^+ + e^- \rightarrow HCOOH \quad (4.7)$$

$$CO_2 + 2H^+ + 2e^- \rightarrow HCOOH$$

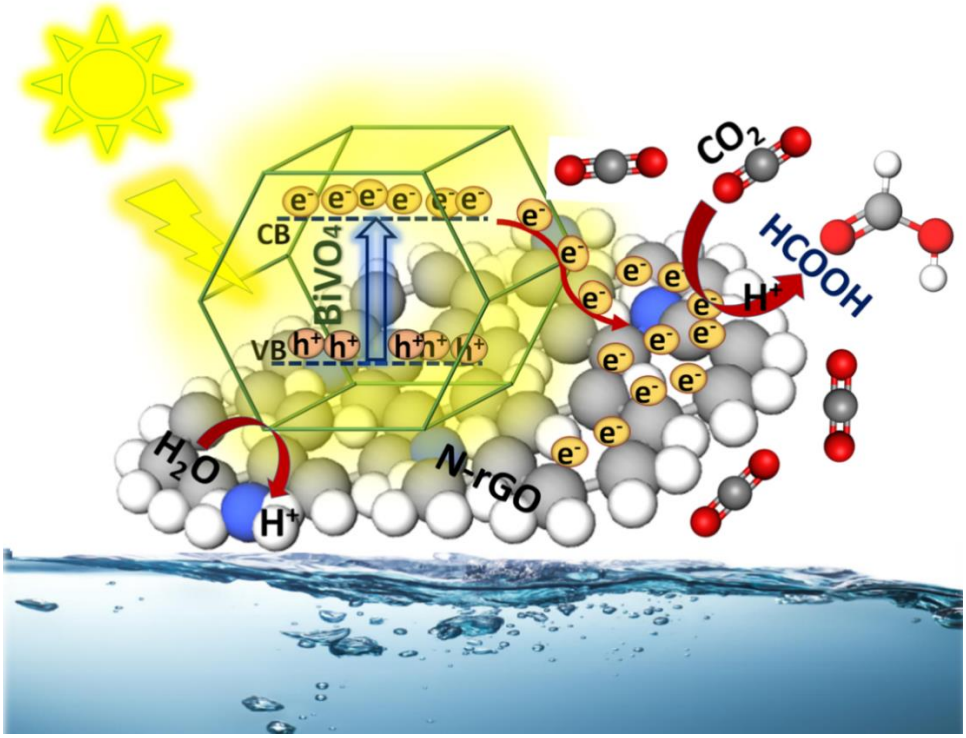


**Fig. 4.10:Schematic portrayal of the mechanism of photocatalytic reduction of $CO_2$ to selective formic acid using 1.5% N-doped (2.5%)rGO/$BiVO_4$ (1.5%N-(2.5%)G/BV) photocatalyst**

Furthermore, the smallest photoluminescence (PL) intensity of 1.5%N-(2.5%)G/BV in Fig. 4.6(c) confirms the lowest $e^-$-$h^+$ recombination efficiency. As evidenced by EIS, band-gap,

and PL, the combination of N-rGO with $BiVO_4$ ensures a notable enhancement in charge separation and migration as well as maximum photo-redox energy to produce improved photocatalytic activity. As a result, there are more photo-induced charge carriers available to improve the photocatalytic reduction of $CO_2$ to formic acid [Fig. 4.8(a)].Photo-induced electrons are accumulated on the $BiVO_4$-CB under visible light illumination. These electrons have strong reductive capabilities and can be transferred to the N-rGO nanosheets. This reduces electron-hole pair recombination and facilitates the transport of electrons to the active catalytic zones for photocatalytic carbon dioxide reduction. The large surface area of the N-rGO allows it to absorb $CO_2$. The photo-induced electrons that convert the adsorbed $CO_2$ into formic acid are accumulated in the catalytic zones of N-rGO. Here, two moles of photoinduced electrons interact with one mole of $CO_2$ and two moles of $H^+$ to reduce them to one mole of formic acid.

## 4.4 Conclusion

The 1.5%N-(2.5%)rGO/$BiVO_4$ photocatalyst is prepared by hydrothermal treatment. N-doping and rGO worked together to increase the photo-absorbance power of the $BiVO_4$ in the visible region of the solar spectrum. 1.5%N-(2.5%)rGO/$BiVO_4$ has the lowest rate of electron-hole pair recombination, the highest thermal stability, an improved specific surface area with a small pore diameter, and a promising band gap (2.06 eV) among all the synthesized photocatalysts. It also exhibits remarkably reduced charge transfer resistance and increased conductivity for improving the separation efficiency of the photo-generated charge carriers. Thus, it is also found that the 1.5%N-(2.5%)rGO/$BiVO_4$ photocatalyst is the most effective active catalyst for increased photocatalytic reduction of $CO_2$ to formic acid, with a rate of around 592.80 μmol $g_{cat.}^{-1}$ $h^{-1}$. Furthermore, N-rGO create new photoinduced reactive zones for charge carriers and improve photocatalytic activity, as shown by the effective charge carrier separation and the relocation of the absorption edge (659.39 nm) into the visible spectrum. N-doping in rGO increases the number of defective sites to capture $CO_2$ for enhanced photocatalytic $CO_2$ reduction to formic acid; the AQY for 1.5%N-(2.5%)rGO/$BiVO_4$ photocatalyst is found to be approximately 0.0148%. The purity of product is also shown by the GCMS analysis of the photocatalytic $CO_2$ reduction to formic acid.

# Chapter 5

## Summary and Future scopes

## 5.1 Outcomes of the research:

To reduce the accumulation of greenhouse gas $CO_2$ in the world environment and to meet the world energy demand, photocatalytic $CO_2$ reduction for selective product generation is one of the most attractive methods among CCUS technology.

- The major outcome of the present research work is the invention of reduced graphene oxide (rGO)-supported three different bismuth (Bi)-based tailor-made photocatalysts namely (i) Cu doped rGO/$Bi_2S_3$ 1D rod shaped nano-capsule, (ii) Cu doped rGO/$Bi_2MoO_6$ 2Dnano-ribbon and (iii) N doped rGO/$BiVO_4$ 2D nano-hexagon for 100% selective production of three industrially important valuable chemicals methanol, ethanol and formic acid, respectively. The optimum extent of doping that maximizes the yield of the selective product is explored for each case. Table 5.1 summarizes the overall research work performed and the results of it.
- Total 22 numbers of Bismuth based nano-materials including 9 number of Bismuth sulfide based, 8 number of Bismuth molybdate based and 5 number of Bismth vanadate based photocatalyst are synthesised, characterized and tested for Photocatalytic $CO_2$ reduction.
- In order to achieve product selectivity, doping using transition metal Cu is found as a superior technique compared to S Scheme heterojunction using CuO. Photo-reduction of $CO_2$ in presence of hydrothermally synthesized rGO-$Bi_2S_3$/CuO S-scheme heterojunction produces methanol (423.52 μmol $g_{cat.}^{-1}$ $h^{-1}$) as well as formic acid (17.48 μmol $g_{cat.}^{-1}$ $h^{-1}$); whereas using 1%Cu (the optimum) doped 1D-$Bi_2S_3$/rGO photocatalyst, the 100% selective methanol ($CH_3OH$) with highest yield of 719 μmol $g_{cat.}^{-1}$ $h^{-1}$ is obtained.
- In 1% Cu doped rGO/$Bi_2S_3$ 1D rod shaped nano-capsule, transition metal Cu is hybridized with carbon (C) of rGO and Bi of $Bi_2S_3$ and formed an interface layer between Cu-$Bi_2S_3$ and rGO which facilitate the highest charge transfer for the selective C1 product-methanol ($CH_3OH$) generation.
- Further, in case of Bismuth based 2D material ($Bi_2MoO_6$ nanoribbon/rGO) containing transition metal (Mo), 2% (the optimum) Cu doping aids to 100% selective C2 product ethanol ($C_2H_5OH$).
- In 2% Cu doped 2D-$Bi_2MoO_6$/rGO nanoribbon, the transition metals Mo and Cu createthebridge of Mo-C-Cu/Mo-O-Cu, which enhance the charge transfer from 2D-$Bi_2MoO_6$ to $CO_2$ trapping sites on rGO-Cu interface as well as aids to supply large

number of electrons (12) to support C-C coupling for selective C2 product-ethanol ($C_2H_5OH$) generation.

- The hydrothermally synthesized 1.5%N-(2.5%)rGO/$BiVO_4$ photocatalyst is the most effective active catalyst for increased photocatalytic reduction of $CO_2$ to formic acid, with a rate of around 592.80 μmol $g_{cat.}^{-1}$ $h^{-1}$.
- In 1.5% N doped rGO/$BiVO_4$, defective centers (C=N/C-N) can enhance the photoinduced charge transfer activity of rGO from $BiVO_4$ to facilitate the $CO_2$ adsorption process on N-rGO surface active zones, where the surface-adsorbed $CO_2$ is further reduced with the help of these photoinduced electrons and produces selective formic acid (HCOOH).

**Table 5.1: Comparative analysis of Photocatalytic activity of different synthesized photocatalyst based on selectivity.**

| **Photocatalyst** | **Product &Yield (μmol $g_{cat.}^{-1}$ $h^{-1}$)** | **Selectivity ($S_{product}$ %)** | **Absorption edge (nm)** | **Band-gap energy (eV)** |
|---|---|---|---|---|
| $Bi_2S_3$ nanostructure | $CH_3OH$: 71.38<br>HCOOH: 25.92 | $S_{CH3OH}$ : 89.2 | 500.0 | 1.90 |
| rGO-$Bi_2S_3$ nanostructure | $CH_3OH$: 91.93<br>HCOOH: 14.84 | $S_{CH3OH}$ : 94.8 | 525.9 | 1.80 |
| $Bi_2S_3$/CuO nanostructure | $CH_3OH$: 207.75<br>HCOOH: 55.89 | $S_{CH3OH}$ : 91.7 | 560.5 | 2.24 |
| rGO-$Bi_2S_3$/CuO S-scheme heterojunction | $CH_3OH$: 423.52<br>HCOOH: 17.48 | $S_{CH3OH}$ : 98.6 | 652.4 | 1.75 |
| $Bi_2S_3$ 1D rod shaped nano-capsule | $CH_3OH$: 77.23<br>HCOOH: 3.089 | $S_{CH3OH}$ : 96 | 530.2 | 1.70 |
| $Bi_2S_3$ 1D rod shaped nano-capsule /rGO | $CH_3OH$: 102.06<br>HCOOH: 2.32 | $S_{CH3OH}$ : 97.7 | 610.6 | 1.51 |
| 0.5%Cu doped $Bi_2S_3$ 1D rod shaped nano-capsule /rGO | $CH_3OH$: 301.72 | $S_{CH3OH}$ : 100 | 649.8 | 1.47 |
| 1%Cu doped $Bi_2S_3$ 1D rod shaped nano-capsule /rGO | $CH_3OH$: 719.0 | $S_{CH3OH}$ : 100 | 706.5 | 1.36 |
| 2%Cu doped$Bi_2S_3$1D rod shaped nano-capsule /rGO | $CH_3OH$: 707.85 | $S_{CH3OH}$ : 100 | 478 | 1.82 |
| 2D-$Bi_2MoO_6$ nanoribbon | $CH_3OH$: 49.20<br>$C_2H_5OH$: 27.17 | $S_{C2H5OH}$ : 36 | 600.0 | 2.49 |
| 2D-$Bi_2MoO_6$ nanoribbon/rGO | $CH_3OH$: 31.81<br>$C_2H_5OH$: 58.80 | $S_{C2H5OH}$ : 65 | 634.0 | 2.25 |
| 1%Cu doped (2D)$Bi_2MoO_6$ nanoribbon | $CH_3OH$: 39.87<br>$C_2H_5OH$: 44.94 | $S_{C2H5OH}$ : 53 | 400.8 | 2.81 |

| | | | | |
|---|---|---|---|---|
| 2%Cu doped (2D)$Bi_2MoO_6$ nanoribbon | $CH_3OH$: 35.37 $C_2H_5OH$: 51.32 | $S_{C2H5OH}$ : 59 | 685.0 | 2.60 |
| 3%Cu doped (2D)$Bi_2MoO_6$ nanoribbon | $CH_3OH$: 37.05 $C_2H_5OH$: 48.70 | $S_{C2H5OH}$ : 56.8 | 378.7 | 5.23 |
| 1%Cu doped (2D)$Bi_2MoO_6$ nanoribbon/rGO | $C_2H_5OH$: 92.68 | $S_{C2H5OH}$ : 100 | 420.7 | 2.17 |
| 2%Cu doped (2D)$Bi_2MoO_6$ nanoribbon/rGO | $C_2H_5OH$: 133.10 | $S_{C2H5OH}$ : 100 | 730.0 | 2.02 |
| 3%Cu doped (2D)$Bi_2MoO_6$ nanoribbon/rGO | $C_2H_5OH$: 121.84 | $S_{C2H5OH}$ : 100 | 380.0 | 5.10 |
| $BiVO_4$ 2D nano-hexagon | HCOOH : 0 | $S_{HCOOH}$ : 0 | 550.0 | 2.50 |
| (2%)rGO/$BiVO_4$ 2D nano-hexagon | HCOOH : 288.8 | $S_{HCOOH}$ : 100 | 536.0 | 2.35 |
| 1% N doped (2.5%)rGO/$BiVO_4$ 2D nano-hexagon | HCOOH : 439.9 | $S_{HCOOH}$ : 100 | 500.05 | 2.20 |
| 1.5% N doped (2.5%)rGO/$BiVO_4$ 2D nano-hexagon | HCOOH : 592.8 | $S_{HCOOH}$ : 100 | 659.39 | 2.06 |
| 2% N doped (2.5%)rGO/$BiVO_4$ 2D nano-hexagon | HCOOH : 568.1 | $S_{HCOOH}$ : 100 | 409.25 | 2.78 |

**Table 5.2: Comparison of the photocatalytic activity of the top three synthesized photocatalysts according to apparent quantum yield.**

| Photocatalyst | Selective Product | Yield ($\mu mol\ g_{cat.}^{-1}\ h^{-1}$) | Apparent quantum yield AQY (%) |
|---|---|---|---|
| 1% Cu-$Bi_2S_3$/rGO | $CH_3OH$ | 719.0 | 1.62 |
| 2% Cu-$Bi_2MoO_6$/rGO | $C_2H_5OH$ | 133.10 | 0.337 |
| 1.5% N-(2.5%)rGO/$BiVO_4$ | HCOOH | 592.8 | 0.0148 |

## 5.2 Future scopes:

The present thesis discussed on the development of highly efficient, recyclable, visible light responsive, environment-friendly transition metal and non-metal doped rGO supported bismuth based photocatalyst exhibiting high photocatalytic activity and AQE, for the generation of selective renewable fuel through photocatalytic $CO_2$ reduction process.

Future scopes of this research work are as follows:

(i) Study on continuous photocatalytic $CO_2$ reduction to selective fuel generation using rGO supported bismuth based photocatalyst.

(ii) Study on the effect of operating conditions (pH, flow rate of water, rate of $CO_2$ adsorption, and intensity of irradiation) on large-scale industry-based production and inexpensive commercialization of selective $CO_2$ reduced product.

(iii) Applications of these bismuth-based photocatalysts supported by rGO in thermoelectric devices, photovoltaic devices, and supercapacitors.

(iv) To boost the photocatalytic activity for the large-scale industry-based production, these synthesised photoctalysts can be further changed by adding various transition metal (Mo, Zn, and Co) doping. They can also be viewed as new prospective photocatalysts that the next generation of researchers can investigate.

## 6. References:


1. Lüthi, D.; Floch, M. L.; Bereiter, B.; Blunier, T.; Barnola, J.-M.; Siegenthaler, U.; Raynaud, D.; Jouzel, J.; Fischer, H.; Kawamura, K.; Stocker, T. F. (2008). High-resolution carbon dioxide concentration record 650,000-800,000 years before present. Nature, 453 (7193), 379–382.
2. Kwilinski, A. (2024). Understanding the nonlinear effect of digital technology development on $CO_2$ reduction. Sustainable Development.
3. De_Richter, R. K., Ming, T., & Caillol, S. (2013). Fighting global warming by photocatalytic reduction of $CO_2$ using giant photocatalytic reactors. Renewable & Sustainable Energy Reviews, 19, 82–106.
4. Fankhauser, S., & Kverndokk, S. (1996). The global warming game — Simulations of a $CO_2$-reduction agreement. Resource and Energy Economics, 18(1), 83–102.
5. Gao, S., Zhu, Y., Umar, M., Kchouri, B., & Safi, A. (2024). Financial inclusion empowering sustainable technologies: Insights into the E-7 economies from COP28 perspectives. Technological Forecasting & Social Change/Technological Forecasting and Social Change, 201, 123177.
6. Jiang, T., He, X., Su, B., Havea, P. H., Wei, K., Kundzewicz, Z. W., & Liu, D. (2024). COP 28: Challenge of coping with climate crisis. The Innovation, 100559.
7. He, Y., Yin, L., Yuan, N., & Zhang, G. (2024). Adsorption and activation, active site and reaction pathway of photocatalytic $CO_2$ reduction: A review. Chemical Engineering Journal, 481, 148754.
8. Song, C. (2006). Global challenges and strategies for control, conversion and utilization of $CO_2$ for sustainable development involving energy, catalysis, adsorption and chemical processing. Catalysis Today, 115(1–4), 2–32.
9. Xiaoding, X., & Moulijn, J. A. (1996). Mitigation of $CO_2$ by Chemical Conversion: Plausible Chemical Reactions and Promising Products. Energy & Fuels, 10(2), 305–325.
10. Li, K., An, X., Park, K. H., Khraisheh, M., & Tang, J. (2014). A critical review of $CO_2$ photoconversion: Catalysts and reactors. Catalysis Today, 224, 3–12.
11. White, J. L., Baruch, M. F., Pander, J. E., Hu, Y., Fortmeyer, I. C., Park, J. E., Zhang, T., Liao, K., Gu, J., Yan, Y., Shaw, T. W., Abelev, E., & Bocarsly, A. B. (2015). Light-Driven Heterogeneous Reduction of Carbon Dioxide: Photocatalysts and Photoelectrodes. Chemical Reviews, 115(23), 12888–12935.

12. Wang, C.; Sun, Z.; Zheng, Y.; Hu, Y. H. (2019). Recent progress in visible light photocatalytic conversion of carbon dioxide. J. Mater. Chem. A., 7, 865-887.
13. Xu, J.; Roghabadi, F. A.; Luo, Y.; Ahmadi, V.; Wang, Q.; Wang, Z.; He, H. (2024). Recent advances in heterogeneous catalysis of solar-driven carbon dioxide conversion. J. Environ. Sci., 140, 165-182.
14. Lingampalli, S. R.; Ayyub, M. M.; Rao, C. N. R. (2017). Recent Progress in the Photocatalytic Reduction of Carbon Dioxide. ACS Omega, 2 (6), 2740–2748.
15. Li, Y.; Hui, D.; Sun, Y.; Wang, Y.; Wu, Z.; Wang, C.; Zhao, J. (2021). Boosting thermo-photocatalytic $CO_2$ conversion activity by using photosynthesis-inspired electron-proton-transfer mediators. Nat. Commun., 12, 123.
16. Wan, L.; Chen, R.; Cheung, D. W. F.; Wu, L.; Luo, J. (2023). Solar driven $CO_2$ reduction: from materials to devices. J. Mater. Chem. A., 11, 12499-12520.
17. Zhou, M.; Wang, Z.; Mei, A.; Yang, Z.; Chen, W.; Ou, S.; Wang, S.; Chen, K.; Reiss, P.; Qi, K.; Ma, J.; Liu, Y. (2023). Photocatalytic $CO_2$ reduction using La-Ni bimetallic sites within a covalent organic framework. Nat. Commun., 14, 2473.
18. Khan, A. A.; Tahir, M. (2019). Recent advancements in engineering approach towards design of photo-reactors for selective photocatalytic $CO_2$ reduction to renewable fuels. J. $CO_2$ Utiliza. (2019), 29, 205–239.
19. Li, D.; Hao, C.; Liu, H.; Zhang, R.; Li, Y.; Guo, J.; Vilancuo, C. C.; Guo, J. (2022). Photocatalytic $CO_2$ Conversion to Ethanol: A Concise Review. Catalysts, 12 (12), 1549.
20. Yao, S.; He, J.; Gao, F.; Wang, H.; Lin, J.; Bai, Y.; Fang, J.; Zhu, F.; Huang, F.; Wang, M. (2023). Highly selective semiconductor photocatalysis for $CO_2$ reduction. J. Mater. Chem. A., 11, 12539-12558.
21. Gawal, P. M., & Golder, A. K. (2024). Vegetal route for synthesis of CQDs/CdS nanocomposites for photocatalytic reduction of $CO_2$ to methanol under visible light. Colloids and Surfaces. A, Physicochemical and Engineering Aspects, 683, 133068.
22. Yan, X., Gao, B., Zheng, X., Cheng, M., Zhou, N., Liu, X., Du, L., Yuan, F., Wang, J., Cui, X., Zhang, G., Kong, W., & Xu, Q. (2024). Cooperatively tailored surface frustrated Lewis pairs and N-doping on $CeO_2$ for photocatalytic $CO_2$ reduction to high-value hydrocarbon products. Applied Catalysis. B, Environmental, 343, 123484.
23. He, F., Zhu, B., Cheng, B., Yu, J., Ho, W., & Macyk, W. (2020). 2D/2D/0D $TiO_2/C_3N_4/Ti_3C_2$ MXene composite S-scheme photocatalyst with enhanced $CO_2$ reduction activity. Applied Catalysis. B, Environmental, 272, 119006.
24. Patial, S., Kumar, R., Raizada, P., Singh, P., Van Le, Q., Lichtfouse, E., Nguyen, D. L. T., & Nguyen, V. H. (2021). Boosting light-driven $CO_2$ reduction into solar fuels: Mainstream avenues for engineering ZnO-based photocatalysts. Environmental Research, 197, 111134.
25. Elavarasan, M., Yang, W., Velmurugan, S., Chen, J. N., Chang, Y. T., Yang, T. C. K., & Yokoi, T. (2022). In-situ infrared investigation of m-$TiO_2$/α-$Fe_2O_3$ photocatalysts and tracing of intermediates in photocatalytic hydrogenation of $CO_2$ to methanol. Journal of $CO_2$ Utilization, 56, 101864.
26. He, L., Zhang, W., Liu, S., & Zhao, Y. (2021). Three-dimensional porous N-doped graphitic carbon framework with embedded CoO for photocatalytic $CO_2$ reduction. Applied Catalysis. B, Environmental, 298, 120546.
27. Zhu, S., Liao, W., Zhang, M., & Liang, S. (2019). Design of spatially separated Au and CoO dual cocatalysts on hollow $TiO_2$ for enhanced photocatalytic activity towards the reduction of $CO_2$ to $CH_4$. Chemical Engineering Journal, 361, 461–469.
28. Montalvo, D., Corro, G., Bañuelos, F., Olivares-Xometl, O., Arellanes, P., & Pal, U. (2023). Selective alcohols production through $CO_2$ photoreduction using $Co_3O_4$ /$TiO_2$ photocatalyst

exploiting synergetic interactions between $Ti^{3+}$, $Co^{2+}$ and $Co^{3+}$. Applied Catalysis. B, Environmental, 330, 122652.
29. Murillo-Sierra, J., Hernández-Ramírez, A., Pino-Sandoval, D., Ruiz-Ruiz, E., & Martínez-Hernández, A. (2022). Promoting multielectron $CO_2$ reduction using a direct Z-scheme $WO_3$/ZnS photocatalyst. Journal of $CO_2$ Utilization, 63, 102122.
30. Raza, A., Shen, H., Haidry, A. A., Sun, L., Liu, R., & Cui, S. (2020). Studies of Z-scheme $WO_3$-$TiO_2$/$Cu_2ZnSnS_4$ ternary nanocomposite with enhanced $CO_2$ photoreduction under visible light irradiation. Journal of $CO_2$ Utilization, 37, 260–271
31. Chen, X., Li, Q., Li, J., Chen, J., & Jia, H. (2020). Modulating charge separation via in situ hydrothermal assembly of low content $Bi_2S_3$ into UiO-66 for efficient photothermocatalytic $CO_2$ reduction. Applied Catalysis. B, Environmental, 270, 118915.
32. Xi, H., Xu, Y., Zou, W., Ji, J., Cai, Y., Wan, H., & Dong, L. (2022). Enhanced methanol selectivity of CuO/$TiO_2$ photocatalytic $CO_2$ reduction: Synergistic mechanism of surface hydroxyl and low-valence copper species. Journal of $CO_2$ Utilization, 55, 101825.
33. Wong, K. J., Foo, J. J., Siang, T. J., & Ong, W. (2023). Transition metal carbide-based photocatalysts for artificial photosynthesis. SmartMat., 5, 1238.
34. Gong, S., Niu, Y., Teng, X., Liu, X., Xu, M., Xu, C., Meyer, T. J., & Chen, Z. (2022). Visible light-driven, selective $CO_2$ reduction in water by In-doped Mo2C based on defect engineering. Applied Catalysis. B, Environmental, 310, 121333.
35. Khan, A. A., & Tahir, M. (2019). Recent advancements in engineering approach towards design of photo-reactors for selective photocatalytic $CO_2$ reduction to renewable fuels. Journal of $CO_2$ Utilization, 29, 205–239.
36. Shehzad, N., Tahir, M., Johari, K., Murugesan, T., & Hussain, M. (2018). Improved interfacial bonding of graphene-$TiO_2$ with enhanced photocatalytic reduction of $CO_2$ into solar fuel. Journal of Environmental Chemical Engineering, 6(6), 6947–6957.
37. Wang, H., Yang, Y., Yuan, X., Teo, W. L., Wu, Y., Tang, L., & Zhao, Y. (2022). Structure–performance correlation guided applications of covalent organic frameworks. Materials Today, 53, 106–133.
38. Cowan, A. J., & Durrant, J. R. (2013). Long-lived charge separated states in nanostructured semiconductor photoelectrodes for the production of solar fuels. Chemical Society Reviews, 42(6), 2281–2293.
39. Júnior, M. a. M., Morais, A., & Nogueira, A. F. (2016). Boosting the solar-light-driven methanol production through $CO_2$ photoreduction by loading $Cu_2O$ on $TiO_2$ -pillared $K_2Ti_4O_9$. Microporous and Mesoporous Materials, 234, 1–11.
40. Wu, Y. A., McNulty, I., Liu, C., Lau, K. C., Liu, Q., Paulikas, A. P., Sun, C. J., Cai, Z., Guest, J. R., Ren, Y., Stamenkovic, V., Curtiss, L. A., Liu, Y., & Rajh, T. (2019). Facet-dependent active sites of a single $Cu_2O$ particle photocatalyst for $CO_2$ reduction to methanol. Nature Energy, 4(11), 957–968.
41. Ren, S., Yang, H., Zhang, D., Gao, F., Nan, C., Li, Z., Zhou, W., Gao, N., & Liang, Z. (2022). Excellent performance of the photoelectrocatalytic $CO_2$ reduction to formate by $Bi_2S_3$/ZIF-8 composite. Applied Surface Science, 579, 152206.
42. Liu, G., Hoivik, N., Wang, K., & Jakobsen, H. (2012). Engineering $TiO_2$ nanomaterials for $CO_2$ conversion/solar fuels. Solar Energy Materials & Solar Cells/Solar Energy Materials and Solar Cells, 105, 53–68.
43. Izumi, Y. (2013). Recent advances in the photocatalytic conversion of carbon dioxide to fuels with water and/or hydrogen using solar energy and beyond. Coordination Chemistry Reviews, 257(1), 171–186.

44. Bankar, B. D., Ravi, K., Tayade, R. J., & Biradar, A. V. (2023). Iridium supported on spinal cubic cobalt oxide catalyst for the selective hydrogenation of $CO_2$ to formic acid. Journal of $CO_2$ Utilization, 67, 102315.
45. Chen, H., Wang, L., Long, D., Zeng, Y., Jiang, S., Chen, W., Zhao, C., Cheng, C., Chen, Y., Lu, M., Li, S., & Chen, X. (2024). Advancing the ethanol pathway during the competitive photocatalytic $CO_2$ reduction in a defective transition metal dichalcogenide. Applied Catalysis B Environment and Energy, 357, 124260.
46. Ochedi, F. O., Liu, D., Yu, J., Hussain, A., & Liu, Y. (2020). Photocatalytic, electrocatalytic and photoelectrocatalytic conversion of carbon dioxide: a review. Environmental Chemistry Letters, 19(2), 941–967.
47. Chandrasekaran, S., Yao, L., Deng, L., Bowen, C., Zhang, Y., Chen, S., Lin, Z., Peng, F., & Zhang, P. (2019). Recent advances in metal sulfides: from controlled fabrication to electrocatalytic, photocatalytic and photoelectrochemical water splitting and beyond. Chemical Society Reviews, 48(15), 4178–4280.
48. Daulbayev, C., Sultanov, F., Bakbolat, B., & Daulbayev, O. (2020). 0D, 1D and 2D nanomaterials for visible photoelectrochemical water splitting. A Review. International Journal of Hydrogen Energy, 45(58), 33325–33342.
49. Samanta, S., & Srivastava, R. (2020). Catalytic conversion of $CO_2$ to chemicals and fuels: the collective thermocatalytic/photocatalytic/electrocatalytic approach with graphitic carbon nitride. Materials Advances, 1(6), 1506–1545.
50. Chen, H., Simoska, O., Lim, K., Grattieri, M., Yuan, M., Dong, F., Lee, Y. S., Beaver, K., Weliwatte, S., Gaffney, E. M., & Minteer, S. D. (2020). Fundamentals, Applications, and Future Directions of Bioelectrocatalysis. Chemical Reviews, 120(23), 12903–12993.
51. Ding, G., Li, C., Ni, Y., Chen, L., Shuai, L., & Liao, G. (2023). Layered double hydroxides and their composites as high-performance photocatalysts for $CO_2$ reduction. EES Catalysis, 1(4), 369–391.
52. Shehzad, N., Tahir, M., Johari, K., Murugesan, T., & Hussain, M. (2018a). A critical review on $TiO_2$ based photocatalytic $CO_2$ reduction system: Strategies to improve efficiency. Journal of $CO_2$ Utilization, 26, 98–122.
53. Yamamoto, M., Yoshida, T., Yamamoto, N., Nomoto, T., Yamamoto, Y., Yagi, S., & Yoshida, H. (2015). Photocatalytic reduction of $CO_2$ with water promoted by Ag clusters in $Ag/Ga_2O_3$ photocatalysts. Journal of Materials Chemistry. A, 3(32), 16810–16816.
54. Liu, N., Zhao, Y., Zhou, S., & Zhao, J. (2020). $CO_2$ reduction on p-block metal oxide overlayers on metal substrates—2D MgO as a prototype. Journal of Materials Chemistry. A, 8(11), 5688–5698.
55. Hori, H., Koike, K., Suzuki, Y., Ishizuka, M., Tanaka, J., Takeuchi, K., & Sasaki, Y. (2002). High-pressure photocatalytic reduction of carbon dioxide using $[fac\text{-}Re(bpy)(CO)_3P(OiPr)_3]+$ (bpy = 2,2′-bipyridine). Journal of Molecular Catalysis. A, Chemical, 179(1–2), 1–9.
56. Gao, Y., Qian, K., Xu, B., Li, Z., Zheng, J., Zhao, S., Ding, F., Sun, Y., & Xu, Z. (2020). Recent advances in visible-light-driven conversion of $CO_2$ by photocatalysts into fuels or value-added chemicals. Carbon Resources Conversion, 3, 46–59.
57. Mustafa, A., Lougou, B. G., Shuai, Y., Wang, Z., & Tan, H. (2020). Current technology development for $CO_2$ utilization into solar fuels and chemicals: A review. Journal of Energy Chemistry/Journal of Energy Chemistry, 49, 96–123.
58. Jeevanandam, J., Sundaramurthy, A., Sharma, V., Murugan, C., Pal, K., Kodous, M. H. A., & Danquah, M. K. (2020b). Sustainability of One-Dimensional Nanostructures. In Elsevier eBooks (pp. 83–113).
59. Low, J., Cao, S., Yu, J., & Wageh, S. (2014). Two-dimensional layered composite photocatalysts. Chemical Communications, 50(74), 10768.

60. Wu, H., Li, X., Tung, C., & Wu, L. (2019). Semiconductor Quantum Dots: An Emerging Candidate for $CO_2$ Photoreduction. Advanced Materials, 31(36).
61. Kuehnel, M. F., Sahm, C. D., Neri, G., Lee, J. R., Orchard, K. L., Cowan, A. J., & Reisner, E. (2018). ZnSe quantum dots modified with a Ni(cyclam) catalyst for efficient visible-light driven $CO_2$ reduction in water. Chemical Science, 9(9), 2501–2509.
62. Rajendran, R., Shrestha, L. K., Minami, K., Subramanian, M., Jayavel, R., & Ariga, K. (2014). Dimensionally integrated nanoarchitectonics for a novel composite from 0D, 1D, and 2D nanomaterials: rGO/CNT/$CeO_2$ ternary nanocomposites with electrochemical performance. Journal of Materials Chemistry. A, 2(43), 18480–18487.
63. Ge, M., Cao, C., Huang, J., Li, S., Chen, Z., Zhang, K. Q., Al-Deyab, S. S., & Lai, Y. (2016). A review of one-dimensional $TiO_2$ nanostructured materials for environmental and energy applications. Journal of Materials Chemistry. A, 4(18), 6772–6801.
64. Zhao, H., Yang, X., Duan, Y., & Shen, Z. (2024). Enhanced $CO_2$ Photoreduction with Noble Metal-Modified CeO2-Synthesis, Mechanisms, and Catalytic Insights: A mini review. ChemCatChem, 16(9), e202301295.
65. Li, Y., Bahamon, D., Albero, J., López, N., & Vega, L. F. (2024). Systematic screening of transition-metal-doped hydroxyapatite for efficient photocatalytic $CO_2$ reduction. Journal of $CO_2$ Utilization, 80, 102692.
66. Gao, Y., Zhang, M., Jin, Y., Zhou, M., Mao, Y., Sun, J., Wang, W., & Song, Z. (2024). Low-coordination transition metal sites on oxygen vacancy enriched strontium titanate-based perovskites enable highly selective photocatalytic $CO_2$ reduction to $CH_4$. Applied Catalysis. B, Environmental, 341, 123348.
67. Chen, J., Yuan, D., & Wang, Y. (2023). Covalent Organic Frameworks Based Heterostructure in Solar-To-Fuel Conversion. Advanced Functional Materials, 33(41).
68. Yang, M. Q., & Xu, Y. J. (2016). Photocatalytic conversion of $CO_2$ over graphene-based composites: current status and future perspective. Nanoscale Horizons, 1(3), 185–200.
69. Fung, C. M., Tang, J. Y., Tan, L. L., Mohamed, A. R., & Chai, S. P. (2020). Recent progress in two-dimensional nanomaterials for photocatalytic carbon dioxide transformation into solar fuels. Materials Today Sustainability, 9, 100037.
70. Wang, L., Chen, W., Zhang, D., Du, Y., Amal, R., Qiao, S., Wu, J., & Yin, Z. (2019). Surface strategies for catalytic $CO_2$reduction: from two-dimensional materials to nanoclusters to single atoms. Chemical Society Reviews, 48(21), 5310–5349.
71. Jain, S., Szunerits, S., & Boukherroub, R. (2018). Graphene-Based Photocatalytic Materials for Conversion of Carbon Dioxide to Solar Fuels. In Elsevier eBooks (pp. 396–412).
72. Li, X., & Wang, J. (2019). One-dimensional and two-dimensional synergized nanostructures for high-performing energy storage and conversion. InfoMat, 2(1), 3–32.
73. Wang, X., Lv, J., Zhang, J., Wang, X. L., Xue, C., Bian, G., Li, D., Wang, Y., & Wu, T. (2020). Hierarchical heterostructure of $SnO_2$ confined on CuS nanosheets for efficient electrocatalytic $CO_2$ reduction. Nanoscale, 12(2), 772–784.
74. Chen, Y., Jia, G., Hu, Y., Fan, G., Tsang, Y. H., Li, Z., & Zou, Z. (2017). Two-dimensional nanomaterials for photocatalytic $CO_2$ reduction to solar fuels. Sustainable Energy & Fuels, 1(9), 1875–1898.
75. Liu, J., Zhang, H., Qiu, M., Peng, Z., Leung, M. K. H., Lin, W. F., & Xuan, J. (2020). A review of non-precious metal single atom confined nanomaterials in different structural dimensions (1D–3D) as highly active oxygen redox reaction electrocatalysts. Journal of Materials Chemistry. A, 8(5), 2222–2245.
76. Lv, X., Lam, F. L. Y., & Hu, X. (2022). A Review on Bismuth Oxyhalide (BiOX, X=Cl, Br, I) Based Photocatalysts for Wastewater Remediation. Frontiers in Catalysis, 2.

77. Meng, L., Qu, Y., & Jing, L. (2021). Recent advances in BiOBr-based photocatalysts for environmental remediation. Chinese Chemical Letters/Chinese Chemical Letters, 32(11), 3265–3276.
78. Freitas, D. V., González-Moya, J. R., Soares, T. a. S., Silva, R. R., Oliveira, D. M., Mansur, H. S., Machado, G., & Navarro, M. (2018). Enhanced Visible-Light Photoelectrochemical Conversion on $TiO_2$ Nanotubes with $Bi_2S_3$ Quantum Dots Obtained by in Situ Electrochemical Method. ACS Applied Energy Materials, 1(8), 3636–3645.
79. Chowdhury, A., Bhan, C., Peela, N. R., & Golder, A. K. (2023). A simple template-free bioinspired route of 1D $Bi_2S_3$ nanorods synthesis for electrochemical $CO_2$ reduction to formate. Journal of Industrial and Engineering Chemistry/Journal of Industrial and Engineering Chemistry - Korean Society of Industrial and Engineering Chemistry, 127, 138–148.
80. Wu, K., Chai, H., Xu, K., Debliquy, M., & Zhang, C. (2023). Effect of {010} crystal facets of $Bi_2MoO_6$ and 1D/2D heterostructures for conductometric room temperature $NH_3$ gas sensors. Sensors and Actuators. B, Chemical, 376, 132983.
81. Li, B., Cao, Z., Wang, S., Wei, Q., & Shen, Z. (2018). BiVO4 quantum dot-decorated $BiPO_4$ nanorods 0D/1D heterojunction for enhanced visible-light-driven photocatalysis. Dalton Transactions, 47(30), 10288–10298.
82. Long, M., Li, D., Zhao, Q., Li, H., Wen, Q., Wang, L., Wu, L., Song, F., & Zhou, J. (2023). A 1D/2D $Bi_2O_3$/g-$C_3N_4$ step-scheme photocatalyst to activate peroxymonosulfate for the removal of tetracycline hydrochloride: insight into the mechanism, reactive sites, degradation pathway and ecotoxicity. Physical Chemistry Chemical Physics/PCCP. Physical Chemistry Chemical Physics, 25(17), 12231–12244.
83. Zhang, L., Li, Y., Li, Q., Fan, J., Carabineiro, S. A., & Lv, K. (2021). Recent advances on Bismuth-based Photocatalysts: Strategies and mechanisms. Chemical Engineering Journal, 419, 129484.
84. Wu, X., Tan, H. L., Zhang, C., Teng, Z., Liu, Z., Ng, Y. H., Zhang, Q., & Su, C. (2023). Recent advances in two-dimensional ultrathin Bi-based photocatalysts. Progress in Materials Science/Progress in Materials Science, 133, 101047.
85. Mondal, A., Prabhakaran, A., Gupta, S., & Subramanian, V. R. (2021). Boosting Photocatalytic Activity Using Reduced Graphene Oxide (RGO)/Semiconductor Nanocomposites: Issues and Future Scope. ACS Omega, 6(13), 8734–8743.
86. Kumar, S. R. A., Mary, D. V., Josephine, G. S., & Ahamed, M. a. R. (2024). Graphene/GO/rGO based nanocomposites: Emerging energy and environmental application– review. Hybrid Advances, 5, 100168.
87. Akhter, R., Hussain, S., & Maktedar, S. S. (2024). Advanced graphene-based (photo & electro) catalysts for sustainable & clean energy technologies. New Journal of Chemistry, 48(2), 437–505.
88. Khavar, A. H. C., Mahjoub, A. R., & Najafi, S. (2024). Enhanced photocatalytic degradation of tetracycline by improving electron flux at the Schottky junction between Bi nanoparticles and $MoS_2$-anchored RGO. Journal of Photochemistry and Photobiology. A, Chemistry, 447, 115270.
89. Fernández-Catalá, J., Greco, R., Navlani-García, M., Cao, W., Berenguer-Murcia, N., & Cazorla-Amorós, D. (2022). g-$C_3N_4$-Based Direct Z-Scheme Photocatalysts for Environmental Applications. Catalysts, 12(10), 1137.
90. Prabhu, P., Jose, V., & Lee, J. (2020). Heterostructured Catalysts for Electrocatalytic and Photocatalytic Carbon Dioxide Reduction. Advanced Functional Materials, 30(24).
91. Song, W., Chong, K. C., Qi, G., Xiao, Y., Chen, G., Li, B., Tang, Y., Zhang, X., Yao, Y., Lin, Z., Zou, Z., & Liu, B. (2024). Unraveling the Transformation from Type-II to Z-Scheme in Perovskite-Based Heterostructures for Enhanced Photocatalytic $CO_2$ Reduction. Journal of the American Chemical Society, 146(5), 3303–3314.

92. Zhou, D., Zhang, J., Jin, Z., Di, T., & Wang, T. (2022). Reduced graphene oxide assisted g-$C_3N_4$/rGO/NiAl-LDHs type II heterostructure with high performance photocatalytic $CO_2$ reduction. Chemical Engineering Journal, 450, 138108.
93. Lu, S., Zhang, S., Li, L., Liu, C., Li, Z., & Luo, D. (2024). Piezoelectric effect-assisted Z-scheme heterojunction $ZnIn_2S_4$/$BaTiO_3$ for improved photocatalytic reduction of $CO_2$ to CO. Chemical Engineering Journal, 483, 149058.
94. Yang, W., Zhou, F., Sun, N., Wu, J., Qi, Y., Zhang, Y., Song, J., Sun, Y., Liu, Q., Wang, X., Mi, J., & Li, M. (2024). Constructing a 3D $Bi_2WO_6$/$ZnIn_2S_4$ direct Z-scheme heterostructure for improved photocatalytic $CO_2$ reduction performance. Journal of Colloid and Interface Science, 662, 695–706.
95. Liu, D., Jiang, L., Chen, D., Hao, Z., Deng, B., Sun, Y., Liu, X., Jia, B., Chen, L., & Liu, H. (2024). Twin S-Scheme g-$C_3N_4$/$CuFe_2O_4$/$ZnIn_2S_4$ Heterojunction with a Self-Supporting Three-Phase System for Photocatalytic $CO_2$ Reduction: Mechanism Insight and DFT Calculations. ACS Catalysis, 5326–5343.
96. Yuan, Z., Xiang, Y., Liu, J., He, H., Jian, X., Zhang, H., Zeng, T., Liu, M., Cao, R., Hu, Y., & Gao, X. (2024). Coordination engineering of the interfacial chemical bond and sulfur vacancies modulated S-scheme charge transfer for efficient photocatalytic $CO_2$ reduction. Separation and Purification Technology, 343, 127114.
97. Zheng, Y., Wang, E., Gao, Y., Zhou, J., & Sun, Z. (2024). Construction of 0D $Ti_3C_2O_2$/2D black phosphorus S-scheme heterostructure for photocatalytic $CO_2$ reduction. Surfaces and Interfaces, 44, 103741.
98. Lee, D. E., Bhosale, R., Devthade, V., Jo, W. K., & Tonda, S. (2024). Defect-enriched $BiOIO_3$/$Ti_3C_2$ MXene 2D/2D Schottky-type heterostructure for efficient and selective $CH_4$ production via $CO_2$ photoreduction: Unveiling the roles of defect inclusion and $Ti_3C_2$ MXene co-catalyst. Journal of Materials Science & Technology. 202, 27-38.
99. Andreou, E. K., Vamvasakis, I., & Armatas, G. S. (2024). Efficient Visible Light Photocatalytic Hydrogen Evolution by Boosting the Interfacial Electron Transfer in Mesoporous Mott–Schottky Heterojunctions of $Co_2P$-Modified $CdIn_2S_4$ Nanocrystals. ACS Applied Energy Materials. 4, 710.
100. Rana, S., Kumar, A., Sharma, G., Dhiman, P., García-Penas, A., & Stadler, F. J. (2023). Recent advances in perovskite-based Z-scheme and S-scheme heterojunctions for photocatalytic $CO_2$ reduction. Chemosphere, 339, 139765.
101. Kumar, A., Khosla, A., Sharma, S. K., Dhiman, P., Sharma, G., Gnanasekaran, L., Naushad, M., & Stadler, F. J. (2023). A review on S-scheme and dual S-scheme heterojunctions for photocatalytic hydrogen evolution, water detoxification and $CO_2$ reduction. Fuel, 333, 126267.
102. Guo, Y., Wang, M., Tian, J., Shen, M., Zhang, L., & Shi, J. (2020). Probing the effect of P-doping in polymeric carbon nitride on $CO_2$ photocatalytic reduction. Dalton Transactions, 49(44), 15750–15757.
103. Kočí, K., Matějů, K., Obalová, L., Krejčíková, S., Lacný, Z., Plachá, D., Čapek, L., Hospodková, A., & Šolcová, O. (2010). Effect of silver doping on the $TiO_2$ for photocatalytic reduction of $CO_2$. Applied Catalysis. B, Environmental, 96(3–4), 239–244.
104. Raes, A., Minja, A. C., Ag, K. R., & Verbruggen, S. W. (2024). Recent advances in metal-doped defective $TiO_2$ for photocatalytic $CO_2$ conversion. Current Opinion in Chemical Engineering, 44, 101013.
105. Zhao, H., Yang, X., Duan, Y., & Shen, Z. (2024). Enhanced $CO_2$ Photoreduction with Noble Metal-Modified CeO2-Synthesis, Mechanisms, and Catalytic Insights: A mini review. ChemCatChem, 16(9), e202301295.
106. Li, Y., Bahamon, D., Albero, J., López, N., & Vega, L. F. (2024). Systematic screening of transition-metal-doped hydroxyapatite for efficient photocatalytic $CO_2$ reduction. Journal of $CO_2$ Utilization, 80, 102692.

107. Gao, Y., Zhang, M., Jin, Y., Zhou, M., Mao, Y., Sun, J., Wang, W., & Song, Z. (2024). Low-coordination transition metal sites on oxygen vacancy enriched strontium titanate-based perovskites enable highly selective photocatalytic $CO_2$ reduction to $CH_4$. Applied Catalysis. B, Environmental, 341, 123348.
108. Li, M. R., Chen, X. W., & Lin, Z. Z. (2024). Enhanced non-metal catalyzed $CO_2$ reduction on doped biphenylene. International Journal of Hydrogen Energy, 62, 520–531.
109. Hammoud, L., Marchal, C., Caps, V., Toufaily, J., Hamieh, T., & Keller, V. (2024). Influence of low level of non-metal doping on g-$C_3N_4$ performance for H2 production from water under solar light irradiation. International Journal of Hydrogen Energy, 51, 285–300.
110. Huong, L. M., Tai, L. T., Dat, N. M., Hai, N. D., An, H., Nam, N. T. H., Hanh, T. T. T., & Hieu, N. H. (2024). Non-metallic X (X = C, N, S, and P) co-doped copper oxide derived from Mangifera indica leaf extract: Synthesis, characterization, density functional theory simulation of structure, and photoactivities. Colloids and Surfaces. A, Physicochemical and Engineering Aspects, 687, 133393.
111. Zhang, Z., Li, H., Wang, X., Su, S., & Xu, J. (2024). S-scheme charge transfer and photoinduced self-heating effect synergistically enhance the solar-driven $CO_2$ reduction over $Cs_3Bi_2Br_9/Bi_2S_3$ hybrid. Chemical Engineering Journal, 152473.
112. Zhou, Y., Han, Q., Zou, Z., Shen, Y., Zhou, X., Qu, H., & Zhu, Y. (2024). Unique dendritic $Bi_2S_3$ with ultrathin nanosheets rich in S vacancy-defect toward promoting highly efficient photothermal $CO_2$ reduction into CO. Catalysis Science & Technology, 14, 2876-2884.
113. Feng, R., Guo, M., Yang, Z., Qiu, J., Wang, Z., & Zhao, Y. (2024). 0D/2D $Bi_2MoO_6$ quantum dots /rGO heterojunction boosting full solar spectrum-driven photothermal catalytic $CO_2$ reduction to solar fuels. Carbon, 224, 119079.
114. Zhang, Y., Liu, S., Guo, X., Mikulčić, H., Xiao, R., & Wang, X. (2024). $F^-$ doped $Bi_2MoO_6$ nanosheets for photoreduction of $CO_2$ with $H_2O$. Journal of Photochemistry and Photobiology. A, Chemistry, 447, 115278.
115. Liu, Y., Deng, Q., Yao, Z., Liang, T., Zhang, S., Zhu, T., Xing, C., Pan, J., Yu, Z., Liang, K., Xie, T., Li, R., & Hou, Y. (2024). Inducing spin polarization via Co doping in the $BiVO_4$ cell to enhance the built-in electric field for promotion of photocatalytic $CO_2$ reduction. Journal of Colloid and Interface Science, 664, 500–510.
116. Li, Z., Liu, B., Zhang, X., Zhang, C., Bai, Y., Liu, J., Wang, Y., Yang, S., Li, R., & Fan, C. (2024). In situ preparation of a novel Z-scheme BiOBr/$BiVO_4$ composite film with enhanced photocatalytic $CO_2$ reduction performance. Sustainable Energy & Fuels, 8, 262-271.
117. Wang, M., Chen, D., & Lu, J. (2024). Recent advances in the construction of structurally diverse catalysts for enhanced photocatalytic $CO_2$ reduction. Separation and Purification Technology, 343, 126917.
118. Tailor, N. K., Singh, S., Afroz, M. A., Pant, K. K., & Satapathi, S. (2024). Unraveling the impact of Cu-doping in lead free halide perovskites for markedly enhancing photocatalytic $CO_2$ reduction performance. Applied Catalysis. B, Environmental, 340, 123247.
119. Zhang, Y., Huang, R., Fang, Y., Wang, J., Yuan, Z., Chen, X., Zhu, W., Cai, Y., & Shi, X. (2024). Modulation of Fe–MOF via second-transition metal ion doping (Ti, Mn, Zn, Cu) for efficient visible-light driven $CO_2$ reduction to $CH_4$. Separation and Purification Technology, 336, 126164.
120. Ding, J., Qiu, C., Zhang, Z., Qu, Q., Fang, C., Zhang, J., Guan, G., & Wan, H. (2024). Insight into the Effect of Valence States of Copper on Enhancing Methanol Selectivity in $CO_2$ Photoreduction.
121. Wang, F., Zeng, F., Yu, Z., Chen, C., Huang, X., Zhang, W., Lan, Y., & Li, J. (2024). A comparative study about the influence of nitrogen doping and oxygen vacancies on the photocatalytic performance of ceria. Surfaces and Interfaces, 46, 103889.

122. Dong, Z., Wang, Y., Zhang, X., Guan, X., Zhang, C., Wu, W., & Fan, C. (2024). Facile synthesis of self-nitrogen-doped carbon spheres for high-efficient photocatalytic $CO_2$ reduction to CO. Materials Letters, 135887.
123. Li, M., Xu, J., Song, Y., Li, Y., Wang, J., & Chen, F. (2024). Construction of $CsPbBr_3$/Carboxyl-modified rGO Heterostrucures for Efficient Photocatalytic Reduction of $CO_2$ to Methanol. CrystEngComm., 26, 1994-2002.
124. Wang, W., Chi, H., Jia, Z., Wang, J., Hao, J., Lv, Y., & Wu, J. (2024). Photocatalytic degradation of bismuth vanadate/graphene nanocomposites. Materials Science and Engineering. B, Solid-state Materials for Advanced Technology/Materials Science & Engineering. B, Solid-state Materials for Advanced Technology, 302, 117217.
125. Zhu, Z., Zhang, Y. C., Lin, W. Y., & Wu, R. J. (2024). Novel TAgNPT/$Cu_2O$ Composite for the Photocatalytic Conversion of $CO_2$ to Methane. Materials Research Bulletin, 112908.
126. Tailor, N. K., Singh, S., Afroz, M. A., Pant, K. K., & Satapathi, S. (2024). Unraveling the impact of Cu-doping in lead free halide perovskites for markedly enhancing photocatalytic $CO_2$ reduction performance. Applied Catalysis. B, Environmental, 340, 123247.
127. Li, H., & Liu, D. (2024). Synthesis of non-noble metal solid solution($Cd_{0.76}Co_{0.17}Mo_{0.07}S$) via MOF precursors for enhanced hydrogen production. Journal of Materials Chemistry. A. 12, 7178-7186.
128. Kim, D., Bhattacharjee, S., Lam, E., Casadevall, C., Rodríguez-Jiménez, S., & Reisner, E. (2024). Photocatalytic $CO_2$ Reduction Using Homogeneous Carbon Dots with a Molecular Cobalt Catalyst. Small. 2400057.
129. Chen, C., Zhang, Q., Liu, F., Zhang, Z., Liu, Q., & Fang, X. (2024). Regulating *COOH intermediate via amino alkylation engineering for exceptionally effective photocatalytic $CO_2$ reduction. Journal of Energy Chemistry/Journal of Energy Chemistry, 92, 282–291.
130. Zou, Y., Shen, Y., Gao, P., Wu, T., Zhou, Q., Liu, L., Chen, X., Sun, S., & An, Q. (2024). Enhanced Selective Photocatalytic $CO_2$ Reduction to CO on AuPd Decorated $Bi_2O_{2.33}$ Nanosheets. Journal of Environmental Chemical Engineering, 112742.
131. Sun, D., Han, J., Xiao, M., Cao, T., Li, Y., & Dong, H. (2024). Creation of molecular-level surface active centers on polymeric carbon nitride for boosting selectively photocatalytic $CO_2$ reduction to CO. Separation and Purification Technology, 338, 126610.
132. Wang, K., Hu, Z., Yu, P., Balu, A. M., Li, K., Li, L., Zeng, L., Zhang, C., Luque, R., Yan, K., & Luo, H. (2023). Understanding Bridging Sites and Accelerating Quantum Efficiency for Photocatalytic $CO_2$ Reduction. Nano-micro Letters, 16(1).
133. Ma, H., Wang, T., Xu, Y., Shi, W., Ma, R., Xia, Z., Yang, Q., Xie, G., & Chen, S. (2024). Phenanthraquinone modified carbon quantum dots covalent-grafted onto Cu-MOF for photocatalytic $CO_2$ reduction: Construction of dual-active sites and parallel charge channels based on the cooperation between photoexcitation and electron-entrap. Applied Catalysis. B, Environmental, 349, 123857.
134. Chen, F. F., Zhou, L., Peng, C., Zhang, D., Li, L., Xue, D., & Yu, Y. (2023). Bimetal-organic layer-derived ultrathin lateral heterojunction with continuous semi-coherent interfaces for boosting photocatalytic $CO_2$ reduction. Applied Catalysis. B, Environmental, 331, 122689.
135. Madhusudan, P., Shi, R., Xiang, S., Jin, M., Chandrashekar, B. N., Wang, J., Wang, W., Peng, O., Amini, A., & Cheng, C. (2021). Construction of highly efficient Z-scheme $Zn_xCd_{1-x}S$/Au@g-$C_3N_4$ ternary heterojunction composite for visible-light-driven photocatalytic reduction of $CO_2$ to solar fuel. Applied Catalysis. B, Environmental, 282, 119600.
136. Qaraah, F. A., Mahyoub, S. A., Hezam, A., Qaraah, A., Xin, F., & Xiu, G. (2022). Synergistic effect of hierarchical structure and S-scheme heterojunction over O-doped g-$C_3N_4$/N-doped $Nb_2O_5$ for highly efficient photocatalytic $CO_2$ reduction. Applied Catalysis. B, Environmental, 315, 121585.

137. Li, X., Liu, H., Luo, D., Li, J., Huang, Y., Li, H., Fang, Y., Xu, Y., & Zhu, L. (2012). Adsorption of $CO_2$ on heterostructure $CdS(Bi_2S_3)/TiO_2$ nanotube photocatalysts and their photocatalytic activities in the reduction of $CO_2$ to methanol under visible light irradiation. Chemical Engineering Journal, 180, 151–158.
138. He, H., Gao, X., Xu, K., Li, H., Hu, Y., Yang, C., & Fu, F. (2022). 1D/0D Z-scheme heterostructure of $Bi_2S_3/Cd_XZn_{1-X}S$ with strong interfacial electric field coupling enhanced mass transfer based on gas-liquid-solid micro interface contact for efficient photothermal synergistic catalytic $CO_2$ reduction to syngas. Chemical Engineering Journal, 450, 138266.
139. Choi, S. Y., Yoon, S. H., Kang, U., Han, D. S., & Park, H. (2021). Standalone photoconversion of $CO_2$ using Ti and $TiO_x$-sandwiched heterojunction photocatalyst of CuO and $CuFeO_2$ films. Applied Catalysis. B, Environmental, 288, 119985.
140. Ali, S., Razzaq, A., Kim, H., & In, S. I. (2022). Activity, selectivity, and stability of earth-abundant $CuO/Cu_2O$/Cu0-based photocatalysts toward $CO_2$ reduction. Chemical Engineering Journal, 429, 131579.
141. Li, N., Liu, X., Zhou, J., Chen, W., & Liu, M. (2020). Encapsulating CuO quantum dots in MIL-125(Ti) coupled with g-$C_3N_4$ for efficient photocatalytic $CO_2$ reduction. Chemical Engineering Journal, 399, 125782.
142. Ávila-López, M. A., Gavrielides, S., Luo, X., Ojoajogwu, A. E., Tan, J. Z., Luévano-Hipólito, E., Torres-Martínez, L. M., & Maroto-Valer, M. M. (2021). Comparative study of $CO_2$ photoreduction using different conformations of CuO photocatalyst: Powder, coating on mesh and thin film. Journal of $CO_2$ Utilization, 50, 101588.
143. Wang, S., Wang, L., & Huang, W. (2020). Bismuth-based photocatalysts for solar energy conversion. Journal of Materials Chemistry. A, 8(46), 24307–24352.
144. Freitas, D. V., González-Moya, J. R., Soares, T. a. S., Silva, R. R., Oliveira, D. M., Mansur, H. S., Machado, G., & Navarro, M. (2018). Enhanced Visible-Light Photoelectrochemical Conversion on $TiO_2$ Nanotubes with $Bi_2S_3$ Quantum Dots Obtained by in Situ Electrochemical Method. ACS Applied Energy Materials, 1(8), 3636–3645.
145. Ge, Z. H., Zhang, B. P., Shang, P. P., Yu, Y. Q., Chen, C., & Li, J. F. (2011). Enhancing Thermoelectric Properties of Polycrystalline $Bi_2S_3$ by Optimizing a Ball-Milling Process. Journal of Electronic Materials, 40(5), 1087–1094.
146. Li, H., Deng, F., Zheng, Y., Hua, L., Qu, C., & Luo, X. (2019). Visible-light-driven Z-scheme rGO/$Bi_2S_3$–BiOBr heterojunctions with tunable exposed BiOBr(102) facets for efficient synchronous photocatalytic degradation of 2-nitrophenol and Cr(vi) reduction. Environmental Science. Nano, 6(12), 3670–3683.
147. Subramanyam, P., Meena, B., Sinha, G. N., Suryakala, D., & Subrahmanyam, C. (2021b). Facile Synthesis and Photoelectrochemical Performance of a $Bi_2S_3$@rGO Nanocomposite Photoanode for Efficient Water Splitting. Energy & Fuels, 35(7), 6315–6321.
148. Han, P., Mihi, A., Ferre-Borrull, J., Pallarés, J., & Marsal, L. F. (2015). Interplay Between Morphology, Optical Properties, and Electronic Structure of Solution-Processed $Bi_2S_3$ Colloidal Nanocrystals. Journal of Physical Chemistry. C, 119(19), 10693–10699.
149. Chen, G., Yu, Y., Zheng, K., Ding, T., Wang, W., Jiang, Y., & Yang, Q. (2015). Fabrication of Ultrathin $Bi_2S_3$ Nanosheets for High-Performance, Flexible, Visible–NIR Photodetectors. Small, 11(24), 2848–2855.
150. Yang, L. X., Ding, Y. B., Luo, S. L., Luo, Y., Deng, F., & Li, Y. (2013). Fast growth with crystal splitting of morphology-controllable $Bi_2S_3$ flowers on $TiO_2$ nanotube arrays. Semiconductor Science and Technology, 28(3), 035005.
151. Wang, S., Wang, L., & Huang, W. (2020). Bismuth-based photocatalysts for solar energy conversion. Journal of Materials Chemistry. A, 8(46), 24307–24352.

152. Yu, T., Liu, Q., Zhu, Z., Wu, W., Liu, L., Zhang, J., Gao, C., & Yang, T. (2021). Construction of a photocatalytic fuel cell using a novel Z-scheme $MoS_2$/rGO/$Bi_2S_3$ as electrode degraded antibiotic wastewater. Separation and Purification Technology, 277, 119276.
153. Chen, J., Qin, S., Song, G., Xiang, T., Xin, F., & Yin, X. (2013). Shape-controlled solvothermal synthesis of $Bi_2S_3$ for photocatalytic reduction of $CO_2$ to methyl formate in methanol. Dalton Transactions, 42(42), 15133.
154. Long, Z., Zhang, G., Du, H., Zhu, J., & Li, J. (2021). Preparation and application of BiOBr-$Bi_2S_3$ heterojunctions for efficient photocatalytic removal of Cr(VI). Journal of Hazardous Materials, 407, 124394.
155. Paul, S., Barman, D., Chowdhury, C., Giri, P. K., & De, S. K. (2021). 3D/2D $Bi_2S_3$/$SnS_2$ heterostructures: superior charge separation and enhanced solar light-driven photocatalytic performance. CrystEngComm, 23(11), 2276–2288.
156. Ijaz, S., Ehsan, M. F., Ashiq, M. N., & He, T. (2015). Synthesis of a $Bi_2S_3$/$CeO_2$ nanocatalyst and its visible light-driven conversion of $CO_2$ into $CH_3OH$ and $CH_4$. Catalysis Science & Technology, 5(12), 5208–5215.
157. He, R., Xu, D., Cheng, B., Yu, J., & Ho, W. (2018). Review on nanoscale Bi-based photocatalysts. Nanoscale Horizons, 3(5), 464–504.
158. Gote, G. H., Bhopale, S. R., More, M. A., & Late, D. J. (2019). Realization of Efficient Field Emitter Based on Reduced Graphene Oxide-Bi2S3 Heterostructures. Physica Status Solidi. A, Applications and Materials Science, 216(18).
159. Wang, Y., Jin, J., Chu, W., Cahen, D., & He, T. (2018). Synergistic Effect of Charge Generation and Separation in Epitaxially Grown BiOCl/$Bi_2S_3$ Nano-Heterostructure. ACS Applied Materials & Interfaces, 10(17), 15304–15313.
160. Tho, N. T. M., Van Cuong, N., Thi, V. H. L., Thang, N. Q., & Dang, P. H. (2023). A novel n–p heterojunction $Bi_2S_3$/$ZnCo_2O_4$ photocatalyst for boosting visible-light-driven photocatalytic performance toward indigo carmine. RSC Advances, 13(24), 16248–16259.
161. Li, S., Dong, K., Cai, M., Li, X., & Chen, X. (2023). A plasmonic S-scheme Au/MIL-101(Fe)/BiOBr photocatalyst for efficient synchronous decontamination of Cr(VI) and norfloxacin antibiotic. eScience, 100208.
162. Wang, C., You, C., Rong, K., Shen, C., Yang, F., & Li, S. (2023). An S-Scheme MIL-101(Fe)-on-BiOCl Heterostructure with Oxygen Vacancies for Boosting Photocatalytic Removal of Cr(VI). Wuli Huaxue Xuebao, 0(0), 2307045.
163. Li, S., Yan, R., Cai, M., Jiang, W., Zhang, M., & Li, X. (2023). Enhanced antibiotic degradation performance of $Cd_{0.5}Zn_{0.5}S$/$Bi_2MoO_6$ S-scheme photocatalyst by carbon dot modification. Journal of Materials Science and Technology/Journal of Materials Science & Technology, 164, 59–67.
164. Cai, M., Liu, Y., Dong, K., Chen, X., & Li, S. (2023). Floatable S-scheme $Bi_2WO_6$/$C_3N_4$/carbon fiber cloth composite photocatalyst for efficient water decontamination. Cuihua Xuebao/Chinese Journal of Catalysis, 52, 239–251.
165. Li, S., Cai, M., Liu, Y., Wang, C., Yan, R., & Chen, X. (2023). Constructing $Cd_{0.5}Zn_{0.5}S$/$Bi_2WO_6$ S-scheme heterojunction for boosted photocatalytic antibiotic oxidation and Cr(VI) reduction. Advanced Powder Materials, 2(1), 100073.
166. Li, S., Cai, M., Liu, Y., Wang, C., Lv, K., & Chen, X. (2022). S-Scheme photocatalyst TaON/$Bi_2WO_6$ nanofibers with oxygen vacancies for efficient abatement of antibiotics and Cr(VI): Intermediate eco-toxicity analysis and mechanistic insights. Cuihua Xuebao/Chinese Journal of Catalysis, 43(10), 2652–2664.
167. Li, S., Cai, M., Wang, C., & Liu, Y. (2023). $Ta_3N_5$/CdS Core–Shell S-scheme Heterojunction Nanofibers for Efficient Photocatalytic Removal of Antibiotic Tetracycline and Cr(VI): Performance and Mechanism Insights. Advanced Fiber Materials/Advanced Fiber Materials, 5(3), 994–1007.

168. Subramanyam, P., Meena, B., Sinha, G. N., Suryakala, D., & Subrahmanyam, C. (2021). Facile Synthesis and Photoelectrochemical Performance of a $Bi_2S_3$@rGO Nanocomposite Photoanode for Efficient Water Splitting. Energy & Fuels, 35(7), 6315–6321.
169. Dai, W., Yu, J., Luo, S., Hu, X., Yang, L., Zhang, S., Li, B., Luo, X., & Zou, J. (2020). $WS_2$ quantum dots seeding in $Bi_2S_3$ nanotubes: A novel Vis-NIR light sensitive photocatalyst with low-resistance junction interface for $CO_2$ reduction. Chemical Engineering Journal, 389, 123430.
170. Duan, J., Sun, P., Zhao, H., Ji, Z., Zhang, D., & Wang, W. (2021). Construction of columnar cactus-like 2D/1D $Cd_xCu_{1-x}S$@CuO shell-core structure photocatalyst for the reduction of $CO_2$ to methanol. Optical Materials, 115, 111016.
171. Kumari, V., Kaushal, S., & Singh, P. P. (2022). Green synthesis of a CuO/rGO nanocomposite using a Terminalia arjuna bark extract and its catalytic activity for the purification of water. Materials Advances, 3(4), 2170–2184.
172. Zhou, C., Cheng, L., Li, Y., Zeng, M., Yang, Y., Wu, J., & Zhao, X. (2018). Novel photoactivation promotes catalytic abatement of CO on CuO mesoporous nanosheets with full solar spectrum illumination. Applied Catalysis. B, Environmental, 225, 314–323.
173. Taraka, T. P. Y., Gautam, A., Jain, S. L., Bojja, S., & Pal, U. (2019). Controlled addition of Cu/Zn in hierarchical CuO/ZnO p-n heterojunction photocatalyst for high photoreduction of $CO_2$ to MeOH. Journal of $CO_2$ Utilization, 31, 207–214.
174. Nogueira, A. E., Oliveira, J. A., Da Silva, G. T. S. T., & Ribeiro, C. (2019). Insights into the role of CuO in the $CO_2$ photoreduction process. Scientific Reports, 9(1).
175. Fiorenza, R., Bellardita, M., Balsamo, S. A., Spitaleri, L., Gulino, A., Condorelli, M., D'Urso, L., Scirè, S., & Palmisano, L. (2022). A solar photothermocatalytic approach for the $CO_2$ conversion: Investigation of different synergisms on CoO-CuO/brookite $TiO_2$-$CeO_2$ catalysts. Chemical Engineering Journal, 428, 131249.
176. Kim, H. R., Razzaq, A., Grimes, C. A., & In, S. I. (2017). Heterojunction p-n-p $Cu_2O$/S-$TiO_2$ /CuO: Synthesis and application to photocatalytic conversion of $CO_2$ to methane. Journal of $CO_2$ Utilization, 20, 91–96.
177. Lashgari, M., Soodi, S., & Zeinalkhani, P. (2017). Photocatalytic back-conversion of $CO_2$ into oxygenate fuels using an efficient ZnO/CuO/carbon nanotube solar-energy-material: Artificial photosynthesis. Journal of $CO_2$ Utilization, 18, 89–97.
178. Jiang, X. X., De Hu, X., Tarek, M., Saravanan, P., Alqadhi, R., Chin, S. Y., & Khan, M. M. R. (2020). Tailoring the properties of g-$C_3N_4$ with CuO for enhanced photoelectrocatalytic $CO_2$ reduction to methanol. Journal of $CO_2$ Utilization, 40, 101222.
179. Nogueira, A. E., Silva, G. T. S. T., Oliveira, J. A., Lopes, O. F., Torres, J. A., Carmo, M., & Ribeiro, C. (2020). CuO Decoration Controls Nb2O5 Photocatalyst Selectivity in $CO_2$ Reduction. ACS Applied Energy Materials, 3(8), 7629–7636.
180. Jiang, Y., Guo, J., Li, X., Wu, G., Mu, M., & Yin, X. (2022). Direct Z-scheme 0D/2D heterojunction of CuO quantum Dots/ultrathin CoAl-LDH for boosting charge separation and photocatalytic $CO_2$ reduction. Solar Energy, 231, 705–715.
181. Edelmannová, M., Lin, K. Y., Wu, J. C., Troppová, I., Čapek, L., & Kočí, K. (2018). Photocatalytic hydrogenation and reduction of $CO_2$ over CuO/ $TiO_2$ photocatalysts. Applied Surface Science, 454, 313–318
182. Wang, Y., Xin, F., Chen, J., Xiang, T., & Yin, X. (2017). Photocatalytic Reduction of $CO_2$ in Isopropanol on $Bi_2S_3$ Quantum Dots/$TiO_2$ Nanosheets with Exposed {001} Facets. Journal of Nanoscience and Nanotechnology, 17(3), 1863–1869.
183. Mandal, A., Maitra, S., Roy, S., Hazra, B., Ray, K., & Kargupta, K. (2023). Selective photo-reduction of $CO_2$ to methanol using Cu-doped 1D-$Bi_2S_3$/rGO nanocomposites under visible light irradiation. New Journal of Chemistry, 47(3), 1422–1434.

184. Li, X., Chen, J., Li, H., Li, J., Xu, Y., Liu, Y., & Zhou, J. (2011). Photoreduction of $CO_2$ to methanol over $Bi_2S_3$/CdS photocatalyst under visible light irradiation. Journal of Natural Gas Chemistry, 20(4), 413–417.
185. Jin, J., & He, T. (2017). Facile synthesis of $Bi_2S_3$ nanoribbons for photocatalytic reduction of $CO_2$ into $CH_3OH$. Applied Surface Science, 394, 364–370.
186. Gusain, R., Kumar, P., Sharma, O. P., Jain, S. L., & Khatri, O. P. (2016). Reduced graphene oxide–CuO nanocomposites for photocatalytic conversion of $CO_2$ into methanol under visible light irradiation. Applied Catalysis. B, Environmental, 181, 352–362.
187. Chen, K., Zhao, X., Zhang, X. J., Zhang, W. S., Wu, Z. F., Wang, H. Y., Han, D. X., & Niu, L. (2021). Enhanced photocatalytic $CO_2$ reduction by constructing an $In_2O_3$–CuO heterojunction with CuO as a cocatalyst. Catalysis Science & Technology, 11(8), 2713–2717.
188. Shi, S., Zhou, S., Liu, S., & Chen, Z. (2017). Photocatalytic activity of erbium-doped $CeO_2$ enhanced by reduced graphene Oxide/CuO cocatalyst for the reduction of $CO_2$ to methanol. Environmental Progress & Sustainable Energy, 37(2), 655–662.
189. Luévano-Hipólito, E., Torres-Martínez, L. M., & Fernández-Trujillo, A. (2021). Ternary ZnO/CuO/Zeolite composite obtained from volcanic ash for photocatalytic $CO_2$ reduction and H2O decomposition. Journal of Physics and Chemistry of Solids, 151, 109917.
190. Ibarra-Rodriguez, L. I., Pantoja-Espinoza, J. C., Luévano-Hipólito, E., Garay-Rodriguez, L. F., Lopez-Ortiz, A., Torres-Guerra, L. M., & Collins-Martinez, V. H. (2022). Formic acid and hydrogen generation from the photocatalytic reduction of $CO_2$ on visible light activated N-$TiO_2$/$CeO_2$/CuO composites. Journal of Photochemistry and Photobiology, 11, 100125.
191. Li, S., Wang, C., Liu, Y., Liu, Y., Cai, M., Zhao, W., & Duan, X. (2023). S-scheme MIL-101(Fe) octahedrons modified $Bi_2WO_6$ microspheres for photocatalytic decontamination of Cr(VI) and tetracycline hydrochloride: Synergistic insights, reaction pathways, and toxicity analysis. Chemical Engineering Journal, 455, 140943.
192. Li, S., Wang, C., Liu, Y., Xue, B., Jiang, W., Liu, Y., Mo, L., & Chen, X. (2021). Photocatalytic degradation of antibiotics using a novel $Ag/Ag_2S/Bi_2MoO_6$ plasmonic p-n heterojunction photocatalyst: Mineralization activity, degradation pathways and boosted charge separation mechanism. Chemical Engineering Journal, 415, 128991.
193. Vattikuti, S. V. P., Police, A. K. R., Shim, J., & Byon, C. (2018). Sacrificial-template-free synthesis of core-shell C@$Bi_2S_3$ heterostructures for efficient supercapacitor and $H_2$ production applications. Scientific Reports, 8(1).
194. Liu, G., Dai, S., Cao, F., Zhu, B., Li, P., & Gu, Y. (2019). Preparation and enhanced nonlinear optical properties of $Bi_2S_3$/RGO composite materials. Optical Materials, 89, 112–117.
195. Roy, S. C., Varghese, O. K., Paulose, M., & Grimes, C. A. (2010). Toward Solar Fuels: Photocatalytic Conversion of Carbon Dioxide to Hydrocarbons. ACS Nano, 4(3), 1259–1278.
196. Fu, J., Jiang, K., Qiu, X., Yu, J., & Liu, M. (2020). Product selectivity of photocatalytic $CO_2$ reduction reactions. Materials Today, 32, 222–243.
197. Albero, J., Peng, Y., & García, H. (2020). Photocatalytic $CO_2$ Reduction to C2+ Products. ACS Catalysis, 10(10), 5734–5749.
198. Zhang, X., Li, X., Zhang, D., Su, N. Q., Yang, W., Everitt, H. O., & Liu, J. (2017). Product selectivity in plasmonic photocatalysis for carbon dioxide hydrogenation. Nature Communications, 8(1), 14542.
199. Dong, C., Xing, M., & Zhang, J. (2016). Economic Hydrophobicity Triggering of $CO_2$ Photoreduction for Selective $CH_4$ Generation on Noble-Metal-Free $TiO_2$–$SiO_2$. Journal of Physical Chemistry Letters, 7(15), 2962–2966.
200. Hiragond, C., Ali, S., Sorcar, S., & In, S. I. (2019). Hierarchical Nanostructured Photocatalysts for $CO_2$ Photoreduction. Catalysts, 9(4), 370.

201. Lan, Y., Xie, Y., Chen, J., Hu, Z., & Cui, D. (2019). Selective photocatalytic $CO_2$ reduction on copper–titanium dioxide: a study of the relationship between CO production and $H_2$ suppression. Chemical Communications, 55(56), 8068–8071.
202. Kong, T., Jiang, Y., & Xiong, Y. (2020). Photocatalytic $CO_2$ conversion: What can we learn from conventional COx hydrogenation? Chemical Society Reviews, 49(18), 6579–6591.
203. Li, M., Hua, B., Wang, L. C., Zhou, Z., Stowers, K. J., & Ding, D. (2022). Discovery of single-atom alloy catalysts for $CO_2$-to-methanol reaction by density functional theory calculations. Catalysis Today, 388–389, 403–409.
204. B. Ávila-Bolívar, R. Cepitis, M. Alam, J. Assafrei, K. Ping, J. Aruväli, A. Kikas, V. Kisand, S. Vlassov, M. Käärik, J. Leis, V. Ivaništšev, P. Starkov, V. Montiel, J. Solla-Gullón, and N. Kongi, Journal of $CO_2$ Utilization, 2022, 59, 101937.
205. Alam, U., Fleisch, M., Kretschmer, I., Bahnemann, D., & Muneer, M. (2017). One-step hydrothermal synthesis of Bi-$TiO_2$ nanotube/graphene composites: An efficient photocatalyst for spectacular degradation of organic pollutants under visible light irradiation. Applied Catalysis. B, Environmental, 218, 758–769.
206. Jin, J., & He, T. (2017). Facile synthesis of $Bi_2S_3$ nanoribbons for photocatalytic reduction of $CO_2$ into $CH_3OH$. Applied Surface Science, 394, 364–370.
207. Li, X., Chen, J., Li, H., Li, J., Xu, Y., Liu, Y., & Zhou, J. (2011). Photoreduction of $CO_2$ to methanol over $Bi_2S_3$/CdS photocatalyst under visible light irradiation. Journal of Natural Gas Chemistry, 20(4), 413–417.
208. Li, X., Liu, H., Luo, D., Li, J., Huang, Y., Li, H., Fang, Y., Xu, Y., & Zhu, L. (2012). Adsorption of $CO_2$ on heterostructure CdS($Bi_2S_3$)/$TiO_2$ nanotube photocatalysts and their photocatalytic activities in the reduction of $CO_2$ to methanol under visible light irradiation. Chemical Engineering Journal, 180, 151–158.
209. Gusain, R., Kumar, P., Sharma, O. P., Jain, S. L., & Khatri, O. P. (2016). Reduced graphene oxide–CuO nanocomposites for photocatalytic conversion of $CO_2$ into methanol under visible light irradiation. Applied Catalysis. B, Environmental, 181, 352–362.
210. Dai, W., Yu, J., Luo, S., Hu, X., Yang, L., Zhang, S., Li, B., Luo, X., & Zou, J. (2020). $WS_2$ quantum dots seeding in $Bi_2S_3$ nanotubes: A novel Vis-NIR light sensitive photocatalyst with low-resistance junction interface for $CO_2$ reduction. Chemical Engineering Journal, 389, 123430.
211. Hu, H., He, Y., Wang, X., Zhang, T., Li, D., Sun, M., & Deng, C. (2024). An intermediary route to CdS/$Bi_2S_3$ architectures with high-activity and stability in photocatalytic water splitting and dye degradation. Materials Science & Engineering. B, Solid-state Materials for Advanced Technology, 305, 117431.
212. Kumar, P., Joshi, C., Barras, A., Sieber, B., Addad, A., Boussekey, L., Szunerits, S., Boukherroub, R., & Jain, S. L. (2017). Core–shell structured reduced graphene oxide wrapped magnetically separable rGO@CuZnO@$Fe_3O_4$ microspheres as superior photocatalyst for $CO_2$ reduction under visible light. Applied Catalysis. B, Environmental, 205, 654–665.
213. Hao, J., Qi, B., Wei, J., Li, D., & Zeng, F. (2021). A Z-scheme $Cu_2O$/$WO_3$ heterojunction for production of renewable hydrocarbon fuel from carbon dioxide. Fuel, 287, 119439.
214. Cheng, M., Yang, S., Chen, R., Zhu, X., Liao, Q., & Huang, Y. (2017). Copper-decorated $TiO_2$ nanorod thin films in optofluidic planar reactors for efficient photocatalytic reduction of $CO_2$. International Journal of Hydrogen Energy, 42(15), 9722–9732.
215. Ma, Y., Jiang, X., Sun, R., Yang, J., Jiang, X., Liu, Z., Xie, M., Xie, E., & Han, W. (2020). Z-scheme $Bi_2O_{2.33}$/$Bi_2S_3$ heterojunction nanostructures for photocatalytic overall water splitting. Chemical Engineering Journal, 382, 123020.

216. Kavil, Y. N., Shaban, Y. A., Farawati, R. K. A., Orif, M. I., Zobidi, M., & Khan, S. U. (2017). Photocatalytic conversion of $CO_2$ into methanol over Cu-C/$TiO_2$ nanoparticles under UV light and natural sunlight. Journal of Photochemistry and Photobiology. A, Chemistry, 347, 244–253.
217. Regmi, C., Kshetri, Y. K., Pandey, R. P., Kim, T. H., Gyawali, G., & Lee, S. W. (2019). Understanding the multifunctionality in Cu-doped $BiVO_4$ semiconductor photocatalyst. Journal of Environmental Sciences, 75, 84–97.
218. Taraka, T. P. Y., Gautam, A., Jain, S. L., Bojja, S., & Pal, U. (2019). Controlled addition of Cu/Zn in hierarchical CuO/ZnO p-n heterojunction photocatalyst for high photoreduction of $CO_2$ to MeOH. Journal of $CO_2$ Utilization, 31, 207–214.
219. Ikram, M., Ali, S., Aqeel, M., Ul-Hamid, A., Imran, M., Haider, J., Haider, A., Shahbaz, A., & Ali, S. (2020). Reduced graphene oxide nanosheets doped by Cu with highly efficient visible light photocatalytic behavior. Journal of Alloys and Compounds, 837, 155588.
220. Gu, L., Wang, J., Cheng, H., Zhao, Y., Liu, L., & Han, X. (2013). One-Step Preparation of Graphene-Supported Anatase $TiO_2$ with Exposed {001} Facets and Mechanism of Enhanced Photocatalytic Properties. ACS Applied Materials & Interfaces, 5(8), 3085–3093.
221. Yin, C., Li, Q., Zheng, J., Ni, Y., Wu, H., Kjøniksen, A. L., Liu, C., Lei, Y., & Zhang, Y. (2022). Progress in regulating electronic structure strategies on Cu-based bimetallic catalysts for $CO_2$ reduction reaction. Advanced Powder Materials, 1(4), 100055.
222. Wang, Z. J., Song, H., Pang, H., Ning, Y., Dao, T. D., Wang, Z., Chen, H., Weng, Y., Fu, Q., Nagao, T., Fang, Y., & Ye, J. (2019). Photo-assisted methanol synthesis via $CO_2$ reduction under ambient pressure over plasmonic Cu/ZnO catalysts. Applied Catalysis. B, Environmental, 250, 10–16.
223. Jin, J., & He, T. (2017). Facile synthesis of $Bi_2S_3$ nanoribbons for photocatalytic reduction of $CO_2$ into $CH_3OH$. Applied Surface Science, 394, 364–370.
224. Wang, Y., Xin, F., Chen, J., Xiang, T., & Yin, X. (2017). Photocatalytic Reduction of $CO_2$ in Isopropanol on $Bi_2S_3$ Quantum Dots/$TiO_2$ Nanosheets with Exposed {001} Facets. Journal of Nanoscience and Nanotechnology, 17(3), 1863–1869.
225. Li, X., Chen, J., Li, H., Li, J., Xu, Y., Liu, Y., & Zhou, J. (2011). Photoreduction of $CO_2$ to methanol over $Bi_2S_3$/CdS photocatalyst under visible light irradiation. Journal of Natural Gas Chemistry, 20(4), 413–417.
226. Li, X., Liu, H., Luo, D., Li, J., Huang, Y., Li, H., Fang, Y., Xu, Y., & Zhu, L. (2012). Adsorption of $CO_2$ on heterostructure CdS($Bi_2S_3$)/$TiO_2$ nanotube photocatalysts and their photocatalytic activities in the reduction of $CO_2$ to methanol under visible light irradiation. Chemical Engineering Journal, 180, 151–158.
227. Gusain, R., Kumar, P., Sharma, O. P., Jain, S. L., & Khatri, O. P. (2016). Reduced graphene oxide–CuO nanocomposites for photocatalytic conversion of $CO_2$ into methanol under visible light irradiation. Applied Catalysis. B, Environmental, 181, 352–362.
228. Dai, W., Yu, J., Luo, S., Hu, X., Yang, L., Zhang, S., Li, B., Luo, X., & Zou, J. (2020). $WS_2$ quantum dots seeding in $Bi_2S_3$ nanotubes: A novel Vis-NIR light sensitive photocatalyst with low-resistance junction interface for $CO_2$ reduction. Chemical Engineering Journal, 389, 123430.
229. Iqbal, F., Mumtaz, A., Shahabuddin, S., Mutalib, M. I. A., Shaharun, M. S., Nguyen, T. D., Khan, M. R., & Abdullah, B. (2020). Photocatalytic reduction of $CO_2$ to methanol over $ZnFe_2O_4$/$TiO_2$ (p–n) heterojunctions under visible light irradiation. Journal of Chemical Technology & Biotechnology, 95(8), 2208–2221.

230. Kumar, P., Joshi, C., Barras, A., Sieber, B., Addad, A., Boussekey, L., Szunerits, S., Boukherroub, R., & Jain, S. L. (2017). Core–shell structured reduced graphene oxide wrapped magnetically separable rGO@CuZnO@$Fe_3O_4$ microspheres as superior photocatalyst for $CO_2$ reduction under visible light. Applied Catalysis. B, Environmental, 205, 654–665.
231. Ye, L.; Deng, Y.; Wang, L.; Xie, H.; Su, F. (2019). Bismuth-Based Photocatalysts for Solar Photocatalytic Carbon Dioxide Conversion. ChemSusChem, 12 (16), 3671 – 3701.
232. Wang, S.; Wang, L.; Huang, W. (2020). Bismuth-based photocatalysts for solar energy conversion. J. Mater. Chem. A., 8, 24307-24352.
233. Shi, M.; Yang, H.; Zhao, Z.; Ren, G.; Meng, X. (2023). Bismuth-based semiconductors applied in photocatalytic reduction processes: fundamentals, advances and future perspectives. Chem. Commun., 59, 4274-4287.
234. Guo, L.; Huang, H.; Mei, L.; Li, M.; Zhang, Y. (2021). Bismuth-based Z-scheme photocatalytic systems for solar energy conversion. Mater. Chem. Front., 5, 2484-2505.
235. Guoa, J.; Shia, L.; Zhaoa, J.; Wang, Y.; Tanga, K.; Zhang, W.; Xie, C.; Yuan, X. (2018). Enhanced visible-light photocatalytic activity of $Bi_2MoO_6$ nanoplates with heterogeneous $Bi_2MoO_{6-x}$@$Bi_2MoO_6$ core-shell structure. Appl. Catal. B: Environ., 224, 692–704.
236. Li, X.; Fang, S.; Ge, L.; Han, C.; Qiu, P.; Liu, W. (2015). Synthesis of flower-like Ag/AgCl-$Bi_2MoO_6$ plasmonic photocatalysts with enhanced visible-light photocatalytic performance. Appl. Catal. B: Environ., 176, 62-69.
237. Di, J.; Zhao, X.; Lian, C.; Ji, M.; Xia, J.; Xiong, J.; Zhou, W.; Cao, X.; She, Y.; Liu, H.; Loh, K. P.; Pennycook, S. J.; Li, H.; Liu, Z. (2019). Atomically-thin $Bi_2MoO_6$ nanosheets with vacancy pairs for improved photocatalytic $CO_2$ reduction. Nano Energy, 61, 54–59.
238. Dai, W.; Long, J.; Yang, L.; Zhang, S.; Xu, Y.; Luo, X.; Zou, J.; Luo, S. (2021). Oxygen migration triggering molybdenum exposure in oxygen vacancy-rich ultra-thin $Bi_2MoO_6$ nanoflakes: Dual binding sites governing selective $CO_2$ reduction into liquid hydrocarbons. J. Energy Chemistry, 61, 281–289.
239. Jia, Y.; Li, J.; Liu, Z.; Wang, Q.; Zhang, W.; Bae, J.-S. ; Liu, C. (2022). Pt-$GdCrO_3$-$Bi_2MoO_6$ ternary heterojunction with high photocatalytic activities for $CO_2$ reduction and water purification. Chem. Engin. J., 437, 135300.
240. Ren, G.; Wei, Z.; Liu, S.; Shi, M.; Li, Z.; Meng, X. (2022). Recent review of $Bi_xMO_y$ (M=V, Mo, W) for photocatalytic $CO_2$ reduction into solar fuels. Chemosphere, 307 (3), 136026.
241. Zhang, G.; Chen, D.; Li, N.; Xu, Q.; Li, H.; He, J.; Lu, J. (2019). Fabrication of $Bi_2MoO_6$/ZnO hierarchical heterostructures with enhanced visible-light photocatalytic activity. Appl. Catal. B: Environ., 250, 313–324.
242. Yu, H.; Jiang, L.; Wang, H.; Huang, B.; Yuan, X.; Huang, J.; Zhang, J.; Zeng, G. (2019). Modulation of $Bi_2MoO_6$-Based Materials for Photocatalytic Water Splitting and Environmental Application: a Critical Review. Small, 15 (23), 1901008.
243. Yang, X.; Xu, X.; Wang, J.; Chen, T.; Wang, S.; Ding, X.; Chen, H. (2021). Insights into the Surface/Interface Modifications of Bi2MoO6: Feasible Strategies and Photocatalytic Applications. Sol. RRL., 5 (2), 2000442.
244. Yang, Z.; Shen, M.; Dai, K.; Zhang, X.; Chen, H. (2018). Controllable synthesis of $Bi_2MoO_6$ nanosheets and their facet-dependent visible-light-driven photocatalytic activity. Appl. Surf. Sci., 430, 505–514.
245. Dai, W.; Yu, J.; Xu, H.; Hu, X.; Luo, X.; Yang, L.; Tu, X. (2016). Synthesis of hierarchical flower-like $Bi_2MoO_6$ microspheres as efficient photocatalyst for photoreduction of $CO_2$ into solar fuels under visible light. CrystEngComm, 18, 3472-3480.

246. Cheng, L.; Liu, L.; Wang, D.; Yang, F.; Ye, J. (2019). Synthesis of bismuth molybdate photocatalysts for $CO_2$ photo-reduction. J. $CO_2$ Utilization., 29, 196–204.
247. Li, X.; Yu, J.; Jaroniec, M.; Chen, X. (2019). Cocatalysts for Selective Photoreduction of $CO_2$ into Solar Fuels. Chem. Rev., 119 (6), 3962–4179.
248. Hu, C.; Tian, N.; Zhang, Y.; Huang, H. (2021). Facet-selective charge separation in two-dimensional bismuth-based photocatalysts. Catal. Sci. Technol., 11, 3659-3675.
249. Zhu, X.; Wang, Z.; Zhong, K.; Li, Q.; Ding, P.; Feng, Z.; Yang, J.; Du, Y.; Song, Y.; Hua, Y.; Yuan, J.; She, Y.; Li, H.; Xu, H. (2022). Mo-O-Bi Bonds as interfacial electron transport bridges to fuel $CO_2$ photoreduction via in-situ reconstruction of black $Bi_2MoO_6/BiO_{2-x}$ heterojunction. Chem. Engin. J., 429, 132204.
250. Xiong, J.; Di, J.; Li, H. (2020).Charge steering in ultrathin 2D nanomaterials for photocatalysis. J. Mater. Chem. A., 8, 12928-12950.
251. Chen, S.; Huang, D.; Cheng, M.; Lei, L.; Chen, Y.; Zhou, C.; Deng, R.; Li, B. (2021). Surface and interface engineering of two-dimensional bismuth-based photocatalysts for ambient molecule activation. J. Mater. Chem. A., 9, 196-233.
252. Nawaz, A.; Goudarzi, S.; Asghari, M. A.; Pichiah, S.; Selopal, G. S.; Rosei, F.; Wang, Z. M.; Zarrin, H. (2021). Review of Hybrid 1D/2D Photocatalysts for Light-Harvesting Applications. ACS Appl. Nano Mater., 4 (11), 11323–11352.
253. Qin, D.; Zhou, Y.; Wang, W.; Zhang, C.; Zeng, G.; Huang, D.; Wang, L.; Wang, H.; Yang, Y.; Lei, L.; Chen, S.; He, D. (2020). Recent advances in two-dimensional nanomaterials for photocatalytic reduction of $CO_2$: insights into performance, theories and perspective. J. Mater. Chem. A., 8, 19156-19195.
254. Marcano, D. C.; Kosynkin, D. V.; Berlin, J. M.; Sinitskii, A.; Sun, Z.; Slesarev, A.; Alemany, L. B.; Lu, W.; Tour, J. M. (2010). Improved Synthesis of Graphene Oxide. ACS Nano., 4 (8), 4806–4814.
255. Kumar, V.; Kim, K.-H.; Park, J.-W.; Hong, J.; Kumar, S. (2017). Graphene and its nanocomposites as a platform for environmental applications. Chem. Engin. J., 315, 210–232.
256. Ke, J.; Duan, X.; Luo, S.; Zhang, H.; Sun, H.; Liu, J.; Tade, M.; Wang, S. (2017). UV-assisted construction of 3D hierarchical rGO/$Bi_2MoO_6$ composites for enhanced photocatalytic water oxidation. Chem. Engin. J., 313, 1447–1453.
257. Tian, G.; Chen, Y.; Zhou, J.; Tian, C.; Li, R.; Wang, C.; Fu, H. (2014). In situ growth of $Bi_2MoO_6$ on reduced graphene oxide nanosheets for improved visible-light photocatalytic activity. CrystEngComm, 16, 842-849.
258. Meng, X.; Zhang, Z. (2017). $Bi_2MoO_6$ co-modified by reduced graphene oxide and palladium ($Pd^{2+}$ and $Pd^0$) with enhanced photocatalytic decomposition of phenol. Appl. Catal. B: Environ., 209, 383–393.
259. Bai, J.; Li, Y.; Li, X.; Liu, L. (2017). Facile preparation of 2D $Bi_2MoO_6$ nanosheets–RGO composites with enhanced photocatalytic activity. New J. Chem., 41, 7783-7790.
260. Khazaeea, Z.; Mahjouba, A. R.; Khavara, A. H. C.; Srivastavab, V.; Sillanpää, M. (2019). Synthesis of layered perovskite Ag, F-$Bi_2MoO_6$/rGO: A surface plasmon resonance and oxygen vacancy promoted nanocomposite as a visible-light photocatalyst. J. Photochem. & Photobio. A: Chem., 379, 130–143.
261. Wang, Y.; Chen, E.; Tang, J. (2022). Insight on Reaction Pathways of Photocatalytic $CO_2$ Conversion. ACS Catal., 12 (12), 7300−7316.
262. Yuan, H.; Cheng, B.; Lei, J.; Jiang, L.; Han, Z. (2021). Promoting photocatalytic $CO_2$ reduction with a molecular copper purpurin chromophore. Nat. Commun., 12, 1835.

263. Fu, F.; Shen, H.; Sun, X.; Xue, W.; Shoneye, A.; Ma, J.; Luo, L.; Wang, D.; Wang, J.; Tang, J. (2019). Synergistic effect of surface oxygen vacancies and interfacial charge transfer on Fe (III)/$Bi_2MoO_6$ for efficient photocatalysis. Appl. Catal. B: Environ., 247, 150–162.
264. Albero, J., Peng, Y., & García, H. (2020). Photocatalytic $CO_2$ Reduction to $C^{2+}$ Products. ACS Catalysis, 10(10), 5734–5749.
265. Suebsom, P.; Phuruangrat, A.; Suwanboon, S.; Thongtem, S.; Thongtem, T. (2020). Enhanced visible-light-driven photocatalytic activity of heterostructure Ag/$Bi_2MoO_6$ nanocomposites synthesized by photoreduction method. Inorga. Chem. Communi., 119, 108120.
266. Zhang, X.-B.; Zhang, L.; Hua, J.-S.; Huang, X.-H. (2016). Facile hydrothermal synthesis and improved photocatalytic activities of $Zn^{2+}$ doped $Bi_2MoO_6$ nanosheets. RSC Adv., 6, 32349-32357.
267. Wei, X.; Yin, Z.; Lyu, K.; Li, Z.; Gong, J.; Wang, G.; Xiao, L.; Lu, J.; Zhuang, L. (2020). Highly Selective Reduction of $CO_2$ to $C^{2+}$ Hydrocarbons at Copper/Polyaniline Interfaces. ACS Catal., 10 (7), 4103–4111.
268. Jitan, S. A.; Li, Y.; Bahamon, D.; Zerjav, G.; Tatiparthi , V. S.; Aubry, C.; Sinnokrot, M.; Matouk, Z.; Rajput, N.; Gutierrez, M.; Al-Ali, K.; Hashaikeh, R.; Pintar, A.; Vega, L. F.; Palmisano, G. (2023). Unprecedented photocatalytic conversion of gaseous and liquid $CO_2$ on graphene-impregnated Pt/Cu-$TiO_2$: The critical role of Cu dopant. J. Environ. Chem. Engin., 11 (2), 109485.
269. Byrne, C.; Moran, L.; Hermosilla, D.; Merayo, N.; Blanco, Á.; Rhatigan, S.; Hinder, S.; Ganguly, P.; Nolan, M.; Pillai, S. C. (2019). Effect of Cu doping on the anatase-to-rutile phase transition in $TiO_2$ photocatalysts: theory and experiments. Appl. Catal. B: Environ., 246, 266-276.
270. Tailor, N. K.; Singh, S.; Afroz, M. A.; Pant, K. K.; Satapathi, S. (2024). Unraveling the impact of Cu-doping in lead free halide perovskites for markedly enhancing photocatalytic $CO_2$ reduction performance. Appl. Catal. B: Environ., 340, 123247.
271. Mandal, A.; Maitra, S.; Roy, S.; Hazra, B.; Ray, K.; Kargupta, K. (2023). Selective photo-reduction of $CO_2$ to methanol using Cu-doped 1D-$Bi_2S_3$/rGO nanocomposites under visible light irradiation. New J. Chem., 47, 1422-1434.
272. Sorcar, S.; Thompson, J.; Hwang, Y.; Park, Y. H.; Majima, T.; Grimes, C. A.; Durrant, J. R.; In, S.-I. (2018). High-rate solar-light photoconversion of $CO_2$ to fuel: controllable transformation from C1 to C2 products. Energy Environ. Sci., 11, 3183-3193.
273. Mishra, R. P.; Mrinalini, M.; Kumar, N.; Bastia, S.; Chaudhary, Y. S. (2023). Efficient Photocatalytic $CO_2$ Reduction with High Selectivity for Ethanol by Synergistically Coupled MXene-Ceria and the Charge Carrier Dynamics. Langmuir, 39 (40), 14189–14203.
274. Alemi, A.A.; Kashfi, R.; Shabani, B. (2014). Preparation and characterization of novel Ln ($Gd^{3+}$, $Ho^{3+}$ and $Yb^{3+}$)-doped $Bi_2MoO_6$ with Aurivillius layered structures and photocatalytic activities under visible light irradiation. J. Mol. Catal. A-Chem., 392, 290–298.
275. Anisimov, V. I.; Zaanen, J.; Andersen, O. K. (1991). Band theory and Mott insulators: Hubbard U instead of Stoner I. Phys. Rev. B., 44, 943-954.
276. Ahmadi, M., Alavi, S. M., & Larimi, A. (2023). Pt–Cu@$Bi_2MoO_6$/$TiO_2$ Photocatalyst for $CO_2$ Reduction. Inorganic Chemistry, 62(49), 20372–20389.
277. Dai, W.; Xiong, W.; Yu, J.; Zhang, S.; Li, B.; Yang, L.; Wang, T.; Luo, X.; Zou, J.; Luo, S. (2020). $Bi_2MoO_6$ Quantum Dots In Situ Grown on Reduced Graphene Oxide Layers: A Novel Electron-Rich Interface for Efficient $CO_2$ Reduction. ACS Appl. Mater. Interfaces., 12 (23), 25861–25874.

278. Dai, W.; Hu, X.; Wang, T.; Xiong, W.; Luo, X.; Zou, J. (2018). Hierarchical $CeO_2/Bi_2MoO_6$ heterostructured nanocomposites for photoreduction of $CO_2$ into hydrocarbons under visible light irradiation. Appl. Surf. Sci., 434, 481-491.
279. Zhao, D.; Xuan, Y.; Zhang, K.; Liu, X. (2021). Highly Selective Production of Ethanol Over Hierarchical $Bi@Bi_2MoO_6$ Composite via Bicarbonate-Assisted Photocatalytic $CO_2$ Reduction. ChemSusChem, 14 (16), 3293-3302.
280. Zhang, X.; Wang, H.; An, W.; Guo, H.; Liu, L.; Cui, W. (2023). Ionic liquid promotes the efficient photocatalytic reduction of $CO_2$ by Cu nanodots modified oxygen-vacancy $Bi_2MoO_6$. Appl. Surf. Sci., 641, 158464.
281. Cheng, M.; Yang, S.; Chen, R.; Zhu, X.; Liao, Q.; Huang, Y. (2017). Int. J. Hydrogen Energy, 42 (15), 9722-9732.
282. Lertthanaphol, N.; Pienutsa, N.; Chusri, K.; Sornsuchat, T.; Chanthara, P.; Seeharaj, P.; K.-Lohsoontorn, P.; Srinives, S. (2021). One-Step Hydrothermal Synthesis of Precious Metal-Doped Titanium Dioxide−Graphene Oxide Composites for Photocatalytic Conversion of $CO_2$ to Ethanol. ACS Omega, 6, 35769−35779.
283. Das, R.; Das, K.; Ray, B.; Vinod, C. P.; Peter, S. C. (2022). Green transformation of $CO_2$ to ethanol using water and sunlight by the combined effect of naturally abundant red phosphorus and $Bi_2MoO_6$. Energy Environ. Sci., 15, 1967-1976.
284. Yergaziyeva, G., Kuspanov, Z., Mambetova, M., Khudaibergenov, N., Makayeva, N., & Daulbayev, C. (2024). Advancements in catalytic, photocatalytic, and electrocatalytic $CO_2$ conversion processes: Current trends and future outlook. Journal of $CO_2$ Utilization, 80, 102682.
285. Sun, Z., Dong, J., Chen, C., Zhang, S., & Zhu, Y. (2021). Photocatalytic and electrocatalytic $CO_2$ conversion: from fundamental principles to design of catalysts. Journal of Chemical Technology and Biotechnology, 96(5), 1161–1175.
286. Muiruri, J. K., Ye, E., Zhu, Q., Loh, X. J., & Li, Z. (2022). Recent advance in nanostructured materials innovation towards photocatalytic $CO_2$ reduction. Applied Catalysis. A, General, 648, 118927.
287. Muiruri, J. K., Ye, E., Zhu, Q., Loh, X. J., & Li, Z. (2022). Recent advance in nanostructured materials innovation towards photocatalytic $CO_2$ reduction. Applied Catalysis. A, General, 648, 118927.
288. Ren, G., Wei, Z., Liu, S., Shi, M., Li, Z., & Meng, X. (2022). Recent review of $Bi_xMO_y$ (M=V, Mo, W) for photocatalytic $CO_2$ reduction into solar fuels. Chemosphere, 307, 136026
289. Wang, S., Wang, L., & Huang, W. (2020). Bismuth-based photocatalysts for solar energy conversion. Journal of Materials Chemistry. A, 8(46), 24307–24352.
290. Hu, X., Guo, R. T., Chen, X., Bi, Z. X., Wang, J., & Pan, W. G. (2022). Bismuth-based Z-scheme structure for photocatalytic $CO_2$ reduction: A review. Journal of Environmental Chemical Engineering, 10(6), 108582.
291. Zhong, X., Li, Y., Wu, H., & Xie, R. (2023). Recent progress in $BiVO_4$-based heterojunction nanomaterials for photocatalytic applications. Materials Science & Engineering. B, Solid-state Materials for Advanced Technology, 289, 116278.
292. Sommers, J. M., Alderman, N. P., Viasus, C. J., & Gambarotta, S. (2017). Revisiting the behaviour of $BiVO_4$ as a carbon dioxide reduction photo-catalyst. Dalton Transactions, 46(19), 6404–6408.
293. Khan, N., Stelo, F., Santos, G. H., Rossi, L. M., Gonçalves, R. V., & Wender, H. (2022). Recent advances on Z-scheme engineered $BiVO_4$-based semiconductor photocatalysts for $CO_2$ reduction: A review. Applied Surface Science Advances, 11, 100289.

294. Hunge, Y. M., Uchida, A., Tominaga, Y., Fujii, Y., Yadav, A. A., Kang, S. W., Suzuki, N., Shitanda, I., Kondo, T., Itagaki, M., Yuasa, M., Gosavi, S., Fujishima, A., & Terashima, C. (2021). Visible Light-Assisted Photocatalysis Using Spherical-Shaped $BiVO_4$ Photocatalyst. Catalysts, 11(4), 460.
295. Kumar, A., Singh, P., Khan, A. a. P., Van Le, Q., Nguyen, V. H., Thakur, S., & Raizada, P. (2022). $CO_2$ photoreduction into solar fuels via vacancy engineered bismuth-based photocatalysts: Selectivity and mechanistic insights. Chemical Engineering Journal, 439, 135563.
296. Lawal, A. T. (2019). Graphene-based nano composites and their applications. A review. Biosensors & Bioelectronics/Biosensors & Bioelectronics (Online), 141, 111384.
297. Li, X., Shen, R., Ma, S., Chen, X., & Xie, J. (2018). Graphene-based heterojunction photocatalysts. Applied Surface Science, 430, 53–107.
298. Xiang, Q., & Yu, J. (2013). Graphene-Based Photocatalysts for Hydrogen Generation. The Journal of Physical Chemistry Letters, 4(5), 753–759.
299. Xu, H., Ma, L., & Jin, Z. (2018). Nitrogen-doped graphene: Synthesis, characterizations and energy applications. Journal of Energy Chemistry, 27(1), 146–160.
300. Zhang, W., Zhou, Q., Li, N., & Li, M. (2023). Enhanced photocatalytic reduction of $CO_2$ into $CH_4$ over N, Eu co-doped TiO2: Insight into the synergistic effect of N and Eu. Applied Catalysis. A, General, 650, 118977.
301. He, L., Zhang, W., Liu, S., & Zhao, Y. (2021). Three-dimensional porous N-doped graphitic carbon framework with embedded CoO for photocatalytic $CO_2$ reduction. Applied Catalysis. B, Environmental, 298, 120546.
302. Yan, X., Gao, B., Zheng, X., Cheng, M., Zhou, N., Liu, X., Du, L., Yuan, F., Wang, J., Cui, X., Zhang, G., Kong, W., & Xu, Q. (2024). Cooperatively tailored surface frustrated Lewis pairs and N-doping on $CeO_2$ for photocatalytic $CO_2$ reduction to high-value hydrocarbon products. Applied Catalysis. B, Environmental, 343, 123484.
303. Liu, B., Liu, M., Tian, L., Guo, F., Xia, Y., Wang, T., Hu, W., & Guan, R. (2021). A novel route to porous N-doping carbon grafted carbon nitride for enhanced photocatalytic activity on $CO_2$ reduction. Applied Surface Science, 540, 148411.
304. Kalpana, S., Bhat, V. S., Hegde, G., & Anantharamaiah, P. (2024). Electrochemical performance of $Zn_xCo_{3-x}O_4$/N-doped rGO nanocomposites for energy storage application. Materials Chemistry and Physics, 319, 129331.
305. Wang, Y., Wang, H., Zhang, T. C., Yuan, S., & Liang, B. (2020). N-doped porous carbon derived from rGO-Incorporated polyphenylenediamine composites for $CO_2$ adsorption and supercapacitors. Journal of Power Sources, 472, 228610.
306. Xiao, J., Wang, Y., Zhang, T. C., & Yuan, S. (2021). rGO/N-porous carbon composites for enhanced $CO_2$ capture and energy storage performances. Journal of Alloys and Compounds, 857, 157534.
307. Kamal, K. M., Narayan, R., Chandran, N., Popović, S., Nazrulla, M. A., Kovač, J., Vrtovec, N., Bele, M., Hodnik, N., Kržmanc, M. M., & Likozar, B. (2022). Synergistic enhancement of photocatalytic $CO_2$ reduction by plasmonic Au nanoparticles on $TiO_2$ decorated N-graphene heterostructure catalyst for high selectivity methane production. Applied Catalysis. B, Environmental, 307, 121181.
308. Hiragond, C. B., Lee, J., Kim, H., Jung, J. W., Cho, C. H., & In, S. I. (2021). A novel N-doped graphene oxide enfolded reduced titania for highly stable and selective gas-phase photocatalytic $CO_2$ reduction into $CH_4$: An in-depth study on the interfacial charge transfer mechanism. Chemical Engineering Journal, 416, 127978.

309. Wang, L., Zhu, B., Cheng, B., Zhang, J., Zhang, L., & Yu, J. (2021). In-situ preparation of $TiO_2$/N-doped graphene hollow sphere photocatalyst with enhanced photocatalytic $CO_2$ reduction performance. Cuihua Xuebao/Chinese Journal of Catalysis, 42(10), 1648–1658.
310. Zhang, J., Shao, S., Zhou, D., Xu, Q., & Wang, T. (2021). ZnO nanowire arrays decorated 3D N-doped reduced graphene oxide nanotube framework for enhanced photocatalytic $CO_2$ reduction performance. Journal of $CO_2$ Utilization, 50, 101584.
311. Huang, L., Mo, S., Zhao, X., Zhou, J., Zhang, Y., Zhou, X., Fan, Y., Xie, Q., & Ye, D. (2024). Co-ZIF-derived dual Co and $Co_3S_4$ nanoparticles encapsulated in N-doped carbon matrix for efficient photocatalytic $CO_2$ reduction. Journal of Environmental Chemical Engineering, 12(3), 112566.
312. Lin, L. Y., Nie, Y., Kavadiya, S., Soundappan, T., & Biswas, P. (2017). N-doped reduced graphene oxide promoted nano $TiO_2$ as a bifunctional adsorbent/photocatalyst for $CO_2$ photoreduction: Effect of N species. Chemical Engineering Journal, 316, 449–460.
313. Bie, C., Zhu, B., Xu, F., Zhang, L., & Yu, J. (2019). In Situ Grown Monolayer N-Doped Graphene on CdS Hollow Spheres with Seamless Contact for Photocatalytic $CO_2$ Reduction. Advanced Materials, 31(42).
314. Li, X., Wei, D., Ye, L., & Li, Z. (2019). Fabrication of $Cu_2O$-RGO/$BiVO_4$ nanocomposite for simultaneous photocatalytic $CO_2$ reduction and benzyl alcohol oxidation under visible light. Inorganic Chemistry Communications/Inorganic Chemistry Communications (Online), 104, 171–177.
315. Chen, L., Zhang, M., Yang, J., Li, Y., Sivalingam, Y., Shi, Q., Xie, M., & Han, W. (2019). Synthesis of $BiVO_4$ quantum dots/reduced graphene oxide composites for $CO_2$ reduction. Materials Science in Semiconductor Processing, 102, 104578.
316. Tahir, M., Iqbal, T., Kiran, H., & Hasan, A. (2019). Insighting role of reduced graphene oxide in $BiVO_4$ nanoparticles for improved photocatalytic hydrogen evolution and dyes degradation. International Journal of Energy Research, 43(6), 2410–2417.
317. Kannan, N., Venkatesh, P. S., Babu, M. G., Paulraj, G., & Jeganathan, K. (2023). Hydrothermally synthesized rGO-$BiVO_4$ nanocomposites for photocatalytic degradation of RhB. Chemical Physics Impact, 6, 100230.
318. Liu, C., Zhang, L., Liu, R., Gao, Z., Yang, X., Tu, Z., Yang, F., Ye, Z., Cui, L., Xu, C., & Li, Y. (2016). Hydrothermal synthesis of N-doped $TiO_2$ nanowires and N-doped graphene heterostructures with enhanced photocatalytic properties. Journal of Alloys and Compounds, 656, 24–32.
319. Ren, Y., & Li, W. (2024). Fabrication of N/K-doped $TiO_2$-Ag nanospheres with efficient charge transfer for enhanced photocatalytic $CO_2$ reduction into $CH_4$. Molecular Catalysis, 562, 114187.
320. Appavu, B., Thiripuranthagan, S., Ranganathan, S., Erusappan, E., & Kannan, K. (2018). $BiVO_4$/N-rGO nano composites as highly efficient visible active photocatalyst for the degradation of dyes and antibiotics in eco system. Ecotoxicology and Environmental Safety, 151, 118–126.
321. Yang, H., Wang, P., Wang, D., Zhu, Y., Xie, K., Zhao, X., Yang, J., & Wang, X. (2017). New Understanding on Photocatalytic Mechanism of Nitrogen-Doped Graphene Quantum Dots-Decorated $BiVO_4$ Nanojunction Photocatalysts. ACS Omega, 2(7), 3766–3773.
322. He, Y., Yin, L., Yuan, N., & Zhang, G. (2024). Adsorption and activation, active site and reaction pathway of photocatalytic $CO_2$ reduction: A review. Chemical Engineering Journal, 481, 148754.

NJC

ROYAL SOCIETY OF CHEMISTRY

PAPER



Cite this: *New J. Chem.*, 2023, **47**, 1422

# Selective photo-reduction of $CO_2$ to methanol using Cu-doped 1D-$Bi_2S_3$/rGO nanocomposites under visible light irradiation†

Arindam Mandal,[a] Soumyajit Maitra,[b] Subhasis Roy,[b] Baisakhi Hazra,[b] Koustuv Ray[c] and Kajari Kargupta*[a]

A novel Cu-doped one dimensional (1D) $Bi_2S_3$ rod-shaped nanocapsule/rGO composite is explored as a photocatalyst for selective reduction of $CO_2$ to methanol. In particular, the effects of Cu doping of rGO supported $Bi_2S_3$ on band gap tuning and on product selectivity are investigated. $Bi_2S_3$ rod-shaped nanocapsules and 0.5, 1, and 2 weight percent Cu-doped $Bi_2S_3$/rGO are synthesised through a hydrothermal approach. The photocatalysts are characterized by XRD, FTIR, UV-Vis spectroscopy, photoluminescence spectroscopy, X-ray photoelectron spectroscopy, and SEM, TEM and EDX analysis. It is revealed that Cu-doped $Bi_2S_3$/rGO for all different compositions offers selective and enhanced production of methanol compared to undoped $Bi_2S_3$/rGO, pristine $Bi_2S_3$, and Cu-doped $Bi_2S_3$ which produce formic acid along with methanol. The optimum 1 weight percent Cu-doped $Bi_2S_3$/rGO photocatalyst, exhibiting the smallest band gap and the lowest rate of recombination of electron–hole pairs, offers the highest photocatalytic activity of 719 μmol $g_{cat.}^{-1}$ $h^{-1}$. DFT studies corroborate the experimental finding of a drastic reduction of the band gap (1.36 eV) of Cu-doped $Bi_2S_3$/graphene and unveil that Cu 3d–C 2p hybridization as well as enhancement of Bi 6p–C 2p hybridization in the presence of copper significantly increases the overall DOS of the system at the Fermi level, resulting in enhancement of electronic conductivity and charge transfer; further deformation in the graphene sheets due to the presence of Cu-$Bi_2S_3$ creates $CO_2$ trapping sites for its efficient adsorption and selective photoreduction.

Received 6th August 2022,
Accepted 28th November 2022

DOI: 10.1039/d2nj03892g

rsc.li/njc

## 1. Introduction

An enormous volume of carbon dioxide is released into the atmosphere due to the escalated use of fossil fuels, resulting in global warming and climate change.[1] Therefore, scientists and researchers across the world are continuously looking for a commercially acceptable conversion of $CO_2$ into value-added chemicals like hydrocarbons. The conversion of $CO_2$ into fuel not only reduces its accumulation in the atmosphere but also allows it to be captured as a fuel feedstock.[2–4] There are various techniques for $CO_2$ conversion based on chemical, biological, thermal, electrochemical, and photochemical methods. Among the different $CO_2$ conversion methods, photocatalytic reduction of $CO_2$ has been recognised as a sustainable proposition as it utilises renewable solar energy and water, both of which are abundant and affordable.[5–8] Photo-reduction of $CO_2$, using solar energy (photons) and water as the reactants to produce hydrocarbons, is an economically viable and environmentally friendly approach. In this regard, a wide variety of semiconducting materials, namely ZnO, CdS, $Fe_2O_3$, $CeO_2$, $WO_3$, CuO, bismuth-based materials, and transition metal complexes, have been extensively investigated for photocatalytic conversion of $CO_2$ to valuable products.[9–13] Most semiconductor materials with a large band gap are incapable of converting $CO_2$ into hydrocarbons in the presence of visible light. The major bottlenecks of this photocatalytic process are poor visible light absorption, fast electron–hole recombination, and multiple products, which lead to poor conversion efficiency and selectivity.[11–13] In order to overcome these obstacles, band gap engineering must be performed by incorporating reduced graphene oxide and metals or non-metals for boosting the conversion efficiency and tailoring product selectivity.[12]

During the last few years, bismuth-based photocatalysts have been gaining a lot of interest in the application of photocatalytic $CO_2$ reduction to solar fuels for their visible light

[a] *Chemical Engineering Department, Jadavpur University, Kolkata, 700032, India. E-mail: karguptakajari2011@gmail.com*
[b] *Chemical Engineering Department, Calcutta University, Kolkata, India*
[c] *Department of Chemical Engineering, Indian Institute of Technology Kharagpur, West Bengal, India*

† Electronic supplementary information (ESI) available. See DOI: https://doi.org/10.1039/d2nj03892g

 

Journal of MATERIALS RESEARCH

Article
DOI:10.1557/s43578-024-01352-2

# Enhanced yield of methanol using rGO-$Bi_2S_3$/CuO heterojunction photocatalyst for $CO_2$ reduction

Arindam Mandal[1], Guruprasad Bhattacharya[2], Kajari Kargupta[1,a)]

[1] Department of Chemical Engineering, Jadavpur University, Kolkata, India
[2] Department of Chemical Engineering, University of Calcutta, Kolkata, India
[a)] Address all correspondence to this author. e-mail: karguptakajari2011@gmail.com; kajari.kargupta@jadavpuruniversity.in

Received: 7 November 2023; accepted: 22 April 2024

**A visible light-induced rGO-$Bi_2S_3$/CuO S-scheme heterojunction photocatalyst is explored for the production of methanol and formic acid through photocatalytic $CO_2$ reduction. In this work, the effect of CuO loading on rGO-$Bi_2S_3$ nano-hollow flower composite are investigated to improve the yield and selectivity of methanol production. The synthesised rGO-$Bi_2S_3$/CuO nanocomposite, being a highly efficient and robust photocatalyst, exhibits the maximum methanol yield of 423.52 µmol $g_{cat.}^{-1}$ $h^{-1}$ along with formic acid. CuO loading on rGO-$Bi_2S_3$ is responsible for achieving the maximum photocatalytic activity of the rGO-$Bi_2S_3$/CuO photocatalyst, the narrowest band gap, the lowest recombination rate of electron–hole pairs, and the increased specific surface area for $CO_2$ capture among all the related photocatalysts, rGO-$Bi_2S_3$, pristine $Bi_2S_3$, and $Bi_2S_3$/CuO nanocomposite. The selectivity of methanol is improved to 98.6% by the rGO-$Bi_2S_3$/CuO heterojunction photocatalyst. The absorption edge (652.4 nm) of the rGO-$Bi_2S_3$/CuO photocatalyst clearly exhibits outstanding visible light absorption and enhanced photo carrier transportation power.**

## Introduction

The increased concentration of the greenhouse gas $CO_2$ in the atmosphere as a result of excessive usage of fossil fuels has a detrimental impact on global climate change. As a result, converting $CO_2$ to sustainable fuels and chemicals is a viable solution to alleviate the world's energy crises and environmental issues [1, 2]. Combining $CO_2$ reduction with renewable energy sources, particularly solar energy, is an intriguing strategy for achieving green conversion, as $CO_2$ can be directly converted into methanol ($CH_3OH$), carbon monoxide (CO), ethanol ($C_2H_5OH$), formic acid (HCOOH), and other compounds in an aqueous solution [2, 3]. Methanol is one of the most anticipated liquid $CO_2$ reduction products due to its suitability for fuel delivery and energy storage. Combining $CO_2$ reduction with renewable energy sources, particularly solar energy, is an exciting technique for achieving green conversion, known as photocatalytic $CO_2$ reduction [3–5]. Because of the increased stability of the $CO_2$ molecule, overall photocatalytic $CO_2$ reduction has a complicated multi-step mechanism. In this process, photon-illuminated semiconductor surfaces generate pairs of electrons and holes, which are transported to the semiconductor surface for the reduction and oxidation of $CO_2$ and $H_2O$, respectively, contending with the severe undesired electron–hole recombination. Due to the inadequate photo-generated electrons and photons, the photoreduction of $CO_2$ to methanol suffers from low conversion and poor selectivity [4–6].

Numerous semiconductor materials have been investigated for their photocatalytic activity, including $TiO_2$ [7], ZnO [8], $Fe_2O_3$ [9], CoO [10, 11], $Co_3O_4$ [12, 13], $WO_3$ [14, 15], $Bi_2S_3$ [16–18], and CuO [19–22]. Among all photocatalysts, bismuth sulphide ($Bi_2S_3$), a useful metal chalcogenide, has versatile embryonic photocatalytic uses due to its high dielectric permittivity, lamellar structure, broad visible light absorption capacity, low bandgap ($E_g$) (1.3 eV), and particularly changeable energy band levels [23–26]. Due to their special characteristics of minimal toxicity and a high bismuth electron count, $Bi_2S_3$ nanoparticles have been acknowledged as one of the most advantageous semiconductors in the healthcare industry [26–28]. Additionally, the distinctive form and tubular crystal structure of $Bi_2S_3$ nanostructures, exhibiting higher charge capacity and altering physical properties, have drawn the attention of researchers. However, $Bi_2S_3$ has a low separation efficiency due to the small





Arindam Mandal

Kajari Kargupta

Professor
CHEMICAL ENGINEERING DEPARTMENT
JADAVPUR UNIVERSITY
Kolkata-700 032